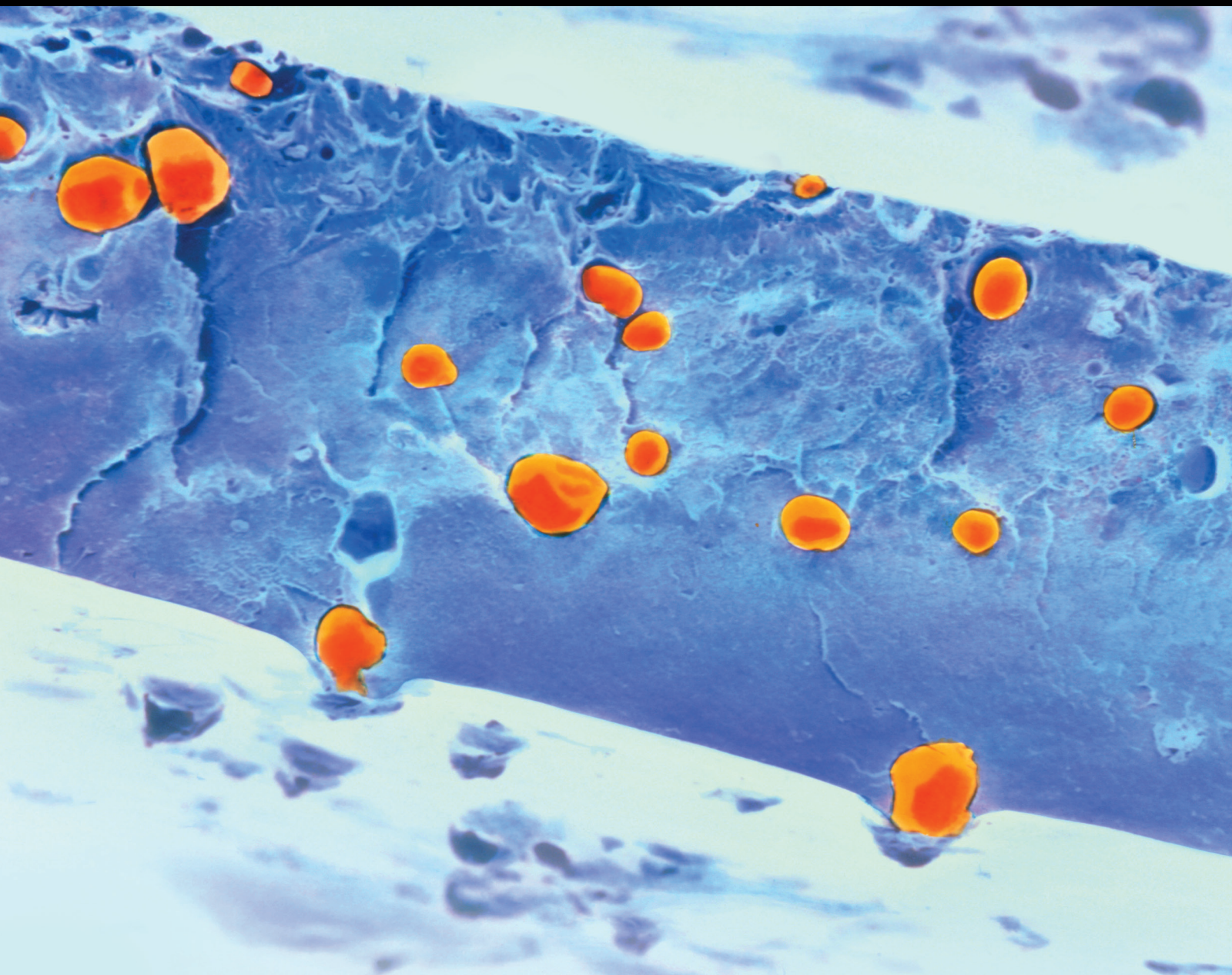


Recent Advances in Cellulose-Based Materials: Synthesis, Characterization, and Their Applications

Guest Editors: Xue-Ming Zhang, Ming-Guo Ma, Jun Yang, Zhouyang Xiang, Jie-Fang Zhu, and Yatimah Alias





Recent Advances in Cellulose-Based Materials: Synthesis, Characterization, and Their Applications

**Recent Advances in Cellulose-Based
Materials: Synthesis, Characterization,
and Their Applications**

Guest Editors: Xue-Ming Zhang, Ming-Guo Ma, Jun Yang,
Zhouyang Xiang, Jie-Fang Zhu, and Yatimah Alias



Copyright © 2016 Hindawi Publishing Corporation. All rights reserved.

This is a special issue published in "International Journal of Polymer Science." All articles are open access articles distributed under the Creative Commons Attribution License, which permits unrestricted use, distribution, and reproduction in any medium, provided the original work is properly cited.

Editorial Board

Domenico Acierno, Italy
Sharif Ahmad, India
Mats R. Andersson, Australia
Luc Averous, France
Massimiliano Barletta, Italy
Christopher Batich, USA
Giuseppe Battaglia, UK
Marc Behl, Germany
Laurent Billon, France
David G. Bucknall, USA
Andrea Camposeo, Italy
Wen Shyang Chow, Malaysia
Jesper Christiansen, Denmark
Yoshiki Chujo, Japan
Angel Concheiro, Spain
Marek Cypryk, Poland
Li Ming Dai, USA
Yulin Deng, USA
Maria Laura Di Lorenzo, Italy
Eliane Espuche, France
Antonio Facchetti, USA
Marta Fernández-García, Spain
Benny Dean Freeman, USA
Jean-François Gérard, France
Peng He, USA
Jan-Chan Huang, USA
Wei Huang, China
Nabil Ibrahim, Egypt
Tadashi Inoue, Japan

Avraam I. Isayev, USA
Koji Ishizu, Japan
Patric Jannasch, Sweden
Nobuhiro Kawatsuki, Japan
J.M. Kenny, Italy
Mubarak A. Khan, Bangladesh
Ruhul A. Khan, Canada
Saad Khan, USA
Jui-Yang Lai, Taiwan
Jose Ramon Leiza, Spain
Guiping Ma, China
Evangelos Manias, USA
Ulrich Maschke, France
Jani Matisons, Australia
Geoffrey R. Mitchell, UK
Subrata Mondal, India
Christian Nielsen, UK
Toribio F. Otero, Spain
Qinmin Pan, Canada
Alessandro Pegoretti, Italy
"Onder Pekcan, Turkey
Zhonghua Peng, USA
Antje Potthast, Austria
Debora Puglia, Italy
Miriam Rafailovich, USA
Arthur J. Ragauskas, USA
Subramaniam Ramesh, Malaysia
Bernabé L. Rivas, Chile
Juan Rodriguez-Hernandez, Spain

Hossein Roghani-Mamaqani, Iran
Pietro Russo, Italy
Mehdi Salami-Kalajahi, Iran
Erol Sancaktar, USA
Albert Schenning, Netherlands
Matthias Schnabelrauch, Germany
Shu Seki, Japan
Vitor Sencadas, Australia
Robert A. Shanks, Australia
Mikhail Shtilman, Russia
Basavarajaiah Siddaramaiah, India
Dennis W. Smith Jr., USA
Atsushi Sudo, Japan
Kohji Tashiro, Japan
Hideto Tsuji, Japan
Masaki Tsuji, Japan
Stefano Turri, Italy
Hiroshi Uyama, Japan
Cornelia Vasile, Romania
Alenka Vesel, Slovenia
Yakov S. Vygodskii, Russia
De-Yi Wang, Spain
Qinglin Wu, USA
Frederik Wurm, Germany
Huining Xiao, Canada
Yiqi Yang, USA
Long Yu, Australia
Philippe Zinck, France

Contents

Recent Advances in Cellulose-Based Materials: Synthesis, Characterization, and Their Applications

Xue-Ming Zhang, Ming-Guo Ma, Jun Yang, Zhouyang Xiang, Jie-Fang Zhu, and Yatimah Alias
Volume 2016, Article ID 8730573, 2 pages

Application of CMC as Thickener on Nanoemulsions Based on Olive Oil: Physical Properties and Stability

C. Arancibia, R. Navarro-Lisboa, R. N. Zúñiga, and S. Matiacevich
Volume 2016, Article ID 6280581, 10 pages

Deposition of Ibuprofen Crystals on Hydroxypropyl Cellulose/Polyacrylamide Gel: Experimental and Mathematic Modeling Releasing

Claudia Alicia Castillo-Miranda, Ana Beatriz Morales-Cepeda, Carlos Fernando Castro-Guerrero, Homero Salas-Papayanopolos, Hugo Alberto Velasco-Ocejo, Jorge Alberto González-Sánchez, Ulises Paramo-Garcia, and Hugo De Alva-Salazar
Volume 2016, Article ID 2634104, 8 pages

Bacteriostatic Substrate by Conductivity Method and Electric Spark Discharge Method Combined with Electrospinning for Silver Dressing

Kuo-Hsiung Tseng, Chaur-Yang Chang, Meng-Yun Chung, and Ya-Lan Tang
Volume 2016, Article ID 9425358, 10 pages

Reaction Behavior of Cellulose in the Homogeneous Esterification of Bagasse Modified with Phthalic Anhydride in Ionic Liquid 1-Allyl-3-methylimidazium Chloride

Hui-Hui Wang, Xue-Qin Zhang, Piao Long, Ai-Ping Zhang, Chuan-Fu Liu, and Run-Cang Sun
Volume 2016, Article ID 2361284, 9 pages

Homogeneous Modification of Sugarcane Bagasse by Graft Copolymerization in Ionic Liquid for Oil Absorption Application

Ming-Jie Chen, Xue-Qin Zhang, Chuan-Fu Liu, and Qing-Shan Shi
Volume 2016, Article ID 6584597, 7 pages

Waste Composite Sensor Designed by Cellulose and Activated Carbon as Ethylene Absorber

S. Ummartyotin and C. Pechyen
Volume 2016, Article ID 3841410, 7 pages

Eggshell and Bacterial Cellulose Composite Membrane as Absorbent Material in Active Packaging

S. Ummartyotin, P. Pisitsak, and C. Pechyen
Volume 2016, Article ID 1047606, 8 pages

Extraction and Hydrophobic Modification of Cotton Stalk Bark Fiber

Ya-Yu Li, Guang-Ming Du, Xin-Jie Feng, Ya-Wei Mu, and De-Qiang Li
Volume 2016, Article ID 8769360, 6 pages

Synthesis and Characterization of Uniform Spherical Nanoporous TiO₂ Aerogel Templated by Cellulose Alcohol-Gel with Enhanced Photocatalytic Activity

Zhiming Liu, Peng Wu, Shaoli Yang, Haiying Wang, and Chunde Jin
Volume 2016, Article ID 9351725, 8 pages



Self-Shrinkage Behaviors of Waste Paper Fiber Reinforced Cement Paste considering Its Self-Curing Effect at Early-Ages

Zhengwu Jiang, Xiuyan Guo, Wenting Li, and Qing Chen

Volume 2016, Article ID 8690967, 12 pages

Editorial

Recent Advances in Cellulose-Based Materials: Synthesis, Characterization, and Their Applications

Xue-Ming Zhang,¹ Ming-Guo Ma,¹ Jun Yang,² Zhouyang Xiang,³
Jie-Fang Zhu,⁴ and Yatimah Alias⁵

¹Beijing Key Laboratory of Lignocellulosic Chemistry, College of Materials Science and Technology, Beijing Forestry University, Beijing 100083, China

²University of British Columbia, Vancouver, BC, Canada

³University of Wisconsin-Madison, Madison, WI, USA

⁴Department of Materials Chemistry, Ångström Laboratory, Uppsala University, 75121 Uppsala, Sweden

⁵University of Malaya, Kuala Lumpur, Malaysia

Correspondence should be addressed to Xue-Ming Zhang; xm_zhang@bjfu.edu.cn

Received 5 October 2016; Accepted 9 October 2016

Copyright © 2016 Xue-Ming Zhang et al. This is an open access article distributed under the Creative Commons Attribution License, which permits unrestricted use, distribution, and reproduction in any medium, provided the original work is properly cited.

Recently, sustainable energy sources and environmental problems have received more attention. As one of the most abundant polysaccharides and renewable resources on the earth, cellulose is widely used in environmental protection, water treatment, biomedical, and other fields owing to its particular characteristics such as mechanical properties, biodegradation, biocompatibility, and low toxicity. More importantly, cellulose could be used as an important resource for the transform to high value-added bioethanol, biomaterials, and biochemicals. Based on its wide applications and excellent properties, this special issue focused on the synthesis and applications of cellulose-based materials and explores the new synthetic methods, characterization analysis techniques, and high value-added applications fields of cellulose materials.

In this special issue, we received 18 papers for submission. Finally, 10 papers were selected for publication. Firstly, we thank the great contributions and enthusiastic support from the authors to the special issue.

Developments of novel cellulose-based materials open up new prospects for cellulose in application of reinforcement, food packaging, and photocatalytic activity. The paper titled “Self-Shrinkage Behaviors of Waste Paper Fiber Reinforced Cement Paste considering Its Self-Curing Effect at Early-Ages” reports self-shrinkage behaviors of waste paper fiber

reinforced cement paste and explored its self-curing effect at early ages. The authors discovered that the waste paper fibers could mitigate the self-shrinkage of cement paste under the wet mixing condition, which displayed significant self-shrinkage cracking control while providing some internal curing. In addition, the paper titled “Extraction and Hydrophobic Modification of Cotton Stalk Bark Fiber” reports the extraction and hydrophobic modification cotton stalk bark fiber. These as-modified materials are expected to be a filler with strengthening effect in wood plastic composites fields. Moreover, the synthesis of uniform spherical nanoporous TiO₂ aerogel templated by cellulose aerogel has been reported in the paper titled “Synthesis and Characterization of Uniform Spherical Nanoporous TiO₂ Aerogel Templated by Cellulose Alcohol-Gel with Enhanced Photocatalytic Activity.” It was found that TiO₂ aerogels displayed uniform sphere shape, good internal morphology, and high specific surface area of 149.95 m² g⁻¹. The authors found that these cellulose aerogels displayed the enhanced photocatalytic activity, which had a high degradation ratio of 92.9% on methyl orange dye.

The paper titled “Waste Composite Sensor Designed by Cellulose and Activated Carbon as Ethylene Absorber” reports the design of waste composite sensor by cellulose and activated carbon as ethylene absorber. It possessed good performance in specific surface area and porosity after chemical

modification. More importantly, these materials displayed the increase ethylene gas adsorption for food packaging.

After that, they applied eggshell and bacterial cellulose composite membrane as absorbent material in active packaging, in which the flexibility and thermal stability of composite were enhanced. These composites also displayed good adsorption experiment on water and vegetable oil capacity due to the existence of eggshell in bacterial cellulose composite. Authors indicated that these cellulose-based composites exhibited the applications potential for absorbent material in active packaging.

Ionic liquid is one of excellent solvents for dissolving of cellulose. The paper titled "Homogeneous Modification of Sugarcane Bagasse by Graft Copolymerization in Ionic Liquid for Oil Adsorption Application" reports the homogeneous modification of sugarcane bagasse by graft copolymerization in ionic liquid for oil adsorption application. Experiment results indicated that the thermal stability of sugarcane bagasse decreased after the homogeneous modification by the graft copolymerization. The study provides an alternative strategy to convert sugarcane bagasse into a value-added material. H. H. Wang et al. researched the reaction behavior of cellulose in the homogeneous esterification of bagasse modified with phthalic anhydride in ionic liquid 1-allyl-3-methylimidazolium chloride. These results provide detailed understanding of the homogenous modification mechanism of lignocellulose.

Moreover, A. B. Morales-Cepeda et al. reported the deposition of ibuprofen crystals on hydroxypropyl cellulose/polyacrylamide gel. K.-H. Tseng et al. combined conductivity method and electric spark discharge method to fabricated bacteriostatic substrate with electrospinning for silver dressing. C. Arancibia et al. investigated the application of CMC as thickener on nanoemulsions based on olive oil.

As mentioned above in the as-reported papers, this special issue provides the recent development of cellulose-based materials. We expect that the rapid progress and further development of these advanced cellulose-based materials will be achieved in the near future.

Acknowledgments

We appreciate the great efforts and contributions from the authors and reviewers to the special issue.

*Xue-Ming Zhang
Ming-Guo Ma
Jun Yang
Zhouyang Xiang
Jie-Fang Zhu
Yatimah Alias*

Research Article

Application of CMC as Thickener on Nanoemulsions Based on Olive Oil: Physical Properties and Stability

C. Arancibia,¹ R. Navarro-Lisboa,¹ R. N. Zúñiga,² and S. Matiacevich¹

¹Food Properties Research Group, Food Science and Technology Department, Facultad Tecnológica, Universidad de Santiago de Chile, Obispo Umaña 050, Estación Central, Santiago, Chile

²Bioprocess Engineering Laboratory, Department of Biotechnology, Universidad Tecnológica Metropolitana, Las Palmeras 3360, Nuñoa, Santiago, Chile

Correspondence should be addressed to C. Arancibia; carla.arancibia@usach.cl

Received 4 June 2016; Accepted 15 September 2016

Academic Editor: Jun Yang

Copyright © 2016 C. Arancibia et al. This is an open access article distributed under the Creative Commons Attribution License, which permits unrestricted use, distribution, and reproduction in any medium, provided the original work is properly cited.

Carboxymethyl cellulose (CMC) is a hydrocolloid with surface activity that could act as emulsifiers in oil-in-water emulsions; however the principal role is that it acts as structuring, thickening, or gelling agent in the aqueous phase. This study aims to evaluate the application of CMC as thickener into nanoemulsions based on olive oil and their influence on particle characteristics, flow behavior, and color. Four nanoemulsions with different oil (5% and 15% w/w olive oil) and CMC (0.5% and 0.75% w/w) concentration and two control samples without CMC added were prepared using Tween 80 as emulsifier. All physical properties studied on nanoemulsions were depending on both oil and CMC concentration. In general, *z*-average particle size varied among 107–121 nm and those samples with 5% oil and CMC were the most polydisperse. The addition of CMC increased anionic charge of nanoemulsions obtaining zeta potential values among –41 and –55 mV. The oil concentration increased both consistency and pseudoplasticity of samples, although samples were more stable to gravitational separation at the highest CMC concentration. Color of nanoemulsions was affected principally by the oil concentration. Finally, the results showed that CMC could be applied in nanoemulsions as thickener increasing their physical stability although modifying their physical properties.

1. Introduction

There has been a growing interest in the use of lipid-based delivery systems, particularly useful for encapsulating and releasing lipophilic bioactive components, including liposomes, conventional emulsions, microemulsions, and nanoemulsions [1–4]. Oil-in-water (O/W) nanoemulsions are a specific type of colloidal dispersion characterizing by very small oil droplet sizes dispersed within an aqueous phase, with each droplet being coated by a protective coating of surface-active molecules and having a radius <100 nm [5–7]. The reduction in the droplet size of O/W emulsions may be beneficial over other types of delivery systems for certain food applications, such as more stability to droplet aggregation and gravitational separation, bulk viscosity, high optical clarity, and its ability to increase the bioavailability of encapsulated active ingredients during digestion [8–11].

Nanoemulsions can be produced from food-grade ingredients using different processing operations, such as mixing, shearing, and homogenization [7]. However, the physicochemical properties of the oil-water interface and homogenization mechanism have a strong impact on physical stability of emulsions. Most polysaccharides behave as emulsion stabilizers by forming an extended network in the continuous phase, which thus becomes highly viscous [11, 12]. Therefore, they can modify the rheological behavior of continuous phase and have an important effect on physical stability of emulsions. These hydrocolloids should be selected according their ability to tailor the desirable physicochemical and sensory attributes such as appearance, texture, and flavor profile [13]. Among food hydrocolloids, cellulose derivatives have gained acceptance for pharmaceutical, cosmetic, food, and packaging uses. They are obtained by replacing the hydroxyl groups with either alkyl or hydroxy-alkyl groups in the cellulose chain.

Carboxymethyl cellulose (CMC), also known as cellulose gum, is an anionic linear polymer, long chain and water soluble, which is manufactured by chemically attaching carboxymethyl groups to the backbone through reacting alkali cellulose with sodium monochloroacetate [14, 15]. Due to its ionic nature, viscosity of CMC dispersions is sensitive to pH and ionic strength, as well as to the presence of other types of electrically charged molecules [14, 16]. In food industry CMC may act as a thickener, emulsion stabilizer, moisture binder, and suspending and improving texture of a wide variety of food products [17] and has the advantage that it is physiologically inert and noncaloric [18]. Besides CMC is thoroughly used because it is odorless and tasteless and forms clear solution without cloudiness or opacity and is commonly used in foods and beverages to prevent gravitational separation of suspended particles and to create desirable textural attributes and mouthfeel [14–16].

In the last time, CMC has been used as an alternative thickener to starch in semisolid dairy products [19–22] due to its technological, sensory, and nutritional advantages. However, less information exists regarding how the CMC acts as thickening agent on food emulsions. In recent studies, the authors reported that CMC macromolecules exhibited a dominating effect on emulsion flow behavior, although the presence and concentration of fat droplets also played an important role [21].

On the other hand, it is known that the intake of oils with healthy features as part of the daily diet helps in preventing cardiovascular disease, hypertension, and some cancers [23, 24]. Olive oil is a natural source of several bioactive compounds as unsaponifiable and soluble fraction, which includes phenolic compounds [25], and has very good organoleptic properties, which could be used in the formulation of foods with healthy features. However, the type of oil not only affects sensory and nutritional properties, but also rheology and stability of emulsions. Each type of oil has its own particular challenges and depends on its physicochemical properties such as solubility, the length-chain of fatty acid, and chemical stability [26, 27]. Thus, it is important to understand the major components influencing the formulation of food emulsions and their effects on physical properties to obtain delivery systems based on nanoemulsions with long-term stability. In this context, the main objective of this work was to evaluate the effect of CMC concentration on physical properties and stability of nanoemulsions with different olive oil content in order to apply CMC as thickener on nanoemulsions.

2. Materials and Methods

2.1. Composition and Preparation of Oil/Water (O/W) Nanoemulsions. Oil-in-water (O/W) nanoemulsions were prepared with extra virgin olive oil (Casta de Peteroa, Terramater S.A., Chile) as dispersed phase, carboxymethyl cellulose (CMC) (CEKOL 30000, Quimatic S.A., Chile) as thickener, Tween 80 (Sigma-Aldrich S.A., France) as emulsifier/surfactant, and purified water from an inverse osmosis system (Vigaflo S.A., Chile). Different formulations were

prepared at two oil concentrations (5 and 15% w/w oil) and two CMC concentrations (0.5 and 0.75% w/w CMC). For each oil concentration, a control sample without thickener was prepared. The surfactant-to-oil ratio used was 6:5, which was previously determined by the optimization of sonication-processing conditions (surfactant-to-oil ratio and sonication time) by Surface Response Methodology (data not shown).

The aqueous phase was prepared dispersing Tween 80 in the purified water using magnetic stirrer (Arex, Velp Scientifica, Italy) at 200 rpm for 30 min at room temperature. Then, oil was added slowly to the aqueous phase and the mixture was stirred using a rotor-stator homogenizer (Wiggen Hauser D130, Germany) at 21200 or 16800 rpm (for samples with 5% or 15% oil, resp.) for 10 min in a water bath at $5 \pm 1^\circ\text{C}$ to avoid warming of samples. In order to obtain nanoemulsions, the coarse emulsions were then homogenized using an ultrasonic processor (VCX500, SONICS & Materials, USA) with a 13 mm (diameter) stainless steel ultrasound probe. Sonication was performed at 80% amplitude, in a pulsed mode of 15 s and 5 s of rest, and at a frequency of 20 Hz, for 21 and 16 min for samples with 5 and 15% oil, respectively.

After that, CMC was added to the O/W nanoemulsions and mixed using a propeller stirrer at 1500 rpm (BS, Velp Scientifica, Italy) at room temperature until their complete dispersion (approximately 40 min). Finally, all samples were transferred to a closed flask and stored under refrigeration ($5 \pm 1^\circ\text{C}$ for 24 h) prior to measurements. At least two batches of each nanoemulsion were prepared.

2.2. Particle Characterization

2.2.1. Particle Size. The droplet size and its distribution for each nanoemulsion were measured by Dynamic Light Scattering (DLS) using a Zetasizer NanoS90 (Malvern Instruments Ltd., UK). A refractive index value of 1.47 was used for the disperse phase (olive oil) and of 1.33 for the continuous phase (water), which was determined by a refractometer (RA-130, Kyoto Electronics, Japan). The particle size of samples was described by the zeta-average particle size (PS) and the size distribution was described by the polydispersity index (PDI) and the size distribution graph. Measurements were made in triplicate for each sample.

2.2.2. Particle Electrical Charge. Based on DLVO (Deyaguin-Landau-Verwey-Overbeek) theory, the emulsion stability is affected by the magnitude of repulsive and attractive forces between emulsion droplets [28]. To evaluate this, zeta potential of each emulsion was determined using a particle electrophoresis instrument (Zetasizer Nano-ZS series, Malvern Instruments, UK). Particle charge data was collected over 30 continuous readings. All measurements were made in duplicate with fresh sample and the zeta potential measurements were reported as the mean of three separate measurements.

2.3. Flow Behavior. Nanoemulsions were measured in a rotational rheometer (RheolabQC, Anton Paar, Austria) using cylinder sensor CC27 for samples with CMC and DG42 for

control samples. At least, two batches of each composition were measured in duplicate at a controlled temperature of $10 \pm 1^\circ\text{C}$ and after loading the samples, it was allowed to stand for 2 min to stabilize and reach the desired temperature.

Flow curve was obtained by recording shear stress values when shearing the samples at linearly increasing shear rates from 1 to 200 s^{-1} through 120 s and down in reverse sequence for the same time [21]. Experimental data from ascending flow curve were fitted to the Ostwald-de Waele model:

$$\sigma = K\dot{\gamma}^n, \quad (1)$$

where σ is the shear stress (Pa), $\dot{\gamma}$ is the shear rate (s^{-1}), K is the consistency index (Pa s^n), and n is the flow behavior index.

2.4. Stability. In order to determine the storage stability, the samples were analyzed using a vertical scan analyzer (Turbiscan MA 2000, Formulacion, France). All emulsions were poured in cylindrical glass tubes (total height ~ 60 mm) and stored for 21 days at 5 and 20°C . The selected temperatures are related to potential storage temperatures of these nanoemulsions. The physical phenomena of destabilization were evaluated through the backscattering (BS) profiles as a function of the sample height into the cylindrical glass.

During storage period, each emulsion showed a cream layer at the top and serum layer at the bottom of cylinders. The extent of creaming was characterized by the creaming index H , since the higher creaming index is representative of the emulsion instability. Normally, the creaming index should start at zero and increase during storage until a fairly constant value, which is reached when all the droplets are packed tightly into the cream layer [16]. This parameter was calculated according to (2) described by Petrovic et al. [29]:

$$\text{Creaming index (\%)} = \left(\frac{H_S}{H_E} \right) \times 100, \quad (2)$$

where H_E is total height of the emulsion (mm) and H_S is the height of cream layer (mm) which were measured as a function of time. All measurements were performed in triplicate for each emulsion.

2.5. Color. Digital images from each nanoemulsion (15 mL samples in a Petri plate of 53 mm diameter and 10 mm height) were captured on a white background through a computer vision system setup, consisting of a black box with four natural daylight (D65) tubes of 18 W (Philips) and a digital camera (Canon Powershot G3 14 MP, Japan) at a distance of 22.5 cm from sample. The camera lens angle and light were at 45° according to Pedreschi et al. [30]. The camera was calibrated using 30 color charts with a colorimeter (CR-410, Konica Minolta, USA). All images were acquired at the same conditions and the camera was remotely controlled by EOS Utility software (Canon, USA). Images were analyzed extracting color values in RGB (red, green, and blue) space using Adobe Photoshop v7.0 program (Adobe Systems Incorporated, USA) and then converted to CIE $L^*a^*b^*$ space, where L^* is black-white component (lightness), a^* is red-green component, and b^* is yellow-blue component.

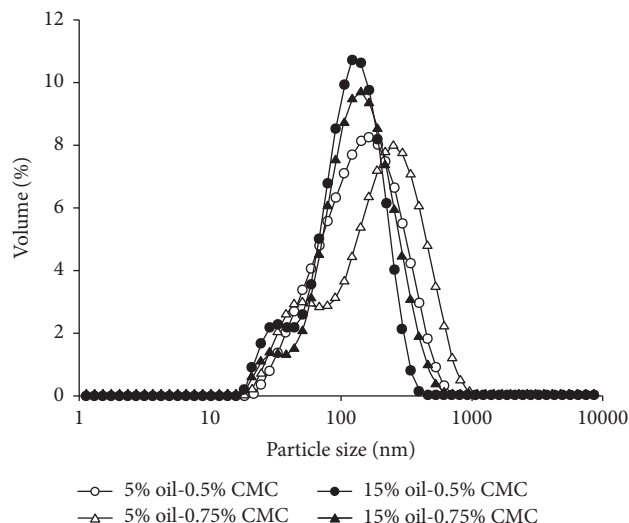


FIGURE 1: Particle size distribution of O/W nanoemulsions with different oil (5%: empty symbols and 15%: filled symbols) and CMC concentration (0.5%: circle and 0.75%: triangle).

The variation of color between day 0 and different storage times (days: 7, 14, and 21) at 5°C was calculated using CIE ΔE_{2000} equation [31]. A color difference (ΔE_{2000}) value higher than 1.5 indicates a subjective assessment of “noticeable” perception of color differences [32].

2.6. Statistical Analysis. A two-way ANOVA (oil concentration and CMC concentration) with interaction between factors was applied to the data. Tukey’s test ($\alpha = 0.05$) was used to calculate the minimum significant difference. All calculations were carried out with XLSTAT Pro software 2015 (Addinsoft, Paris, France).

3. Results

3.1. Particle Characterization. Figure 1 shows the size distribution graphs, which indicate the droplet distribution of different nanoemulsions with CMC based on volume percentage of droplets as a function of zeta-average size. All samples exhibited monomodal particle distribution, but the width of the distributions decreased with increasing oil concentration. In general, the zeta-average particle size (PS) of different samples varied slightly among 106.7 and 121.3 nm according to the composition; however, sample polydispersity increased strongly with CMC concentration in nanoemulsions with 5% oil, but not on those with 15% oil. This difference in the effect of adding theoretically similar CMC concentration on polydispersity of nanoemulsions with different oil concentration can be due to the higher effective concentration of CMC in the aqueous phase of nanoemulsions with 15% oil. An increase in viscosity of the aqueous phase when CMC concentration increases can minimize droplet mobility, delaying collision frequency, and reducing droplet coalescence [21]. In the case of nanoemulsions with 5% oil, it was observed that CMC addition increased their polydispersity due probably

TABLE 1: Two-way ANOVA of particle size (PS), polydispersity index (PdI), and zeta potential (ZPot) for O/W nanoemulsions based on olive oil with different CMC concentrations. F and p values.

Parameters	Main effects				Interactions	
	A: oil concentration		B: CMC concentration		A \times B	
	F	p	F	p	F	p
PS (nm)	0.08	0.79	8.00	<0.01	1.72	0.21
PdI (—)	19.23	<0.01	5.34	0.02	3.61	0.04
ZPot (mV)	10.40	<0.01	938.48	<0.01	10.33	<0.01

TABLE 2: Mean values and significant differences of particle size (PS), polydispersity index (PdI), and zeta potential (ZPot) for O/W nanoemulsions based on olive oil with different CMC concentrations.

Oil concentration (% w/w)	CMC concentration (% w/w)	PS (nm)	PdI (—)	ZPot (mV)
5	0	106.65 \pm 2.56 ^b	0.28 \pm 0.02 ^b	-19.18 \pm 0.79 ^b
	0.5	119.50 \pm 5.49 ^a	0.40 \pm 0.07 ^a	-45.55 \pm 1.43 ^d
	0.75	121.33 \pm 3.36 ^a	0.41 \pm 0.09 ^a	-52.50 \pm 0.91 ^e
15	0	112.96 \pm 0.62 ^{ab}	0.26 \pm 0.02 ^b	-14.05 \pm 0.79 ^a
	0.5	118.45 \pm 7.52 ^{ab}	0.27 \pm 0.02 ^b	-41.43 \pm 3.10 ^c
	0.75	117.90 \pm 8.69 ^{ab}	0.28 \pm 0.01 ^b	-54.76 \pm 2.24 ^e

^{a-e}Means within a column with common superscripts did not differ significantly ($p > 0.05$).

to lower concentration of CMC into the aqueous phase, which it can not be enough to reduce droplet flocculation and coalescence. Nanoemulsions were measured after 24 h of storage; therefore the polydispersity of samples can be affected by the mechanisms of emulsion destabilization, as coalescence and flocculation. Besides, at very low concentration, the added hydrocolloids have a destabilizing effect on the emulsions, since the depletion flocculation induced by the nonadsorbing hydrocolloids causes enhanced serum separation of the emulsions [11].

ANOVA results showed that only CMC concentration affected significantly ($p < 0.05$) particle size (PS) of nanoemulsions (Table 1), but only significant differences ($p < 0.05$) on PS were found between the sample with 5% oil and 0.75% CMC and control sample with 5% oil (Table 2). Regarding polydispersity index (PdI), oil and CMC concentration as well as their interaction had a significant effect ($p < 0.05$) on PdI values (Table 1). The effect of CMC was different depending on oil concentration; in samples with 5% oil, the addition of CMC increased PdI values from 0.28 to 0.41, but in the 15% oil-nanoemulsions, PdI values almost did not vary (from 0.26 to 0.28) (Table 2). It can be due, as previously it was commented, to the increase of viscosity of continuous phase that reduces particle movement which delayed the phenomena of coalescence and flocculation.

Electrical charge of nanoemulsions, measured as zeta potential (ZPot), was affected significantly ($p < 0.05$) by oil and CMC concentration and by binary interaction of both factors (Table 1); however the factor that more influenced ZPot was CMC concentration (F value = 938.48). Control samples (without CMC added) showed ZPot values of -19.18 and -14.05 mV for samples with 5 and 15% oil, respectively. These results are in agreement with other studies where

nanoemulsions were stabilized with the same nonionic surfactant (Tween 80) [33, 34]. Also, it has been reported that a nonionic emulsifier/surfactant can give a negative charge to oil droplets, due to preferential adsorption of hydroxyl ions from the aqueous phase or due to the presence of anionic impurities such as free fatty acids in the surfactant or oil phases [16].

When CMC was added into nanoemulsions, the magnitude of ZPot values increased significantly ($p < 0.05$) for both oil concentrations (Table 2). Samples with 0.5% CMC and different oil concentration showed ZPot values significantly different ($p < 0.05$), but when CMC was increased to 0.75% no differences were found between electrical charges of nanoemulsions with different oil content. Nevertheless, the strong negative ζ -potential observed in these nanoemulsions is due to the presence of CMC, which is an anionic hydrocolloid. The anionic groups in the polymer chain of CMC and its surface properties can stabilize the nanoemulsions, since they can be absorbed to the interfacial layer, but their stabilizing action depends on the possible interactions and competition between previously adsorbed species [11, 35].

Finally, it has been reported that emulsions with zeta potential more positive than +30 mV or more negative than -30 mV can be considered stable, since electrical charge of droplets is strong enough to assume that repulsive forces between droplets are predominant in the system [34, 36]. Thus, the nanoemulsions with CMC could be considered stable against the physical mechanisms of destabilization.

3.2. Flow Behavior. Figure 2 shows flow curves of CMC-based nanoemulsions with different oil concentration. All samples with CMC exhibited Non-Newtonian and shear

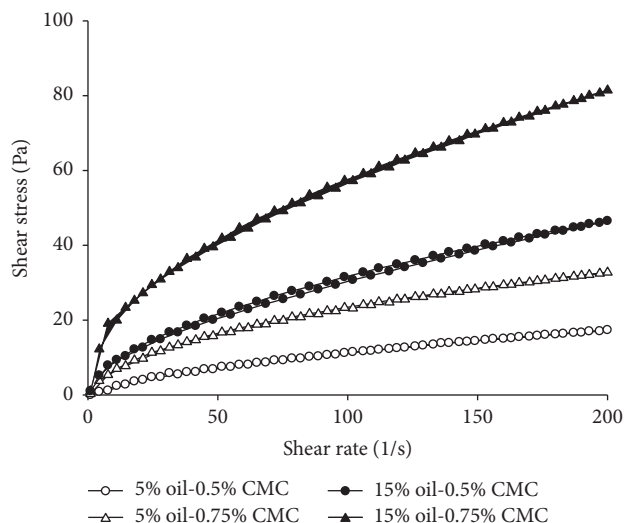


FIGURE 2: Flow curves of O/W nanoemulsions with different oil (5%: empty symbols and 15%: filled symbols) and CMC concentration (0.5%: circle and 0.75%: triangle).

thinning flow behavior, having observed clear differences among them. Nanoemulsions with the highest oil and CMC concentration presented a higher degree of shear thinning behavior due principally to disruption of the spatial organization of oil droplets and CMC chains, being aligned in the direction of the shearing forces [21, 37]. This behavior is in agreement with other studies on emulsions with CMC and other polymers [13, 21, 38]. Nanoemulsions without CMC added showed a Newtonian flow behavior with flow behavior index values (n) around 1 (Table 3).

It is well known in the literature that CMC dispersions show a shear thinning behavior and its rheological properties have been adequately described by Ostwald-de Waele model [21, 39–41]. In this study, the flow curves of all CMC-based nanoemulsions were also successfully fitted to Ostwald-de Waele model with R^2 among 96.7–99.9%. ANOVA results of flow parameters showed a significant effect ($p < 0.05$) of factors studied (CMC and oil concentration) and the binary interaction between them on consistency index (K) and flow behavior index (n) values. As observed in Table 3, no significant differences were found between control nanoemulsions with different oil concentration, but when CMC was added, consistency and pseudoplasticity of samples increased. In general, K values increased significantly as increasing CMC and oil concentration, probably caused by the increase of resistance to flow due to polymer-solvent interaction. An increase of the effective volume fraction of the dispersed phase in these nanoemulsions, by an increase of oil concentration, results in a narrower distance between particles, which leads to packing of the oil droplets, and these interparticle interactions are stronger [13, 21]. Besides, the addition of CMC increased the viscosity of continuous phase since extended CMC chains start to overlap and entangle, resulting in a transient network structure increasing the resistance to flow [21, 42]. Regarding flow behavior index, by increasing CMC and oil concentration n values decreased

TABLE 3: Mean values and significant differences of flow parameters (K : consistency index and n : flow behavior index) for O/W nanoemulsions based on olive oil with different CMC concentrations.

Oil concentration (% w/w)	CMC concentration (% w/w)	K (Pa s n)	n (—)
	0	0.001 ± 0.0001^d	1.01 ± 0.001^a
5	0.5	0.53 ± 0.01^c	0.65 ± 0.01^b
	0.75	2.02 ± 0.05^b	0.53 ± 0.01^c
15	0	0.01 ± 0.001^d	1.01 ± 0.001^a
	0.5	2.21 ± 0.10^b	0.57 ± 0.01^d
	0.75	4.78 ± 0.26^a	0.49 ± 0.01^e

^{a-c}Means within a column with common superscripts did not differ significantly ($p > 0.05$).

significantly from 0.65 to 0.49, giving rise in a pseudoplastic behavior (Table 3). Pseudoplasticity represents an irreversible structural breakdown that may occur as a result of the spatial redistribution of the particles under a shear field by alignment of nonspherical particles (CMC) with the flow field or deformation and disruption of flocs (oil droplets) [16].

3.3. Stability. According to physical parameters results, nanoemulsions with 0.75% CMC at the two oil concentrations should be more stable to gravitational separation, since the physical basis of gravitational separation gives by Stokes' Law that the rate of droplet creaming should decrease as droplet size decreases, the density difference between phases decreases, and the aqueous phase viscosity increases [16]. In this case, samples with the highest CMC concentration presented higher consistency index (K) values (Table 3) than control samples and nanoemulsions with 0.5% CMC, and they showed the highest stability at two storage temperatures studied, observing phenomena of destabilization from day 15.

Figure 3 shows backscattering profiles (%) along the tube length for nanoemulsions prepared with different CMC and olive oil concentration at 5°C. Diverse destabilization processes were observed depending on CMC-olive oil ratio used, being all samples stable until 15 storage days. The emulsions containing 0.5 : 5 (% w : w) CMC-olive oil showed a high backscattering variation, making the most unstable emulsion (Figure 3(a)). This can be attributed to the high polydispersity index level of these samples (Table 2), which detected a small population of large particle that may cause instability by creaming during long-term storage [26]. Also, the instability phenomenon was attributed to physical mechanisms of destabilization as coalescence or flocculation, since according to the theory of multiple light scattering a variation of percentage of backscattering at tube middle is associated with an increase in droplet size [43].

For the samples prepared with 0.5 : 15 (% w : w) CMC-olive oil, a decrease of the backscattering at the bottom of the tube was observed (Figures 3(a) and 3(b)), but one peak was observed in the top of the tube at the last time (21 days), which indicates gravitational phase separation of the emulsion by

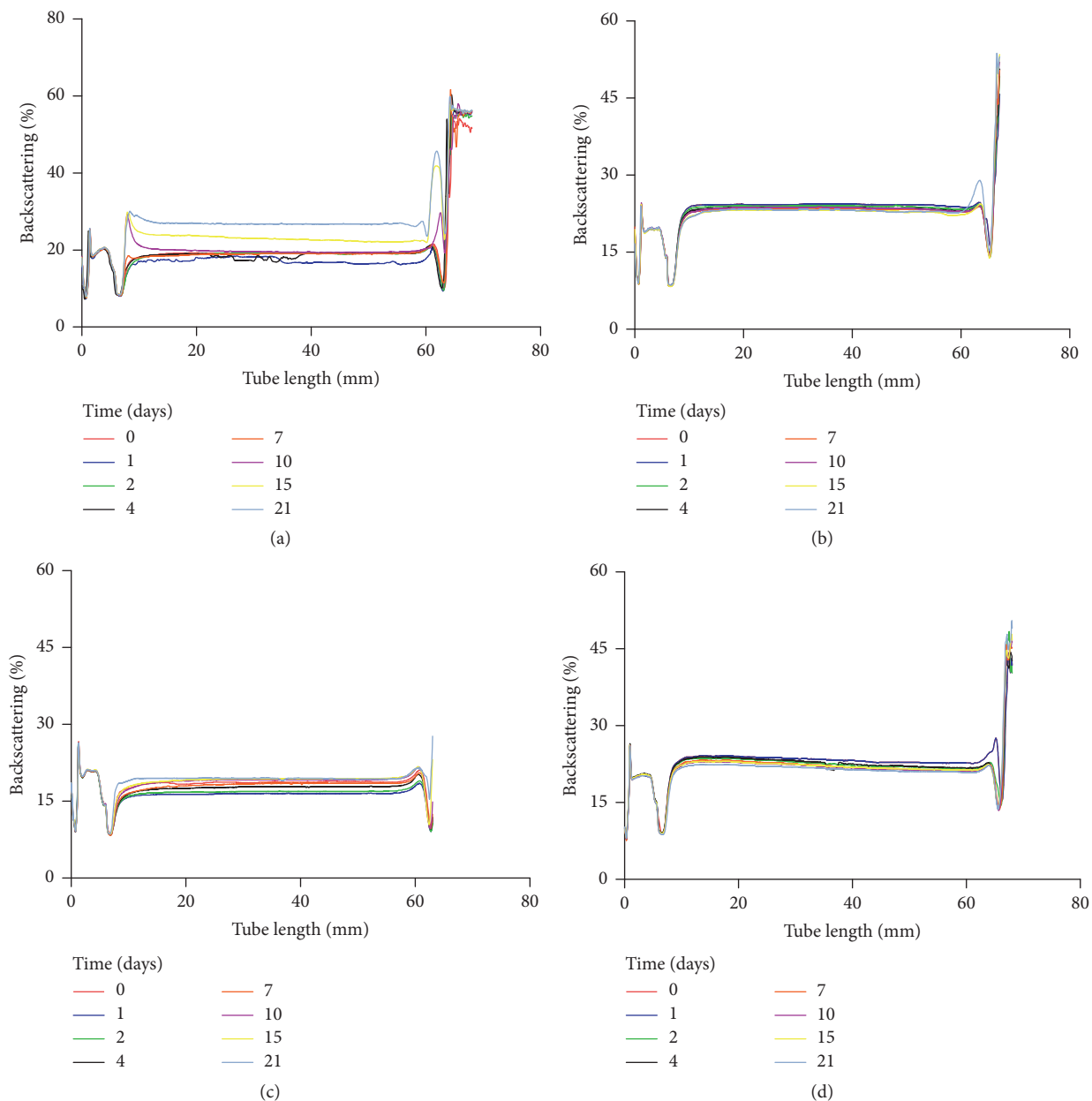


FIGURE 3: Backscattering profiles as a function of the tube length after 21 days in quiescent conditions for nanoemulsions prepared at 5°C with (a) CMC-olive oil (0.5:5%), (b) CMC-olive oil (0.5:15%), (c) CMC-olive oil (0.75:5%), and (d) CMC-olive oil (0.75:15%).

creaming. Nevertheless, these results are consistent with the creaming index that showed low values. The observation may be explained by the consistence induced by the high level of olive oil in the emulsion formulation (consistency index values, Table 3).

The samples prepared with high CMC concentration showed the same behavior in function of olive oil in comparison with 0.5% CMC, but in general the highest stability values were obtained using a concentration of 0.75% CMC (Figures 3(c) and 3(d)). This result may demonstrate that, at high CMC concentration, the creaming stability was improved, which could be by an increase in the apparent viscosity due to the hydrocolloid contribution of the continuous aqueous phase.

Previous researchers [44] have also reported that the addition of CMC to whey protein-based emulsion improved the physical stability. Other results indicated that the replacement of 0.3% (w/w) xanthan gum with 0.5% (w/w) CMC showed a significant increase in storage stability as compared to the control sample [17]. Also, as the CMC concentration increases, the droplets become smaller and the polydispersity was narrower, so that more stable emulsions can be expected [29].

The dependence of emulsion creaming index on the CMC-olive oil concentration in discontinuous phase at the different time and temperature is presented in Table 4. Practically all prepared emulsions storage at 5°C was more stable

TABLE 4: Creaming index of O/W nanoemulsions stabilized by CMC and with different olive oil concentration during 21 days of storage at 5°C and 20°C.

Storage time (day)	CMC: olive oil concentration (% w/w)				
	Control*	0.5:5	0.5:15	0.75:5	0.75:15
Creaming index at 5°C					
0	1.65 ± 0.44 ^{aA}	3.39 ± 0.07 ^{bA}	0.72 ± 0.02 ^{aA}	1.87 ± 0.2 ^{aA}	1.13 ± 0.11 ^{aA}
15	3.54 ± 0.72 ^{aB}	5.68 ± 0.98 ^{aB}	5.82 ± 0.49 ^{aB}	5.63 ± 0.37 ^{aB}	5.15 ± 0.74 ^{aB}
21	4.17 ± 0.11 ^{cB}	6.60 ± 0.65 ^{bB}	20.73 ± 1.07 ^{aC}	5.68 ± 0.31 ^{bB}	6.48 ± 0.49 ^{bB}
Creaming index at 20°C					
0	0.34 ± 0.02 ^{aA}	5.15 ± 0.61 ^{cA}	5.57 ± 0.67 ^{cA}	5.07 ± 0.86 ^{cA}	2.15 ± 0.69 ^{bA}
15	3.05 ± 0.18 ^{aB}	11.25 ± 0.85 ^{bB}	27.65 ± 0.73 ^{dB}	10.63 ± 0.85 ^{bB}	21.63 ± 0.63 ^{cB}
21	3.38 ± 0.08 ^{aB}	12.05 ± 0.45 ^{bB}	31.69 ± 0.74 ^{dC}	12.35 ± 0.65 ^{bC}	22.34 ± 1.07 ^{cB}

^{a-c}Significant ($p < 0.05$) differences among samples with different CMC-olive oil concentration from the same incubation time.

^{A-C}Significant ($p < 0.05$) differences among the same sample but with different incubation time.

* Control: without CMC added.

TABLE 5: Two-way ANOVA of lightness (L^*), red-green component (a^*), and yellow-blue component (b^*) for O/W nanoemulsions based on olive oil with different CMC concentrations. F and p values.

Parameters	Main effects				Interactions	
	A: oil concentration		B: CMC concentration		A × B	
	F	p	F	p	F	p
L^*	5.13	0.04	80.37	<0.01	0.29	0.75
a^*	46.50	<0.01	3.44	0.38	0.25	0.78
b^*	119.42	<0.01	5.00	0.02	0.22	0.80

in the fresh form (storage time = 0) in comparison with 20°C. The difference among different O/W nanoemulsions became more obvious after 21 days of storage. Therefore, changes in the storage temperature affected the stability of emulsion because it can increase the droplet-droplet collision frequency, which can promote aggregation under conditions, where there is not a strong repulsion between the droplets [45]. Besides, an increase in the temperature can reduce the apparent viscosity promoting an increase in the creaming phenomenon [16].

All nanoemulsions stored at 5°C showed lower creaming index values at day 15, which is associated with very stable emulsions, because no serum layer separation in the tube was observed; therefore the creaming layer resulted slight. Conversely, the nanoemulsion containing 0.5:15 (% w:w) CMC-olive oil had the lowest stability among all these samples (Table 4). On the other hand, the storage of nanoemulsion at 20°C showed significant differences among CMC-olive oil samples ($p < 0.05$), where the highest creaming index value was obtained with 0.5:15 (% w:w) CMC-olive oil. When serum layer appears with time (i.e., the creaming index increased), it indicates a decrease in sedimentation stability or a clarification at the bottom of tube [29]. This indicated that using low olive oil concentration and high CMC concentration led to improvement of the physical stability to produce nanoemulsion. These samples showed the highest resistance against flocculation, coalescence, and phase separation in comparison with other samples, which can be due to the increase in the apparent viscosity when

0.75% CMC was added. This result is in agreement with a previous work [46], where it was observed that CMC addition reduced creaming index when 30% oil was added.

3.4. Color. Two-way ANOVA showed that only main factors had a significant effect ($p < 0.05$) on color parameters of different nanoemulsions (Table 5). L^* (lightness) and b^* (yellow-blue coordinate) were affected significantly ($p < 0.05$) by oil and CMC concentrations, while a^* values varied significantly ($p < 0.05$) with oil concentration. The addition of CMC into nanoemulsions decreased L^* values, but an increase of CMC concentration did not show effect on sample lightness (Table 6). This effect could be attributed to the structure of the CMC shape into nanoemulsions. The CMC could modify the spatial distribution of oil droplets, forming droplet aggregates which affect the scattering efficiency, since a decrease of the efficiency of light scattering decreases lightness of the emulsions [47]. The effect of hydrocolloids on color parameters is not clear in the literature, although hydrocolloids have been observed to modify instrumental color in some products. Chung et al. [48] showed in mixed colloidal dispersions based on emulsions that the lightness increased with increasing fat and surfactant content, while starch content had a little effect. In another study, Chung et al. [49] on mixed systems of locust bean gum (LBG) and emulsion obtained that the lightness decreased with increasing LBG concentration. Arancibia et al. [22] studied the effect of thickener type on color of semisolid desserts with different fat content and obtained that by increasing

TABLE 6: Mean values and significant differences of lightness (L^*), red-green component (a^*), and yellow-blue component (b^*) for O/W nanoemulsions based on olive oil with different CMC concentrations.

Oil concentration (% w/w)	CMC concentration (% w/w)	L^*	a^*	b^*
5	0	88.04 ± 0.26^a	-8.93 ± 1.27^{ab}	-33.40 ± 1.96^b
	0.5	80.90 ± 1.02^b	-7.42 ± 0.60^a	-29.99 ± 1.21^b
	0.75	81.13 ± 1.16^b	-7.57 ± 2.55^a	-29.92 ± 4.46^b
15	0	86.48 ± 1.02^a	-12.39 ± 3.02^{bc}	-21.80 ± 2.95^a
	0.5	80.26 ± 2.13^b	-13.42 ± 0.59^c	-19.20 ± 0.91^a
	0.75	79.95 ± 1.00^b	-13.50 ± 1.55^c	-17.39 ± 2.47^a

^{a-c} Means within a column with common superscripts did not differ significantly ($p > 0.05$).

CMC levels in skimmed-milk samples L^* increased; however, when starch levels increased in this type of samples, L^* values decreased.

Red-green (a^*) and yellow-blue (b^*) components varied with oil concentration, and the negative magnitude of these parameter values increased significantly as increasing oil concentration, at two CMC concentrations studied (Table 6). This effect can be due to the presence of pigments in the olive oil, as chlorophylls and carotenoids [50]. The concentration of chlorophylls and carotenoids in olive oil varies between 4.9–24.4 and 4.5–13.29 mg/kg respectively, depending on olive variety [51]. Chlorophyll pigments account for the greenness of this type of oils, while carotenoids account for their yellowness. In this case, the nanoemulsions with the highest oil concentration exhibited a more-intense green color than samples with 5% oil, while a decrease of yellowness with an increase of oil concentration was observed, which indicated that presence of carotenoids in olive oil did not affect the color of nanoemulsions. The increase of blueness can be due to the presence of chlorophyll “a” and chlorophyllide “a” that give a color bluish-green to olive oil [50].

To evaluate the effect of storage on color of nanoemulsions with CMC, the color differences between day 0 and different storage times (7, 14, and 21 days) were calculated as ΔE_{2000} color variation (Figure 4). At day 7, it was observed that samples with 0.75% CMC showed a higher color variation with values higher than 2, which indicated that color differences between these samples were noticeable to the human eye [32]. At day 14, the difference of color varied slightly in all nanoemulsions, although this increment was more evident in samples with the lowest oil concentration. At final storage time, variation of color depended principally on the emulsion stability since all samples showed creaming and phase separation affecting CIEDE₂₀₀₀ values. In general, almost all samples showed color differences noticeable to the human eye (values higher than 1.5).

4. Conclusions

The addition of CMC into nanoemulsions based on olive oil affected slightly the particle size of nanoemulsions, since it varied between 107 and 121 nm. All physical properties studied of nanoemulsions were depending on both oil and

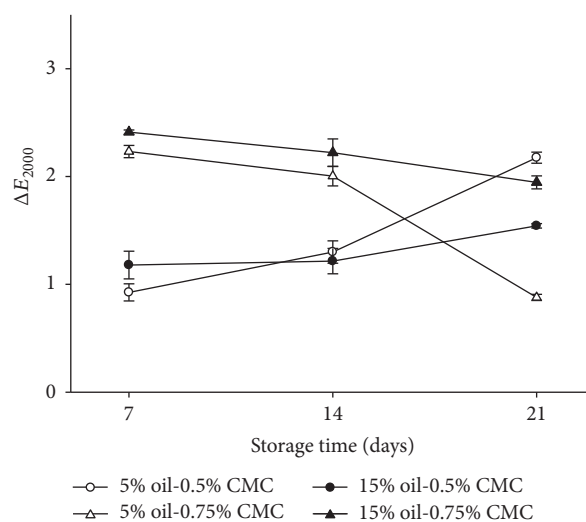


FIGURE 4: Difference of color (ΔE_{2000}) with respect to initial time (day 0) of storage at 5°C of different O/W nanoemulsions (5% oil: empty symbols, 15% oil: filled symbols, 0.5% CMC: circle, and 0.75% CMC: triangle).

CMC concentration. Oil concentration affected principally color and flow properties of samples. However, the consistency obtained by the addition of CMC increased the stability of emulsions. Finally, the results showed that CMC could be applied as thickener into nanoemulsions based on olive oil, increasing their physical stability, but modifying their physical properties.

Competing Interests

The authors declare that there are no competing interests regarding the publication of this paper.

Acknowledgments

The authors are grateful for financial support from CONICYT for Project FONDECYT POSTDOCTORADO no. 3150537 and fellowship awarded to author Rosa Navarro (Programa de Becas de Doctorado Nacional no. 21130758) and USACH (VRIDEI and Technological Faculty) for Project

Basal MECESUP-USA1555LD. Author R. N. Zúñiga thanks Initiation R&D program from UTEM.

References

- [1] Y. Li and D. J. McClements, "Influence of non-ionic surfactant on electrostatic complexation of protein-coated oil droplets and ionic biopolymers (alginate and chitosan)," *Food Hydrocolloids*, vol. 33, no. 2, pp. 368–375, 2013.
- [2] M. Guttoff, A. H. Saberi, and D. J. McClements, "Formation of vitamin D nanoemulsion-based delivery systems by spontaneous emulsification: factors affecting particle size and stability," *Food Chemistry*, vol. 171, pp. 117–122, 2015.
- [3] Y. Liang, S.-S. Wong, S. Quang Pham, and J. J. Tan, "Effects of globular protein type and concentration on the physical properties and flow behaviors of oil-in-water emulsions stabilized by micellar casein-globular protein mixtures," *Food Hydrocolloids*, vol. 54, pp. 89–98, 2016.
- [4] P. J. García-Moreno, A. Guadix, E. M. Guadix, and C. Jacobsen, "Physical and oxidative stability of fish oil-in-water emulsions stabilized with fish protein hydrolysates," *Food Chemistry*, vol. 203, pp. 124–135, 2016.
- [5] E. Troncoso, J. M. Aguilera, and D. J. McClements, "Fabrication, characterization and lipase digestibility of food-grade nanoemulsions," *Food Hydrocolloids*, vol. 27, no. 2, pp. 355–363, 2012.
- [6] D. J. McClements, "Nanoemulsion-based oral delivery systems for lipophilic bioactive components: nutraceuticals and pharmaceuticals," *Therapeutic Delivery*, vol. 4, no. 7, pp. 841–857, 2013.
- [7] R. Adjonu, G. Doran, P. Torley, and S. Agboola, "Formation of whey protein isolate hydrolysate stabilised nanoemulsion," *Food Hydrocolloids*, vol. 41, pp. 169–177, 2014.
- [8] T. Tadros, P. Izquierdo, J. Esquena, and C. Solans, "Formation and stability of nano-emulsions," *Advances in Colloid and Interface Science*, vol. 108–109, pp. 303–318, 2004.
- [9] L.-C. Peng, C.-H. Liu, C.-C. Kwan, and K.-F. Huang, "Optimization of water-in-oil nanoemulsions by mixed surfactants," *Colloids & Surfaces A: Physicochemical and Engineering Aspects*, vol. 370, no. 1–3, pp. 136–142, 2010.
- [10] Y. Yang, C. Marshall-Breton, M. E. Leser, A. A. Sher, and D. J. McClements, "Fabrication of ultrafine edible emulsions: comparison of high-energy and low-energy homogenization methods," *Food Hydrocolloids*, vol. 29, no. 2, pp. 398–406, 2012.
- [11] E. Dickinson, "Hydrocolloids as emulsifiers and emulsion stabilizers," *Food Hydrocolloids*, vol. 23, no. 6, pp. 1473–1482, 2009.
- [12] D. Xu, J. Zhang, Y. Cao, J. Wang, and J. Xiao, "Influence of microcrystalline cellulose on the microrheological property and freeze-thaw stability of soybean protein hydrolysate stabilized curcumin emulsion," *LWT—Food Science and Technology*, vol. 66, pp. 590–597, 2016.
- [13] C. Chung, B. Degner, and D. J. McClements, "Understanding multicomponent emulsion-based products: influence of locust bean gum on fat droplet—starch granule mixtures," *Food Hydrocolloids*, vol. 35, pp. 315–323, 2014.
- [14] A. Nussinovitch, *Hydrocolloid Applications: Gum Technology in the Food and Other Industries*, Blackie Academic and Professional, London, UK, 1997.
- [15] S. Bayarri, L. González-Tomás, and E. Costell, "Viscoelastic properties of aqueous and milk systems with carboxymethyl cellulose," *Food Hydrocolloids*, vol. 23, no. 2, pp. 441–450, 2009.
- [16] D. J. McClements, *Food Emulsions: Principles, Practices and Techniques*, CRC Press, Boca Raton, Fla, USA, 2005.
- [17] H. Mirhosseini, C. P. Tan, A. Aghlara, N. S. A. Hamid, S. Yusof, and B. H. Chern, "Influence of pectin and CMC on physical stability, turbidity loss rate, cloudiness and flavor release of orange beverage emulsion during storage," *Carbohydrate Polymers*, vol. 73, no. 1, pp. 83–91, 2008.
- [18] L.-M. Zhang, "New water-soluble cellulosic polymers: a review," *Macromolecular Materials and Engineering*, vol. 286, no. 5, pp. 267–275, 2001.
- [19] R. H. Jellema, A. M. Janssen, M. E. J. Terpstra, R. A. De Wijk, and A. K. Smilde, "Relating the sensory sensation 'creamy mouthfeel' in custards to rheological measurements," *Journal of Chemometrics*, vol. 19, no. 3, pp. 191–200, 2005.
- [20] S. Bayarri, I. Chuliá, and E. Costell, "Comparing λ -carrageenan and an inulin blend as fat replacers in carboxymethyl cellulose dairy desserts. Rheological and sensory aspects," *Food Hydrocolloids*, vol. 24, no. 6–7, pp. 578–587, 2010.
- [21] C. Arancibia, S. Bayarri, and E. Costell, "Comparing carboxymethyl cellulose and starch as thickeners in oil/water emulsions. Implications on rheological and structural properties," *Food Biophysics*, vol. 8, no. 2, pp. 122–136, 2013.
- [22] C. Arancibia, C. Castro, L. Jublot, E. Costell, and S. Bayarri, "Colour, rheology, flavour release and sensory perception of dairy desserts. Influence of thickener and fat content," *LWT—Food Science and Technology*, vol. 62, no. 1, pp. 408–416, 2015.
- [23] J. López-Miranda, F. Pérez-Jiménez, E. Ros et al., "Olive oil and health: summary of the II international conference on olive oil and health consensus report, Jaén and Córdoba (Spain) 2008," *Nutrition, Metabolism & Cardiovascular Diseases*, vol. 20, no. 4, pp. 284–294, 2010.
- [24] M. Ruiz-Canela and M. A. Martínez-González, "Olive oil in the primary prevention of cardiovascular disease," *Maturitas*, vol. 68, no. 3, pp. 245–250, 2011.
- [25] F. Visioli and C. Galli, "Biological properties of olive oil phytochemicals," *Critical Reviews in Food Science and Nutrition*, vol. 42, no. 3, pp. 209–221, 2002.
- [26] D. T. Piorkowski and D. J. McClements, "Beverage emulsions: recent developments in formulation, production, and applications," *Food Hydrocolloids*, vol. 42, part 1, pp. 5–41, 2014.
- [27] D. J. McClements, E. A. Decker, and Y. Park, "Controlling lipid bioavailability through physicochemical and structural approaches," *Critical Reviews in Food Science and Nutrition*, vol. 49, no. 1, pp. 48–67, 2009.
- [28] S. Tammak, H. Mirhosseini, C. P. Tan, H. M. Ghazali, and K. Muhammad, "Physicochemical properties, rheological behavior and morphology of pectin-pea protein isolate mixtures and conjugates in aqueous system and oil in water emulsion," *Food Hydrocolloids*, vol. 56, pp. 405–416, 2016.
- [29] L. B. Petrovic, V. J. Sovilj, J. M. Katona, and J. L. Milanovic, "Influence of polymer-surfactant interactions on o/w emulsion properties and microcapsule formation," *Journal of Colloid and Interface Science*, vol. 342, no. 2, pp. 333–339, 2010.
- [30] F. Pedreschi, J. León, D. Mery, and P. Moyano, "Development of a computer vision system to measure the color of potato chips," *Food Research International*, vol. 39, no. 10, pp. 1092–1098, 2006.
- [31] M. R. Luo, G. Cui, and B. Rigg, "The development of the CIE 2000 colour-difference formula: CIEDE2000," *Color Research and Application*, vol. 26, no. 5, pp. 340–350, 2001.
- [32] Y. Yang, J. Ming, and N. Yu, "Color image quality assessment based on CIEDE2000," *Advances in Multimedia*, vol. 2012, Article ID 273723, 6 pages, 2012.

- [33] L. Salvia-Trujillo, M. A. Rojas-Graü, R. Soliva-Fortuny, and O. Martín-Belloso, "Effect of processing parameters on physicochemical characteristics of microfluidized lemongrass essential oil-alginate nanoemulsions," *Food Hydrocolloids*, vol. 30, no. 1, pp. 401–407, 2013.
- [34] L. Salvia-Trujillo, A. Rojas-Graü, R. Soliva-Fortuny, and O. Martín-Belloso, "Physicochemical characterization and antimicrobial activity of food-grade emulsions and nanoemulsions incorporating essential oils," *Food Hydrocolloids*, vol. 43, pp. 547–556, 2015.
- [35] E. Dickinson, "Hydrocolloids at interfaces and the influence on the properties of dispersed systems," *Food Hydrocolloids*, vol. 17, no. 1, pp. 25–39, 2003.
- [36] B. Heurtault, P. Saulnier, B. Pech, J.-E. Proust, and J.-P. Benoit, "Physico-chemical stability of colloidal lipid particles," *Biomaterials*, vol. 24, no. 23, pp. 4283–4300, 2003.
- [37] P. Bellalta, E. Troncoso, R. N. Zúñiga, and J. M. Aguilera, "Rheological and microstructural characterization of WPI-stabilized O/W emulsions exhibiting time-dependent flow behavior," *LWT—Food Science and Technology*, vol. 46, no. 2, pp. 375–381, 2012.
- [38] M. Dolz, M. J. Hernández, J. Delegido, M. C. Alfaro, and J. Muñoz, "Influence of xanthan gum and locust bean gum upon flow and thixotropic behaviour of food emulsions containing modified starch," *Journal of Food Engineering*, vol. 81, no. 1, pp. 179–186, 2007.
- [39] M. A. Cancela, E. Álvarez, and R. Maceiras, "Effects of temperature and concentration on carboxymethylcellulose with sucrose rheology," *Journal of Food Engineering*, vol. 71, no. 4, pp. 419–424, 2005.
- [40] X. H. Yang and W. L. Zhu, "Viscosity properties of sodium carboxymethylcellulose solutions," *Cellulose*, vol. 14, no. 5, pp. 409–417, 2007.
- [41] S. Bayarri, T. Smith, T. Hollowood, and J. Hort, "The role of rheological behaviour in flavour perception in model oil/water emulsions," *European Food Research and Technology*, vol. 226, no. 1-2, pp. 161–168, 2007.
- [42] U. Kästner, H. Hoffmann, R. Dönges, and J. Hilbig, "Structure and solution properties of sodium carboxymethyl cellulose," *Colloids and Surfaces A: Physicochemical and Engineering Aspects*, vol. 123-124, pp. 307–328, 1997.
- [43] M. C. García, M. C. Alfaro, N. Calero, and J. Muñoz, "Influence of polysaccharides on the rheology and stabilization of α -pinene emulsions," *Carbohydrate Polymers*, vol. 105, no. 1, pp. 177–183, 2014.
- [44] K. Kika, F. Korlos, and V. Kiosseoglou, "Improvement, by dry-heating, of the emulsion-stabilizing properties of a whey protein concentrate obtained through carboxymethylcellulose complexation," *Food Chemistry*, vol. 104, no. 3, pp. 1153–1159, 2007.
- [45] G. Davidov-Pardo, C. E. Gumus, and D. J. McClements, "Lutein-enriched emulsion-based delivery systems: influence of pH and temperature on physical and chemical stability," *Food Chemistry*, vol. 196, pp. 821–827, 2016.
- [46] C. Arancibia, L. Jublot, E. Costell, and S. Bayarri, "Flavor release and sensory characteristics of o/w emulsions. Influence of composition, microstructure and rheological behavior," *Food Research International*, vol. 44, no. 6, pp. 1632–1641, 2011.
- [47] D. J. McClements, "Colloidal basis of emulsion color," *Current Opinion in Colloid and Interface Science*, vol. 7, no. 5-6, pp. 451–455, 2002.
- [48] C. Chung, B. Degner, and D. J. McClements, "Physicochemical characteristics of mixed colloidal dispersions: models for foods containing fat and starch," *Food Hydrocolloids*, vol. 30, no. 1, pp. 281–291, 2013.
- [49] C. Chung, B. Degner, and D. J. McClements, "Designing reduced-fat food emulsions: locust bean gum-fat droplet interactions," *Food Hydrocolloids*, vol. 32, no. 2, pp. 263–270, 2013.
- [50] M. J. Moyano, F. J. Heredia, and A. J. Meléndez-Martínez, "The color of olive oils: the pigments and their likely health benefits and visual and instrumental methods of analysis," *Comprehensive Reviews in Food Science and Food Safety*, vol. 9, no. 3, pp. 278–291, 2010.
- [51] B. Gandul-Rojas and M. I. Mínguez-Mosquera, "Chlorophyll and carotenoid composition in virgin olive oils from various Spanish olive varieties," *Journal of the Science of Food and Agriculture*, vol. 72, no. 1, pp. 31–39, 1996.

Research Article

Deposition of Ibuprofen Crystals on Hydroxypropyl Cellulose/Polyacrylamide Gel: Experimental and Mathematic Modeling Releasing

Claudia Alicia Castillo-Miranda,¹ Ana Beatriz Morales-Cepeda,¹ Carlos Fernando Castro-Guerrero,² Homero Salas-Papayanopolos,¹ Hugo Alberto Velasco-Ocejo,¹ Jorge Alberto González-Sánchez,³ Ulises Paramo-Garcia,¹ and Hugo De Alva-Salazar¹

¹*División de Estudios de Posgrado e Investigación, Instituto Tecnológico de Ciudad Madero, Juventino Rosas y Jesús Urueta s/n, Colonia Los Mangos, 89318 Ciudad Madero, TAMPS, Mexico*

²*CONACyT-Instituto de Investigaciones Eléctricas, Reforma 113, Colonia Palmira, Cuernavaca 62490, MOR, Mexico*

³*Departamento de Ciencias Básicas del Instituto Tecnológico de Ciudad Madero, Juventino Rosas y Jesús Urueta s/n, Colonia Los Mangos, 89318 Ciudad Madero, TAMPS, Mexico*

Correspondence should be addressed to Ana Beatriz Morales-Cepeda; abmoralesc@itcm.edu.mx

Received 12 May 2016; Revised 28 August 2016; Accepted 6 September 2016

Academic Editor: Ming-Guo Ma

Copyright © 2016 Claudia Alicia Castillo-Miranda et al. This is an open access article distributed under the Creative Commons Attribution License, which permits unrestricted use, distribution, and reproduction in any medium, provided the original work is properly cited.

The crystallization of nonsteroidal anti-inflammatory drug [2-(4-isobutyl-phenyl) propionic acid] ibuprofen (IBP) on a hydroxypropyl cellulose (HPC) and polyacrylamide (PAAm) gel was studied as well as the release kinetics of the drug. The IBP was crystallized on the gel surface of HPC/PAAm. It had a prismatic shape and the growth was made in an aqueous medium; the crystallinity grade of the gels HPC/PAAm and HPC/PAAm-IBU increased to 68% and to 58%, respectively. The release of IBP is performed by two means: by a non-Fickian diffusion process and by relaxation of the chains of the gel; without regard to temperature and the diffusion media, this correlates with the lower critical solution temperature (LCST) of the proposed gel. This polymer matrix provides an option for releasing nonsteroidal anti-inflammatory drugs in a temperature range of 35–39°C. Korsmeyer and Peppas mathematical model was simulated for data releases, statistically significant at 95% confidence level.

1. Introduction

Gels represent a major group of biomaterials; they are considered intelligent systems, as they have a swelling response depending upon selective environmental conditions such as pH, temperature, ionic strength, and electric and magnetic field [1, 2]. Within the gels we find hydrogels, which are synthesized using water as reacting medium. To achieve selective medium, responsive hydrogels have been synthesized from various homopolymers and copolymers, with recent wider applicability, as monomers combine to provide good mechanical properties, along with other monomers that

give gels a hydrophilic material nature, as well as a selective response to environmental conditions.

In recent years, there has been an increased interest in hydrogels, and they have been extensively studied as drug delivery systems that allow the release of the right amount of the active ingredient, at the appropriate time and at specific sites within the body. Previous studies of the HPC/PAAm gels have been performed; the phase behavior has been studied, and it was found that the LCST and UCST (upper critical solution temperature) depend on the amount of HPC. The gel described in this paper has a LCST of 38.3°C and an UCST of 29.1°C [3].

Several authors reported the simulation of drug releases from delivery system using hydroxypropyl methylcellulose (HPMC) [4] to elucidate the mass transport and possibility to predict the effect of design parameters tablets.

This research demonstrates that ibuprofen is crystallized on a HPC/PAAm gel and then released. Crystallization is due to the ability of IBP to form the crystals on diamond shape and to stack on the gel due to the solvent and to the LCST and UCST of the gels. The nonsteroidal anti-inflammatory drug (NSAID) release kinetics was studied in two media, buffer saline and ethanol-water system. The mathematical models were used to find a correlation with experimental data.

2. Experimental

2.1. Materials. In this paper we used hydroxypropyl cellulose (HPC) with average molecular weight (M_w) of ~80,000 g/mol, acrylamide (AAm, purity 97%), methylenebisacrylamide (MBAm, purity 99%), tetramethylethylenediamine (TEMED, purity 99%), ibuprofen (IBP), ammonium persulfate (APS, purity 98%), and divinyl sulfone (DVS, purity 97%), all of which were purchased from Sigma-Aldrich. Deionized (DI) water and phosphate buffered solution (PBS) at pH 7.38 were supplied by Hycl.

2.2. Synthesis of Hydrogels. The synthesis of HPC/PAAm hydrogels was synthesized according to the method of Castro et al. [3] at a ratio of 25/75 wt%. The reaction was carried out in a four-necked flask with a temperature control at $40 \pm 1^\circ\text{C}$ and an inert nitrogen atmosphere. The solution consisted of 90% deionized water and 10% of reagents in the desired amount to work. At the beginning, 1 g of HPC was diluted in 20 mL of DI water, and the mixture was allowed to stir at room temperature for about 15 hours to achieve a homogeneous solution. Then, the reactor was purged with nitrogen and 3 g of AAm was added. Thus, 0.06 g of APS was dissolved with 0.003 g of MBAm in a vial containing 8 mL of DI water, and in another vial containing the same amount of water 0.06 g of TEMED was dissolved; both vials were stirred for 20 minutes. Once well dissolved, the content of first vial was injected in the reactor, then 0.3 mL of DVS was added, and finally the second vial was injected in the reactor. The polymerization was done for 1 hour at 40°C in an inert atmosphere and with constant stirring at pH 7. After the reaction, the solution was poured in a petri dish, and it was allowed to dry at 40°C in an oven with vacuum for one week. Once dried, the resulting films were washed with DI water in order to remove the nonreacted substances and then they were left to dry again.

2.3. Deposition of IBP. The deposition of IBP on the gel was carried out according to the method of Risbud et al. [5]. The NSAID was loaded into the samples by inserting them into an aqueous solution of the drug at a concentration of 5 mg/mL of IBP at room temperature for 48 hours. After this time, the excess of solution was removed from the gels, then frozen at -10°C for 48 hours, and finally allowed to stand at room temperature for constant weight.

2.4. Drug Release. Once the samples were loaded with the drug, we proceeded to perform the release studies. These studies were done with the dried gel after the incorporation of the NSAID. All of the release experiments were carried out in a heating bath at a controlled temperature (35, 37, and 39°C) with electromagnetic vibrations (80 cycles/min) using as release means PBS at pH 7.4 and ethanol-water solution (50 : 50) at pH 7. The release kinetics was measured by taking samples at different intervals of time and determining the drug concentration by UV spectroscopy at wavelengths of 261 nm for samples released in PBS and 255 nm in samples released from ethanol-water solution using a UV-Vis spectrophotometer, Perkin-Elmer (model Lambda 10).

2.5. Kinetic Study of the Release of IBP. Release profiles (concentration of drug released versus time) were calculated using absorbance data. The nature of NSAID diffusion from the gels was determined to indicate what model it fits.

Mathematical models proposed by Higuchi [6] and Korsmeyer and Peppas [7] are among the most widely used to analyze and describe the mechanism by which the release process occurs. Higuchi proposed a mathematical model widely used to describe the empirical process of the drug delivery, which complies with Fick's law and is represented as follows:

$$\frac{M_t}{M_\infty} = kt^{1/2}, \quad (1)$$

where M_t/M_∞ is the released fraction of IBP in a time interval t and k is the constant release rate.

The mathematical model proposed by Korsmeyer and Peppas is linear for values equal to $M_t/M_\infty < 0.6$. This model attempts to explain release mechanisms where erosion and/or dissolution of the matrix occurs and is a generalized form of Higuchi equation (1) [8], which is expressed as

$$\frac{M_t}{M_\infty} = kt^n, \quad (2)$$

where k is the release rate constant which incorporates structural and geometric features of the delivery system and n is an exponent that indicates the mechanism by which drug release occurs. The exponent value n provides information on drug's kinetics release; so if n is equal to 0.5, the drug release occurs through a diffusion phenomenon, Fickian (Higuchi mathematical model) type; if the value of n falls between 0.5 and 1, it indicates that the drug release is caused by a non-Fickian mechanism or anomalous diffusion, and when n equals 1, the mechanism of drug release depends on the process of relaxation of the polymer chains [1].

Equation (2) described the first 60% of the release behavior of hypothetical distribution. Later, Korsmeyer and Peppas [7] described an empirical equation, for three Fickian diffusional cases. The case II of the Peppas equations for Fickian and anomalous release was used in this study:

$$\frac{M_t}{M_\infty} = \frac{2k_0}{C_0 l} t. \quad (3)$$

2.6. Characterization of Gels. The samples were characterized using Fourier Transform Infrared (FTIR) spectroscopy in a Perkin-Elmer device (model Spectrum One) in attenuated total reflectance (ATR) mode using the frequency range 4000–600 cm^{-1} . Thermal properties were carried out using Differential Scanning Calorimetry (DSC) in a Perkin-Elmer device model Pyris 1. The sample was heated from 0°C to 200°C at a rate of 10°C/min, under a nitrogen atmosphere. Micrographs of the samples were prepared in a Scanning Electronic Microscope (SEM) JEOL model JSM-5900 using a size of sample 1 cm^2 ; the gels were sputtered with a gold layer. The samples were analyzed with energy dispersive X-ray spectroscopy (EDX), using the EDX instrumentation attached to the SEM, with a Bruker Analyzer operating at 133 eV. X-ray diffraction of the samples was performed with a Bruker AXS D8 Advance diffractometer using $\text{CuK}\alpha$ radiation; the samples were cut into squares with sides of 0.5 cm.

Degree of crystallinity was calculated according to

$$X_C = \frac{I_{\text{Crystalline}}}{I_{\text{Crystalline}} + I_{\text{Amorphous}}} * 100. \quad (4)$$

The degree of crystallinity of the gels was calculated by Peak Height method. For cellulosic materials, the apparent crystallinity is calculated from the height ratio between the intensity of the crystalline peak (22–24° in 2θ) and the intensity of the noncrystalline material (18° in 2θ).

3. Results and Discussion

3.1. Infrared Spectroscopy. The infrared spectrum of the synthesized xerogel HPC/PAAm is shown in Figure 1(c). At 3338 cm^{-1} , a broad peak attributable to the strong symmetric stretching NH of the PAAm can be seen and the peak at 3182 cm^{-1} is another one of high intensity corresponding to the stretch OH in the HPC [8]. Moreover, the peak at 2929 cm^{-1} of asymmetrical stretching of the CH_3 groups in HPC is observed as well as the peak at 2867 cm^{-1} due to the symmetric stretching band of CH_2 in the cellulosic derivative [9]. At 1653 cm^{-1} , there is a very strong peak attributed to the stretching of carbonyl bond (C=O) in PAAm, with a little peak at 1602 cm^{-1} which is not so strong due to the bending NH group of the PAAm. The absorption band at 1450 cm^{-1} corresponds to the asymmetric CH_2 (deformation band of the PAAm and HPC). The next peak is the 1408 cm^{-1} attributed to CH_2 out of plane symmetrical bending. The absorption band at 1271 cm^{-1} was assigned to a CN vibration of PAAm. At 1123 cm^{-1} , there is a medium peak attributed to COC stretching and crosslinking reactions.

The spectrum of pure IBP and the gel is shown in (a) and (b) in Figure 1. The spectrum (b), in addition to the previously described bands of the gel HPC/PAAm, shows the characteristic peak of the IBP at 1719 cm^{-1} , attributed to the stretching of the carbonyl group C=O (typical of the carboxyl function COOH) [10]. The peaks at 3080 cm^{-1} and 770–735 cm^{-1} also indicate that the structure of IBP is present

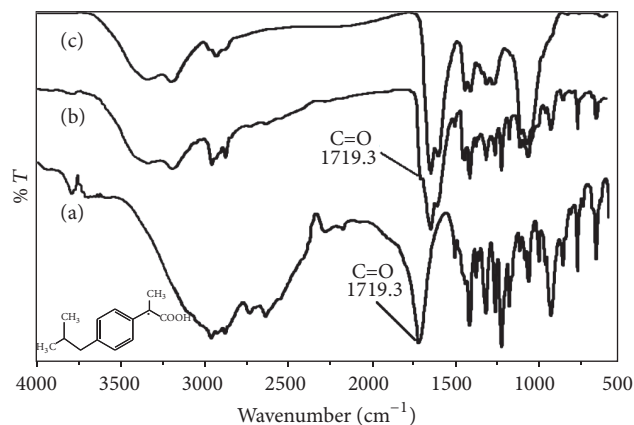


FIGURE 1: FTIR spectra of (a) IBP, (b) HPC/PAAm-IBP, and (c) HPC/PAAm.

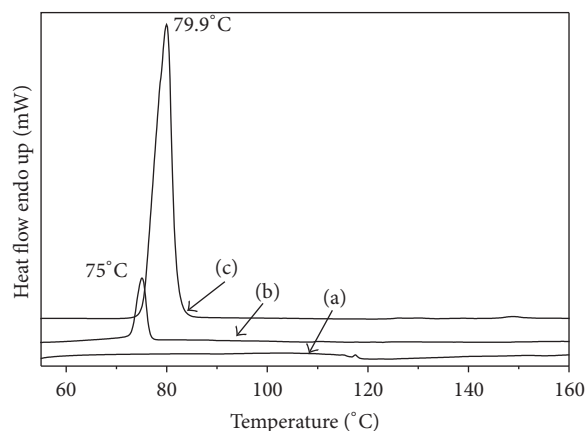


FIGURE 2: DSC thermograms of (a) HPC/PAAm, (b) IBP, and (c) polymer with IBP.

on the sample and that there is an orthosubstitution in the aromatic ring of IBP.

3.2. Thermal Analysis. De Brabander et al. [10] showed that ethyl cellulose compatible with IBP has a glass transition temperature (T_g) of about 70 to 80°C, depending on the amount of cellulose derivative. In Figure 2, the results of DSC analysis are shown. In the curve corresponding to IBP, there is a peak around 77°C, which is characteristic of the active ingredient and corresponds to the melting point of IBP [11]. The curve of the gel with IBP has a peak at 75°C; this shows that there is a polymer-drug interaction. When there is single T_g in a composite of two compounds that has its own T_g , then the system is fully miscible [12]. According to the literature, at 75–76°C of temperature, the IBP is prismatic and irregular in shape [13].

3.3. Morphology and Structure. The yellowish appearance in the xerogel (Figure 3(a)) is conferred by PAAm and the swollen gel looks transparent, due to the water incorporated in the matrix.

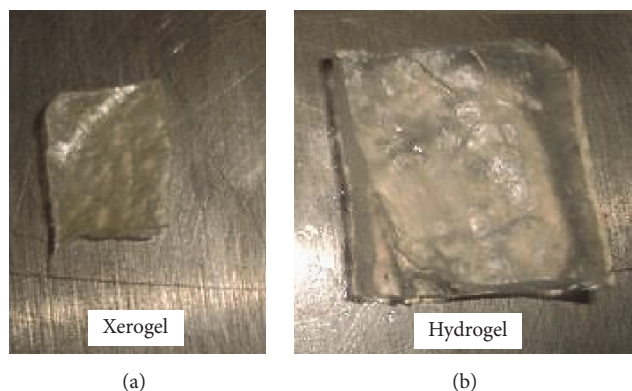


FIGURE 3: Photographs of the samples: xerogel and hydrogel.

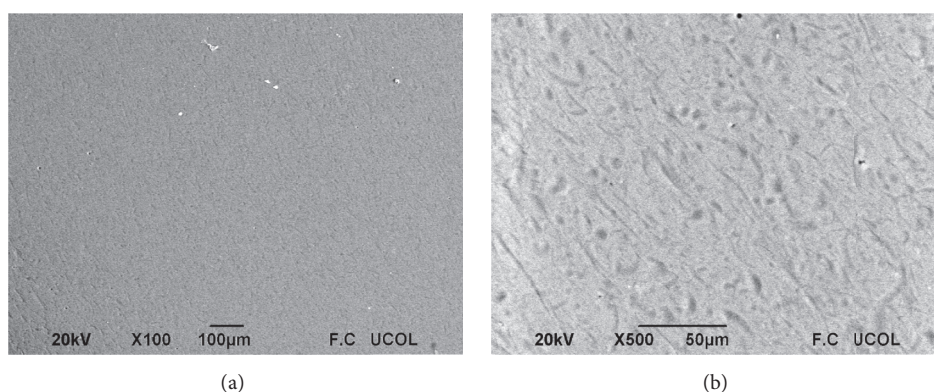


FIGURE 4: SEM micrographs of the HPC/PAAm xerogel surface at (a) 100x and (b) 500x.

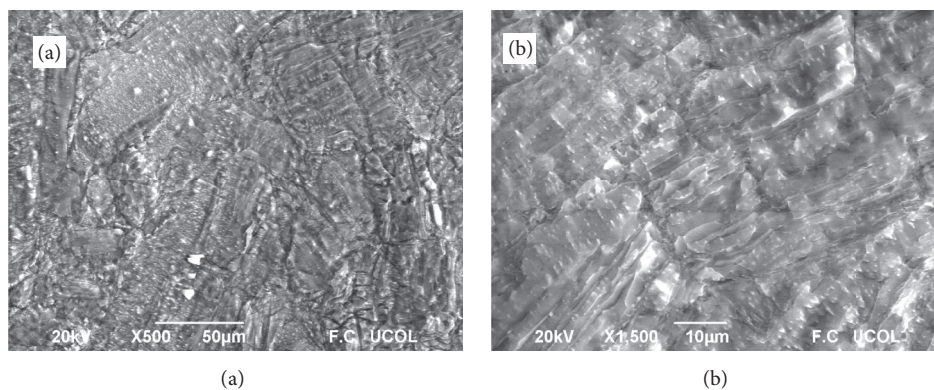


FIGURE 5: SEM micrographs of the IBP surface: (a) 500x and (b) 1500x.

In Figure 4, SEM micrographs of the sample HPC/PAAm are shown at different magnifications (100x and 500x). The pure gel has a smooth and uniform surface without the presence of agglomerates. The uniformity presented by the film indicates that there is no phase separation between the HPC and PAAm. There are pores of $6\ \mu\text{m}$ in diameter; the formation of channels that facilitate migration of solvent is also present.

Figure 5 corresponds to samples containing pure IBP. The images show a surface with many features, with cuts in

different directions and a few shiny white spots that stand out. The sample was compressed and formed a tablet; no crystals are seen.

In Figure 6 are shown SEM micrographs at 100x and 500x of the HPC/PAAm films with IBP incorporated. A surface with rugged relief is seen in the images; this is due to the inclusion of clusters of various shapes and sizes homogeneously distributed throughout the film; these clusters correspond to crystals of IBP. This corroborates the incorporation of the drug and the existence of a drug-polymer interaction, which

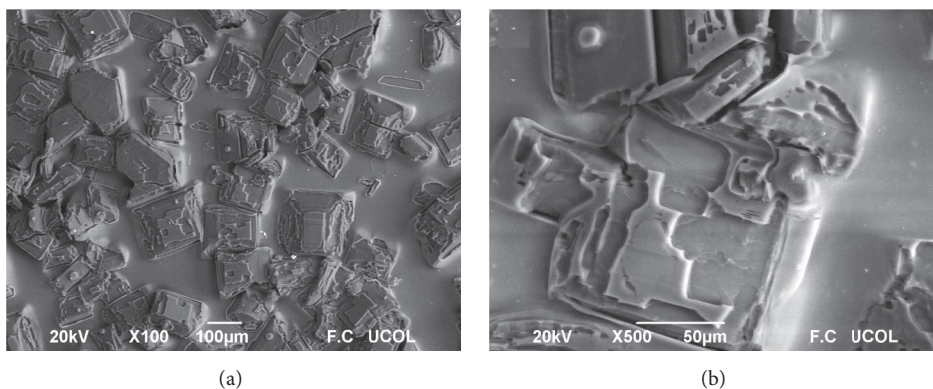


FIGURE 6: SEM micrographs of the surface of HPC/PAAm films with IBP: (a) 100x and (b) 500x.

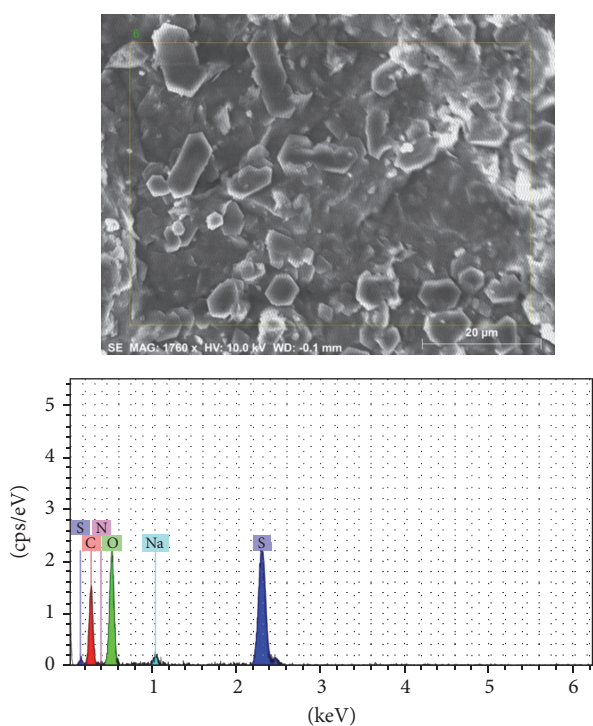


FIGURE 7: EDX analysis of the HPC/PAAm xerogel surface.

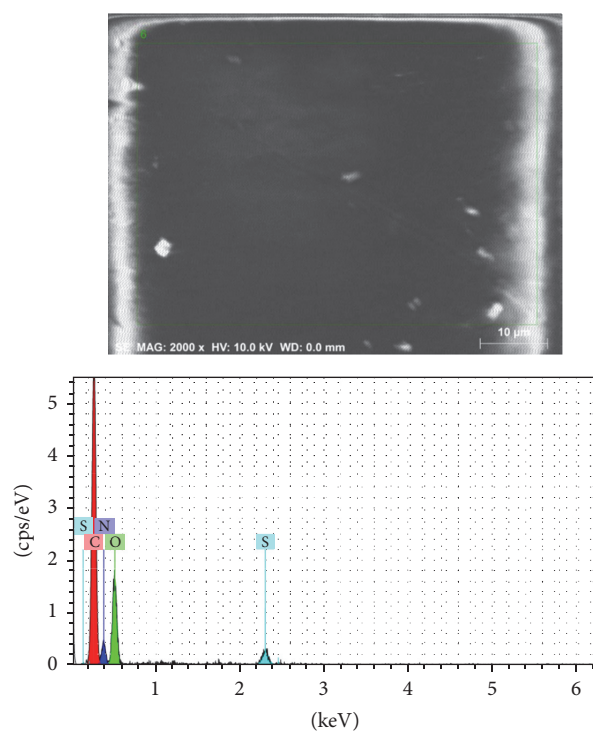


FIGURE 8: EDX analysis of the HPC/PAAm with ibuprofen, xerogel surface.

was also observed by FTIR spectra and DSC calorimetry. The clusters are shaped in some cases as a diamond with a length of $101.8\ \mu\text{m}$ and they grow vertically with $60\ \mu\text{m}$, assuming that ibuprofen is adhered to the surface in an average area of $9003\ \mu\text{m}^2$ (Figure 6(a)). Like other authors, induction to crystallization temperature is observed near 40°C , where there is presence of growth of the crystals in the shape of circles, squares, or diamonds [14]. The time of formation of the crystals indicates that, after one hour, the crystals have sizes of $100\ \mu\text{m}$, and they extend from the bottom plane of the gel substrate to the top.

The HPC/PAAm gels are negative thermosensitive; because the quantity of polyacrylamide has an influence

on the LCST [15–18], PAAm changes the LCST of HPC, a polymer that is known to have this property [19].

Figure 7 shows an EDX analysis of the HPC/PAAm pure polymer. The spectrum shows the presence of carbon, oxygen, sodium, and sulfur; no nitrogen was detected with the EDX. The quantitative analysis gave, in atomic percentages (at.%), C 51.74 at.%, O 38 at.%, S 9.43 at.%, and Na 0.83 at.%. Figure 8 shows an EDX analysis performed on the polymer after absorbing ibuprofen. The analysis detected the presence of nitrogen, but no sodium was detected on the polymer. The composition of the sample with ibuprofen was C 56.92 at.%, O 26.16 at.%, N 16.11 at.%, and S 0.81 at.%. Interestingly, sulfur was detected on both samples; APS and DVS both contain

TABLE 1: ANOVA data of mathematical models used to ascertain drug release for buffer solution.

Temperature (°C)	Zero order		First order		Higuchi	
	R^2	F^0	R^2	F^0	R^2	F^0
35	0.5540	0.005	0.439	0.0150	0.67534	0.00063521
37	0.557	0.00503	0.4312	0.0167	0.6898	0.00050198
39	0.764	0.00265	0.6517	0.00167	0.7706	0.00010684

TABLE 2: ANOVA data of mathematical models used to ascertain drug release for ethanol-water.

Temperature (°C)	Zero order		First order		Higuchi	
	R^2	F^0	R^2	F^0	R^2	F^0
35	0.6924	2.331×10^{-24}	0.3679	1.4299×10^{-6}	0.8579	1.2814×10^{-22}
37	0.63585	6.841×10^{-16}	0.3998	7.4200×10^{-9}	0.80601	1.083×10^{-24}
39	0.54493	9.202×10^{-13}	0.308706	7.685×10^{-7}	0.7168	2.060×10^{-19}

sulfur, so this is the source of S in the samples; the ratio C/S is higher on the sample containing ibuprofen than on the sample of the polymer without the NSAID; this difference is attributed to the presence of IBP that elevated the content of carbon relative to sulfur.

3.4. Drug Release. In the PBS solution, more IBP is released than in the ethanol-water solution, about 1.17 mg/mL at 35°C and 0.58 mg/mL at 39°C in PBS, while in ethanol-water the maximum is 0.45 mg/mL at 39°C and the minimum is 0.23 mg/mL at 37°C. This suggests that the kinetics of crystallization of ibuprofen on the gel surface is preferred in PBS than in an ethanol-water solution, as various authors state that it depends on temperature, and temperatures below 40°C promote supersaturation of ibuprofen [14].

In order to determine the drug release kinetic model describing the dissolution profile, Matlab software was used. The simulation of the drug release of ibuprofen in buffer solution (PBS) and ethanol-water solution (EWS) was done using the mathematic models: zero, first, Higuchi, and Korsmeyer-Peppas. ANOVA results are summarized in Tables 1 and 2 for zero, first, and Higuchi models and those for Korsmeyer-Peppas model for both solvents are in Table 3. The F -values are not statistically significant (Tables 2 and 3). The confidence level is low around 80%; this demonstrates that the release of IBU is not “zero” and “first order.” According to the results of the kinetics of IBP, n values are lower than 0.5; this corresponds to the ranges described by the Higuchi model, indicating the existence of several simultaneous processes in the diffusion phenomenon of ibuprofen [20].

In the first stage of this diffusional process, described by zero, first, and Higuchi, n for Fickian diffusion is >0.5 .

Cylindrical samples were used, $n = 0.121$ and $K = 0.477$, for the Korsmeyer-Peppas model. The Korsmeyer-Peppas simulation was correlated by ANOVA results for both solvents of IBU medium. From the calculated F^0 , it can be inferred that the parameters and the interactions considered in the experimental design are statistically significant at 95% confidence level. The contribution of Korsmeyer-Peppas simulation is shown in Figure 9; in this figure, the

TABLE 3: ANOVA data of mathematical model Korsmeyer-Peppas simulation.

Solvent	Temperature (°C)	R^2	F^0
Buffer	35	0.86906	0.000052
Buffer	37	0.93486	0.00000314
Buffer	39	0.94927	0.00000115
Ethanol-water	35	0.79316	1.3162×10^{-18}
Ethanol-water	37	0.823801	4.9406×10^{-26}
Ethanol-water	39	0.745548	6.6297×10^{-21}

Korsmeyer-Peppas contribution is shown as an isotherm. It can be observed from Table 3 that the parameter F is the most significant factor with 37°C for both solvents. The best solvent to release the IBP is the buffer solution. Using the simulation, the release of ibuprofen at the first 50 minutes is clearly demonstrated. The mathematical model of Korsmeyer-Peppas is the best correlation between the minimum diffusional exponents.

If we try to correlate the observations from the SEM micrographs, where IBP clusters are seen, there is a threshold of dispersed percolation, and the critical percolation probability is preferred at 39°C in an ethanol-water solution. The buffer solution releases IBP in smaller quantities without diffusion restriction by polymeric chain relaxation or erosion.

3.5. XRD. Figure 10 shows the powder diffractograms of the pure polymer and of the polymer with IBP. The result for pure HPC/PAAm, shown in Figure 10(a), is very similar to HPC with a molar substitution (MS) of 4 [21], with reflections of 2θ at 7° and 21°; the material of the diffractogram has a low degree of crystallinity, as it shows an amorphous halo diffraction pattern [22], and the sample is noisy, with the peak at 40° being broad and having noise. The diffractogram of the HPC/PAAm gel is shown in Figure 10(b); the intensity of the peak at 21° is increased and the sample looks less amorphous; however, the peaks of IBP are not seen on the diffractogram, and this indicates that there is a reduction in crystallinity or

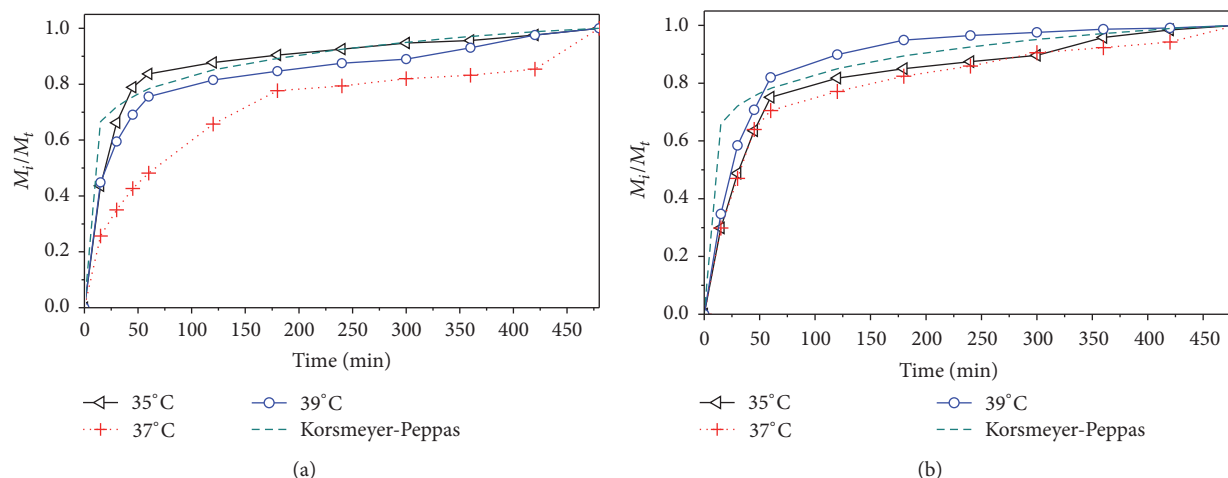


FIGURE 9: Release of IBP using (a) buffer solution and (b) ethanol-water.

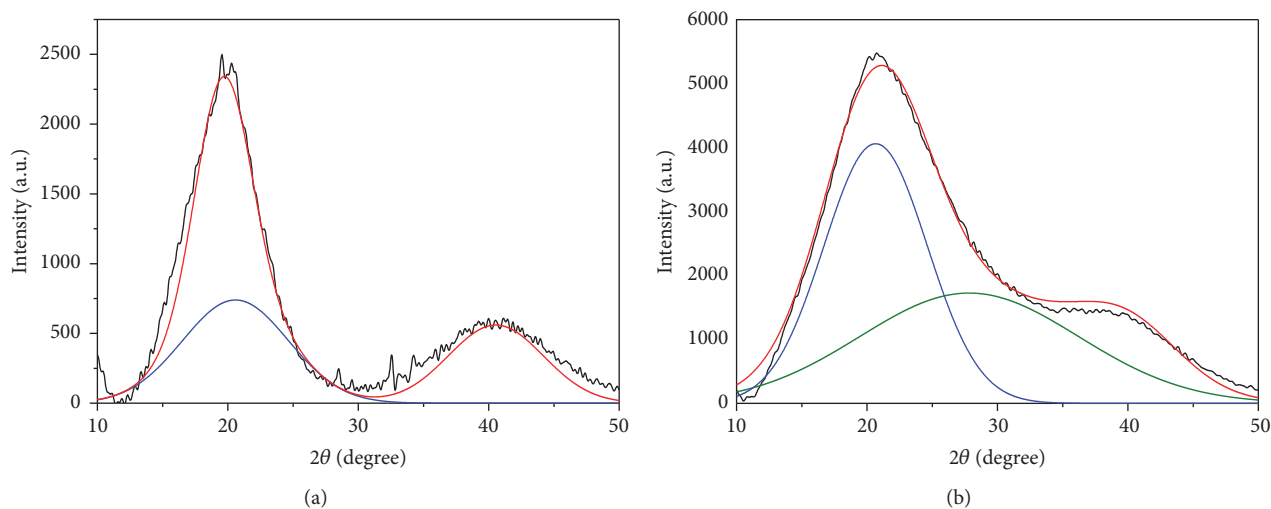


FIGURE 10: Powder diffractograms of (a) HPC/PAAm and (b) HPC/PAAm with IBP.

a change in crystal size because there is a higher quantity of polymers [4, 23–25].

The crystallization grades of the samples were calculated for the HPC/PAAm gel, having 68% of crystallinity, and the sample HPC/PAAm-IBP has 58% of crystallinity; the results are according to reports in literature [23, 24].

4. Conclusions

IBP was incorporated into HPC/PAAm films and the release kinetics was measured. The incorporation of the NSAID was verified with FTIR. The spectra showed that the IBP peaks are present on the films after the incorporation of the drug; this observation was confirmed with the DSC thermograms, which showed a peak at 75–77°C consistent with the presence of IBP on the polymer. The peak showed by DSC suggested that IBP crystals had a prismatic shape [13] and that there is a polymer-drug interaction. The SEM micrographs showed the presence of IBP crystals on the surface of the polymer,

corroborating the results of FTIR and DSC. EDX indicated a change in the ratio C/S in the samples, suggesting the incorporation of a molecule having carbon and no sulfur, as the molecule of ibuprofen. There is a change in the size of the crystals of IBP during the process of incorporation of the NSAID to the polymer, as indicated by XRD.

The HPC/PAAm gel is able to release the IBP that was incorporated in the polymer. The polymer was able to release 1.1 mg/mL of IBP at 35°C in PBS; the kinetics of the drug release is a non-Fickian phenomenon. In this case, the NSAID is released by a diffusion phenomenon and by viscoelastic relaxation of the polymer during the simultaneous swelling process [1].

Competing Interests

The authors declare that there is no conflict of interests regarding the publication of this article.

Acknowledgments

C. Castillo-Miranda and H. Velasco-Ocejo would like to thank SEP and CONACYT (no. 572436) for the scholarship for graduate studies. The authors are grateful to Mr. D. Pozas Zepeda (University of Colima, Faculty of Science) and R. Morán (National Autonomous University of Mexico, Campus IER Cuernavaca) for the SEM images. The article was published with the support of PRODEP.

References

- [1] A. K. Bajpai, S. K. Shukla, S. Bhanu, and S. Kankane, "Responsive polymers in controlled drug delivery," *Progress in Polymer Science*, vol. 33, no. 11, pp. 1088–1118, 2008.
- [2] X. Chen, S. Wang, M. Lu et al., "Formation and characterization of light-responsive TEMPO-oxidized konjac glucomannan microspheres," *Biomacromolecules*, vol. 15, no. 6, pp. 2166–2171, 2014.
- [3] C. Castro, A. Morales, A. Koschella, and T. Heinze, "Phase behaviour of hydroxypropyl cellulose/polyacrylamide gels," *Macromolecular Symposia*, vol. 296, no. 1, pp. 429–435, 2010.
- [4] J. Siepmann and N. A. Peppas, "Modeling of drug release from delivery systems based on hydroxypropyl methylcellulose (HPMC)," *Advanced Drug Delivery Reviews*, vol. 48, no. 2-3, pp. 139–157, 2001.
- [5] M. V. Risbud, A. A. Hardikar, S. V. Bhat, and R. R. Bhonde, "pH-sensitive freeze-dried chitosan-polyvinyl pyrrolidone hydrogels as controlled release system for antibiotic delivery," *Journal of Controlled Release*, vol. 68, no. 1, pp. 23–30, 2000.
- [6] T. J. Higuchi, "Mechanism of sustained-action medication. Theoretical analysis of rate of release of solid drugs dispersed in solid matrices," *Journal of Pharmaceutical Sciences*, vol. 52, no. 12, pp. 1145–1149, 1963.
- [7] R. W. Korsmeyer and N. A. Peppas, "Macromolecular and modeling aspects of swelling-controlled systems," in *Controlled Release Delivery Systems*, T. J. Roseman and S. Z. Mansdorf, Eds., pp. 77–90, Dekker, New York, NY, USA, 1983.
- [8] J. Mark, *Polymer Data Handbook*, Oxford University Press, New York, NY, USA, 1999.
- [9] C. F. Castro-Guerrero and D. G. Gray, "Chiral nematic phase formation by aqueous suspensions of cellulose nanocrystals prepared by oxidation with ammonium persulfate," *Cellulose*, vol. 21, no. 4, pp. 2567–2577, 2014.
- [10] C. De Brabander, G. Van Den Mooter, C. Vervaet, and J. P. Remon, "Characterization of ibuprofen as a nontraditional plasticizer of ethyl cellulose," *Journal of Pharmaceutical Sciences*, vol. 91, no. 7, pp. 1678–1685, 2002.
- [11] J. D. Higgins, T. P. Gilmor, S. A. Martellucci, R. D. Bruce, and H. G. Brittain, "Ibuprofen," in *Analytical Profiles of Drug Substances and Excipients*, H. G. Brittain, Ed., vol. 27, pp. 265–300, Academic Press, New York, NY, USA, 2001.
- [12] R. J. Babu, W. Brostow, I. M. Kalogeras, and S. Sathigari, "Glass transitions in binary drug + polymer systems," *Materials Letters*, vol. 63, no. 30, pp. 2666–2668, 2009.
- [13] G. M. Khan and Z. Jiabi, "Preparation, characterization, and evaluation of physicochemical properties of different crystalline forms of ibuprofen," *Drug Development and Industrial Pharmacy*, vol. 24, no. 5, pp. 463–471, 1998.
- [14] A. Rashid, E. T. White, T. Howes, J. D. Litster, and I. Marziano, "Growth rates of ibuprofen crystals grown from ethanol and aqueous ethanol," *Chemical Engineering Research and Design*, vol. 90, no. 1, pp. 158–161, 2012.
- [15] J. Heiko, L. Vander, H. Sebastiaan, O. Wouter, and B. Piet, "Stimulus-sensitive hydrogels and their application in chemical (micro) analysis," *The Royal Society of Chemistry*, vol. 128, pp. 325–331, 2003.
- [16] A. S. Hoffman, P. S. Stayton, V. Bulmus et al., "Really smart bioconjugates of smart polymers and receptor proteins," *Journal of Biomedical Materials Research*, vol. 52, no. 4, pp. 577–586, 2000.
- [17] Y. Qiu and K. Park, "Environment-sensitive hydrogels for drug delivery," *Advanced Drug Delivery Reviews*, vol. 53, no. 3, pp. 321–339, 2001.
- [18] S. H. Cho, M. S. Jhon, S. H. Yuk, and H. B. Lee, "Temperature-induced phase transition of poly(*N,N*-dimethylaminoethyl methacrylate-*co*-acrylamide)," *Journal of Polymer Science, Part B: Polymer Physics*, vol. 35, no. 4, pp. 595–598, 1997.
- [19] R. S. Werbowyj and D. G. Gray, "Ordered phase formation in concentrated hydroxypropylcellulose solutions," *Macromolecules*, vol. 13, no. 1, pp. 69–73, 1980.
- [20] D. R. Lide, *Handbook of Chemistry and Physics*, CRC, Boca Raton, Fla, USA, 76th edition, 1996.
- [21] R. J. Samuels, "Solid-state characterization of the structure and deformation behavior of water-soluble hydroxypropylcellulose," *Journal of Polymer Science Part A*, vol. 7, no. 7, pp. 1197–1258, 1969.
- [22] R. Talukder, C. Reed, T. Dürig, and M. Hussain, "Dissolution and solid-state characterization of poorly water-soluble drugs in the presence of a hydrophilic carrier," *AAPS PharmSciTech*, vol. 12, no. 4, pp. 1227–1233, 2011.
- [23] M. Nagpal, S. K. Singh, and D. Mishra, "Superporous hybrid hydrogels based on polyacrylamide and chitosan: characterization and *in vitro* drug release," *International Journal of Pharmaceutical Investigation*, vol. 3, no. 2, pp. 88–94, 2013.
- [24] S. V. Dalvi and R. N. Dave, "Analysis of nucleation kinetics of poorly water-soluble drugs in presence of ultrasound and hydroxypropyl methyl cellulose during antisolvent precipitation," *International Journal of Pharmaceutics*, vol. 387, no. 1-2, pp. 172–179, 2010.
- [25] L. Segal, I. J. Creely, A. E. Martin Jr., and C. M. Conrad, "An empirical method for estimating the degree of crystallinity of native cellulose using the X-ray diffractometer," *Textile Research Journal*, vol. 29, no. 10, pp. 786–794, 1959.

Research Article

Bacteriostatic Substrate by Conductivity Method and Electric Spark Discharge Method Combined with Electrospinning for Silver Dressing

Kuo-Hsiung Tseng, Chaur-Yang Chang, Meng-Yun Chung, and Ya-Lan Tang

Department of Electrical Engineering, National Taipei University of Technology, Taipei, Taiwan

Correspondence should be addressed to Kuo-Hsiung Tseng; khtseng@ee.ntut.edu.tw

Received 30 May 2016; Revised 15 August 2016; Accepted 31 August 2016

Academic Editor: Ming-Guo Ma

Copyright © 2016 Kuo-Hsiung Tseng et al. This is an open access article distributed under the Creative Commons Attribution License, which permits unrestricted use, distribution, and reproduction in any medium, provided the original work is properly cited.

This study uses the conductivity method, Electric Spark Discharge Method, and the electrospinning technique to develop a better silver-based antibacterial agent. The preparation process is free of chemical substances and also conforms to the green energy-saving process. The silver iodide was prepared in an iodine agar medium by using the conductivity method. Multiple bacteriostasis experiments showed that the molds grew in the position with iodine of the culture medium after 6 days, as well as in the position with silver iodide after 10 days. The results prove that silver iodide has better bacteriostatic ability than povidone iodine. The nanosilver colloid was prepared in the PVA solution by using the Electric Spark Discharge Method. UV-Vis, Zetasizer, and SEM-EDX analyses proved that the PVA solution contained nanosilver colloid with good suspension stability. Finally, the electrospinning technique was used to spin the PVA solution with nanosilver colloid into the PVA nanofibrous membrane. According to UV-Vis analysis, the absorption peak of this nanofibrous membrane is about 415 nm, meaning this nanofibrous membrane contains nucleate nanosilver colloid, and is very suitable for antiseptic dressing.

1. Introduction

Ever since British researcher Alexander Fleming published his paper on penicillin with bactericidal action in 1929, biomedical circles have put great efforts into the research and development of different antibiotics in order to resist different bacteria; thus, the history of human antibacterial reaches a new milestone, prolonging the average life. Although antibiotics have strong sterilizing effect, if they are applied improperly and fail to completely kill bacteria, then the surviving bacteria evolve into drug-fast variant bacteria by gene mutation. When antibiotics lose their effect on bacteria, infectious diseases are more easily spread as the transport velocity increases, making it more difficult for humans to fight infectious diseases [1, 2]. Therefore, solving resistance to antibiotics and seeking other methods to kill infectious bacteria have become important topics of medical technology in this century.

Skin is the protection layer for isolating bacteria. When the skin is hurt, the dressing plays an important role of wound

care. The method of open dressing is used in the danger of infection or the tissue fluid is not stopping. Normally, when the tissue fluid is still flowing or the wound is not clean, the bacteriostasis is to avoid the deterioration of the wound and the sterilization to heal it. Moreover, if a suitable moist environment is provided, it will accelerate wound healing. To meet the needs of the aforementioned wound care, the development of the dressing, medicine, and assisted therapy is much more improved, such as silver ion, nanosilver particles, nanofibrous membrane, and iontophoretic transdermal drug delivery system.

Silver was actually extensively used as an antibiotic material before antibiotics were invented. However, after the extensive development of antibiotics, the antibacterial role of silver was gradually neglected. In recent years, due to the rapid development of nanotechnology and bacterial resistance, research has again paid attention to silver and silver nanoparticles in biomedical materials [3–5]. Therefore, the development of silver dressing has become a very important part of wound care. At present, silver-bearing dressing

has been extensively used to treat chronic wounds, as the dressing releases silver ions to control bacteria [6–8]. In addition, because the sterilization of silver is physical, there will not be any drug resistance problem [9]. Among the silver dressing preparation methods, the physical method has cleaner silver particles than the chemical method. Therefore, this paper uses the conductivity method, Electric Spark Discharge Method, and the electrospinning technique to research a better silver-based antibacterial agent.

There have been many studies regarding electrospinning, but also a few studies that mix PVA with collagen. For example, the nanofibrous membrane of PVA can remedy the defects of traditional nonwoven fabric [10]. According to FTIR analysis, spun yarn contains collagen. In terms of antibacteria, some studies employed chitosan as the antibacterial material to successfully spin biodegradable dressing [11]. Other studies used the electrospinning technique to jet collagen nanofiber, where the mean size of the fiber was about 100 nm, and examined collagen spinning for fibroblast culture in vitro [12].

2. Material and Methods

In recent years, many nanometals have been developed and applied to medical products. The nanometal preparation methods encompass physical, chemical, and mechanical. Many studies have used ESDM to prepare nanometal, which is a preparation method that takes the principle of a physical electrical spark discharge [13–15]. In comparison to the mechanical and chemical methods, the nanometal preparation process by ESDM is free from pollution, and the nanoparticles are easily collected.

2.1. Principle of Preparing Nanosilver Colloid by ESDM. EDM is a hot working method that converts electrical energy to thermal energy in order to quickly melt a workpiece. The method of using EDM to melt the metal surface to obtain nanometal colloid is called the Electric Spark Discharge Method (ESDM) [16–18]. Figure 1 shows the process of preparing nanometal colloid by ESDM, where d_{gap} is the distance between two electrodes. Here, d_{min} and d_{max} are defined as the minimum distance and maximum distance of the electrode gap, respectively, when the EDM discharge succeeds.

- (1) When $d_{\text{gap}} > d_{\text{max}}$, the dielectric fluid has high resistance; thus, the discharge circuit forms an open circuit, as shown in Figure 1(a).
- (2) When $d_{\text{min}} \leq d_{\text{gap}} \leq d_{\text{max}}$, the electric field intensity is enough to make the dielectric fluid have slight resistivity; thus, an arc is generated between the two electrodes. The electrons quickly impact the upper electrode (anode) in the discharge process, and the cations flow towards the cathode slowly, as shown in Figure 1(b).
- (3) In the spark discharge process, the arc temperature is enough to melt the electrode material nearby the arc and gasify the dielectric fluid in the electrode gap.

TABLE I: Nanosilver colloid preparation parameters.

Discharge pulse ($T_{\text{ON}}-T_{\text{OFF}}$)	20-10 μs
Current setting (IP)	1-1.4 A
Capacitor	No
DI water	40 mL
Metal wire size	1 mm
Pressure	1 atm
SERVO.	1/2
SENS.	1/2
z-axis	1/2
Discharge time	60 sec
Metal purity	99.99%
Temperature	25°C

The pressure generated by the gasification expansion of the dielectric fluid compels the molten metal to scatter in the dielectric fluid. The fine particles sputtered in the dielectric fluid are rapidly cooled and condensed by the peripheral cold dielectric fluid to nanoparticles, as shown in Figure 1(c).

- (4) When discharge is complete, the dielectric fluid reverts to the state of insulation, as shown in Figure 1(d).

The nanometal colloid can be prepared by ESDM through the aforesaid process. As the electrode gap is the main factor influencing the process, the interelectrode distance shall be readjusted by the servo control system [19].

Figure 2 shows the architecture of preparing nanometal colloid by EDM. In this paper, the upper electrode and lower electrode are made of silver. The charging/discharging circuit provides the impulse voltage required when the electrode is discharging. The servo control system controls the electrode gap, as it judges the interelectrode distance according to the feedback signal of the electrode current, and the driving system and motor readjust the distance between the working electrodes (z-axis); thus, the electrode gap maintains a good discharge interval and the success rate of discharge rises. When the electrode gap is 10~100 μm , two electrodes successfully generate arc discharge. The electrode surface is turned molten by the arc temperature and rapidly scattered in the dielectric fluid, which is then cooled and condensed by dielectric fluid to silver nanoparticles [20, 21].

ESDM is used to prepare nanosilver colloid in this paper. The process is characterized by simple and rapid preparation and mass production and is free from any chemical substances; thus, it is a method conforming to green energy-saving process. Table 1 lists the process parameters. The upper and lower electrodes are made of metal silver, with a diameter of 1 mm and purity approaching 99.99%. The preparation environment is the standard condition, the $T_{\text{ON}}-T_{\text{OFF}}$ parameter of the discharge circuit is set as 20-10 μs , the beaker capacity is 40 mL, SERVO., SENS., and z-axis parameters are set as 1/2, and the dielectric fluid is deionized water (DI water).

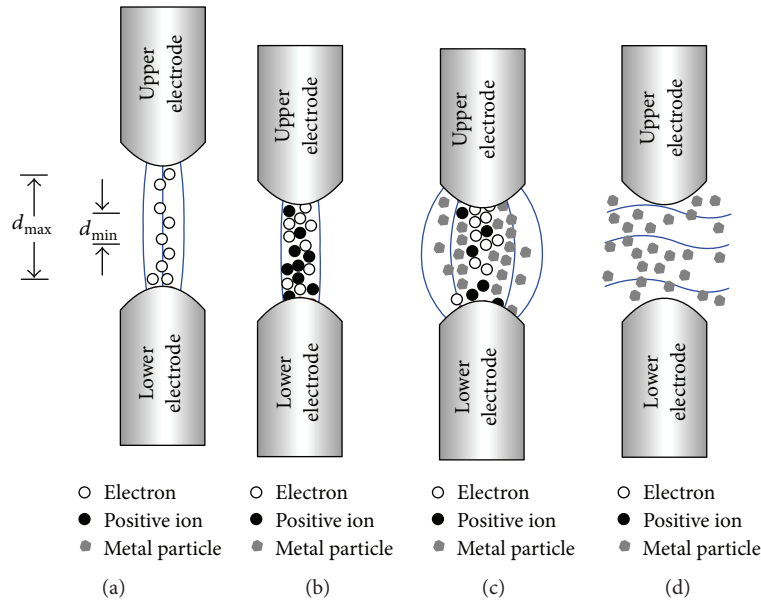


FIGURE 1: Process of preparing nanometal colloid by ESDM.

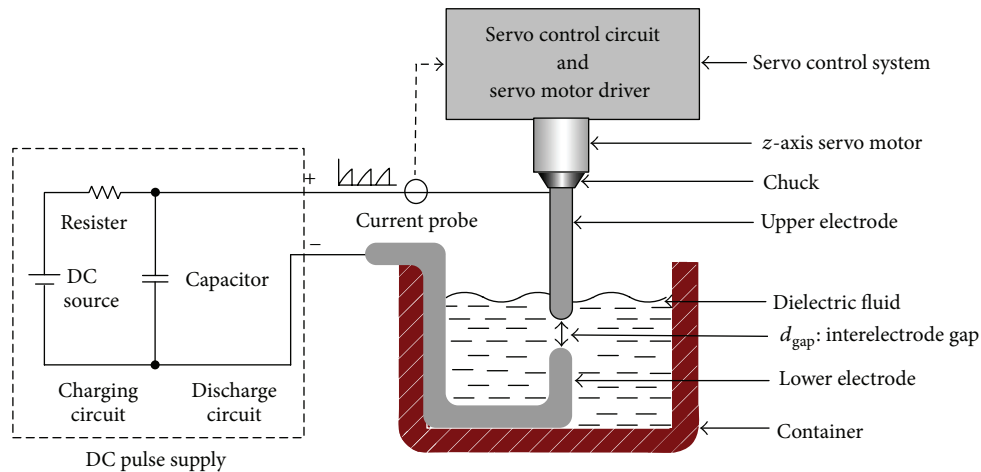


FIGURE 2: Architecture of preparing nanometal colloid by EDM.

In terms of the physical and chemical properties of the nanosilver colloid in this paper, the absorption spectrum, suspension stability, particle size, and composition of the ESDM prepared nanosilver colloid are analyzed by UV-Visible Spectroscopy (UV-Vis), Zetasizer, and SEM-EDX. The UV-Vis analysis results show that there is an obvious absorbance peak at 410 nm, as shown in Figure 3(a). The Zetasizer analysis results show that the average Zeta-Potential is about -39.3 mV, meaning the nanosilver colloid has good suspension stability, as shown in Figure 3(b). The SEM analysis results show that the particle size of nanosilver colloid is about 20 nm, as shown in Figure 3(c). The EDX analysis results show that the principal component of nanosilver colloid is silver, and carbon and oxygen are provided by water and the kargogel, respectively, for analysis, as shown in Figure 3(d).

2.2. Preparation of Silver Iodide by Conductivity Method. Povidone iodine is extensively used as a disinfectant, as it slowly releases iodine on the wound tissue for bacteriostasis. As silver has good bacteriostatic ability, if iodine is replaced by silver iodide, then the bacteriostatic effect can be enhanced. This paper uses the conductivity method to prepare silver iodide and examines the bacteriostatic ability of silver iodide according to the fungal growth in the bacteria culture medium.

The preparation of silver iodide by using the conductivity method is by combining the silver and iodine ions in the iodine agar medium into a silver iodide under the electric field effect. Regarding the production of the iodine agar medium, 192 g water and 8 g advanced agar powder are prepared in an agar solution at a concentration of 4%. The solution is stirred and heated to 90°C , and the agar solution is

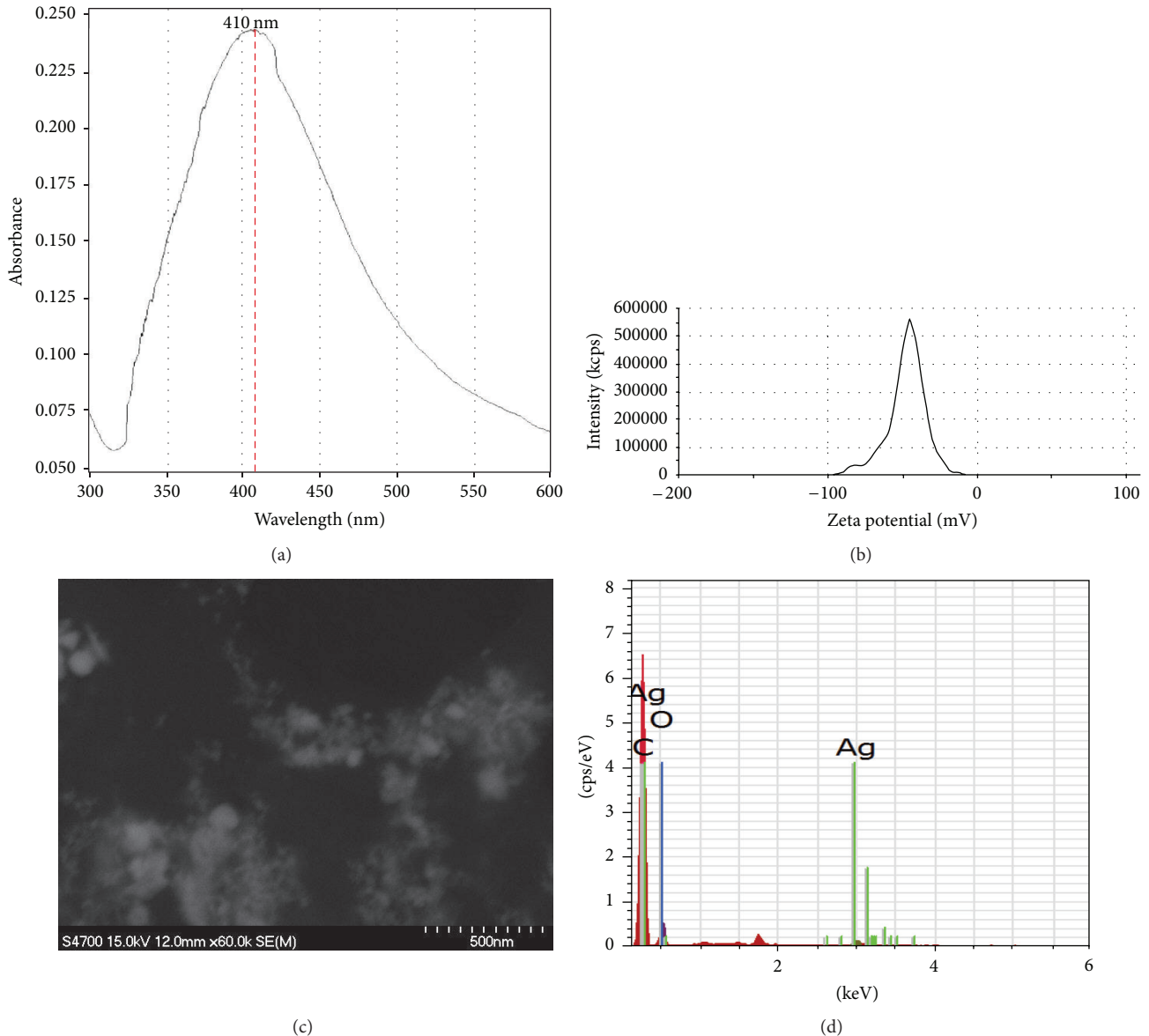


FIGURE 3: Nanosilver colloid (a) UV-Vis analysis, (b) Zetasizer analysis, (c) SEM image, and (d) EDX component analysis.

mixed with 4 c.c. povidone iodine and poured into the culture dish. The solution is cooled and solidified into an iodine agar medium. As the agar powder contains starch, the iodine agar medium is dark blue.

In terms of preparing silver iodide by the conductivity method, a silver wire and a silver sheet are inserted in the iodine agar medium as electrodes, the anode of the DC voltage source is connected to the silver sheet, and the cathode is connected to the silver wire; thus, the interelectrode current is maintained at 10 mA within 10 minutes, as shown in Figure 4. In the conductance process, the silver ions at the anode are combined with the electronegative iodine ions to form a light yellow silver iodide. The aforesaid silver wire has a diameter of 1 mm, and the silver sheet is 1 mm thick, 1 cm long, and 1 cm wide.

2.3. Combine ESDM with Electrospinning to Prepare Silver Nanoparticle PVA Nanofibrous Membrane. Traditional textile technology uses melt spinning, dry spinning, or gel spinning to weave fiber, with a diameter of $2\ \mu\text{m}$ ~ $100\ \mu\text{m}$, and its size is a micrometer scale. The fabric woven by the electrospinning technique has a nanoscale diameter, higher porosity, and larger surface area, and the pore size is smaller than that woven by the traditional technique. Therefore, the nanofibrous membrane made by the electrospinning technique has high toughness and tear resistance.

A schematic diagram of electrospinning is shown in Figure 5(a). The high polymer solution is placed in the injector. Under the action of a strong electric field, the solution forms a so-called Taylor cone at the nozzle position. A bunch of polymer stream is ejected from the cone tip and

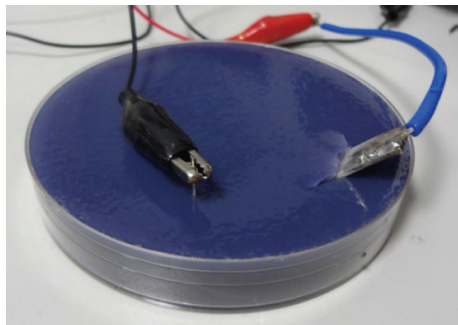


FIGURE 4: Preparing silver iodide by the conductivity method.

sprayed on the fiber collector in a helical whipping action under the attraction of the electric field. During ejection, the electric field aligns the polymer molecules into a fiber yarn within one microsecond. As the fiber filament is pulled and extended, its diameter is one thousandth of the fiber produced by the general micrometer nozzle, and the diameter of the end product is about 150 nm. The fiber made by this method has high moisture permeability, high porosity, and high specific surface area; thus, it is extensively used in filtration, tissue engineering, biomedicine, and wound dressing material [22, 23].

In order to prepare PVA nanofibrous membrane with a good bacteriostatic effect, ESDM is used to prepare the silver nanoparticle PVA solution, and the electrospinning machine sprays the silver nanoparticle PVA solution into PVA nanofibrous membrane. The principle of preparing the silver nanoparticle PVA solution is the same as the principle for preparing nanosilver colloid in DI water, that is, the preparation method stated in Section 2.1. The only difference is that the PVA solution, at a concentration of 10%, is prepared to replace the DI water, and the silver nanoparticles can be dispersed in the PVA solution. Finally, the aforesaid silver nanoparticle PVA solution is placed in the electrospinning machine and sprayed into the PVA nanofibrous membrane. Figure 5(b) shows the electrospinning machine used in this paper. The red frame is the main action part of the electrospinning machine. This paper uses UV-Vis to observe the characteristics of the PVA nanofibrous membrane and checks whether the silver nanoparticles are nucleated in PVA and wrapped in PVA.

3. Results and Discussion

3.1. Experiment on Bacteriostasis of Silver Iodide. In order to know the feasibility of using silver iodide in dressing, as prepared by the conductivity method, this paper used bacteriostasis experiments to observe the bacteriostatic effect of silver iodide and iodine. In order to avoid errors in the experimental results, the experiment was conducted twice, and the correctness of the first experiment was rechecked by the result of the second experiment.

The molds were placed in the iodine agar medium for the first experiment, and mold growth in the culture medium was observed on Day 3, Day 6, and Day 10. First, equivalent molds

TABLE 2: Conductance silver iodide bacteriostasis experiment (unit cm).

Culture medium	Day						
	1st experiment				2nd experiment		
	Day 1	Day 3	Day 6	Day 10	Day 1	Day 6	Day 10
Agar part	0	2	4	6	0	2	4.5
Povidone iodine part	0	0	1.2	2.8	0	0	2.2
Silver iodide part	0	0	0	2.8	0	0	2

are placed in the lower right part, lower left part, and upper part of the iodine agar medium, as shown in Figure 6(a). The orifice in the lower right part resulted from the removal of the silver wire electrode. As the silver wire electrode is connected to the cathode of the power supply, the negatively charged iodine ions are repelled by the cathodic electrons, and this part of the culture medium is white and free of iodine ion. The orifice in the lower left part resulted from the removal of the silver sheet electrode. As the silver sheet electrode is connected to the anode of the power supply, the iodine ions and silver ions can be combined into silver iodide. The mold growth in the culture medium on Day 3, Day 6, and Day 10 is as shown in Figures 6(b), 6(c), and 6(d), respectively. Figure 6(b) shows that the molds breed only in the position without iodine ion. Figure 6(c) shows that the iodine in the culture medium is all dissipated after 6 days; thus, the culture medium is white. The lower left part of the culture medium is silver iodide; thus, it is light yellow. The mold begins to grow in the upper part with iodine. Figure 6(d) shows that while the mold has grown in the lower left part with silver iodide, the mold is less than that of the other two parts.

The locations of mold in the culture medium for the second experiment are the same as the first experiment, as shown in Figure 7(a). The mold growth in the culture mediums on Day 6 and Day 10 is as shown in Figures 7(b) and 7(c), respectively. The experimental results show that the mold grew fastest in the position free of iodine and then in the position with iodine, followed by the mold growing most slowly in the position with silver iodide. This result matches the result of Experiment 1.

In the two experiments on the bacteriostasis of the agar medium, the growths of the molds in various parts of the culture mediums are as shown in Table 2 and Figure 8. According to the results of two repeated experiments, the silver ions from conductance and the iodine ions can be combined into silver iodide. The experimental results show that iodine can actually inhibit the fungal growth; however, the silver iodide has better bacteriostatic effect. This conductivity method can be used for preparing povidone iodine in the future, meaning that the povidone iodine solution containing silver ions can enhance bacteriostatic ability.

3.2. Silver Nanoparticle PVA Nanofibrous Membrane Characteristic Analysis. In order to know the characteristics of

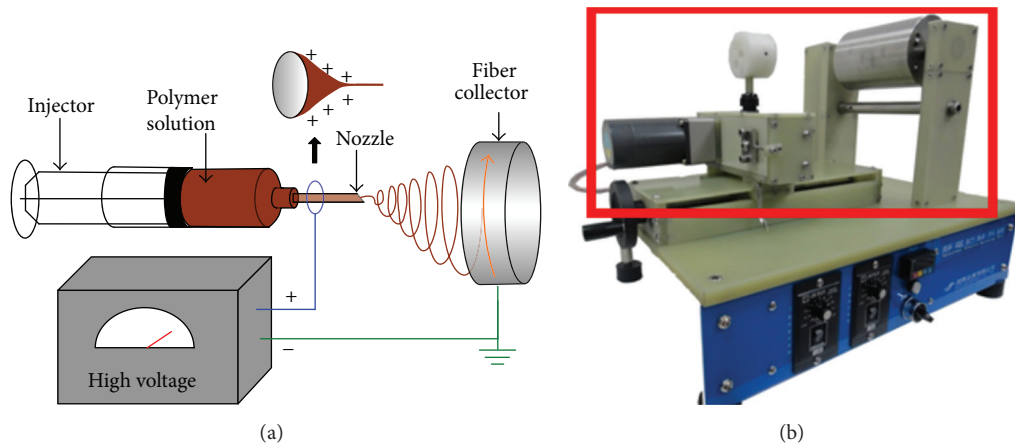


FIGURE 5: (a) Schematic diagram of electrospinning apparatus and (b) electrospinning machine.

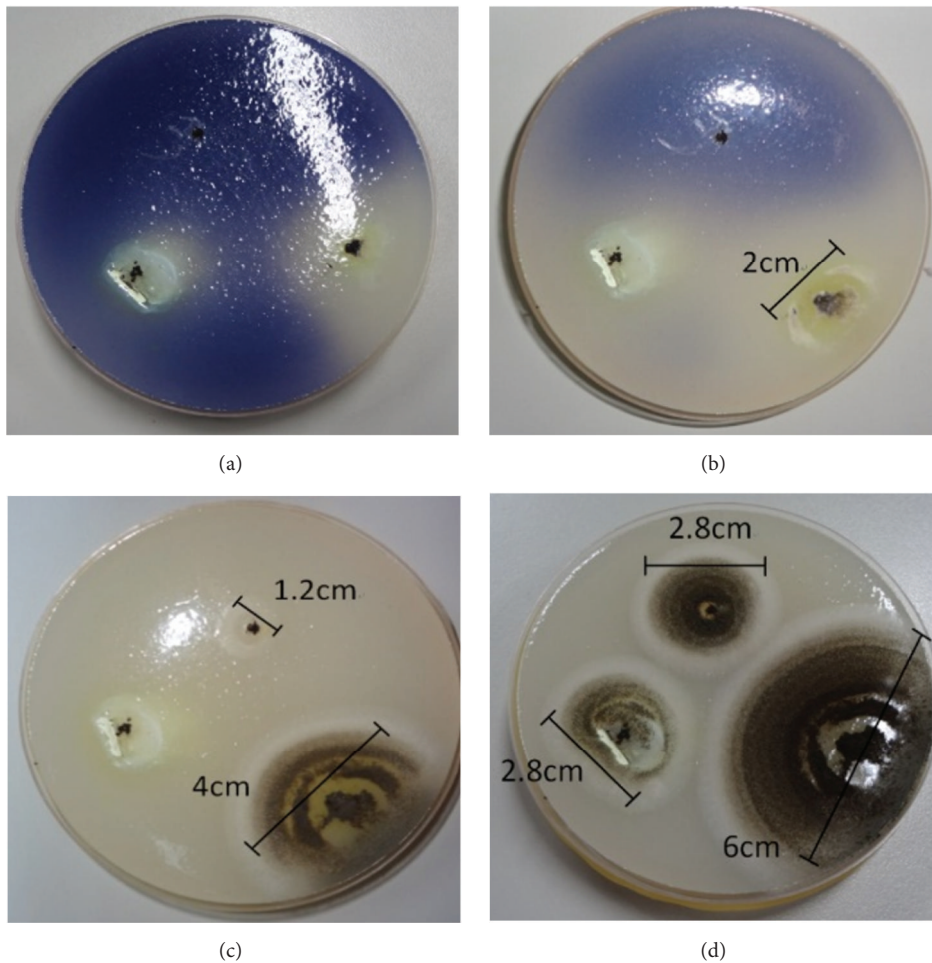


FIGURE 6: Silver iodide from conductance for the first time of (a) placement of molds, (b) 3 days after placement of molds, (c) 6 days after placement of molds, and (d) 10 days after placement of molds.

the PVA solution of nanosilver colloid, the absorption spectrum is observed by UV-Vis. The absorption spectrum of nanosilver colloid of DI water, as shown in Figure 3(a), is compared with the absorption spectrum of PVA solution of

nanosilver colloid, as shown in Figure 9. The wavelength of the PVA solution nanosilver colloid is about 420 nm, the wavelength of nanosilver colloid of DI water is about 410 nm, and the difference is 10 nm, which is the red shift.

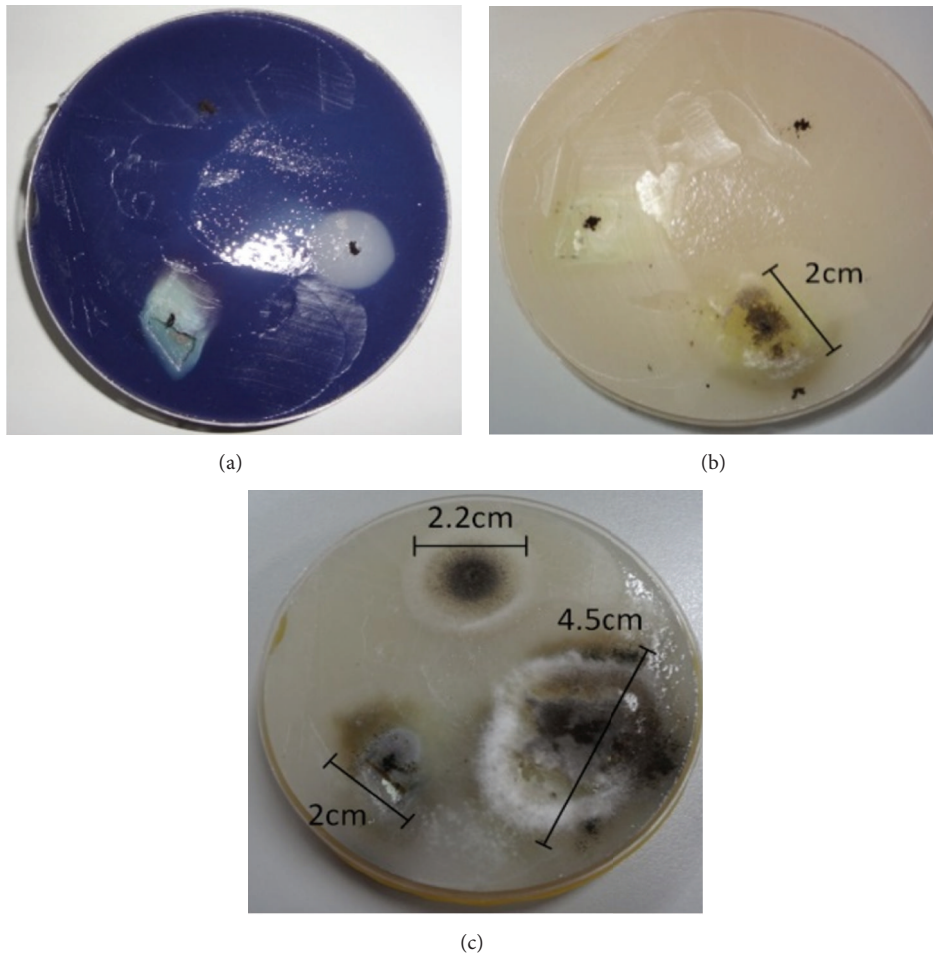


FIGURE 7: Silver iodide from conductance in (a) placement of molds, (b) 6 days after placement of molds, and (c) 10 days after placement of molds.

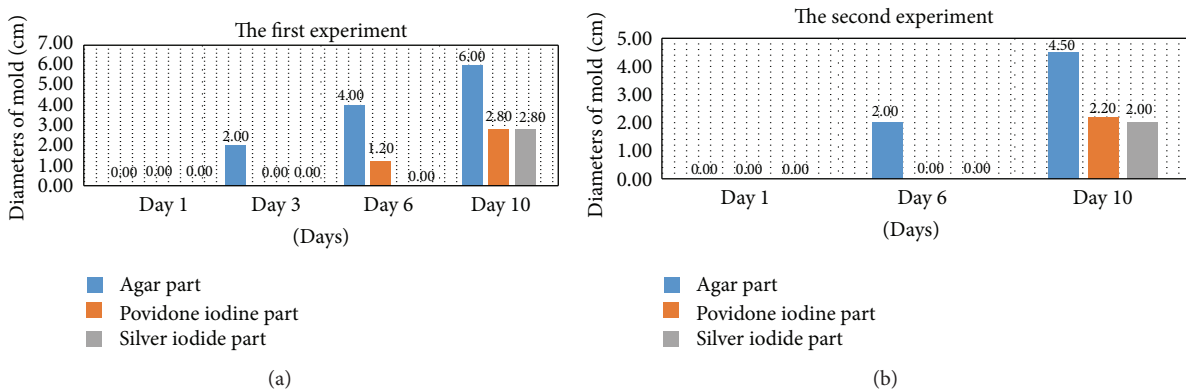


FIGURE 8: Bar graphs of conductance silver iodide bacteriostasis experiment for (a) result of the first experiment and (b) result of the second experiment.

Therefore, the PVA solution material is silver nanoparticle, and its absorption value is larger than the silver nanoparticles in DI water, meaning its concentration is higher than the silver nanoparticles in DI water.

The nanofibrous membrane, as prepared by the electro-spinning machine, is light yellow, as shown in Figure 10. In

order to further know the absorption peak of this nanofibrous membrane and review whether this nanofibrous membrane has nucleate silver nanoparticles, the nanofibrous membrane is affixed to a quartz sample cell, as shown in Figure 11. The UV-Vis analysis result of the membrane affixed to the quartz sample cell is as shown in Figure 12. The spectrogram shows

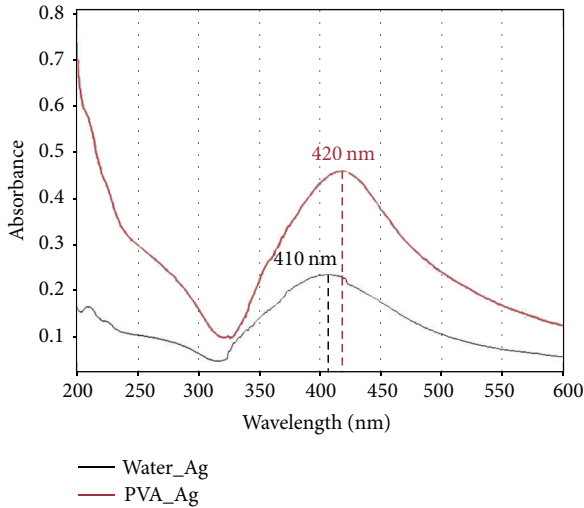


FIGURE 9: UV absorption spectrogram of water phase silver nanoparticle and PVA silver nanoparticle.

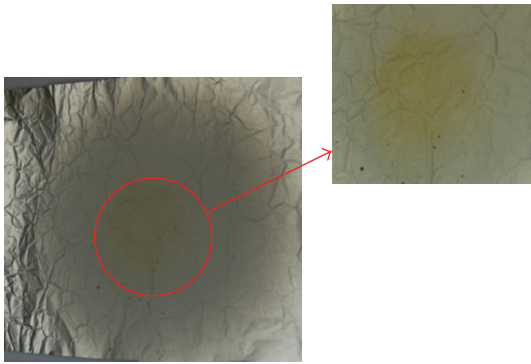


FIGURE 10: PVA electrostatic spun yarn with nanosilver colloid.

that the nanofibrous membrane has an approximate absorption peak of 415 nm, which is approximately identical to silver nanoparticles. Therefore, this membrane does actually contain nucleate silver nanoparticles. As this membrane contains nanosilver colloid, it has sterilizing effect, and the PVA is innocuous and not harmful to the human body. Therefore, the nanofibrous membrane can be used in antiseptic dressing, gas mask membrane filters, and so forth.

3.3. The Application of Combining the Silver Iodide and Silver Nanoparticle PVA Nanofibrous Membrane. Due to the fact that the characteristics of silver iodide and silver nanoparticle PVA nanofibrous membrane are separately suitable for bacteriostasis, sterilization, and moist environment for the wound, this study combined them to a brand new wound care. The schematic diagram of the combined method is shown in Figure 13. First, place the iodine agar on the wounds and conduct the silver iodide into the possibly infective part. When the silver iodide touched the wounds, it will make the pathogen dead which is the purpose of sterilization. Then the silver nanoparticle PVA nanofibrous membranes cover the silver iodide. The fiber of the membrane can maintain the

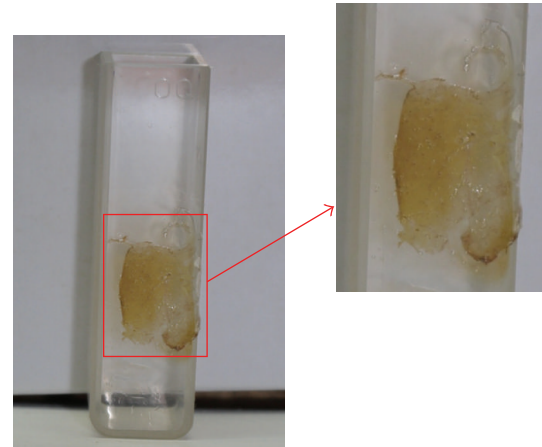


FIGURE 11: Quartz tube attached with PVA yarn with nanosilver colloid.

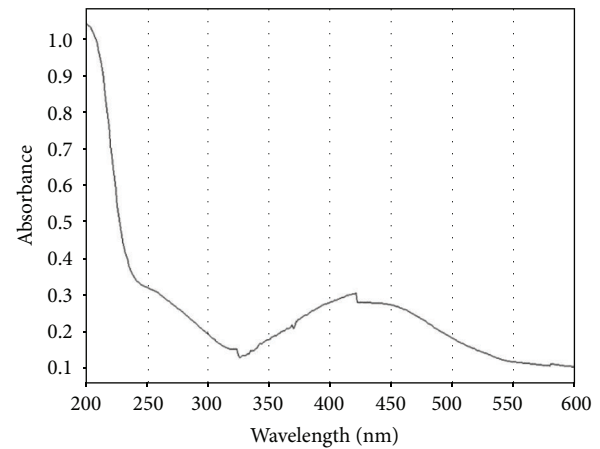


FIGURE 12: UV-Vis of PVA yarn with nanosilver colloid.

moist of healing environment and absorb most of the tissue fluid. When the two things made contact, the membrane will release the nanosilver particles which will suppress the growth of the bacterial and the generation of the odor.

4. Conclusions

As silver has strong bacteriostatic ability, and the bacteria will not become drug-fast, silver and silver nanoparticles are applicable to dressing. This paper uses the conductivity method, electric spark method, and the electrospinning technique to research a better silver-bearing dressing preparation method. This preparation process is free from chemical substances; thus, it matches the method of green energy-saving processes, as prepared silver particles are cleaner than that created by the chemical method, and they are safe for humans. The findings are described as follows.

- (1) Silver ion is successfully ionized from silver electrodes by using the conductivity method, which combines the iodine ion in the iodine agar medium into silver iodide. Multiple bacteriostasis experiments prove that

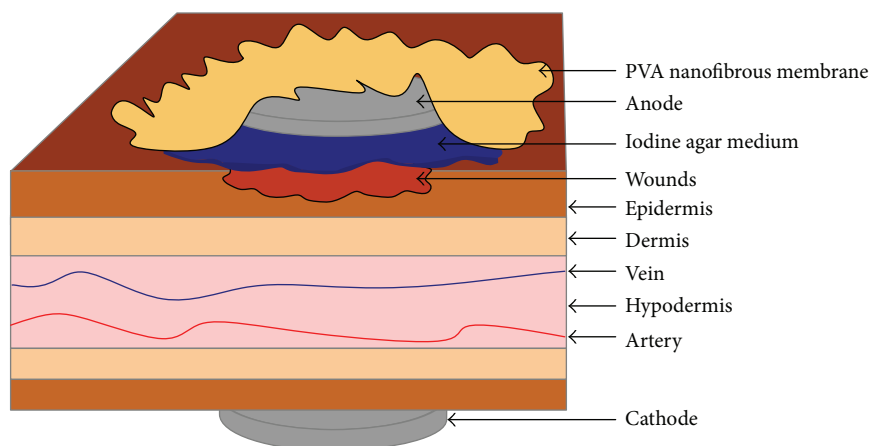


FIGURE 13: The schematic diagram of combining the silver iodide and silver nanoparticle PVA nanofibrous membrane.

silver iodide has a better bacteriostatic effect than povidone iodine. This conductivity method can be combined with the preparation of povidone iodine in the future, in order that the povidone iodine solution containing silver ions can enhance its bacteriostatic ability.

- (2) Nanosilver colloid is successfully prepared in DI water by ESDM. According to the analysis results of UV-Vis, Zetasizer, and SEM-EDX, the principal component of this solution is silver, the wavelength of the nanosilver colloid is about 410 nm, Zeta-Potential is about -39.3 mV, and particle size is about 20 nm. These data show that the solution actually does contain nanoscale silver colloid with good suspension stability.
- (3) Nanosilver colloid is successfully prepared in PVA solution by ESDM. The wavelength of this nanosilver colloid is about 420 nm, and the absorption value is larger than the silver nanoparticle in DI water, meaning the concentration of nanosilver colloid is higher than the nanosilver colloid in DI water.
- (4) The light yellow silver nanoparticle PVA nanofibrous membrane is successfully prepared by ESDM and the electrospinning technique. The UV-Vis analysis result shows that the absorption peak of this membrane is about 415 nm, which is enough to prove that the silver nanoparticles have been wrapped in a PVA nanofibrous membrane. Therefore, this nanofiber has good antibacterial ability and is suitable for antiseptic dressing.
- (5) Combination of the silver iodide and silver nanoparticle PVA nanofibrous membrane in the wound care will give effect of bacteriostasis and sterilization to the wounds. Also, it will provide a more suitable and faster healing environment.

Competing Interests

The authors declare that there is no conflict of interests regarding the publication of this paper.

Acknowledgments

The authors would like to thank the Ministry of Science and Technology, China (MOST 103-2221-E-027-070-), for financially supporting this research.

References

- [1] D. L. Monnet, F. M. MacKenzie, J. M. López-Lozano et al., "Antimicrobial drug use and methicillin-resistant *Staphylococcus aureus*, Aberdeen, 1996–2000," *Emerging Infectious Diseases*, vol. 10, no. 8, pp. 1432–1441, 2004.
- [2] T. D. Hollingsworth, N. M. Ferguson, and R. M. Anderson, "Will travel restrictions control the international spread of pandemic influenza?" *Nature Medicine*, vol. 12, no. 5, pp. 497–499, 2006.
- [3] S. Srinivasan, P. T. Sudheesh Kumar, S. V. Nair, S. V. Nair, K. P. Chennazhi, and R. Jayakumar, "Antibacterial and bioactive α - and β -chitin hydrogel/ nanobioactive glass ceramic/nano silver composite scaffolds for periodontal regeneration," *Journal of Biomedical Nanotechnology*, vol. 9, no. 11, pp. 1803–1816, 2013.
- [4] A. Oya, S. Yoshida, Y. Abe, T. Iizuka, and N. Makiyama, "Antibacterial activated carbon fiber derived from phenolic resin containing silver nitrate," *Carbon*, vol. 31, no. 1, pp. 71–73, 1993.
- [5] H.-K. Lee, M.-J. Shim, J.-S. Lee, and S.-W. Kim, "Characteristics of CO gas adsorption on modified natural zeolite," *Materials Chemistry and Physics*, vol. 44, no. 1, pp. 79–84, 1996.
- [6] R. E. Burrell, J. P. Hegggers, G. J. Davis, and J. B. Wright, "Efficacy of silver-coated dressings as bacterial barriers in a rodent burn sepsis model," *Wounds*, vol. 11, no. 4, pp. 64–71, 1999.
- [7] S.-F. Lo, M. Hayter, C.-J. Chang, W.-Y. Hu, and L.-L. Lee, "A systematic review of silver-releasing dressings in the management of infected chronic wounds," *Journal of Clinical Nursing*, vol. 17, no. 15, pp. 1973–1985, 2008.

- [8] J. B. Wright, K. Lam, D. Hansen, and R. E. Burrell, "Efficacy of topical silver against fungal burn wound pathogens," *American Journal of Infection Control*, vol. 27, no. 4, pp. 344–350, 1999.
- [9] I. Sondi and B. Salopek-Sondi, "Silver nanoparticles as antimicrobial agent: a case study on *E. coli* as a model for Gram-negative bacteria," *Journal of Colloid and Interface Science*, vol. 275, no. 1, pp. 177–182, 2004.
- [10] J.-P. Guggenbichler, M. Böswald, S. Lugauer, and T. Krall, "A new technology of microdispersed silver in polyurethane induces antimicrobial activity in central venous catheters," *Infection*, vol. 27, no. 1, pp. S16–S23, 1999.
- [11] H.-J. Jeon, S.-C. Yi, and S.-G. Oh, "Preparation and antibacterial effects of Ag-SiO₂ thin films by sol-gel method," *Biomaterials*, vol. 24, no. 27, pp. 4921–4928, 2003.
- [12] J. A. Matthews, G. E. Wnek, D. G. Simpson, and G. L. Bowlin, "Electrospinning of collagen nanofibers," *Biomacromolecules*, vol. 3, no. 2, pp. 232–238, 2002.
- [13] C.-Y. Liao, K.-H. Tseng, and H.-S. Lin, "Preparation of metallic aluminum compound particles by submerged arc discharge method in aqueous media," *Metallurgical and Materials Transactions B*, vol. 44, no. 1, pp. 91–97, 2013.
- [14] J.-K. Lung, J.-C. Huang, D.-C. Tien et al., "Preparation of gold nanoparticles by arc discharge in water," *Journal of Alloys and Compounds*, vol. 434–435, pp. 655–658, 2007.
- [15] D.-C. Tien, K.-H. Tseng, C.-Y. Liao, J.-C. Huang, and T.-T. Tsung, "Discovery of ionic silver in silver nanoparticle suspension fabricated by arc discharge method," *Journal of Alloys and Compounds*, vol. 463, no. 1–2, pp. 408–411, 2008.
- [16] S. Tariq Jilani and P. C. Pandey, "Analysis and modelling of EDM parameters," *Precision Engineering*, vol. 4, no. 4, pp. 215–221, 1982.
- [17] M. Gostimirovic, P. Kovac, M. Sekulic, and B. Skoric, "Influence of discharge energy on machining characteristics in EDM," *Journal of Mechanical Science and Technology*, vol. 26, no. 1, pp. 173–179, 2012.
- [18] S. Son, H. Lim, A. S. Kumar, and M. Rahman, "Influences of pulsed power condition on the machining properties in micro EDM," *Journal of Materials Processing Technology*, vol. 190, no. 1–3, pp. 73–76, 2007.
- [19] K. H. Tseng, Y.-S. Kao, and C.-Y. Chang, "Development and implementation of a micro-electric discharge machine: real-time monitoring system of fabrication of nanosilver colloid," *Journal of Cluster Science*, vol. 27, no. 2, pp. 763–773, 2016.
- [20] K.-H. Tseng, J.-L. Chiu, H.-L. Lee, Y.-S. Kao, and D.-C. Tien, "Spark parameter monitoring feedback system for preparation of nanosilver colloid in EDM," *Materials and Manufacturing Processes*, vol. 31, no. 2, pp. 186–193, 2016.
- [21] D.-C. Tien, C.-Y. Liao, J.-C. Huang et al., "Novel technique for preparing a nano-silver water suspension by the arc-discharge method," *Reviews on Advanced Materials Science*, vol. 18, no. 8, pp. 750–756, 2008.
- [22] Z.-M. Huang, Y.-Z. Zhang, M. Kotaki, and S. Ramakrishna, "A review on polymer nanofibers by electrospinning and their applications in nanocomposites," *Composites Science and Technology*, vol. 63, no. 15, pp. 2223–2253, 2003.
- [23] K. H. Hong, "Preparation and properties of electrospun poly (vinyl alcohol)/silver fiber web as wound dressings," *Polymer Engineering & Science*, vol. 47, no. 1, pp. 43–49, 2007.

Research Article

Reaction Behavior of Cellulose in the Homogeneous Esterification of Bagasse Modified with Phthalic Anhydride in Ionic Liquid 1-Allyl-3-methylimidazium Chloride

Hui-Hui Wang,¹ Xue-Qin Zhang,¹ Piao Long,¹ Ai-Ping Zhang,² Chuan-Fu Liu,¹ and Run-Cang Sun³

¹State Key Laboratory of Pulp and Paper Engineering, South China University of Technology, Guangzhou 510640, China

²College of Materials and Energy, Guangdong Key Laboratory for Innovative Development and Utilization of Forest Plant Germplasm, South China Agricultural University, Guangzhou 510642, China

³Beijing Key Laboratory of Lignocellulosic Chemistry, Beijing Forestry University, Beijing 100083, China

Correspondence should be addressed to Chuan-Fu Liu; chfliu@scut.edu.cn

Received 3 June 2016; Revised 11 August 2016; Accepted 31 August 2016

Academic Editor: Antje Potthast

Copyright © 2016 Hui-Hui Wang et al. This is an open access article distributed under the Creative Commons Attribution License, which permits unrestricted use, distribution, and reproduction in any medium, provided the original work is properly cited.

In order to elucidate the reaction behavior of cellulose component in bagasse, the homogeneous phthalation of bagasse was investigated comparatively with the isolated cellulose in 1-allyl-3-methylimidazium chloride (AmimCl) with phthalic anhydride (PA) at the dosage of 10–50 mmol/g. The phthalation degrees of bagasse and the isolated cellulose were in the range of 5.66% to 22.71% and 11.61% to 44.11%, respectively. A phthalation degree increase of cellulose was proportional to phthalic anhydride dosage due to its regular macromolecular structure and followed the equation $y_{\text{PDI}} = 0.004x - 0.02$. FT-IR and 2D HSQC NMR analyses confirmed the attachment of phthaloyl group. The phthalation reactivity of the three hydroxyls in the isolated cellulose followed the order of C-6 > C-2 > C-3, and the more selective phthalation to C-6 position was found in the cellulose component in bagasse. These results provide detailed understanding of the homogenous modification mechanism of lignocellulose.

1. Introduction

Bagasse, an abundant agricultural lignocellulosic by-product, represents a potentially sustainable biomass resource to create fuels, chemicals, and composites to replace fossil-based products. The bioproducts derived from bagasse have been applied in many industrial fields such as coating, food-packing, and painting [1, 2], paving the way to replace the fossil-based products.

However, bagasse presents considerable chemical and physical inertness, such as complex structure, strong hydrogen bonds, and high crystallinity of cellulose, which restricts the dissolution of bagasse in common organic or inorganic solvents. Fortunately, some novel solvents or solvent systems have been reported to dissolve lignocellulosic materials [3–5]. Among these novel solvents, ionic liquids (ILs) have received much attention due to the recoverability, designability, extremely low vapor pressure, inflammability, and

thermal and chemical stability [6]. The bridge between ILs and biomass has been built from over ten years ago [7], and many homogeneous modifications of lignocellulose have been investigated in ILs [8, 9], among which esterification of the available reactive hydroxyls is relatively easily accomplished. However, due to the obstacle to obtain detailed information of esterified lignocellulose, the homogeneous esterification mechanism was little studied.

To obtain more detailed structural information, many efforts have been devoted to establish efficient solvent systems for the complete and nonderivative dissolution of plant cell walls. Ball-milling was reported to benefit the dissolution of lignocellulose for spectroscopic analysis [10]. The combination of ball-milling and efficient solvent systems makes the characterization of lignocellulosic cell walls with 2D HSQC NMR feasible, which could offset the lack of detailed information provided by solid-state ¹³C-NMR commonly

used in the previous studies [11, 12]. Based on ball-milling, a so-called “gel-state NMR method” was developed with solution-state 2D NMR [13, 14]. The assignment of the correlations in 2D HSQC NMR spectra was reported from various cellulose models [15], providing the database of cell wall samples for further investigation.

Considering the complex structure and various linkages among different components of lignocellulose, the homogeneous phthalation of lignocellulose was investigated comparatively with the isolated component under the same conditions to elucidate the mechanism. In the present study, the isolated cellulose and bagasse were comparatively phthalated. The phthalated samples were characterized with FT-IR, ^1H NMR, ^{13}C NMR, and 2D HSQC NMR to study the reaction behavior of cellulose fractions in bagasse phthalation. The thermal stability of the phthalated samples was also studied with thermogravimetric analysis (TGA).

2. Material and Methods

2.1. Materials. Bagasse was obtained from a local factory (Jiangmen, China). It was dried in sunlight and cut into small pieces. The cut bagasse was ground and screened to prepare 20–40 mesh size particles (450–900 μm). The dried ground samples were extracted with toluene-ethanol (2:1, v/v) for 4 h and then dried in a cabinet oven with air circulation at 50°C for 24 h. The extractive-free bagasse was divided into two parts: one was finely ball-milled for 48 h in a planetary BM4 ball-miller (Grinder, Beijing, China) at 608 rpm for further characterization and modification and the other for the isolation of cellulose. The contents of cellulose, hemicelluloses, and lignin in the extractive-free bagasse were determined as 44.85%, 33.13%, and 19.14%, respectively, according to the standard NREL methods [16].

1-Allyl-3-methylimidazolium chloride (AmimCl) IL was purchased from Chengjie Chemical Co., Ltd. (Shanghai, China), and used as received. Phthalic anhydride (PA) and other chemicals were of analytical grade and were purchased from Guangzhou Chemical Reagent Factory (Guangdong, China).

2.2. Isolation of Cellulose from Bagasse. Cellulose was isolated from the extractive-free bagasse according to the previous literature [12]. Briefly, the extractive-free bagasse was delignified at 75°C for 2 h with sodium chlorite at pH 3.8–4.0, adjusted by 10% acetic acid. The solid residues were collected by filtration, washed with distilled water until neutral pH, then washed with ethanol, and dried in a cabinet oven for 16 h at 50°C. The solid residues were extracted with 10% NaOH at a solid to liquor ratio of 1:20 g/mL for 10 h at 20°C. The alkaline extraction procedure was repeated thrice to remove the noncellulosic substances. The solid residues were filtered out, washed thoroughly with distilled water, then washed with ethanol, and dried in an oven with air circulation at 50°C for 24 h.

2.3. Homogeneous Phthalation. The isolated cellulose (4.8 g) was finely ball-milled for 48 h in a planetary BM4 ball-miller (Grinder, Beijing, China) at 608 rpm. Ball-milled cellulose

or bagasse (0.5 g) was dispersed in 10 g AmimCl at room temperature with agitation under nitrogen atmosphere for 10 min, and the suspension was stirred at 90°C for 4 h to obtain a clear solution. PA was added portionwise to the solution with the dosage of 10, 20, 30, 40, and 50 mmol/g, respectively. The mixture was agitated at 90°C for 90 min under N_2 atmosphere for phthalation. After the required time, the resulted solution was cooled to room temperature and added into 200 mL ethanol with agitation. The suspension was further continuously stirred for 12 h to thoroughly precipitate the phthalated products. The solid residues were filtered out, thoroughly washed with ethanol (four times, total 800 mL) to remove unreacted PA, AmimCl, and byproducts, and freeze-dried for further characterization [17].

2.4. Determination of Phthalation Degree. The substituted hydroxyl contents of phthalated samples were determined based on the equivalent volume of NaOH and HCl standard solution by back-titration method [18] according to the following:

$$\text{SHC} = \frac{c_{\text{NaOH}} \times V_{\text{NaOH}} - c_{\text{HCl}} \times V_{\text{HCl}}}{2} \times \frac{1000}{m}, \quad (1)$$

where SHC (mmol/g) is the substituted hydroxyls contents, m (g) is the dry weight of sample analyzed, c_{NaOH} (mol/L) is the molarity of NaOH standard solution, V_{NaOH} (mL) is the consumed volume of NaOH standard solution, c_{HCl} (mol/L) is the molarity of HCl standard solution, and V_{HCl} (mL) is the consumed volume of HCl standard solution.

Based on the assumption that cellulose is composed of anhydroglucose (AGU), the theoretical hydroxyl contents of the unmodified cellulose were calculated from its macromolecular structure according to (2), the theoretical hydroxyl contents of phthalated bagasse samples were calculated based on the contents of three main components according to (3), and phthalation degree of cellulose and bagasse was calculated based on (4).

$$\text{THC}_C = \frac{1000}{162} \times 3, \quad (2)$$

where THC_C is the theoretical hydroxyl groups content of unmodified cellulose, 162 g/mol is the molar mass of AGU, and 3 is the number of hydroxyl groups on each AGU.

$$\text{THC}_B = \text{THC}_C \times 44.85\% + \text{THC}_H \times 33.13\% + \text{THC}_L \times 19.14\%, \quad (3)$$

where THC_B , THC_C , THC_H , and THC_L are the theoretical hydroxyl groups content of the unmodified bagasse, cellulose, hemicelluloses, and lignin, respectively, and 44.85%, 33.13%, and 19.14% are the contents of cellulose, hemicelluloses, and lignin, respectively, in the extractive-free bagasse. The theoretical hydroxyl contents of the unmodified hemicelluloses and lignin were 15.15 and 5.13 mmol/g (data not shown).

$$\text{PD} = \frac{\text{SHC}}{\text{THC}} \times 100\%, \quad (4)$$

where PD is the phthalation degree, SHC is the substituted hydroxyl contents, and THC is the theoretical hydroxyl contents.

TABLE I: The substituted hydroxyl contents and phthalation degrees of the phthalated cellulose and bagasse.

Sample no.	Temp. (°C)	PA dosage ^a (mmol/g)	Solvent	Time (h)	THC ^b (mmol/g)	SHC ^c (mmol/g)	PD ^d (%)
C1	90	10	AmimCl	1.5	18.52	2.15	11.61
C2	90	20	AmimCl	1.5	18.52	2.61	14.09
C3	90	30	AmimCl	1.5	18.52	3.71	20.03
C4	90	40	AmimCl	1.5	18.52	5.51	29.75
C5	90	50	AmimCl	1.5	18.52	8.17	44.11
S1	90	10	AmimCl	1.5	14.31	0.81	5.66
S2	90	20	AmimCl	1.5	14.31	1.47	10.27
S3	90	30	AmimCl	1.5	14.31	1.94	13.56
S4	90	40	AmimCl	1.5	14.31	2.92	20.41
S5	90	50	AmimCl	1.5	14.31	3.25	22.71

^aThe ratio of phthalic anhydride (mmol) to biomass material (g, bagasse or cellulose).

^bTheoretical hydroxyls content of unmodified biomass material.

^cSubstituted hydroxyl contents determined by back titration.

^dPhthalation degree.

2.5. Characterization. FT-IR spectra were obtained on FT-IR spectrophotometer (Nicolet 510) using a KBr disk containing approximately 1% finely ground samples. Thirty-two scans were taken for each sample with a resolution of 2 cm^{-1} in transmittance mode in the range of $4000\text{--}400\text{ cm}^{-1}$.

The ^1H NMR, ^{13}C NMR, and 2D HSQC NMR spectra were recorded from 40 mg samples in 0.5 mL DMSO- d_6 on a Bruker Advance III 600 MHz spectrometer (Germany). The ^1H NMR and ^{13}C NMR spectra were recorded according to the previous literature [19]. For the ^1H NMR analysis, the detailed collecting and processing parameters were as follows: number of scans, 16; receiver gain, 61; acquisition time, 2.7263 s; relaxation delay, 1.0 s; pulse width, 11.0 s; spectrometer frequency, 600.17 MHz; and spectral width, 12019.2 Hz. For ^{13}C NMR analysis, the detailed collecting and processing parameters were as follows: number of scans, 10000; receiver gain, 187; acquisition time, 0.9088 s; relaxation delay, 2.0 s; pulse width, 12.0 s; spectrometer frequency, 150.91 MHz; and spectral width, 36057.7 Hz. For 2D HSQC analysis, the detailed collecting and processing parameters were listed as follows: number of scans, 32; receiver gain, 187; relaxation delay, 1.5 s; pulse width, 11.0 s; acquisition time, 0.1420 s; spectra frequency, 600.17/150.91 Hz; and spectra width, 7211.5/24875.6 Hz.

The thermal stability of cellulose samples was studied using thermogravimetric analysis (TGA) on a thermal analyzer (SDT Q600, TA Instrument). The apparatus was continually flushed with nitrogen. The sample weighed between 8 and 10 mg, and the scans were run from 50°C to 500°C at a heating rate of $10^\circ\text{C}/\text{min}$.

3. Results and Discussion

3.1. Homogeneous Phthalation of Cellulose in Bagasse. It is well known that the complex inhomogeneous structure of bagasse is formed by three main components including

cellulose, hemicelluloses, and lignin. Actually, the homogeneous phthalation of bagasse is the phthalation of the abundant reactive hydroxyl groups in the three main components. Therefore, in order to elucidate the mechanism of homogeneous phthalation, the isolated cellulose was comparatively phthalated under the same conditions as bagasse to estimate the detailed reaction behavior of cellulose in the phthalation of bagasse mixture in AmimCl, as listed in Table I.

Theoretically, each AGU contains three hydroxyl groups, and the free hydroxyl group content of the isolated cellulose is 18.52 mmol/g. After phthalation in AmimCl, some of the hydroxyl groups were substituted, as shown in Table I. With the increment of PA dosage from 10 to 20, 30, 40, and 50 mmol/g, the substituted hydroxyl contents in the phthalated cellulose estimated from back titration increased from 2.15 to 2.61, 3.71, 5.51, and 8.17 mmol/g, respectively, and the free hydroxyl content decreased from 16.37 to 15.91, 14.81, 13.01, and 10.35 mmol/g, respectively. Correspondingly, the phthalation degree increased from 11.61% to 14.09%, 20.03%, 29.75%, and 44.11%, respectively. These results confirmed the occurrence of phthalation of the isolated cellulose under the selected conditions. Similarly, the substituted hydroxyl contents in bagasse increased from 0.81 to 1.47, 1.94, 2.92, and 3.25 mmol/g, respectively, with the increment of PA dosage from 10 to 20, 30, 40, and 50 mmol/g. The free hydroxyl group content in unmodified bagasse, that is, the theoretical hydroxyls content, was 14.31 mmol/g estimated from the three main components based on their contents. The free hydroxyl content correspondingly decreased from 13.50 to 12.84, 12.37, 11.39, and 11.06 mmol/g, respectively, and the phthalation degree increased from 5.66% to 10.27%, 13.56%, 20.41%, and 22.71%, respectively. Comparatively, the phthalation degree of bagasse was lower than that of the isolated cellulose, indicating the higher phthalation ability of the isolated cellulose. Comparatively, the decreased phthalation degree of bagasse was due to the different contents and reactivity of hydroxyls in the three main components compared with

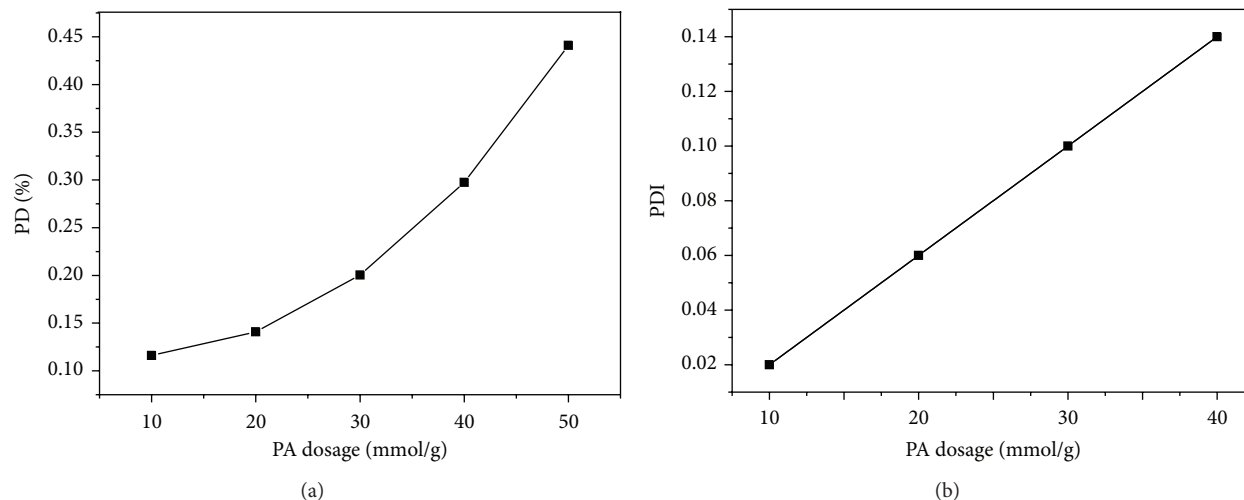


FIGURE 1: Dependence of phthalation degree ((PD), (a)) and phthalation degree increase ((PDI), (b)) on phthalic anhydride dosage.

the isolated ones. In addition, a very interesting phenomenon was found for the phthalation degree increase (PDI): PDI of cellulose was proportional to phthalic anhydride dosage, which followed the equation of $y_{\text{PDI}} = 0.004x - 0.02$, as shown in Figure 1. This regular relation was probably due to the regular macromolecular structure of cellulose. The detailed differences of the hydroxyl reactivity in different positions need to be further clarified.

3.2. FT-IR Analysis. FT-IR spectra of unmodified cellulose (C0, spectrum a) and phthalated cellulose samples (C1, spectrum b; C3, spectrum c; C4, spectrum d) are illustrated in Figure 2. The bands were assigned based on the reported literatures [20, 21]. Compared with unmodified cellulose, the noticeable bands at 1716, 1602, 1327, and 747 cm^{-1} in the phthalated samples correspond to carbonyl group in esters, aromatic ring vibration, C-O stretching in carboxyl, and out-of-plane C-H bending of benzene, respectively. The presence of these bands indicated the successful phthalation of cellulose. It should be noted that the intensities of these bands increased with the increment of PA dosage, corresponding to the increased substituted hydroxyl contents and phthalation degree in Table 1.

3.3. NMR Analysis. To further elucidate the detailed behavior of hydroxyls in different positions in AGU during phthalation, the unmodified (C0) and phthalated cellulose (C5) as well as phthalated bagasse (S5) were further characterized with 1D (^1H and ^{13}C) and 2D (HSQC) NMR technology in $\text{DMSO}-d_6$, as illustrated in Figures 3 and 4.

^1H NMR spectra of unmodified cellulose (C0, spectrum a), phthalated cellulose (C5, spectrum b), and phthalated bagasse (S5, spectrum c) are present in Figure 3. As can be seen, the relevant signals are present in two regions, namely, the AGU protons region (4.50–3.00 ppm) and the phthaloyl protons region (8.00–7.00 ppm). Compared with unmodified

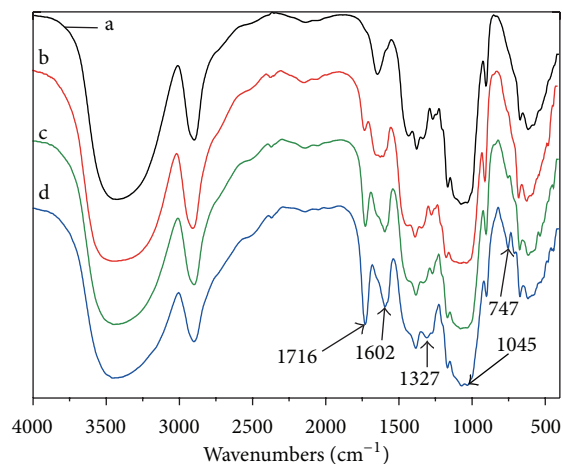


FIGURE 2: FT-IR spectra of unmodified cellulose (C0, spectrum a) and modified cellulose with phthalic anhydride dosage at 10 (C1, spectrum b), 30 (C3, spectrum c), and 40 (C4, spectrum d) mmol/g.

cellulose, the presence of peaks at 7.87 (H-10), 7.76 (H-13), 7.69 (H-11), and 7.60 (H-12) ppm for phthaloyl protons in the phthalated cellulose and phthalated bagasse confirmed the phthalation of cellulose and bagasse.

The ^{13}C NMR spectra of unmodified cellulose (C0, spectrum d), phthalated cellulose (C5, spectrum e), and phthalated bagasse (S5, spectrum f) exhibit main signals in Figure 3; the carbon skeletons of AGU at 102.83 (C-1), 80.43 (C-4), 75.27 (C-5), 75.27 (C-3), 70.38 (C-2), and 60.74 (C-6) ppm were well resolved. In the region 180–120 ppm, the cross-peaks at 168.85 (C-7), 167.57 (C-14), 134.95 (C-8), 133.34 (C-9), 132.20 (C-13), 131.71 (C-10), 130.86 (C-12), and 129.09 (C-11) ppm were assigned to carbons of the phthaloyl groups, respectively, in phthalated cellulose and phthalated bagasse, confirming the attachment of phthaloyl groups onto cellulose and bagasse. This result was consistent

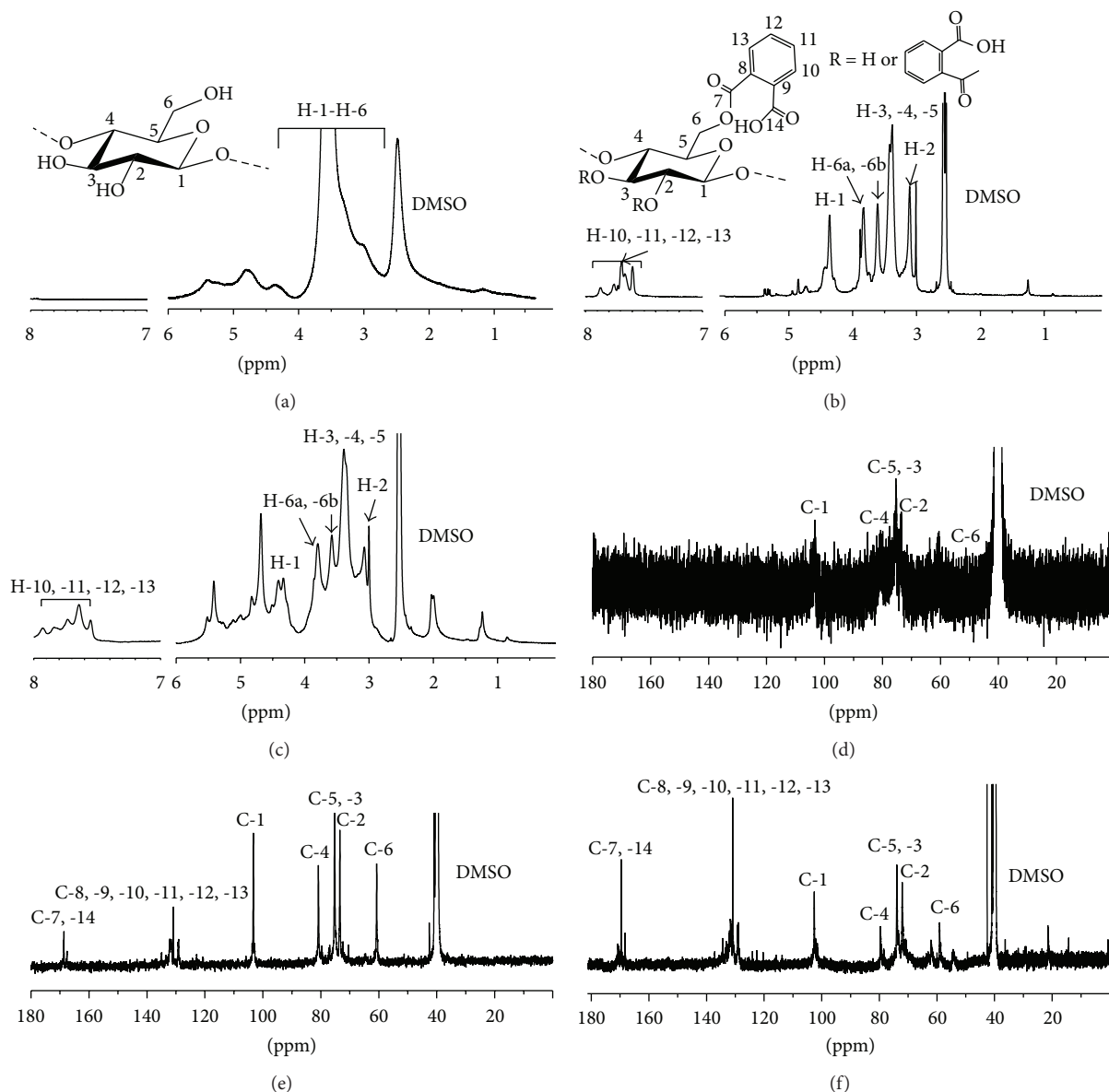


FIGURE 3: The ^1H ((a), (b), and (c)) and ^{13}C ((d), (e), and (f)) NMR spectra of unmodified cellulose (C0), phthalated cellulose (C5), and phthalated bagasse (S5).

with the previously reported esterification of wood with cyclic anhydride (succinic anhydride, maleic anhydride, and phthalic anhydride) as main monoesterification below 100°C [22]. However, the reactivity of hydroxyls from phthalated cellulose and phthalated bagasse during homogeneous phthalation could not be revealed from the ^1H NMR and ^{13}C NMR analyses. Therefore, further investigation with 2D HSQC was necessary.

The HSQC spectra of unmodified cellulose (C0, spectrum a) and phthalated cellulose (C5, spectra b and d), as well as the carbohydrate regions of phthalated bagasse (S5, spectrum c), are shown in Figure 4. The primary polysaccharide correlation peaks in HSQC spectra appeared in the range of 110–55 ppm (^{13}C) and 6.0–2.5 ppm (^1H). These correlations

were assigned based on cellulose models reported previously [15], as listed in Table 2. The primary peaks of cellulose internal units (C-I) in this region were clearly observed from the unmodified cellulose at 73.49/3.06 [C-I₂ (C₂/H₂)], 75.33/3.36 [C-I₃ (C₃/H₃)], 80.85/3.33 [C-I₄ (C₄/H₄)], 77.14/3.18 [C-I₅ (C₅/H₅)], and 103.44/4.33 [C-I₁ (C₁/H₁)] ppm; the two internal C-I₆ (C₆/H₆) peaks were also distinctively located at 60.77/3.79 and 60.77/3.58 ppm.

The end-group correlations were well resolved in the unmodified cellulose; however, some peaks were superimposed with other peaks. The correlations for non-reducing-end C-NR₆ (C₆/H₆) were well separated from the internal C-I₆ (C₆/H₆) and appeared at 61.50/3.69 and 61.50/3.39 ppm. That for C-NR₄ (C₄/H₄) was clearly present

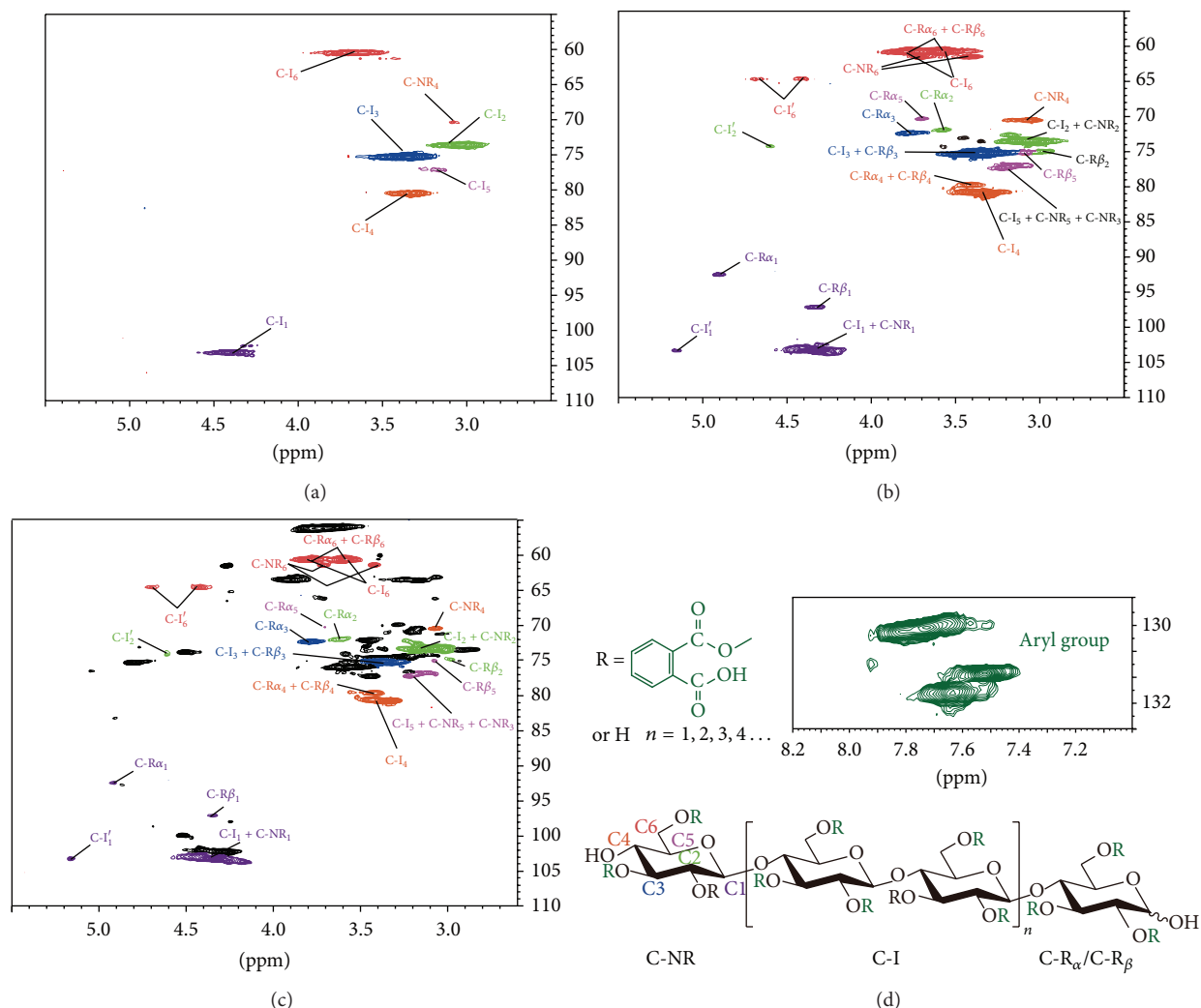


FIGURE 4: 2D HSQC NMR spectra of unmodified cellulose (C0, spectrum a), phthalated cellulose (C5, spectra b and d), and phthalated bagasse (S5, spectrum c).

TABLE 2: Primary NMR correlations in $\text{DMSO-}d_6$ for cellulose modified with phthalic anhydride.

Glycosyl residue		^1H & ^{13}C chemical shifts (ppm)						
		1	2	3	4	5	6a	6b
Cellulose (internal)	^1H	4.31	3.05	3.36	3.30	3.16	3.56	3.77
	^{13}C	103.26	73.56	75.24	80.97	77.18	60.74	60.74
Cellulose (NR)	^1H	4.23	2.98	3.15	3.05	3.16	3.39	3.69
	^{13}C	103.65	73.77	77.07	70.54	77.18	61.50	61.50
Cellulose ($\text{R}\alpha$)	^1H	4.89	3.16	3.69	3.31	3.68	3.56	3.72
	^{13}C	92.44	72.68	72.11	81.36	70.25	60.80	60.80
Cellulose ($\text{R}\beta$)	^1H	5.14	2.93	3.25	3.31	3.06	3.56	3.72
	^{13}C	103.31	74.93	75.24	81.36	75.13	60.80	60.80

at 70.54/3.05 ppm, while the correlations at 73.77/2.98 ppm for C-NR_2 (C_2/H_2) were located very close to the internal C-I_2 (C_2/H_2). Those for C-NR_3 (C_3/H_3) and C-NR_5 (C_5/H_5) had the coincident chemical shifts and overlapped with the internal C-I_5 (C_5/H_5) correlation at 77.07/3.18 ppm. The anomeric peak from non-reducing-end C-NR_1 appeared

at 103.65/4.23 ppm (C_1/H_1). The α - and β -anomer from reducing-end correlations of cellulose were clearly separated from those of the internal units. The C_1/H_1 correlation from the reducing-terminal-end of α -D-glucuronic polysaccharide (α -D-Glcp) ($\text{C-R}\alpha_1$) was at 92.44/4.89 ppm, while the analogous β -D-Glcp ($\text{C-R}\beta_1$) correlation was at 103.31/5.14 ppm.

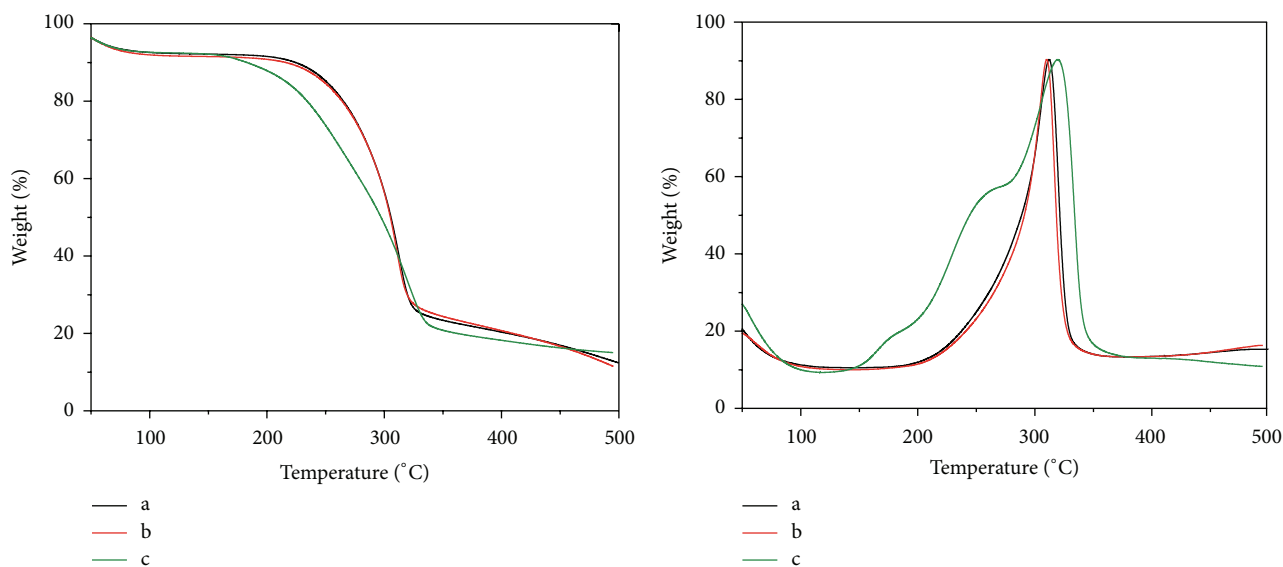


FIGURE 5: The TG/DTG curves of unmodified cellulose (C0, curve a) and phthalated cellulose samples (C1, curve b; C5, curve c).

Despite the conformational complexity, primary peaks were evidently assigned from α -D-Glcp: 72.68/3.16 [C-R α_2 (C₂/H₂)], 72.11/3.69 [C-R α_3 (C₃/H₃)], and 70.25/3.68 [C-R α_5 (C₅/H₅)] ppm. Similarly, C-R β_2 (C₂/H₂) and C-R β_5 (C₅/H₅) were well resolved at 74.93/2.93 and 75.13/3.06 ppm, respectively. However, C-R β_3 (C₃/H₃) was coincident with C-I₃ at 75.24/3.25 ppm. In addition, C-R α_4 (C₄/H₄) and C-R β_4 (C₄/H₄) were coincident at 81.36/3.31 ppm; C-R α_6 (C₆/H₆) and C-R β_6 (C₆/H₆) also were close together at 60.80/3.72 and 60.80/3.56 ppm and were buried between the internal C-I₆ peaks. These results indicated that ball-milling treatment led to the severe degradation of cellulosic macromolecules.

Compared with those in the unmodified cellulose, the reducing-end and non-reducing-end peaks, which resulted from low-molecular fractions, were significantly improved in the phthalated cellulose and the phthalated bagasse, indicating the degradation of cellulose macromolecules in IL AmimCl during dissolution and modification. This result corresponded to the FT-IR analysis, and similar degradation was also reported in the previous publications [23, 24]. The primary internal cellulose peaks were clearly observed in the phthalated cellulose (C5) and bagasse (S5) at 73.54/3.07 [C-I₂ (C₂/H₂)], 75.11/3.36 [C-I₃ (C₃/H₃)], 80.74/3.37 [C-I₄ (C₄/H₄)], 77.00/3.45 [C-I₅ (C₅/H₅)], and 103.23/4.34 [C-I₁ (C₁/H₁)] ppm; the two internal C-I₆ (C₆/H₆) peaks were also distinctively located at 60.66/3.79 and 60.52/3.60 ppm.

The presence of the correlations from aryl groups in the phthalated cellulose confirmed the attachment of phthaloyl group onto cellulose. More importantly, two peaks from substituted C₆ in phthalated internal units (C-I'₆) [C-I'₆ (C₆/H₆)] appeared at 64.70/3.79 and 64.70/4.42 ppm, and the peak from substituted C₂ in internal unit [C-I'₂ (C₂/H₂)] was located at 74.21/4.60 ppm, confirming the successful phthalation of cellulose at C-6 and C-2 positions. However, the substituted C₃ was almost not detected, which suggested that most of phthaloyl group was attached onto C-6 and C-2

positions. The relative percentage of phthalation on different positions could be evaluated upon the integral area of the characteristic substituted correlations. The results indicated that 24.1% and 75.9% of phthaloyl group were attached to C₂ and C₆ positions, respectively. The relative percentage of phthalation at C-6, C-2, and C-3 positions of cellulose in phthalated bagasse S5 was 94.74%, 5.26%, and 0, respectively. These results indicated that the reaction behavior of cellulose in bagasse was similar to the isolated cellulose and the phthalation was more selective to C-6 position in bagasse than that in the isolated cellulose. Obviously, the phthalation degree of the three hydroxyls in AGU followed the order of C-6 > C-2 > C-3. This order was consistent with the propionylation and butyrylation in AmimCl [25]. On the other hand, the phthalation degree of the hydroxyls on each position was easily calculated based on the integral area of the characteristic substituted and unsubstituted correlations. The results showed that the phthalation degree in the isolated cellulose was 6.30%, 2.01%, and 0, respectively, while that in bagasse was 15.15%, 2.63%, and 0, respectively. These results were consistent with the abovementioned phthalation order of three hydroxyls. The relatively more selective phthalation for the hydroxyl to C-6 position of cellulose component in bagasse than the isolated cellulose was primarily due to the differences of the phthalation reactivity of more complicated hydroxyls in bagasse.

3.4. Thermal Analysis. The thermal behavior of unmodified cellulose and phthalated cellulose was studied by TGA in N₂ atmosphere. Figure 5 illustrates the TGA and DTG curves of the unmodified cellulose (C0, curve a) and phthalated cellulose (C1, curve b; C5, curve c). The decrease below 100°C was due to loss of moisture. The initial decomposition temperature of samples C0, C1, and C5 was 251°C, 245°C, and 213°C, respectively. At 50% weight loss, the decomposition temperature occurred at 304°C, 305°C, and 297°C for samples

C0, C1, and C5, respectively. The DTG curves suggested that the modified cellulose had higher thermal degradation rate than the unmodified one. These data indicated that the decreased thermal stability of phthalated cellulose is consistent with the results reported previously [26]. Besides, the initial and midpoint decomposition temperatures of sample C5 were both lower than those of sample C1, indicating that high phthalation degree tended to weaken thermal stability of modified cellulose.

4. Conclusions

The phthalation degree of bagasse and the isolated cellulose ranged from 5.66% to 22.71% and from 11.61% to 44.11%, respectively. The phthalation degree increase of cellulose was proportional to phthalic anhydride dosage, which followed the equation of $y_{\text{PDI}} = 0.004x - 0.02$ under the selected conditions. The reactivity of the three hydroxyls in cellulose followed the order of C-6 > C-2 > C-3, and more selective phthalation to C-6 positions of cellulose component was found in bagasse than in the isolated cellulose. These results provide a detailed understanding of the homogenous modification mechanism of lignocellulose.

Competing Interests

The authors declare that they have no competing interests.

Acknowledgments

This work was financially supported by the National Natural Science Foundation of China (31170550 and 31170555), the Fundamental Research Funds for the Central Universities (2014ZG0046), and the National Program for Support of Top-Notch Young Professionals.

References

- [1] C. T. Duan, N. Zhao, X. L. Yu, X. Y. Zhang, and J. Xu, "Chemically modified kapok fiber for fast adsorption of Pb^{2+} , Cd^{2+} , Cu^{2+} from aqueous solution," *Cellulose*, vol. 20, no. 2, pp. 849–860, 2013.
- [2] K. Y. Foo, L. K. Lee, and B. H. Hameed, "Preparation of activated carbon from sugarcane bagasse by microwave assisted activation for the remediation of semi-aerobic landfill leachate," *Bioresource Technology*, vol. 134, pp. 166–172, 2013.
- [3] F. C. Lu and J. Ralph, "Non-degradative dissolution and acetylation of ball-milled plant cell walls: high-resolution solution-state NMR," *Plant Journal*, vol. 35, no. 4, pp. 535–544, 2003.
- [4] M. Fasching, P. Schröder, R. P. Wollboldt, H. K. Weber, and H. Sixta, "A new and facile method for isolation of lignin from wood based on complete wood dissolution," *Holzforschung*, vol. 62, no. 1, pp. 15–23, 2008.
- [5] T. Q. Yuan, J. He, F. Xu, and R. C. Sun, "A new vision in the research of biomass resources: complete-lignocellulose-dissolution system," *Progress in Chemistry*, vol. 22, no. 2-3, pp. 472–481, 2010.
- [6] S. D. Zhu, Y. X. Wu, Q. M. Chen et al., "Dissolution of cellulose with ionic liquids and its application: a mini-review," *Green Chemistry*, vol. 8, no. 4, pp. 325–327, 2006.
- [7] R. P. Swatloski, S. K. Spear, J. D. Holbrey, and R. D. Rogers, "Dissolution of cellose with ionic liquids," *Journal of the American Chemical Society*, vol. 124, no. 18, pp. 4974–4975, 2002.
- [8] E. Rude and M.-P. G. Laborie, "Carbon-13 cross-polarization magic-angle-spinning nuclear magnetic resonance investigation of the interactions between maleic anhydride grafted polypropylene and wood polymers," *Applied Spectroscopy*, vol. 62, no. 5, pp. 563–568, 2008.
- [9] J. C. P. De Melo, E. C. Da Silva Filho, S. A. A. Santana, and C. Airoidi, "Maleic anhydride incorporated onto cellulose and thermodynamics of cation-exchange process at the solid/liquid interface," *Colloids and Surfaces A: Physicochemical and Engineering Aspects*, vol. 346, no. 1-3, pp. 138–145, 2009.
- [10] C. Qu, T. Kishimoto, M. Kishino, M. Hamada, and N. Nakajima, "Heteronuclear single-quantum coherence nuclear magnetic resonance (HSQC NMR) characterization of acetylated fir (*Abies sachalinensis* MAST) wood regenerated from ionic liquid," *Journal of Agricultural and Food Chemistry*, vol. 59, no. 10, pp. 5382–5389, 2011.
- [11] X.-W. Peng, J.-L. Ren, and R.-C. Sun, "Homogeneous esterification of xylan-rich hemicelluloses with maleic anhydride in ionic liquid," *Biomacromolecules*, vol. 11, no. 12, pp. 3519–3524, 2010.
- [12] C.-F. Liu, R.-C. Sun, M.-H. Qin et al., "Chemical modification of ultrasound-pretreated sugarcane bagasse with maleic anhydride," *Industrial Crops and Products*, vol. 26, no. 2, pp. 212–219, 2007.
- [13] H. Kim, J. Ralph, and T. Akiyama, "Solution-state 2D NMR of ball-milled plant cell wall gels in DMSO- d_6 ," *BioEnergy Research*, vol. 1, no. 1, pp. 56–66, 2008.
- [14] H. Kim and J. Ralph, "Solution-state 2D NMR of ball-milled plant cell wall gels in DMSO- d_6 /pyridine- d_5 ," *Organic and Biomolecular Chemistry*, vol. 8, no. 3, pp. 576–591, 2010.
- [15] H. Kim and J. Ralph, "A gel-state 2D-NMR method for plant cell wall profiling and analysis: a model study with the amorphous cellulose and xylan from ball-milled cotton linters," *RSC Advances*, vol. 4, no. 15, pp. 7549–7560, 2014.
- [16] A. Sluiter, B. Hames, R. Ruiz et al., "Laboratory analytical procedure (LAP): determination of structural carbohydrates and lignin in biomass," Tech. Rep. NREL/TP-510-42618, National Renewable Energy Laboratory, Golden, Colo, USA, 2008.
- [17] M. J. Chen and Q. S. Shi, "Transforming sugarcane bagasse into bioplastics via homogeneous modification with phthalic anhydride in ionic liquid," *ACS Sustainable Chemistry & Engineering*, vol. 3, no. 10, pp. 2510–2515, 2015.
- [18] C. F. Liu, A. P. Zhang, W. Y. Li, F. X. Yue, and R. C. Sun, "Succinylation of cellulose catalyzed with iodine in ionic liquid," *Industrial Crops and Products*, vol. 31, no. 2, pp. 363–369, 2010.
- [19] C.-Y. Chen, M.-J. Chen, X.-Q. Zhang, C.-F. Liu, and R.-C. Sun, "Per-O-acetylation of cellulose in dimethyl sulfoxide with catalyzed transesterification," *Journal of Agricultural and Food Chemistry*, vol. 62, no. 15, pp. 3446–3452, 2014.
- [20] M. J. Chen, C. Y. Chen, C. F. Liu, and R. C. Sun, "Homogeneous modification of sugarcane bagasse with maleic anhydride in 1-butyl-3-methylimidazolium chloride without any catalysts," *Industrial Crops and Products*, vol. 46, pp. 380–385, 2013.
- [21] J. Wu, H. Zhang, J. Zhang, and J.-S. He, "Homogeneous acetylation and regioselectivity of cellulose in a new ionic liquid," *Chemical Journal of Chinese Universities*, vol. 27, no. 3, pp. 592–594, 2006.

- [22] H. Matsuda, "Preparation and utilization of esterified woods bearing carboxyl groups," *Wood Science and Technology*, vol. 21, no. 1, pp. 75–88, 1987.
- [23] C. F. Liu, R. C. Sun, A. P. Zhang et al., "Homogeneous modification of sugarcane bagasse cellulose with succinic anhydride using an ionic liquid as reaction medium," *Carbohydrate Research*, vol. 342, no. 7, pp. 919–926, 2007.
- [24] C. F. Liu, R. C. Sun, A. P. Zhang, and J. L. Ren, "Preparation of sugarcane bagasse cellulosic phthalate using an ionic liquid as reaction medium," *Carbohydrate Polymers*, vol. 68, no. 1, pp. 17–25, 2007.
- [25] Y. Luan, J. Zhang, M. Zhan, J. Wu, J. Zhang, and J. He, "Highly efficient propionylation and butyralation of cellulose in an ionic liquid catalyzed by 4-dimethylminopyridine," *Carbohydrate Polymers*, vol. 92, no. 1, pp. 307–311, 2013.
- [26] C.-F. Liu, R.-C. Sun, A.-P. Zhang, M.-H. Qin, J.-L. Ren, and X.-A. Wang, "Preparation and characterization of phthalated cellulose derivatives in room-temperature ionic liquid without catalysts," *Journal of Agricultural and Food Chemistry*, vol. 55, no. 6, pp. 2399–2406, 2007.

Research Article

Homogeneous Modification of Sugarcane Bagasse by Graft Copolymerization in Ionic Liquid for Oil Absorption Application

Ming-Jie Chen,^{1,2} Xue-Qin Zhang,² Chuan-Fu Liu,² and Qing-Shan Shi¹

¹State Key Laboratory of Applied Microbiology Southern China, Guangdong Provincial Key Laboratory of Microbial Culture Collection and Application, Guangdong Institute of Microbiology, Guangzhou 510070, China

²State Key Laboratory of Pulp and Paper Engineering, South China University of Technology, Guangzhou 510640, China

Correspondence should be addressed to Qing-Shan Shi; shiqingshan@hotmail.com

Received 7 April 2016; Accepted 4 August 2016

Academic Editor: Jun Yang

Copyright © 2016 Ming-Jie Chen et al. This is an open access article distributed under the Creative Commons Attribution License, which permits unrestricted use, distribution, and reproduction in any medium, provided the original work is properly cited.

Sugarcane bagasse, lignocellulosic residue from the sugar industry, is an abundant and renewable bioresource on the earth. The application of ionic liquids in sugarcane bagasse biorefinery is gaining increasing interest. The homogeneous modification of sugarcane bagasse by free radical initiated graft copolymerization of acrylate monomers using 1-allyl-3-methylimidazolium chloride as solvent was performed. A variety of sugarcane bagasse graft copolymers with different weight percent gain were prepared via adjusting the monomer dosage. FT-IR studies confirmed the success in attaching the poly(acrylate) side chains onto sugarcane bagasse. Oil absorbency studies suggested that the sugarcane bagasse graft copolymers were potential biobased materials for effective treatment of ester-based oils. SEM studies showed that the sugarcane bagasse graft copolymers displayed a dense morphology structure. Thermogravimetric analysis demonstrated that the thermal stability of sugarcane bagasse decreased after the homogeneous modification by the graft copolymerization. The present study provides an alternative strategy to convert sugarcane bagasse into a value-added functional biobased material.

1. Introduction

There is growing interest in turning agroindustrial waste biomass into valuable chemicals and materials. The initial interest in this biomass refinery originates from the challenges of resource depletion and waste accumulation [1]. Biorefinery offers the possibility of replacing traditional fossil resources with natural bioresources to manufacture industrial and daily products. Sugarcane bagasse is a typical lignocellulosic waste residue produced by sugar industry. It is estimated that approximately 1.5×10^8 dry tons of sugarcane bagasse is produced worldwide annually [2]. It is commonly used as a primary fuel source for sugar mills and the production of pulp, paper, and board in substitution of wood [3]. However, there is a potential to make better use of the renewable resource by producing novel functional biobased materials.

Modification by graft copolymerization is an effective approach tailoring the material properties of lignocellulosic biomass. It is achieved by attaching side chains (graft) onto

the biomass substrate. Functional surfaces, for example, pH-responsive [4], hydrophobic [5], and antimicrobial [6], of lignocellulosic biomass have been created by the graft approach. However, the cell wall of lignocellulosic biomass is a highly crystalline composite of cellulose, lignin, and hemicellulose, which makes it insoluble in any traditional solvent systems. The modification of the biomass has to be operated at heterogeneous reaction mediums, which achieve low efficiency. To achieve efficient modification of the biomass, the application of a good solvent is mandatory [7].

Ionic liquids, with strong hydrogen bond donor-acceptor ability, are found to be excellent solvents for lignocellulosic biomass [8, 9]. The application of ionic liquids in biomass refinery is booming over the past decade, due to the designable properties of ionic liquids to meet the challenges of sustainable chemistry [10]. Homogeneous acylation of lignocellulosic materials has been carried out in ionic liquids, which is demonstrated to be an advanced technique with higher degree of substitution (~94%) than the heterogeneous acylation [11]. The dissolution of biomass destroys

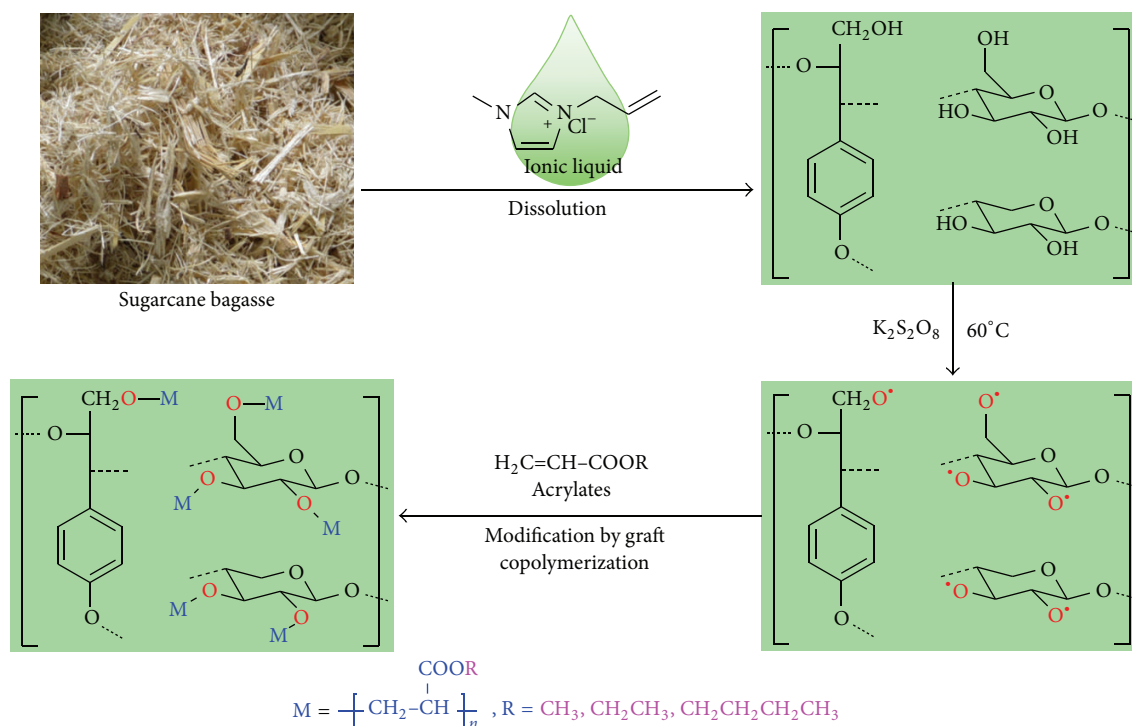


FIGURE 1: Chemical processes for sugarcane bagasse modification by free radical initiated graft copolymerization.

the crystalline structure of the material and releases the hydroxyl groups from hydrogen bonding, thus making the biomass accessible to chemical reagents. Importantly, the components, namely, cellulose, hemicellulose, and lignin, of lignocellulosic biomass have equal opportunities in reaction with anhydrides using 1-butyl-3-methylimidazolium chloride as medium [12]. The development of homogeneous modification of biomass using ionic liquids as mediums has set up an advanced strategy for preparation of novel biobased functional materials.

The homogeneous modification of wood by free radical initiated graft copolymerization of acrylamide using 1-(2-hydroxyethyl)-3-methylimidazolium chloride as medium is performed in a previous study [13]. It is demonstrated that the ionic liquid is a more effective reaction medium for the graft copolymerization than water [13]. However, 1-(2-hydroxyethyl)-3-methylimidazolium chloride is hydroxyl group containing ionic liquid, which is not a suitable solvent for the free radical initiated graft copolymerization of sugarcane bagasse, since the hydroxyl group is the reactive site (Figure 1) in the graft copolymerization [14]. On the other hand, the previous research is limited in the graft copolymerization of acrylamide [13], which is a hydrophilic monomer, while the introduction of hydrophobic side chains to the lignocellulosic biomass is mandatory in most situations.

In the present study, the graft copolymerization of hydrophobic acrylate monomers onto sugarcane bagasse was achieved using 1-allyl-3-methylimidazolium chloride (AMIMCl) as reaction medium. The chemical structure, morphology, thermal stability, and oil absorption capacity of the sugarcane bagasse graft copolymers were studied. It was

suggested that homogeneous graft copolymerization using ionic liquid as solvent was an advanced technique to transform sugarcane bagasse into value-added biobased materials.

2. Material and Methods

2.1. Materials. Sugarcane bagasse was obtained from Guangxi Guitang (Group) Co. Ltd. (Guigang, China). It was washed with hot water (90°C) for three times and ground to prepare 40–60-mesh size particles. The ground sugarcane bagasse was dewaxed by toluene-ethanol (2:1 v/v) extraction for 12 h and oven-dried at 50°C for 24 h. The dewaxed sugarcane bagasse was pretreated by a planetary ball-miller for 4 h.

AMIMCl was purchased from Shanghai Cheng Jie Chemical Co. Ltd. (Shanghai, China) and used as received. Methyl acrylate, ethyl acrylate, and butyl acrylate were chemically pure and purchased from Shanghai Ling Feng Chemical Co. Ltd. (Shanghai, China). The acrylates were purified by vacuum distillation prior to use. Potassium persulfate ($\text{K}_2\text{S}_2\text{O}_8$) and ethanol were purchased from Aladdin Industrial Inc. (Shanghai, China). Machine oil, cooking oil, and diesel oil were supplied by Guangzhou Yu Shao Traded Co. Ltd. (Guangzhou, China).

2.2. Preparation of Sugarcane Bagasse Graft Copolymers. Sugarcane bagasse (1 g) was dispersed in AMIMCl (49 g) at room temperature. The mixture of sugarcane bagasse/AMIMCl was stirred at 110°C under N_2 atmosphere for 5 h to guarantee the complete dissolution. Upon the complete dissolution of sugarcane bagasse, acrylate and potassium persulfate (0.05 g, 0.185 mmol) were added into the sugarcane bagasse/AMIMCl

solution, and the mixture was stirred at 60°C for 24 h to achieve the graft reaction. After the reaction complete, the resulting solution was poured into 500 mL isopropanol. The precipitant was filtered out, thoroughly washed with isopropanol for five times and then with acetone for three times, and oven-dried at 50°C for 24 h to obtain the sugarcane bagasse graft copolymer. The weight percent gain (WPG) of sugarcane bagasse graft copolymers was calculated according to

$$\text{WPG} = 100\% \times \frac{(M_1 - M_0)}{M_0}, \quad (1)$$

where M_0 is the oven dry weight of sugarcane bagasse before dissolving. M_1 is the oven dry weight of sugarcane bagasse graft copolymers.

2.3. Determination of Oil Absorbency. A weight amount of sugarcane bagasse graft copolymer was immersed in excess oil at room temperature. The sample was taken out from the oil after reaching the swelling equilibrium. The excess oil from the surfaces of the sample was wiped out with filter paper. The oil absorption capacity was calculated by

$$\text{Oil absorption capacity} = \frac{(m - m_0)}{m_0} \text{ (g/g)}, \quad (2)$$

where m_0 and m are the weights of sample before and after oil absorption, respectively.

2.4. Characterization. Fourier transform infrared spectroscopy (FT-IR) was performed using a BRUKER TENSOR 27 FT-IR spectrophotometer. KBr disc containing 1% finely ground samples was applied for the spectrum collection. Thirty-two scans were collected per spectrum at a resolution of 4 cm^{-1} .

For scanning electron microscope (SEM) analysis, the samples were fixed to a metal stub with carbon tapes and coated with gold-palladium using sputter coaters. A LEO 1530VP scanning electron microscope (LEO, Germany) with an accelerating voltage of 10 kV was used to obtain secondary electron images.

To perform the thermogravimetric analysis (TGA), the sample (9-10 mg) was heated from 40°C to 600°C at a heating rate of 10°C/min in a Q500 thermogravimetric analyzer (TA Instruments, USA) in nitrogen atmosphere.

3. Results and Discussion

3.1. Synthesis of the Sugarcane Bagasse Graft Copolymers. Free radical initiated graft copolymerization was applied to prepare the graft copolymers in the present study. The scheme for acrylate monomers graft copolymerization onto sugarcane bagasse in ionic liquid using $\text{K}_2\text{S}_2\text{O}_8$ as initiator was shown in Figure 1. As a result of the attachment of the poly(acrylate) side chains onto the sugarcane bagasse fractions, the weight of sugarcane bagasse increases after the graft copolymerization modification. The WPG of control sample (Table 1, SCB sample) was -14.5%, suggesting the decomposition of

TABLE 1: Preparation of sugarcane bagasse graft copolymers.

Entry	Monomer	Monomer dosage		WPG/%
		Volume/mL	Mole/mmol	
SCB	—	0	0	-14.5
MA1	Methyl acrylate	1	11.0	-4.3
MA2	Methyl acrylate	2	22.1	-0.7
MA3	Methyl acrylate	3	33.1	9.9
MA4	Methyl acrylate	4	44.1	16.2
EA1	Ethyl acrylate	1	9.4	-1.7
EA2	Ethyl acrylate	2	18.8	7.8
EA3	Ethyl acrylate	3	28.2	13.7
EA4	Ethyl acrylate	4	37.6	25.5
BA1	Butyl acrylate	1	6.9	2.4
BA2	Butyl acrylate	2	13.9	9.1
BA3	Butyl acrylate	3	20.8	10.5
BA4	Butyl acrylate	4	27.8	15.5

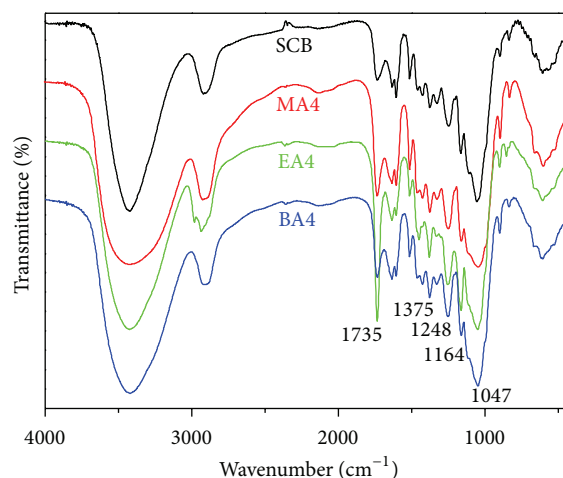


FIGURE 2: FT-IR spectra of sugarcane bagasse and the graft copolymers.

sugarcane bagasse fractions during the dissolution in ionic liquid [15]. The WPG of sugarcane bagasse graft copolymers increased with the increasing monomer dosage, and a series of sugarcane bagasse graft copolymers with WPG in the range of -5%–25.5% were prepared (Table 1). The WPG of sugarcane bagasse graft poly(ethyl acrylate) was 25.5% upon the monomer dosage of 4 mL/g, while it was 16.2% and 15.5% for poly(methyl acrylate) and poly(butyl acrylate), respectively. It was suggested that ethyl acrylate was the most reactive monomer for the modification of sugarcane bagasse with free radical initiated graft copolymerization.

3.2. Chemical Structure Confirmed by FT-IR. The FT-IR spectra of native sugarcane bagasse and the graft copolymers are shown in Figure 2. For a better comparability, the spectra were normalized to the band at 1047 cm^{-1} , which is assigned to the glycosidic linkage (C-O-C) stretching vibration in cellulose and hemicelluloses [16]. The characteristic vibrations of the graft poly(acrylates) moieties were identified at 1735 cm^{-1}

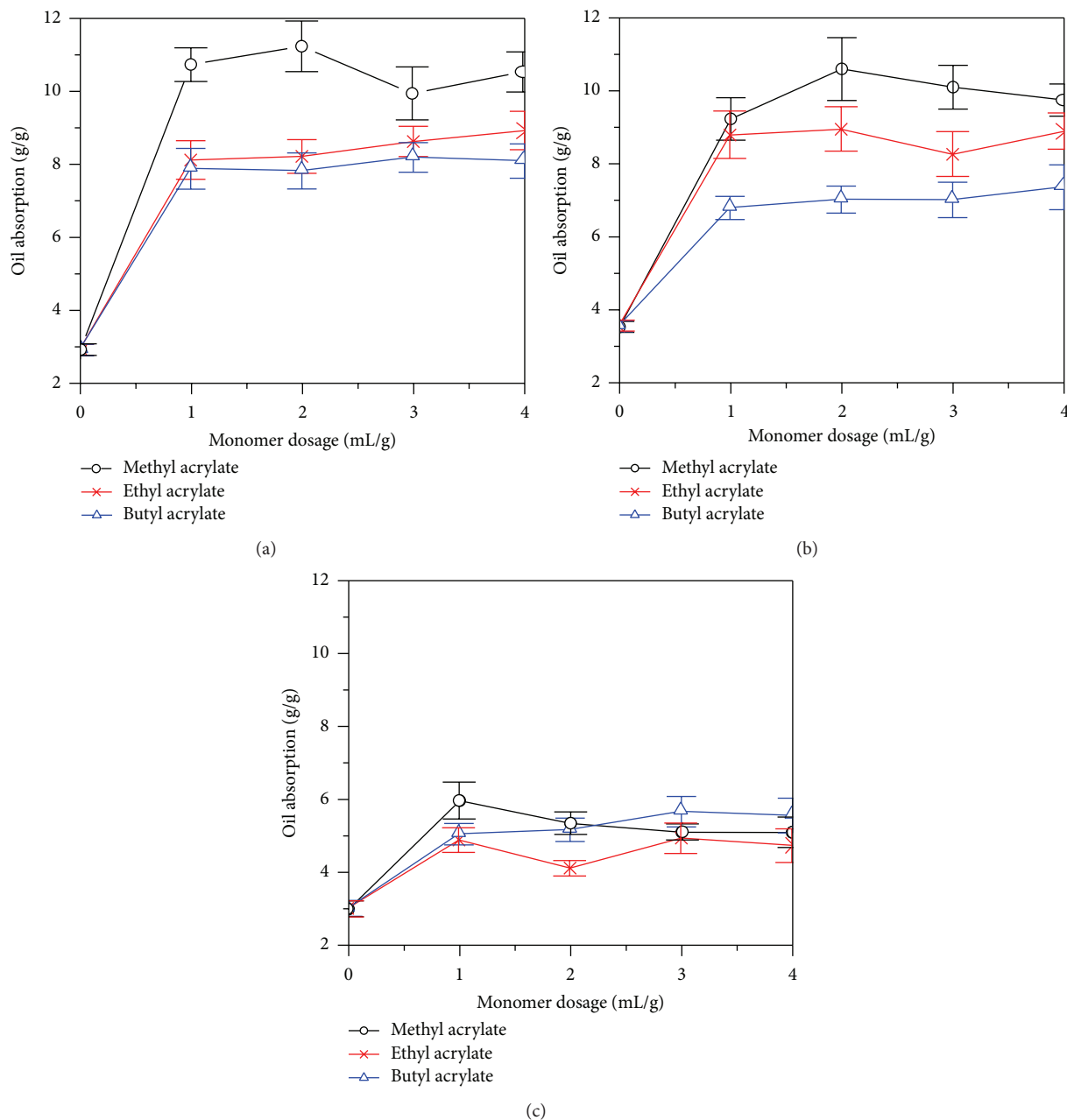


FIGURE 3: Oil absorption capacity of the sugarcane bagasse graft copolymers. (a) Machine oil absorption capacity; (b) cooking oil absorption capacity; (c) diesel oil absorption capacity.

associated with the carbonyl ($\text{C}=\text{O}$) stretching vibration [17], 1375 cm^{-1} associated with the methyl ($\text{C}-\text{H}$) deformation vibrations, and 1248 cm^{-1} and 1164 cm^{-1} associated with the $\text{C}-\text{O}$ stretching vibrations [18, 19]. An increase in the intensity of these bands was observed after the graft copolymerization reaction suggesting the poly(acrylate) side chains were attached onto the sugarcane bagasse successfully.

3.3. Oil Absorption Capacities of the Sugarcane Bagasse Graft Copolymers. The oil absorption capacities of sugarcane bagasse (SCB sample) and the graft copolymers are shown

in Figure 3. Clearly, the graft copolymers were more effective at absorbing oil than sugarcane bagasse (SCB sample). Sugarcane bagasse is a natural composite of cellulose, hemicellulose, and lignin with highly crystalline structure and large amount of hydrophilic hydroxyl groups, which make it a poor oil absorption material. After the graft copolymerization with acrylates, the hydrophilic hydroxyl groups of sugarcane bagasse were substituted by the hydrophobic poly(acrylate) side chains. As a result of the substitution of the hydroxyl groups, the modified sugarcane bagasse was more accessible than the unmodified one to oil [20].

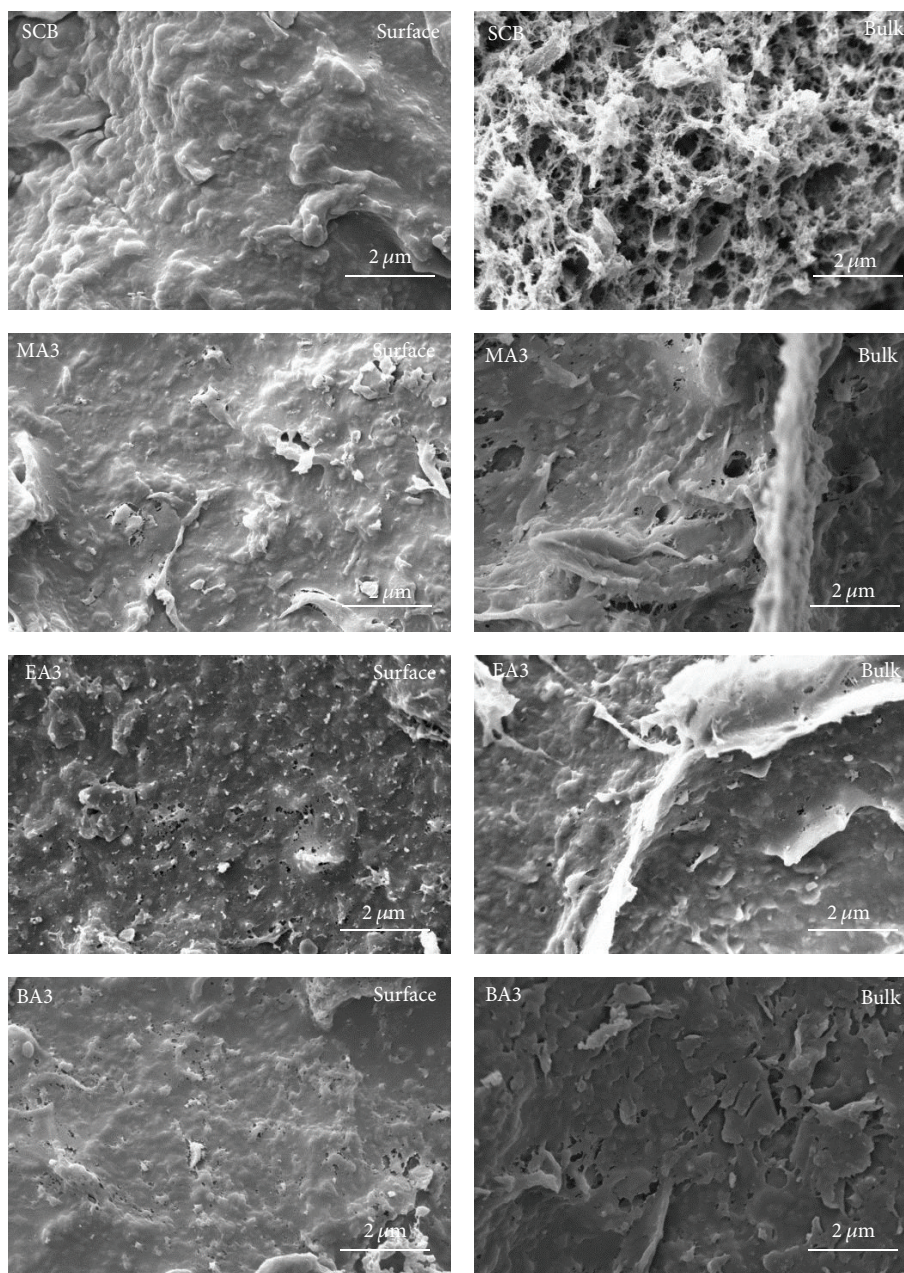


FIGURE 4: SEM photos of the sugarcane bagasse graft copolymers.

It was interesting to find that there was no clear relationship between the oil absorption capacity and the monomer dosage, even though the WPG of graft copolymers increased with the increasing monomer dosage. However, it was reported that the oil absorption capacity increased with the increasing WPG of sugarcane bagasse acetates [21]. In general, the increasing WPG of the sugarcane bagasse acetates corresponds to the increasing degree of substitution (DS) of hydroxyl groups [21], while it is not always the case for the modification of sugarcane bagasse by graft copolymerization. Two chemical reactions, namely, the substitution of hydroxyl groups and the polymerization of the monomers, take place at the same time for the graft copolymerization

[14]. Both increments of DS of hydroxyl groups and degree of polymerization (DP) of side chains would result in the increment of WPG. Increasing the monomer dosage would result in the increment of DP of side chains, while the DS of hydroxyl groups keep unchanged. The WPG of sugarcane bagasse graft copolymers increased with the increasing DP of the poly(acrylate) side chains. However, the oil absorption capacity of the sugarcane bagasse graft copolymers did not change with the increasing monomer dosage, owing to the unchanged DS of hydroxyl groups.

The oil absorption capacities of the graft copolymers differed according to the oil and monomer species. The sugarcane bagasse graft poly(methyl acrylate) showed being

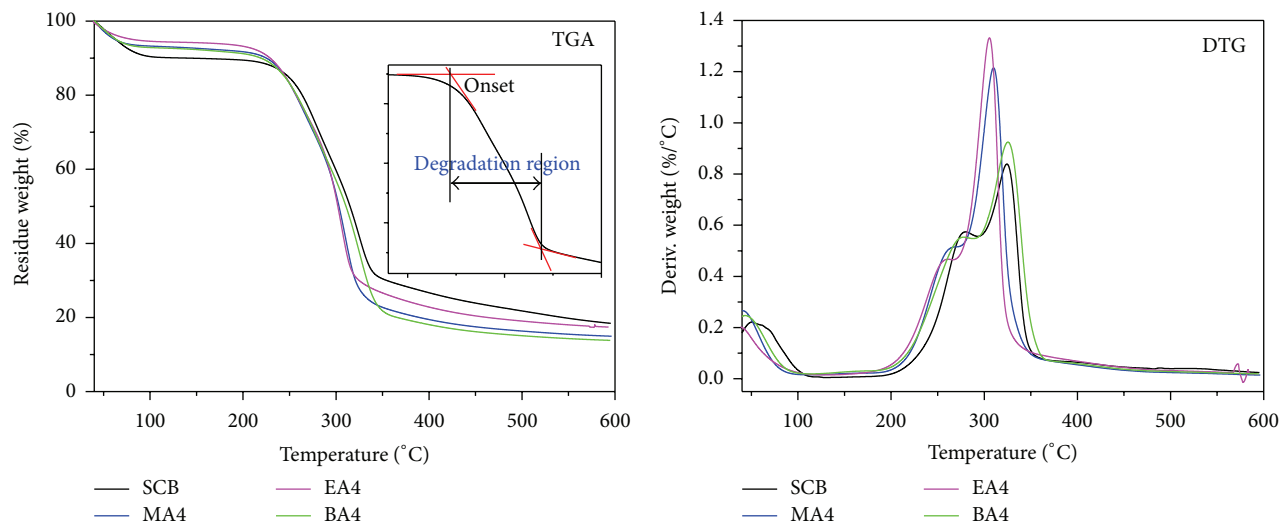


FIGURE 5: TGA/DTG curves of the sugarcane bagasse graft copolymers. The inset figure in TGA showed the method in determining the onset degradation temperature and the degradation region.

the most effective for the absorption of machine oil and cooking oil, while diesel oil absorption capacities of the modified sugarcane bagasse were more or less the same (Figure 3). The machine oil and cooking oil were majorly composed of esters, while the diesel was composed of long chain alkane. Acrylates were composed of three parts, namely, allyl group, ester group, and alkane chain (R group). The reason why sugarcane bagasse graft poly(acrylate) showed higher absorbency to machine oil and cooking oil than to diesel oil is that both poly(acrylate) and machine/cooking oil contain ester groups. Increasing the chain length of R group of the acrylates from CH_3 to $\text{CH}_2\text{CH}_2\text{CH}_2\text{CH}_3$ would result in the decrease of ester group content of sugarcane bagasse graft copolymers. Thus, sugarcane bagasse graft poly(methyl acrylate) had the highest ester content and showed being most efficient for oil absorption.

3.4. Morphology of the Sugarcane Bagasse Graft Copolymers.

To better understand the enhanced oil absorption behavior of sugarcane bagasse by graft copolymerization modification, the morphology of the sugarcane bagasse derivatives was examined using SEM (Figure 4). The photomicrograph of sugarcane bagasse regenerated from AMIMCl showed a highly porous bulk structure with a homogenous surface (Figure 4, SCB). Both the bulk and surface of sugarcane bagasse graft copolymers showed dense architecture. SEM studies suggested that the oil absorption of sugarcane bagasse was due to the oil penetration into the bulk pores. As a result, the oil absorption of sugarcane bagasse should depend on the pore volume of the material but be independent of oil type. It fitted well with the oil absorbency study that the oil absorption of sugarcane bagasse showed no significant difference for machine oil, cooking oil, and diesel oil. The dense architecture of sugarcane bagasse graft copolymers suggested that the oil absorption of sugarcane bagasse derivatives was not oil held by pores. The introduction of lipophilic groups

by graft copolymerization increased oil absorption capacity sugarcane bagasse derivatives.

3.5. Thermal Stability of the Sugarcane Bagasse Graft Copolymers.

The TGA/derivative thermogravimetry (DTG) curves of the sugarcane bagasse graft copolymers are shown in Figure 5. The weight loss below 105°C was attributed to the volatilization of water. The water content of unmodified sugarcane bagasse (Figure 5, SCB) was 9.7%, and it was 4.7%–7.6% for the modified ones (Figure 5, MA4, EA4, and BA4). It was suggested that the substitution of hydroxyl groups by the hydrophobic poly(acrylate) side chains resulted in the improvement of sugarcane bagasse hydrophobicity. The onset thermal degradation temperature of the unmodified sugarcane bagasse was 244°C , and it was 228°C for all the modified ones. The decrease in the onset thermal degradation temperature was due to the substitution of hydroxyl groups which broke down the hydrogen bonding network of sugarcane bagasse [22]. The degradation region (Figure 5) of the unmodified sugarcane bagasse was 94°C , and those were 105°C , 96°C , and 121°C for the sugarcane bagasse graft poly(methyl acrylate), poly(ethyl acrylate), and poly(butyl acrylate), respectively. The broadened degradation region of the modified sugarcane bagasse was mainly due to the low onset thermal degradation temperature. The DTG curves suggested that the modified sugarcane bagasse had higher thermal degradation rate than the unmodified one. In summary, the homogeneous graft copolymerization would decrease the thermal stability of modified sugarcane bagasse.

4. Conclusion

Lipophilic sugarcane bagasse derivatives were prepared by homogeneous free radical initiated graft copolymerization in ionic liquid. The efficiency of the graft copolymerization was characterized by WPG and controlled by stoichiometric

methods. The oil absorption capacity of sugarcane bagasse was significantly improved by the graft copolymerization due to the introduction of hydrophobic groups. The oil absorption of sugarcane bagasse graft poly(acrylate) copolymers was attributed to the lipophilic behavior of the samples. The copolymerization processes resulted in the decrease in the thermal stability of sugarcane bagasse by reducing the onset thermal degradation temperature and raising the thermal degradation rate.

Competing Interests

The authors declare that they have no competing interests.

Acknowledgments

This work was financially supported by State Key Laboratory of Pulp and Paper Engineering (201602), the Scientific and Technological Project of Guangdong Province (nos. 2013B091500080, 2013B050800023, and 2015A010105019).

References

- [1] L. A. Pfaltzgraff, M. De Bruyn, E. C. Cooper, V. Budarin, and J. H. Clark, "Food waste biomass: a resource for high-value chemicals," *Green Chemistry*, vol. 15, no. 2, pp. 307–314, 2013.
- [2] C. A. Cardona, J. A. Quintero, and I. C. Paz, "Production of bioethanol from sugarcane bagasse: status and perspectives," *Bioresource Technology*, vol. 101, no. 13, pp. 4754–4766, 2010.
- [3] Wikipedia, "Bagasse," 2015, <https://en.wikipedia.org/wiki/Bagasse>.
- [4] E. Cabane, T. Keplinger, V. Merk, P. Hass, and I. Burgert, "Renewable and functional wood materials by grafting polymerization within cell walls," *ChemSusChem*, vol. 7, no. 4, pp. 1020–1025, 2014.
- [5] Y. C. Fu, G. Li, H. P. Yu, and Y. X. Liu, "Hydrophobic modification of wood via surface-initiated ARGET ATRP of MMA," *Applied Surface Science*, vol. 258, no. 7, pp. 2529–2533, 2012.
- [6] H. P. Yu, Y. C. Fu, G. Li, and Y. X. Liu, "Antimicrobial surfaces of quaternized poly[(2-dimethyl amino)ethyl methacrylate] grafted on wood via ARGET ATRP," *Holzforschung*, vol. 67, no. 4, pp. 455–461, 2013.
- [7] M. A. Ermeydan, E. Cabane, P. Hass, J. Koetz, and I. Burgert, "Fully biodegradable modification of wood for improvement of dimensional stability and water absorption properties by poly(ϵ -caprolactone) grafting into the cell walls," *Green Chemistry*, vol. 16, no. 6, pp. 3313–3321, 2014.
- [8] I. Kilpeläinen, H. Xie, A. King, M. Granstrom, S. Heikkinen, and D. S. Argyropoulos, "Dissolution of wood in ionic liquids," *Journal of Agricultural and Food Chemistry*, vol. 55, no. 22, pp. 9142–9148, 2007.
- [9] D. A. Fort, R. C. Remsing, R. P. Swatloski, P. Moyna, G. Moyna, and R. D. Rogers, "Can ionic liquids dissolve wood? Processing and analysis of lignocellulosic materials with 1-n-butyl-3-methylimidazolium chloride," *Green Chemistry*, vol. 9, no. 1, pp. 63–69, 2007.
- [10] R. D. Rogers and K. R. Seddon, "Ionic liquids—solvents of the future?" *Science*, vol. 302, no. 5646, pp. 792–793, 2003.
- [11] H. Xie, A. King, I. Kilpeläinen, M. Granstrom, and D. S. Argyropoulos, "Thorough chemical modification of wood-based lignocellulosic materials in ionic liquids," *Biomacromolecules*, vol. 8, no. 12, pp. 3740–3748, 2007.
- [12] D. Chen, A.-P. Zhang, C.-F. Liu, and R.-C. Sun, "Modification of sugarcane bagasse with acetic anhydride and butyric anhydride in ionic liquid 1-butyl-3-methylimidazolium chloride," *BioResources*, vol. 7, no. 3, pp. 3476–3487, 2012.
- [13] L. Y. Guo, T. J. Shi, and Z. Li, "Dissolution of fir powder and its graft copolymer in ionic liquid," *European Journal of Wood and Wood Products*, vol. 69, no. 3, pp. 383–389, 2011.
- [14] D. Roy, M. Semsarilar, J. T. Guthrie, and S. Perrier, "Cellulose modification by polymer grafting: a review," *Chemical Society Reviews*, vol. 38, no. 7, pp. 2046–2064, 2009.
- [15] P. Varanasi, P. Singh, M. Auer, P. D. Adams, B. A. Simmons, and S. Singh, "Survey of renewable chemicals produced from lignocellulosic biomass during ionic liquid pretreatment," *Biotechnology for Biofuels*, vol. 6, no. 1, article 14, 2013.
- [16] M. Hauptmann, W. Gindl-Altmatter, C. Hansmann et al., "Wood modification with tricene," *Holzforschung*, vol. 69, no. 8, pp. 985–991, 2015.
- [17] M. Traoré, J. Kaal, and A. Martínez Cortizas, "Application of FTIR spectroscopy to the characterization of archeological wood," *Spectrochimica Acta Part A: Molecular and Biomolecular Spectroscopy*, vol. 153, pp. 63–70, 2016.
- [18] P. Anbinder, C. Macchi, J. Amalvy, and A. Somoza, "Chitosan-graft-poly(n-butyl acrylate) copolymer: synthesis and characterization of a natural/synthetic hybrid material," *Carbohydrate Polymers*, vol. 145, pp. 86–94, 2016.
- [19] S. Wang, Q. Wang, X. Fan et al., "Synthesis and characterization of starch-poly(methyl acrylate) graft copolymers using horseradish peroxidase," *Carbohydrate Polymers*, vol. 136, pp. 1010–1016, 2016.
- [20] A. E.-A. A. Said, A. G. Ludwick, and H. A. Aglan, "Usefulness of raw bagasse for oil absorption: a comparison of raw and acylated bagasse and their components," *Bioresource Technology*, vol. 100, no. 7, pp. 2219–2222, 2009.
- [21] X. F. Sun, R. C. Sun, and J. X. Sun, "Acetylation of sugarcane bagasse using NBS as a catalyst under mild reaction conditions for the production of oil sorption-active materials," *Bioresource Technology*, vol. 95, no. 3, pp. 343–350, 2004.
- [22] J. L. Wen, Y. C. Sun, L. Y. Meng, T. Q. Yuan, F. Xu, and R.-C. Sun, "Homogeneous lauroylation of ball-milled bamboo in ionic liquid for bio-based composites production: part I: modification and characterization," *Industrial Crops and Products*, vol. 34, no. 3, pp. 1491–1501, 2011.

Research Article

Waste Composite Sensor Designed by Cellulose and Activated Carbon as Ethylene Absorber

S. Ummartyotin^{1,2} and C. Pechyen^{1,2}

¹Advanced Functional Polymeric Materials Research Group, Faculty of Science and Technology, Thammasat University, Patumtani 12120, Thailand

²Materials Research Center, HORIBA Scientific and Thammasat University, Patumtani 12120, Thailand

Correspondence should be addressed to S. Ummartyotin; sarute.ummartyotin@gmail.com and C. Pechyen; chiravoot.p@gmail.com

Received 3 April 2016; Accepted 11 May 2016

Academic Editor: Ming-Guo Ma

Copyright © 2016 S. Ummartyotin and C. Pechyen. This is an open access article distributed under the Creative Commons Attribution License, which permits unrestricted use, distribution, and reproduction in any medium, provided the original work is properly cited.

Activated carbon was successfully derived from scrap tile waste from thermochemical conversion. Chemical and physical modifications were therefore employed to modify the specific surface area and porosity of activated carbon. Cellulose was successfully extracted from palm front. Designation of waste composite was prepared by cellulose and activated carbon. Less than 30 wt% of activated carbon was integrated into cellulose sheet matrix. It was important to note that there is no change in mechanical and morphological properties. Small amount of activated carbon was well dispersed. In order to investigate the feasibility of composite as active packaging, oxygen permeation rate and ethylene gas adsorption ability were preliminary investigated.

1. Introduction

In recent years, the push towards the development of biobased materials has been evident. Numerous approaches have been extremely investigated on the feasibility of biobased materials for many purposes. The emergence of biobased material played an important role on many industrial sectors such as automotive part, electronic device, pharmaceutical and medical research, and food technology [1–7]. Up to the present time, the category of biobased material was versatile depending on available resources. It was related to cellulose and its derivative, chitin-chitosan, polylactic acid, polybutylene succinate, and starch. The use of biobased materials was therefore selected due to environmentally friendly purpose, nontoxicity, and value-added concept for agricultural product. On the other hand, biobased materials were therefore considered as biomass. The existence of these biobased resources should be preferably investigated as well as their feasibility in order to replace the conventional nonrenewable materials. Moreover, due to the growth of worldwide population, it should be encouraged that the emergence

of novel technology based on “green product and process” be endorsed. It was involved in the design of product and process which minimizes the use and the generation of hazardous materials. To become innovative in green technology, numerous approaches have been investigated from academic research to industrial commercialization. One of the excellent strategic routes was related to waste development.

To the best of our knowledge, the management of municipal solid waste was considered as important issue for city authorities and planners due to increment in population, urbanization, and limited land space. It was consequently considered as the major concern to environmental health [8–13]. This probably had many effects on environmental treatment challenges such as leachate generation and air pollution. As a consequence, it may combine with political, social, and economic issues, as well as the availability of land, which were major concerns to be addressed in land evaluation and management. In addition, increment in worldwide population led to increase in fossil fuel consumption, rendering increment in greenhouse gas emission. This might be considered as environmental issue. In order to solve

this technical issue, converting solid waste to conventional product was favorably remarked to be an option. To be sustainable and renewable, the design of product based on solid waste should be preferably developed. This concept led to solving the landfill space, environmental issue as well as nonpollution.

To respond to this scenario, waster composite was considered as an important key challenge to solve this issue [14–16]. One solid waste was due to activated carbon derived from scrap tile waste. From the fundamental point of view, scrap tire throughout the world is approximately 1 billion per year and it sets to be increased in the future as car and truck transportation continues to expand. Up to the present time, reutilization of scrap tile was comparatively much below annually generated tire. One of the successful strategic approaches of the reutilization of scrap tile waste was involved in activated carbon formation. After pyrolysis of scrap tile waste, the existence of activated carbon with high specific surface area and porosity was presented. It was considered as a viable market for the end product of the waste [17–20]. On the other hand, another waste was involved in cellulose derived from palm frond. At this presence, palm frond was relatively considered as biomass. The availability of palm frond was therefore versatile in many areas of academic research and industrial commercialization [21–23]. To the best of our knowledge, utilization of palm frond was related to biorefinery which comparatively referred to a promising concept of utilizing biomass or any other renewable resources as feedstock to produce energy and platform chemicals and materials [24, 25]. It was definitely considered as one of the excellent techniques to reduce carbon footprint and dependency on fossil fuel for sustainable development. One of the excellent strategic approaches of biorefinery of palm frond was biological production of cellulose. From conventional reaction, cellulose was therefore derived from palm frond. The properties of cellulose were evident to have numerous features such as high thermal stability, chemical resistance, and excellent mechanical properties.

In order to have a successful waste development program, the design on composite from waste was therefore investigated. Activated carbon was successfully derived from scarp tile waster, whereas cellulose was extracted from palm frond. The structure and properties of waste based composite were therefore evaluated based on ethylene absorber.

2. Experimental

2.1. Chemical Reagents and Materials. Scrap tile was provided as a gift from Patomchai Hitech Co., Ltd., Nakhon Pathom, Thailand. Analytical grade of hydrochloric acid, HCl, was purchased from Merck (analytical reagent assay 37%, Merck KGaA, Darmstadt, Germany). Analytical grade of sulfuric acid, H₂SO₄, was also purchased from Merck (analytical reagent assay 95%, Merck KGaA, Darmstadt, Germany). Analytical grade of sodium hydroxide (NaOH) was purchased from Sigma Aldrich, Thailand. All chemical reagents were used as received without further purification. Palm frond was provided as a gift from Oil Palm Estate, Thailand.

2.2. Methods. Scrap tile as received was cut into small pieces. It was washed with deionized water and dried in an oven at 100°C for 24 hours. Afterwards, it had undergone pyrolysis process at 800°C for 1 hour. The dried scrap tile was ground and sieved into particle size smaller than 500 μm. The ratio of 1:1 of analytical grade of hydrochloric acid and sulfuric acid was poured into activated carbon. The reaction was set at 80°C for 2 hours. Then, it was filtered with Buchner funnel connected to a Buchner flask and a vacuum pump. It was washed with distilled water until neutral pH. The obtained carbons were characterized by nitrogen adsorption-desorption isotherms at –196°C. The surface area and total pore volume of activated carbons, which were determined by application of the Brunauer-Emmett-Teller (BET) and t-plot methods, were achieved as high as 604.31 m²/g and 0.715 cm³/g, respectively. Prior to composite preparation, it was stored in desiccator in order to prevent moisture absorption. Freshly cut palm fronds were obtained from the Oil Palm Estate, Surat Thani, Thailand. The leaflet was left in the estate and only petiole part was taken for the characterization purpose. The palm frond was naturally sun-dried until the moisture content dropped to below 20%. It was ground to a particle with diameter size of 2 mm. The ground sample was sieved through 0.5 mm mesh to remove the powdery tiny particles (powder). The meshed sample was further dried at 45°C in an oven until the moisture content dropped below 10% before it could be used in water extraction. Cellulose derived from palm frond was related to paper-making process. It was chemically modified by using sodium hydroxide. The water was removed from the suspension through filtration with a Buchner funnel fitted with Polytetrafluoroethylene membrane filter (0.1 m mesh, 90 mm diameter), which was connected to a Buchner flask and a vacuum pump. The volume of cellulose suspension was adjusted to achieve a bacterial cellulose disc with the dried weight of 0.25 g. The filtration was continued until the wet sheet of cellulose was formed. The wet sheet was then dried between two Polytetrafluoroethylene membranes under the applied pressure of 58 psi. To fabricate waste composite small amount of activated carbon derived from scrap tile was integrated into cellulose sheet. The ratio of structure of composite was therefore evaluated. Properties of waste composite were investigated based on ethylene absorber.

3. Results and Discussion

Cellulose was successfully extracted from palm frond by conventional reaction technique. It was well dispersed in water. Additional information on cellulose properties was similar to our many previous literatures. As-extracted cellulose suspension was preliminary tested on active alkali. Lignin and its impurities were removed, and cellulose fibril was distributed into water based suspension form. On the other hand, activated carbon was successfully derived from scrap tile waste. The process was involved in pyrolysis under controlled atmosphere. Activated carbon was in the powder-like form in black color. It should be remarkably stored in desiccators in order to prevent water absorption issue.

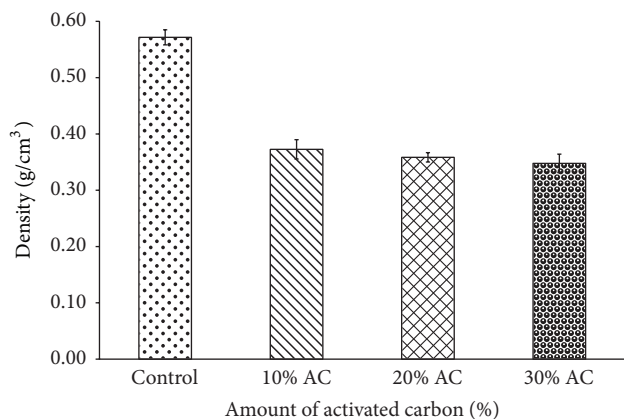


FIGURE 1: Density of activated carbon and cellulose sheet composite.

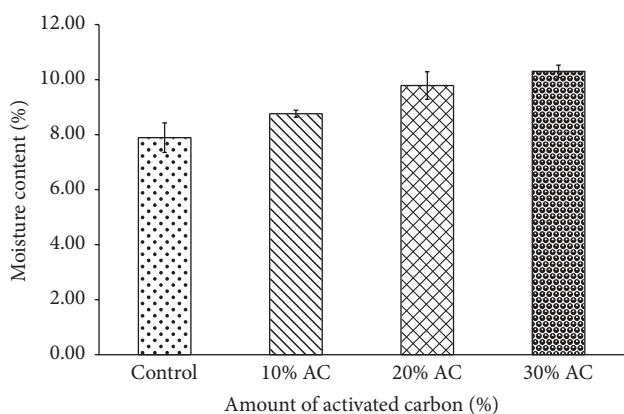


FIGURE 2: Moisture content of activated carbon and cellulose sheet composite.

To design cellulose and activated carbon based composite, less than 30 wt% of activated carbon was integrated into cellulose sheet. It was important to note that the density of composite was significantly less than neat cellulose sheet. Figure 1 exhibits the density of activated carbon and cellulose based composite. The neat cellulose sheet was provided for comparison. The existence of activated carbon can induce high porosity through the network. Due to its light weight, it can be therefore distributed into cellulose sheet. The activated carbon can therefore play an important role for the feasibility of its higher adsorption performance.

After that, moisture content and water absorption were therefore investigated for waste composite. Figures 2 and 3 exhibit the moisture content and water absorption of waste composite. The neat cellulose sheet was also provided for comparison. The ability of moisture content and water absorption ability of composite were significantly superior. From the structural point of view, the molecular structure of cellulose was composed of 3 positions of hydroxyl group; it was therefore easy to be activated for hydrogen bond formation in between cellulose molecular unit and water. Compared to waste composite, the existence of activated carbon was presented in cellulose network. It exhibited high specific surface area and porosity. Significant effort was made

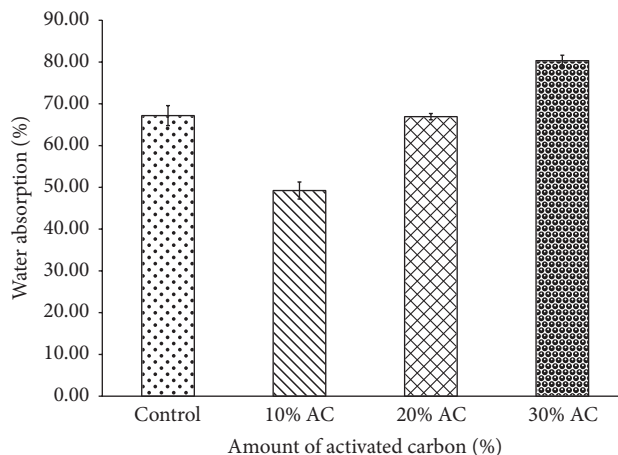


FIGURE 3: Water absorption of activated carbon and cellulose sheet composite.

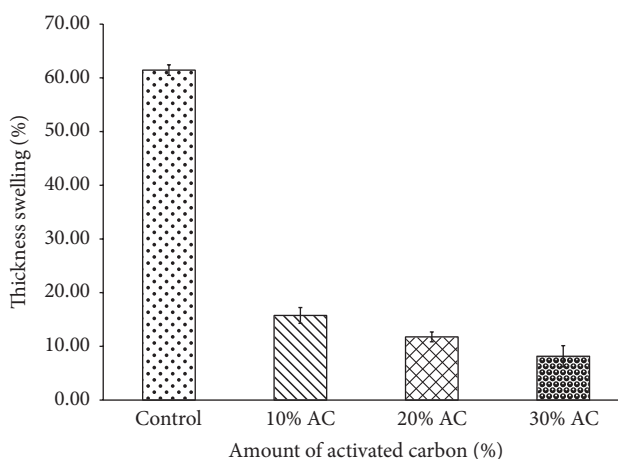


FIGURE 4: Thickness swelling of activated carbon and cellulose sheet composite.

to investigate waste composite for moisture content and water absorption ability. It was remarkable to note that, due to high absorption ability of cellulose and activated carbon, waste composite was successfully designed as absorbent material. However, it should be avoided due to the difference in physical properties. Cellulose was presented in sheet form, similar to paper, whereas activated carbon was successfully derived in powder form. The design of waste composite should be preferably considered regarding the mechanical properties if flexibility will be selected in particular application. On the other hand, the tendency of moisture content and water absorption was relatively high with the increment in percentage of activated carbon. It may be involved in agglomeration behavior of activated carbon and difficulty in controllable distribution of activated carbon. Although, the moisture content and water adsorption ability were still superior, the correlation of mechanical properties should be considered.

Thickness swelling was therefore evaluated and it is presented in Figure 4. It theoretically referred to mechanical strength of waste composite. The experiment was conducted

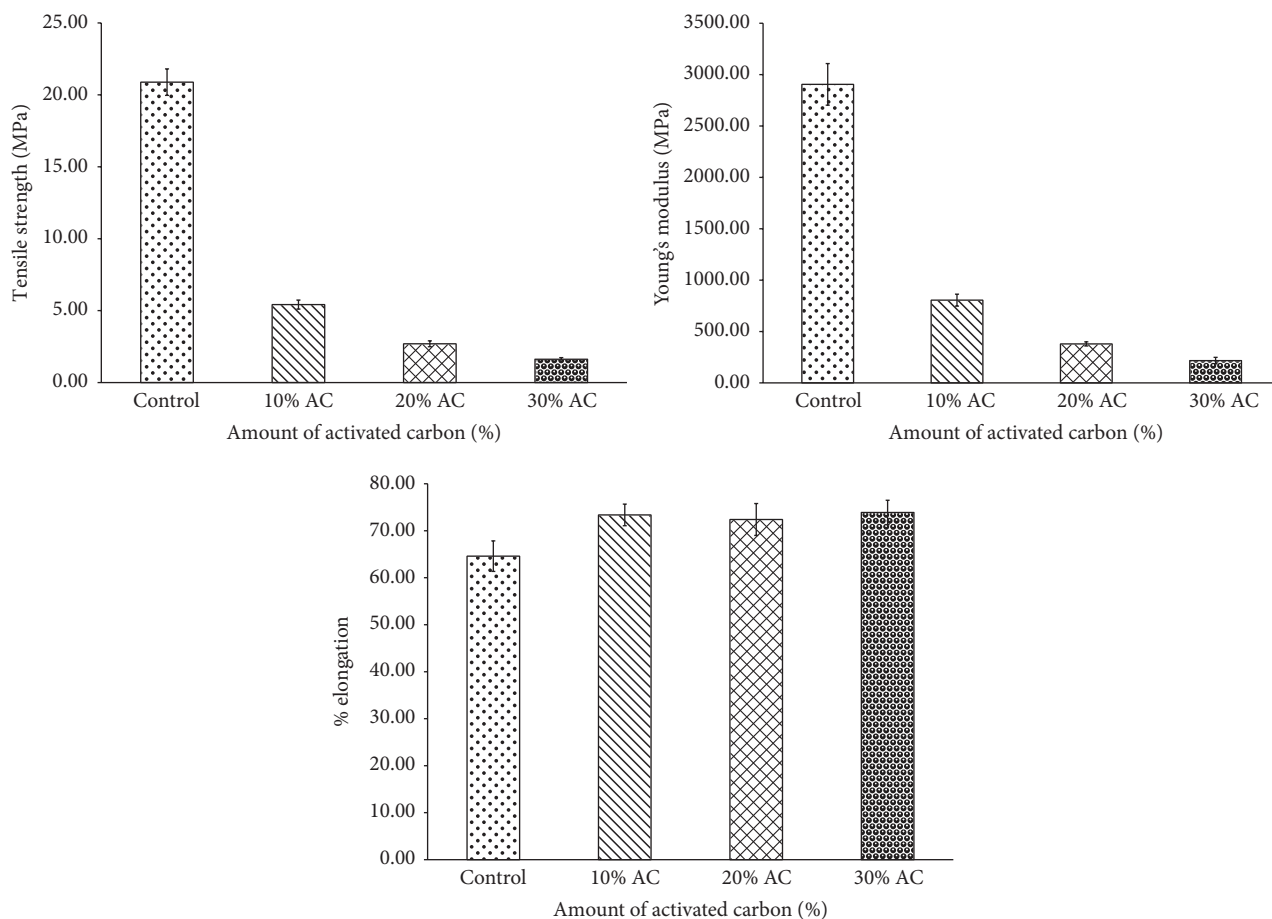


FIGURE 5: Mechanical properties of activated carbon and cellulose sheet composite.

at ambient temperature. The neat cellulose sheet was also provided for comparison. There is no effect of temperature on water absorption and mechanical properties in this part. It was important to note that significant reduction in thickness swelling was observed in waste composite. In case of cellulose sheet, there is free space between cellulose networks. Water molecule can be attached on the hydroxyl position of cellulose; it was therefore swelled. The thickness of sample was subsequently observed. On the contrary, this phenomenon was different compared to waste composite. The existence of activated carbon was considered as obstacle to swelling. Waste composite presented the good feature of dimensional stability. The percentage of thickness swelling was reduced from 60 to 15, 12, and 8%, respectively.

Mechanical properties of activated carbon and cellulose sheet composite were therefore observed. The investigation was based on tensile strength, Young's modulus, and elongation at break, respectively. Figure 5 exhibits the mechanical properties of waste composite. The neat cellulose sheet was provided for comparison. It was remarkable to note that waste composite presented inferiority in technical data of tensile strength and Young's modulus. The activated carbon may agglomerate on the free space of cellulose fibril. The existence of activated carbon was provided for the difficulty of cellulose network on bonding formation. On the other hand,

it was involved in sorption properties of activated carbon. Due to excellent specific surface area and porosity, it can be adsorbed both gas and liquid; significant reduction in tensile strength and Young's modulus was therefore investigated. On the other hand, the elongation at break of waste composite was still in similar region. The increment of elongation at break of waste composite was less than 5%. The reason was due to the fact that the amount of activated carbon can be considered for two different purposes: adsorbed and controlled dimensional stability. It may be called the reinforcement part; no significance of elongation at break was therefore observed.

Morphological properties of activated carbon and cellulose sheet composite were therefore observed as exhibited in Figure 6. The neat cellulose sheet was provided for comparison. The morphology of cellulose sheet presented the fibril network. There is free space in between cellulose sheets. The orientation of cellulose sheet was random. The size of cellulose fibril was nonuniform. The aspect ratio (L:D) was estimated to be 15–20, depending on mechanical crushing technique. The variation in size of cellulose did not provide any significant alteration in adsorption ability. However, compared to waste composite, the small amount of activated carbon existed in the free space in between cellulose networks. With the higher amount of integration, it became

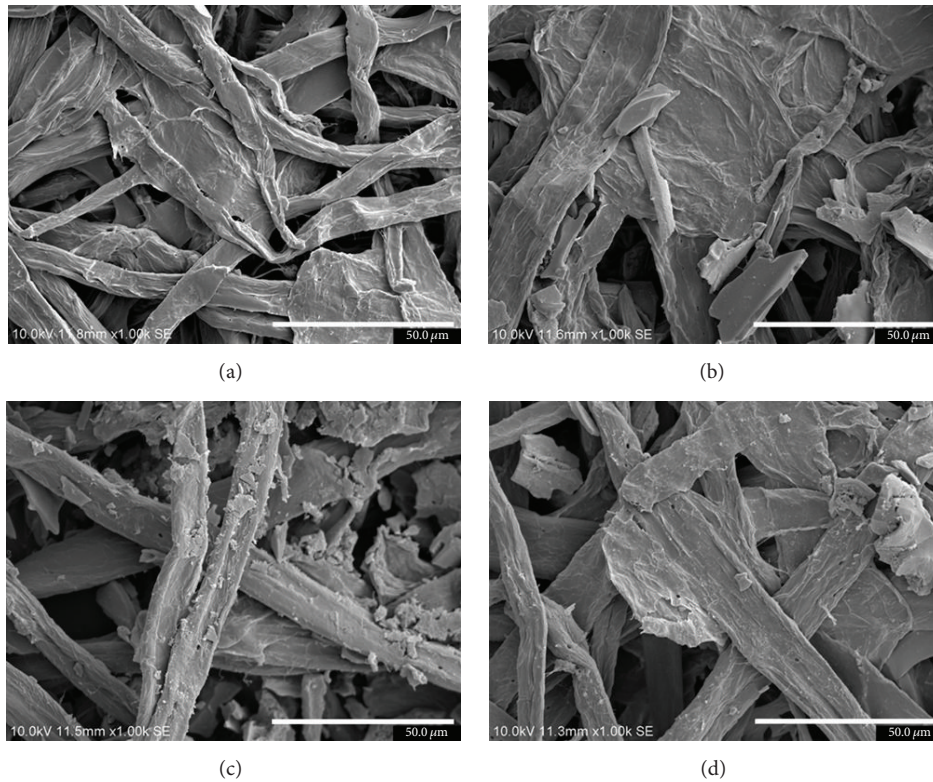


FIGURE 6: Morphological properties of activated carbon and cellulose sheet composite: (a) neat cellulose sheet, (b) 10 wt% of activated carbon filled cellulose sheet, (c) 20 wt% of activated carbon filled cellulose sheet, and (d) 30 wt% of activated carbon filled cellulose sheet.

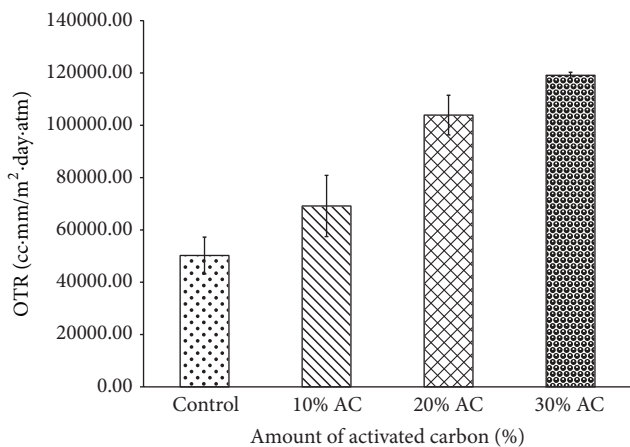


FIGURE 7: Oxygen transmission rate of activated carbon and cellulose sheet composite.

agglomerated. To avoid this agglomeration issue, correlation of amount of activated carbon and its processing should be controlled. However, the morphological properties of waste composite were not having any differences. It was presented in 3D network in cellulose sheet. Small amount of activated carbon existed in between.

Oxygen permeation test and ethylene gas adsorption of activated carbon and cellulose sheet composite were investigated. Figures 7 and 8 exhibit the oxygen permeation

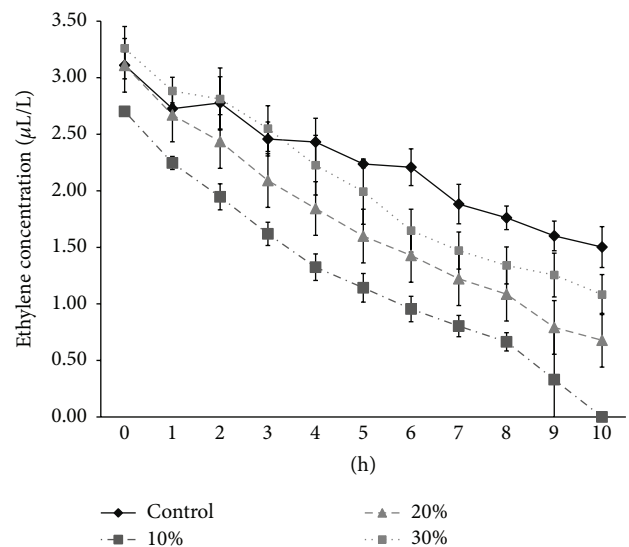


FIGURE 8: Investigation of ethylene gas adsorption of activated carbon and cellulose sheet composite.

test and ethylene gas adsorption of waste composite. The neat cellulose sheet was provided for comparison. The ability of oxygen permeation of waste composite was superior compared to neat cellulose sheet. With the increment in activated carbon, significant enhancement in specific surface area and porosity was therefore observed. Oxygen gas was

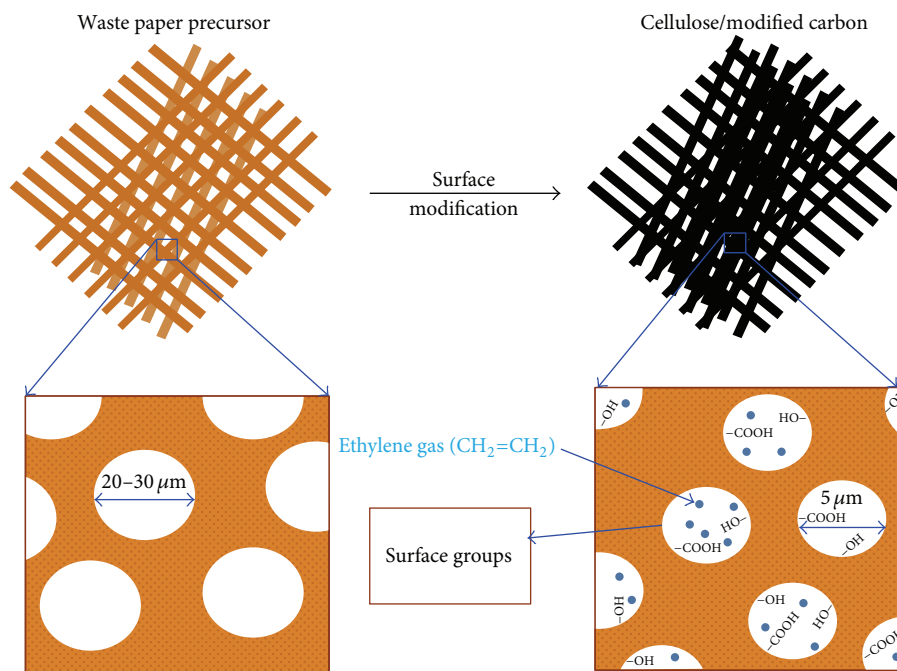


FIGURE 9: Mechanism of ethylene gas absorption on activated carbon and cellulose composite.

thus transmitted and it can be therefore stored on the surface of activated carbon. Three times oxygen permeation ability was therefore observed for waste composite compared to neat cellulose sheet.

Contrary to ethylene adsorption ability, the ability of ethylene gas absorption was therefore detrimental. Waste composite with 10 wt% reinforcement of activated carbon was provided the superiority on technical data. The investigation was conducted for 10 hours. The reason was due to the fact that, with excess integration of activated carbon, it may adsorb water and air from environment. The less space for ethylene gas absorption was consequently provided. Another reason was due to agglomeration on activated carbon. It may provide significant reduction on ethylene adsorption ability.

Figure 9 exhibits the ethylene gas absorption mechanism of activated carbon and cellulose composite. It was important to note that, without activated carbon, chemical reactive groups such as $-OH$ and $-COOH$ do not exist. The role of modified activated carbon can be induced to have the chemical bonding between ethylene gas and reactive functional group within the porous structure of modified carbon inserted to cellulose matrix. The small size of porosity provided significant efforts on specific surface area, rendering the existence of modified activated carbon which can induce superiority in absorption compared to neat cellulose.

4. Conclusion

Activated carbon was successfully derived from scrap tile waste from thermochemical conversion. The high performance in specific surface area and porosity was therefore

observed after chemical modification. Cellulose was successfully extracted from palm front. The morphological properties of derived cellulose acted as network-like structure. Designation of waste composite was prepared between cellulose and activated carbon. Young's modulus and tensile strength of composite were reduced, while elongation at break was increased. It was important to note that there is no change in morphological properties. The existence of activated carbon was in the pore of cellulose network. Oxygen permeation rate was reduced for waste composite, while ethylene gas adsorption was increased. Waste composite presented the strong idea on the utilization for being ethylene absorber for food packaging.

Competing Interests

There is no conflict of interests regarding the publication of this paper.

Acknowledgments

The authors gratefully acknowledge the financial support from NSTDA University Industry Research Collaboration (NUI-RC). The authors also acknowledge the Center for Advanced Studies in Materials and Packaging TU Institute for Advanced Studies, Faculty of Science and Technology, Thammasat University.

References

- [1] S. Ummartyotin and M. Sain, "Preparation of a cellulose and water-based resin composite," *Materials Letters*, vol. 123, pp. 70–74, 2014.

- [2] K. Rittirong, S. Uasopon, P. Prachayawasin, N. Euaphantasate, K. Aiempnanakit, and S. Ummartyotin, "CTAB as a soft template for modified clay as filler in active packaging," *Data in Brief*, vol. 3, pp. 47–50, 2015.
- [3] S. Ummartyotin and H. Manuspiya, "A critical review on cellulose: from fundamental to an approach on sensor technology," *Renewable and Sustainable Energy Reviews*, vol. 41, pp. 402–412, 2015.
- [4] S. Ummartyotin and H. Manuspiya, "An overview of feasibilities and challenge of conductive cellulose for rechargeable lithium based battery," *Renewable and Sustainable Energy Reviews*, vol. 50, pp. 204–213, 2015.
- [5] S. Ummartyotin and B. Tangnorawich, "Utilization of eggshell waste as raw material for synthesis of hydroxyapatite," *Colloid and Polymer Science*, vol. 293, no. 9, pp. 2477–2483, 2015.
- [6] S. Ummartyotin and C. Pechyen, "Microcrystalline-cellulose and polypropylene based composite: a simple, selective and effective material for microwavable packaging," *Carbohydrate Polymers*, vol. 142, pp. 133–140, 2016.
- [7] S. Ummartyotin, J. Juntaro, M. Sain, and H. Manuspiya, "Development of transparent bacterial cellulose nanocomposite film as substrate for flexible organic light emitting diode (OLED) display," *Industrial Crops and Products*, vol. 35, no. 1, pp. 92–97, 2012.
- [8] P. Sathishkumar, M. Arulkumar, and T. Palvannan, "Utilization of agro-industrial waste *Jatropha curcas* pods as an activated carbon for the adsorption of reactive dye Remazol Brilliant Blue R (RBBR)," *Journal of Cleaner Production*, vol. 22, no. 1, pp. 67–75, 2012.
- [9] S. K. Najafi, "Use of recycled plastics in wood plastic composites—a review," *Waste Management*, vol. 33, no. 9, pp. 1898–1905, 2013.
- [10] S. Kang, H. Li, J. Lei, L. Liu, B. Cai, and G. Zhang, "A new utilization approach of the waste heat with mid-low temperature in the combined heating and power system integrating heat pump," *Applied Energy*, vol. 160, pp. 185–193, 2015.
- [11] X. Yang, H. S. Choi, C. Park, and S. W. Kim, "Current states and prospects of organic waste utilization for biorefineries," *Renewable and Sustainable Energy Reviews*, vol. 49, pp. 335–349, 2015.
- [12] W. M. Budzianowski, "A review of potential innovations for production, conditioning and utilization of biogas with multiple-criteria assessment," *Renewable and Sustainable Energy Reviews*, vol. 54, pp. 1148–1171, 2016.
- [13] K. O'Callaghan, "Technologies for the utilisation of biogenic waste in the bioeconomy," *Food Chemistry*, vol. 198, pp. 2–11, 2016.
- [14] N. Chaukura, W. Gwenzu, T. Bunhu, D. T. Ruziwa, and I. Pumure, "Potential uses and value-added products derived from waste polystyrene in developing countries: a review," *Resources, Conservation and Recycling*, vol. 107, pp. 157–165, 2016.
- [15] A. Jain, R. Balasubramanian, and M. P. Srinivasan, "Hydrothermal conversion of biomass waste to activated carbon with high porosity: a review," *Chemical Engineering Journal*, vol. 283, Article ID 14005, pp. 789–805, 2016.
- [16] M. J. Ahmed and M. Ahmaruzzaman, "A review on potential usage of industrial waste materials for binding heavy metal ions from aqueous solutions," *Journal of Water Process Engineering*, vol. 10, pp. 39–47, 2016.
- [17] B. Acevedo and C. Barriocanal, "Texture and surface chemistry of activated carbons obtained from tyre wastes," *Fuel Processing Technology*, vol. 134, article 4451, pp. 275–283, 2015.
- [18] B. Acevedo, C. Barriocanal, I. Lupul, and G. Gryglewicz, "Properties and performance of mesoporous activated carbons from scrap tyres, bituminous wastes and coal," *Fuel*, vol. 151, pp. 83–90, 2015.
- [19] R. Acosta, V. Fierro, A. Martinez de Yuso, D. Nabarlantz, and A. Celzard, "Tetracycline adsorption onto activated carbons produced by KOH activation of tyre pyrolysis char," *Chemosphere*, vol. 149, pp. 168–176, 2016.
- [20] P. Hadi, K. Y. Yeung, J. Guo, H. Wang, and G. McKay, "Sustainable development of tyre char-based activated carbons with different textural properties for value-added applications," *Journal of Environmental Management*, vol. 170, pp. 1–7, 2016.
- [21] N. A. S. Ramli and N. A. S. Amin, "Catalytic hydrolysis of cellulose and oil palm biomass in ionic liquid to reducing sugar for levulinic acid production," *Fuel Processing Technology*, vol. 128, pp. 490–498, 2014.
- [22] W. R. W. Daud and F. M. Djuned, "Cellulose acetate from oil palm empty fruit bunch via a one step heterogeneous acetylation," *Carbohydrate Polymers*, vol. 132, article 9995, pp. 252–260, 2015.
- [23] J. Lamaming, R. Hashim, O. Sulaiman, C. P. Leh, T. Sugimoto, and N. A. Nordin, "Cellulose nanocrystals isolated from oil palm trunk," *Carbohydrate Polymers*, vol. 127, pp. 202–208, 2015.
- [24] M. L. Gerardo, S. Van Den Hende, H. Vervaeren, T. Coward, and S. C. Skill, "Harvesting of microalgae within a biorefinery approach: a review of the developments and case studies from pilot-plants," *Algal Research*, vol. 11, pp. 248–262, 2015.
- [25] T. Suganya, M. Varman, H. H. Masjuki, and S. Renganathan, "Macroalgae and microalgae as a potential source for commercial applications along with biofuels production: a biorefinery approach," *Renewable and Sustainable Energy Reviews*, vol. 55, pp. 909–941, 2016.

Research Article

Eggshell and Bacterial Cellulose Composite Membrane as Absorbent Material in Active Packaging

S. Ummartyotin,^{1,2} P. Pisitsak,³ and C. Pechyen^{1,2}

¹Advanced Functional Polymeric Materials Research Group, Faculty of Science and Technology, Thammasat University, Patum Thani 12120, Thailand

²Materials Research Center, HORIBA Scientific and Thammasat University, Patum Thani 12120, Thailand

³Department of Textile Science and Technology, Faculty of Science and Technology, Thammasat University, Patum Thani 12120, Thailand

Correspondence should be addressed to S. Ummartyotin; sarute.ummartyotin@gmail.com and C. Pechyen; chiravoot.p@gmail.com

Received 3 April 2016; Accepted 16 May 2016

Academic Editor: Ming-Guo Ma

Copyright © 2016 S. Ummartyotin et al. This is an open access article distributed under the Creative Commons Attribution License, which permits unrestricted use, distribution, and reproduction in any medium, provided the original work is properly cited.

Bacterial cellulose and eggshell composite was successfully developed. Eggshell was mixed with bacterial cellulose suspension and it was casted as a composite film. CaCO₃ derived from eggshell was compared with its commercial availability. It can be noted that good dispersion of eggshell particle was prepared. Eggshell particle was irregular in shape with a variation in size. It existed in bacterial cellulose network. Characterization on composite was focused on thermal and mechanical properties. It showed that flexibility and thermal stability of composite were enhanced. No significant effect of mechanical properties was therefore observed. The thermal stability of composite was stable up to 300°C. The adsorption experiment on water and vegetable oil capacity was performed. The enhancement on adsorption was due to the existence of eggshell in bacterial cellulose composite. It exhibited the potential to be a good candidate for absorbent material in active packaging.

1. Introduction

In recent years, the push on development on bio-based materials has been evident. Numerous efforts have been extensively developed in many types of bio-based products such as cellulose and derivatives, chitin and chitosan based materials, polylactic acid, polybutylene succinate, and starch as well as soy protein [1–3]. The role of bio-based materials can be employed in many sectors of application such as infrastructure, automotive part, and electronic device as well as active packaging [4–6]. One of the most effective bio-based materials was focused on cellulose [7–9]. From the fundamental point of view, it was remarkable to note that cellulose was considered as the most abundant naturally occurring biopolymer. It was commonly found in the cell walls of plant and certain algae. Cellulose derived from plant presented the excellence in terms of cost effectiveness, safety, and availability of raw materials. However, cellulose derived from bacterial specie presented the good effectiveness on purity

and homogeneity [10]. The most effective specie was focused on *Acetobacter xylinum*. It presented the low coefficient of thermal expansion and also it was an outstanding reinforcing agent for the design of environmentally friendly composites. It is renewable and biodegradable. Young's modulus of its single fibril was measured to be as high as 114 GPa. It also has attractive features of high degree of crystallinity, high degree of polymerization (14,400), and high specific area (37 m²/g) [11–13]. From the past, our research group was focused on the development of bacterial cellulose and the study of its application [2, 4, 14, 15]. One successful project was involved in the development of bacterial cellulose as a flexible substrate for electronic device. Although bacterial cellulose composite presents the flexibility and transparency and it gains many interests in the further development in electronic industries such as flexible device, the use of bacterial cellulose based materials provided high water absorption ability. Due to the high absorption ability of bacterial cellulose, the development of bacterial cellulose as absorbent materials has been

currently developed. It was important to note that the properties of interest of bacterial cellulose were involved in extremely hydrophilic feature in nature. As a result, BC will often have poor interface with hydrophobic polymer. However, from the viewpoint of food industry, absorbent materials have been currently developed for the shelf life of food [16, 17]. To gain higher quality of food product, food packaging has been extensively developed to become active such as high absorption of water and oxygen and antimicrobial properties as well as freshness control. However, due to the versatility of food, the research on active packaging was very dynamic in order to satisfy on quality of food from production plant, logistics, and transportation as well as consumer. In order to gain the water absorption ability of bacterial cellulose in food packaging, the development of eggshell and bacterial cellulose composite membrane has been extensively developed. It was important to note that eggshell was considered as industrial by-products that have been considered as waste. It was disposed in landfill every year. From the structural point of view, it was important to note that eggshell was considered as a natural bio-based product [18, 19]. The main component was due to calcium carbonate with very high porosity feature. The research on the use of eggshell as absorbent materials has been therefore improved [20]. Moreover, in order to support the environmentally friendly policy, bio-based materials have been encouraged to develop [21]. To support the use of waste with higher efficiency, modification of eggshell as a composite with bacterial cellulose as absorbent materials should be tailored.

In this research work, we wish to study the development of eggshell and bacterial cellulose composite membrane. Structure and properties of composite membrane were also evaluated. The experiment on absorption ability was therefore determined.

2. Experimental

2.1. Materials. Bacterial cellulose was successfully extracted from nata de coco product (chaokoh coconut gel in syrup, Ampol Food Processing Ltd., Nakhon Pathom, Thailand), an indigenous dessert of which main component was reported as bacterial cellulose. Characterizations of bacterial cellulose extracted from nata de coco were carried out in previous work; its characteristics matched those of bacterial cellulose extracted from the culture of *Acetobacter xylinum*.

Eggshell was collected from canteen, Faculty of Science and Technology, Thammasat University. It was washed with methanol and then dried in an oven at 100°C for 24 hours. After that, it was milled and pressed through a sieve with a 25-micron mesh. Analytical grade of NaOH and methanol were purchased from Sigma Aldrich, Thailand, and they were used as received without further purification.

2.2. Methods

2.2.1. Extraction and Purification of Bacterial Cellulose. Bacterial cellulose was extracted from nata de coco. The nata de coco gel was first rinsed with distilled water and blended

using a laboratory blender. The bacterial cellulose suspension was then treated in 0.1 M NaOH at 80°C for 20 min to remove any remaining microorganisms, medium component, and soluble polysaccharides. The purified bacterial cellulose was then thoroughly washed with distilled water until pH was neutral. Additional information has been published in our previous research article [4, 22].

2.2.2. Fabrication of Bacterial Cellulose and Eggshell Composite Membrane. To fabricate the composite membrane, the bacterial cellulose sheet was first prepared from bacterial cellulose suspension. The weight ratio between bacterial cellulose and eggshell was controlled as 1:0.5, 1:1, 1:2, and 1:5, respectively. After that, it was stirred for 3 hours until homogenization was achieved. To fabricate composite membrane, water from suspension was removed through filtration with a Buchner funnel fitted with Polytetrafluoroethylene membrane filter (0.1 m mesh and 90 mm diameter), which was connected to a Buchner flask and a vacuum pump. The filtration was continued until the wet sheet of bacterial cellulose was formed. The wet sheet was then dried between two Polytetrafluoroethylene membranes under the applied pressure of 58 psi, following the paper hand sheet formation standard SCAN C 26:76. The sample should be stored in desiccator for water absorption prevention. Characterization techniques such as X-ray diffraction, X-ray fluorescence, Fourier transform infrared, thermogravimetric analysis, scanning electron microscope, and transmission electron microscope were employed to investigate the properties of eggshell and its composite membrane.

2.2.3. Adsorption Activity of Bacterial Cellulose and Eggshell Composite Membrane. The adsorption activity of bacterial cellulose and eggshell composite membrane was focused on water and vegetable oil. To determine the absorption capacity of the products, a gravimetric method was applied. An accurately weighed quantity of the sample (0.5 g) (m_1) was immersed in 100 mL of distilled water and vegetable oil at room temperature until maximal swelling. The time was operated overnight and then the weight of maximum swelling was detected.

The absorption capacity was calculated as g H₂O/g dry and g vegetable/g dry of composite using the following equation:

$$\text{Adsorption capacity (g/g)} = \frac{m_2 - m_1}{m_1}, \quad (1)$$

where m_1 means the weight of dried sample, whereas m_2 is the weight of tested sample. In all cases, five measurements were performed in order to calculate the statistical average.

2.3. Characterizations

2.3.1. X-Ray Diffraction. Eggshell particle was investigated on crystal structure by X-ray diffraction (XRD, Phillips P.W. 1830 diffractometer). It was employed by using nickel-filtered CuK α radiation. Diffraction patterns were recorded over a range of 10–80. The scan rate was set for 3° per min. Prior to

TABLE 1: Elemental analysis of eggshell.

Element (wt%)	Ca	O	Mg	Al	S	Others
Eggshell	42.8	49.5	6.11	0.936	0.343	0.311
CaCO ₃ (commercial)	53.4	37.6	7.74	1.24	0.018	0.002

investigation, the sample should be stored in desiccator for moisture absorption prevention.

2.3.2. Scanning Electron Microscope. Eggshell particle and its composite membrane were investigated on morphological properties by SEM (a JOEL JSM-6301F scanning microscope). The machine was operated at an acceleration voltage of 5 kV to identify the morphological properties of powders. Before investigation, the samples were sputter-coated with Au to enhance the electrical conductivity.

2.3.3. Thermogravimetric Analysis. Thermal degradation behavior of the eggshell particle and its composite membrane was determined by thermogravimetric analysis (TA-5000 TGA, TA Instruments, DE, USA). Each sample (10 mg) was heated with a heating rate of 10°C/min in nitrogen atmosphere from 30°C to 800°C. The TGA balance flow meter was set at 20 psi N₂, while the purge flow meter was adjusted to 20 psi of synthetic air.

2.3.4. X-Ray Fluorescence. XRF (a Phillips 1404 XRF Wavelength Disperse Spectrometer) was used to determine the trace element of sample. It was equipped with an array of five analyzing crystals and fitted with a Rh X-ray tube target. A vacuum was used as the medium of analyses to avoid interaction of X-rays with air particle. 1 g of sample was mixed with 6 g of H₃BO₃ and consequently pressed under 10 tons of force.

2.3.5. Fourier Transforms Infrared. FTIR was performed on a Bruker Vector 22 mid-IR spectroscopy (Bruker, Germany). All FTIR absorption spectra were recorded over 4000–400 cm⁻¹ wavenumbers region at a resolution of 8 cm⁻¹ with 1024 scans using a deuterated triglycine sulfate (DTGS) detector. A straight line between two lowest points in the respective spectra region was chosen as a baseline. Potassium bromide (KBr) acting as a nonabsorbing medium was mixed with a solid sample (0.3–0.5 wt%) by an agate mortar and pestle to prepare a pellet specimen.

2.3.6. Tensile Test. The tensile tests were conducted in accordance to the ISO Standard number ISO 527:1996. The sample was cut with a Zwick cutter into dog-bone specimen type 5A. The samples had the overall length and the gauge length of 75 and 20 mm, respectively. The initial distance between grips was 50 mm and its width at the grip end was 12.5 mm. The width at the narrowest part was 4 mm and the thickness was 0.3–0.5 mm. The testing speed was 1 mm/min. The specimens were preconditioned at 20°C in 54% relative humidity in a desiccator containing a saturated solution of Mg(NO₃)₂ for at least 48 h prior to testing. The tensile test was conducted using

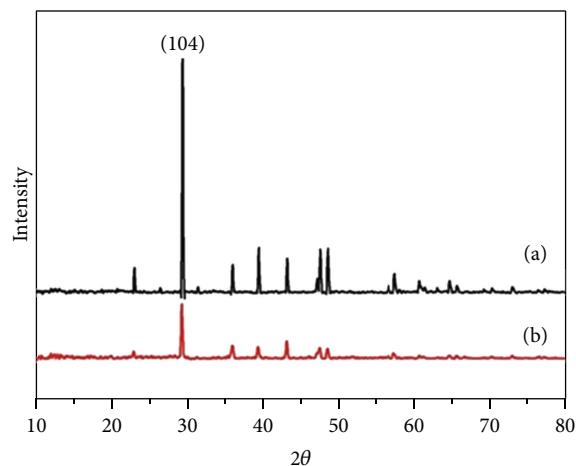


FIGURE 1: X-ray diffraction pattern of (a) eggshell and (b) commercial calcium carbonate.

Instron universal material testing machine (Instron 4502, Instron Corporation, MA, USA) equipped with a 1 kN load cell. At least 10 specimens were tested per sample to obtain a statistical average.

3. Results and Discussion

3.1. Characterization of Eggshell from Renewable Resource. Table 1 exhibits element analysis of eggshell. It was important to note that chemical composition of eggshell was associated with CaCO₃. The main component was focused on calcium and oxygen and it was remarkable to note that it can be considered as effective resource for calcium oxide. However, the variation in the amount of element was still varied due to feed of the hen and it was contaminated by the inner membrane of egg. To use eggshell with higher efficiency, the controllability on elemental analysis should be performed.

X-ray diffraction pattern of eggshell was investigated and the commercial CaCO₃ was provided for comparison. Figure 1 exhibits the X-ray diffraction pattern. It was remarkable to note that there is no phase of impurities. The existence of peak was involved in CaCO₃. The characteristic peak was associated with JCPDS number 47-1743. The result presented the existence of CaCO₃ derived from eggshell waste. Furthermore, it was important to note that the preferential orientation was determined using a texture coefficient (*hkl*). The full width at half maximum (FWHM) of the 100% intensity (104) peak at $2\theta = 29.5$ was determined for all calcium carbonate derived from eggshell. It illustrated that the highest value was in the (104) plane for the sample, which indicated that crystal orientation is uniform in *x*- and *z*-orientation. The crystal size was estimated by the Scherrer

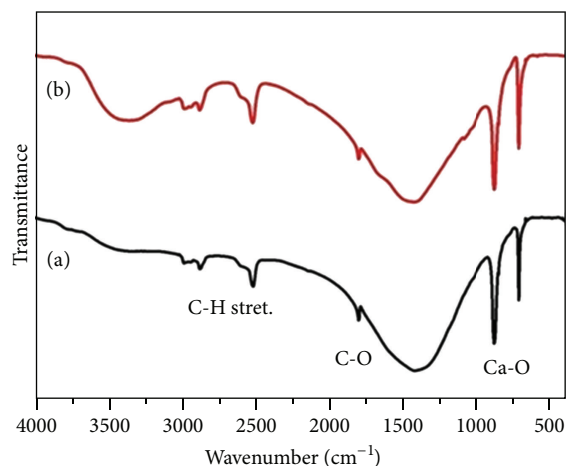


FIGURE 2: FTIR pattern of (a) eggshell and (b) commercial calcium carbonate.

formula: $D = K\lambda/\beta \cos \theta$, where D is crystallite size, K is a constant of 0.9, λ is the X-ray wavelength, β is full width at half maximum (FWHM), and θ is the diffraction peak. The (104) peak was used to estimate the crystal and it was found to be 50–70 nm.

Figure 2 exhibits FTIR pattern of eggshell particle and commercial CaCO_3 was provided for comparison. Both results presented the similar feature of pattern. The intense band was observed at 3600 cm^{-1} due to the vibration of the OH group attached to Ca^{2+} . It can be implied that surface of eggshell exhibited hydrophilic properties. In order to prevent this concern, eggshell should be stored in desiccator. Moreover, the characteristic peak position at 1500 cm^{-1} was due to C-O stretching. The remaining part of carbonate still existed. The wavenumber at 700 cm^{-1} belonged to Ca-O stretching. It can be noted that the composition of eggshell was referred to calcium carbonate. This discussion was strongly associated with XRD experiment.

In the case of eggshell particle, it was suspended in water solution. It was important to note that most of the particles were precipitated within a minute leaving a clear aqueous supernatant immediately after the preparation. From the fundamental point of view, due to the nature of eggshell, it presented the hydrophilic feature on surface. To determine the particle size of eggshell, the good distribution of eggshell particle should be controlled. This indicated that eggshell particle was facile to aggregate in an aqueous suspension, suggesting that ultrasonic process should be performed. From the theoretical point of view, it was important to note that eggshell particle can be stabilized by two main forces. The one was focused on van der Waals' interactions and the other one was focused on electrostatic repulsive force. When the attraction force is less than repulsive force, the particle was dispersed, and if the attraction force exceeds the repulsive force, the particle tended to form aggregates. It was important to note that the determination of particle of eggshell and good distribution should be performed in order to prevent any error from measurement.

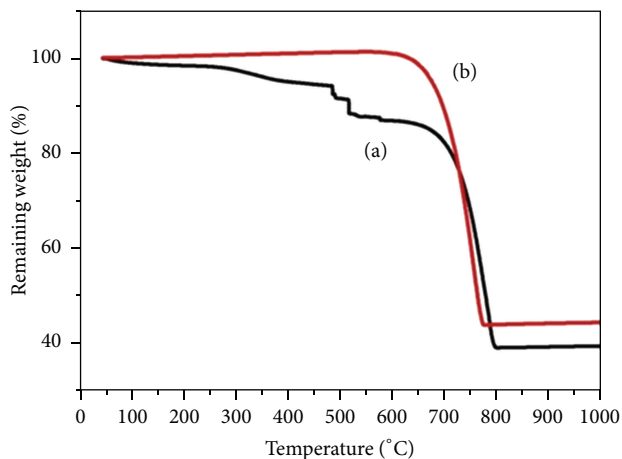


FIGURE 3: Thermogravimetric analysis of (a) eggshell and (b) commercial CaCO_3 .

Furthermore, the stability of eggshell particle was therefore investigated. Thermogravimetric analysis was conducted. The analysis was used to determine the weight loss as a function of elevated temperature. Figure 3 exhibits the thermal decomposition of eggshell particle and commercial CaCO_3 was provided for comparison. It can be noted that when the thermal temperature reached 400°C , small weight loss was observed due to water absorption on eggshell particle. This indicated that the surface of eggshell exhibited hydrophilic feature. Moreover, decomposition can be categorized into three different regions. Within the temperature region of $400\text{--}800^\circ\text{C}$, the large region of weight loss was therefore observed. This was due to the change in structure of CaCO_3 to calcium oxide ceramic. From the theoretical point of view, CaCO_3 can be changed to calcium oxide when high temperature was applied. This discussion was strongly associated with X-ray diffraction experiment. Moreover, with the increment on temperature in the range of $800\text{--}1000^\circ\text{C}$, no weight loss was therefore observed due to that, suggesting that the decomposition was completely performed.

3.2. Characterization of Eggshell and Bacterial Cellulose Composite Membrane

3.2.1. Characterization of Bacterial Cellulose and Eggshell Composite Membrane. Eggshell and bacterial cellulose composite membrane was successfully prepared. It was important to note that the weight ratio between bacterial cellulose and eggshell was controlled as 1:0.5, 1:1, 1:2, and 1:5, respectively. Figure 4 exhibits the thermal decomposition of bacterial cellulose and eggshell composite membrane. The decomposition temperature can be categorized into three different regions, similar to neat eggshell waste. From room temperature to 300°C , small weight loss can be observed due to effect of water absorption. With the temperature range from $300\text{--}700^\circ\text{C}$, the large decomposition was therefore observed due to decomposition of bacterial cellulose and the calcium carbonate which was considered as the main

TABLE 2: Mechanical properties of bacterial cellulose and eggshell composite membrane.

Composites	Young's modulus (MPa)	Tensile strength (MPa)	Elongation (%)
Neat bacterial cellulose sheet	4.16 ± 0.003	13.2 ± 0.005	3.17 ± 0.005
Bacterial cellulose and eggshell (1 : 0.5 wt%)	3.89 ± 0.001	7.05 ± 0.001	1.81 ± 0.003
Bacterial cellulose and eggshell (1 : 1 wt%)	0.40 ± 0.002	2.53 ± 0.002	6.29 ± 0.003
Bacterial cellulose and eggshell (1 : 2 wt%)	0.42 ± 0.001	1.47 ± 0.002	3.50 ± 0.001
Bacterial cellulose and eggshell (1 : 5 wt%)	0.12 ± 0.002	0.78 ± 0.001	6.37 ± 0.002

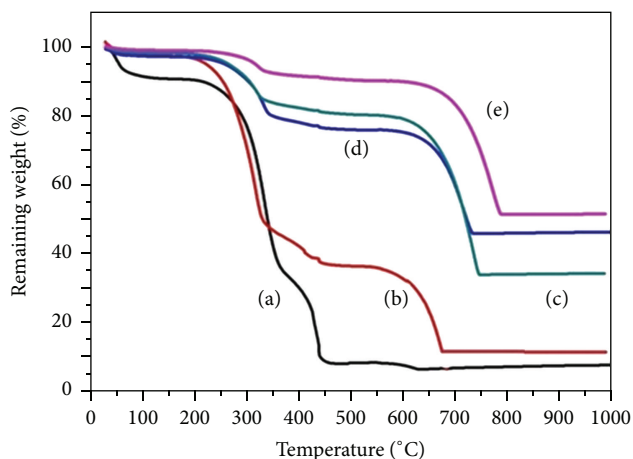


FIGURE 4: Thermal decomposition of eggshell and bacterial cellulose composite membrane. (a) Neat bacterial cellulose. (b) 1 : 0.5 weight ratio of bacterial cellulose and eggshell. (c) 1 : 1 weight ratio of bacterial cellulose and eggshell. (d) 1 : 2 weight ratio of bacterial cellulose and eggshell. (e) 1 : 5 weight ratio of bacterial cellulose and eggshell.

component of eggshell. Moreover, in the region of 700–1000°C, high stability of weight loss was detected; there is no change due to weight loss. The residual was due to char from bacterial cellulose and calcium oxide due to decomposition of eggshell. Also, the amount of residual was very high, similar to the amount of eggshell in bacterial cellulose composite.

Mechanical properties of bacterial cellulose and eggshell composite membrane were investigated. Young's modulus, tensile strength, and elongation were determined. Table 2 exhibits the mechanical properties of eggshell composite membrane. The mechanical properties of neat bacterial cellulose were provided for comparison. Young's modulus and tensile strength were decreased with the increment of eggshell. Due to the difference in physical properties of bacterial cellulose and eggshell particle, eggshell particle was embedded into bacterial cellulose network. From the structural point of view, the structure of bacterial cellulose presented nanonetwork or a three-dimensional network structure of fiber with air interstices in between; when the tensile stress was applied to the bacterial cellulose, the stress would be transferred through the fiber network. However, in all cases of bacterial cellulose and eggshell composite membrane, although significant enhancement in adsorption ability was therefore observed, the inferior mechanical properties were subsequently detected, suggesting that the optimization

between bacterial cellulose and eggshell particle should be controlled in order to tailor the excellent performance of adsorption and mechanical properties. To gain the flexibility of composite membrane, the correlation of bacterial cellulose and eggshell should be incorporated into polymer matrix and it can be further facilitated for use in many packaging industries. On the other hand, it was remarkable to note that mechanical properties were slightly decreased when amount of eggshell particle was filled. The reason was due to the fact that the existence of eggshell particle did not provide the strong chemical bonding with bacterial cellulose such as ionic and covalent bonds. It may provide only physical bonding such as van der Waals' force. The increase in the loading of biomicroparticle in the resulting biomicrocomposites will begin to experience more and more particle-to-particle interaction rather than the intended particle-to-polymer interaction. Particle-to-particle interaction will lead to particle agglomerations and poor mechanical properties. Composite was therefore provided less amount of mechanical properties compared to neat bacterial cellulose.

Figure 5 exhibits the morphological properties of eggshell and bacterial cellulose composite membrane. The neat of bacterial cellulose sheet was provided for comparison. In composite structure, the existence of eggshell powder was filled in the network of bacterial cellulose. From the structural point of view, the structure of bacterial cellulose consisted of fibril network. The air-space existed in between. It was remarkable to note that as exhibited in many literatures bacterial cellulose network provided the excellent specific surface area and porosity. The existence of eggshell powder was filled into bacterial cellulose network. It can be rendered on the increment of specific surface area. The existence of eggshell in bacterial cellulose network can be also offered the significant enhancement of thermal stability and adsorption ability.

3.2.2. Adsorption Activity of Bacterial Cellulose and Eggshell Composite Membrane. To employ bacterial cellulose and eggshell composite membrane in packaging industries, the development of absorbent materials has been researched. In food industry, packaging has been extensively designed for high adsorption ability for water and vegetable. Since both of them were enormously employed in food processing, to design the appropriate active packaging for high adsorption ability of water and vegetable oil was one of the important key factors in order to maintain the quality and shelf life of food. From the structural point of view, the properties of bacterial cellulose and eggshell particle exhibited high specific surface

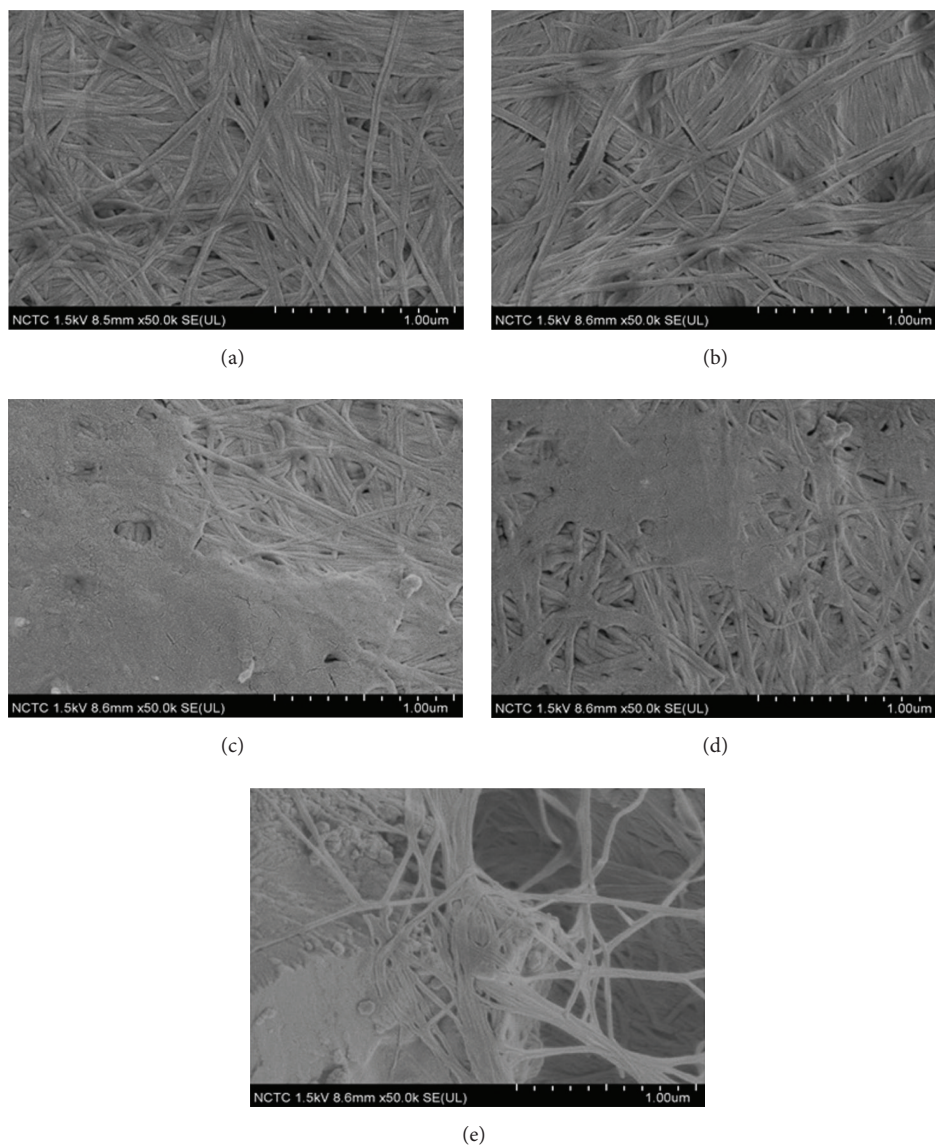


FIGURE 5: Morphological properties of eggshell and bacterial cellulose composite membrane (a) neat bacterial cellulose. (b) 1:0.5 weight ratio of bacterial cellulose and eggshell. (c) 1:1 weight ratio of bacterial cellulose and eggshell. (d) 1:2 weight ratio of bacterial cellulose and eggshell. (e) 1:5 weight ratio of bacterial cellulose and eggshell.

area. It was therefore considered as absorbent materials. Bacterial cellulose was considered as network-like structure of fibrils containing hydroxyl group along glucose unit. The repulsion force was enrolled and it provided the free space along bacterial cellulose network. Hydrogen formation can occur from the reaction of glucose unit with water and vegetable oil. It involved intermolecular and intramolecular force in between. High adsorption ability was therefore observed. This discussion was strongly associated with vegetable oil. The hydroxyl group from bacterial cellulose network and polyol group from vegetable oil were therefore involved. A significant effort on bonding formation was employed to consider on adsorption ability in water and vegetable oil for bacterial cellulose. The objective is to investigate

the feasibility of high water and vegetable oil absorbency and the strength of composite. The role of water and vegetable oil can be cross-linked with the hydroxyl position of bacterial cellulose. Swelling aspect was subsequently detected. Table 3 and Figure 6 exhibit the water adsorption capacity and vegetable oil adsorption capacity of bacterial cellulose and eggshell composite membrane. Moreover, it can be remarkable to note that the ability of adsorption increased with respect to amount of eggshell particle. The eggshell particle existed in the network of bacterial cellulose as investigated by SEM analysis. Eggshell particle shows high specific surface area and porosity. It therefore provided high adsorption ability. Another reason was involved in calcium atom from eggshell particle; it can be dissolved in water and

TABLE 3: Water adsorption capacity and vegetable oil adsorption capacity of bacterial cellulose and eggshell composite membrane.

Composites	Water adsorption capacity (g/g)	Vegetable oil adsorption capacity (g/g)
Neat bacterial cellulose sheet	0.0658 ± 0.003	0.2631 ± 0.013
Bacterial cellulose and eggshell (1 : 0.5 wt%)	0.4588 ± 0.023	0.7195 ± 0.036
Bacterial cellulose and eggshell (1 : 1 wt%)	0.4849 ± 0.024	0.7732 ± 0.039
Bacterial cellulose and eggshell (1 : 2 wt%)	0.6479 ± 0.032	1.3285 ± 0.066
Bacterial cellulose and eggshell (1 : 5 wt%)	1.0501 ± 0.052	1.5275 ± 0.076

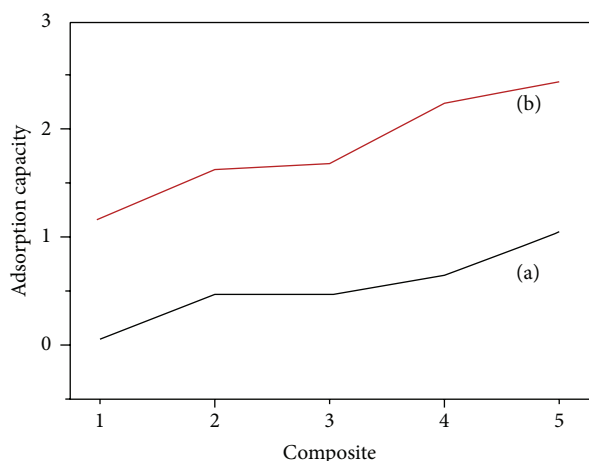


FIGURE 6: Adsorption capacity of bacterial cellulose and eggshell composite membrane. (a) Water adsorption. (b) Vegetable oil adsorption. (1) Neat bacterial cellulose. (2) 1:0.5 weight ratio of bacterial cellulose and eggshell. (3) 1:1 weight ratio of bacterial cellulose and eggshell. (4) 1:2 weight ratio of bacterial cellulose and eggshell. (5) 1:5 weight ratio of bacterial cellulose and eggshell.

subsequently formed the chemical bond between bacterial cellulose. It provided an attracted force to water and vegetable oil molecule. However, it was controversial that the free space in bacterial cellulose network was still less due to the existence of eggshell and the adsorption ability over water and vegetable oil molecule might be consequently less. Due to the cuticle composition in eggshell, it still had the porosity. The water and vegetable oil were still adsorbed in bacterial cellulose and eggshell waste composite. It was suggested that composite provided significant ability to adsorption of water and vegetable oil molecule. It exhibited the excellent performance and qualified as the excellent candidate for adsorbent material in food packaging.

4. Conclusion

Bacterial cellulose and eggshell composite membrane was successfully developed. Eggshell particle was mixed with bacterial cellulose suspension and it was casted as a film composite. Characterization on eggshell waste can confirm that the main composition of eggshell is referred CaCO_3 with high porosity. The development of bacterial cellulose and eggshell composite membrane was preliminary tested on water and vegetable oil absorption ability. It exhibited

the potential to use eggshell as absorbent materials in active packaging.

Competing Interests

The authors declare that there are no competing interests regarding the publication of this paper.

Acknowledgments

The authors gratefully acknowledge the financial support provided by Thammasat University under the TU Research Scholar. The Contract no. is 11/2559.

References

- [1] O. Faruk, A. K. Bledzki, H.-P. Fink, and M. Sain, "Biocomposites reinforced with natural fibers: 2000–2010," *Progress in Polymer Science*, vol. 37, no. 11, pp. 1552–1596, 2012.
- [2] S. Ummartyotin and H. Manuspiya, "A critical review on cellulose: from fundamental to an approach on sensor technology," *Renewable and Sustainable Energy Reviews*, vol. 41, pp. 402–412, 2015.
- [3] P. S. Guru and S. Dash, "Sorption on eggshell waste—a review on ultrastructure, biomineralization and other applications," *Advances in Colloid and Interface Science*, vol. 209, pp. 49–67, 2014.
- [4] S. Ummartyotin, J. Juntaro, M. Sain, and H. Manuspiya, "Development of transparent bacterial cellulose nanocomposite film as substrate for flexible organic light emitting diode (OLED) display," *Industrial Crops and Products*, vol. 35, no. 1, pp. 92–97, 2012.
- [5] M. Z. Elsabee and E. S. Abdou, "Chitosan based edible films and coatings: a review," *Materials Science and Engineering C*, vol. 33, no. 4, pp. 1819–1841, 2013.
- [6] J. Liu, X. Zhan, J. Wan, Y. Wang, and C. Wang, "Review for carrageenan-based pharmaceutical biomaterials: favourable physical features versus adverse biological effects," *Carbohydrate Polymers*, vol. 121, pp. 27–36, 2015.
- [7] N. Lavoine, I. Desloges, A. Dufresne, and J. Bras, "Microfibrillated cellulose—its barrier properties and applications in cellulosic materials: a review," *Carbohydrate Polymers*, vol. 90, no. 2, pp. 735–764, 2012.
- [8] H. P. S. Abdul Khalil, A. H. Bhat, and A. F. Ireana Yusra, "Green composites from sustainable cellulose nanofibrils: a review," *Carbohydrate Polymers*, vol. 87, no. 2, pp. 963–979, 2012.
- [9] A. Carlmark, E. Larsson, and E. Malmström, "Grafting of cellulose by ring-opening polymerisation—a review," *European Polymer Journal*, vol. 48, no. 10, pp. 1646–1659, 2012.

- [10] C. Wu, "Production and characterization of optically transparent nanocomposite film," in *Faculty of Forestry*, University of Toronto, Toronto, Canada, 2010.
- [11] K.-Y. Lee, J. J. Blaker, and A. Bismarck, "Surface functionalisation of bacterial cellulose as the route to produce green polylactide nanocomposites with improved properties," *Composites Science and Technology*, vol. 69, no. 15-16, pp. 2724–2733, 2009.
- [12] K.-Y. Lee, P. Bharadia, J. J. Blaker, and A. Bismarck, "Short sisal fibre reinforced bacterial cellulose polylactide nanocomposites using hairy sisal fibres as reinforcement," *Composites Part A: Applied Science and Manufacturing*, vol. 43, no. 11, pp. 2065–2074, 2012.
- [13] K.-Y. Lee, K. K. C. Ho, K. Schluffer, and A. Bismarck, "Hierarchical composites reinforced with robust short sisal fibre preforms utilising bacterial cellulose as binder," *Composites Science and Technology*, vol. 72, no. 13, pp. 1479–1486, 2012.
- [14] S. Ummartyotin, J. Juntaro, M. Sain, and H. Manuspiya, "Si-O barrier technology for bacterial cellulose nanocomposite flexible displays," *Carbohydrate Polymers*, vol. 86, no. 1, pp. 337–342, 2011.
- [15] S. Ummartyotin and H. Manuspiya, "An overview of feasibilities and challenge of conductive cellulose for rechargeable lithium based battery," *Renewable and Sustainable Energy Reviews*, vol. 50, pp. 204–213, 2015.
- [16] C. E. Realini and B. Marcos, "Active and intelligent packaging systems for a modern society," *Meat Science*, vol. 98, no. 3, pp. 404–419, 2014.
- [17] L. Barbosa-Pereira, I. Angulo, J. M. Lagarón, P. Paseiro-Losada, and J. M. Cruz, "Development of new active packaging films containing bioactive nanocomposites," *Innovative Food Science & Emerging Technologies*, vol. 26, pp. 310–318, 2014.
- [18] H. Yu, Q. Tang, J. Wu et al., "Using eggshell membrane as a separator in supercapacitor," *Journal of Power Sources*, vol. 206, pp. 463–468, 2012.
- [19] P. Suppakul, K. Jutakorn, and Y. Bangchokedee, "Efficacy of cellulose-based coating on enhancing the shelf life of fresh eggs," *Journal of Food Engineering*, vol. 98, no. 2, pp. 207–213, 2010.
- [20] D. Podstawczyk, A. Witek-Krowiak, K. Chojnacka, and Z. Sadowski, "Biosorption of malachite green by eggshells: mechanism identification and process optimization," *Bioresource Technology*, vol. 160, pp. 161–165, 2014.
- [21] T. Boronat, V. Fombuena, D. Garcia-Sanoguera, L. Sanchez-Nacher, and R. Balart, "Development of a biocomposite based on green polyethylene biopolymer and eggshell," *Materials and Design*, vol. 68, pp. 177–185, 2015.
- [22] K. O-Rak, E. Phakdeeparaphan, N. Bunnak, S. Ummartyotin, M. Sain, and H. Manuspiya, "Development of bacterial cellulose and poly(vinylidene fluoride) binary blend system: structure and properties," *Chemical Engineering Journal*, vol. 237, pp. 396–402, 2014.

Research Article

Extraction and Hydrophobic Modification of Cotton Stalk Bark Fiber

Ya-Yu Li, Guang-Ming Du, Xin-Jie Feng, Ya-Wei Mu, and De-Qiang Li

College of Chemical Engineering, Xinjiang Agricultural University, Urumqi, Xinjiang 830052, China

Correspondence should be addressed to Ya-Yu Li; 835084132@qq.com

Received 28 March 2016; Accepted 28 April 2016

Academic Editor: Jun Yang

Copyright © 2016 Ya-Yu Li et al. This is an open access article distributed under the Creative Commons Attribution License, which permits unrestricted use, distribution, and reproduction in any medium, provided the original work is properly cited.

Cotton stalk bark fiber (CSBF) was extracted at high temperature and under high pressure, under the condition of the alkali content of 11 wt%. Experimental results proved that the extraction yield of CSBF was 27.3 wt%, and the residual alkali concentration was 2.1 wt%. Then five kinds of modifiers including methyl methacrylate (MMA), MMA plus initiator, epoxy propane, copper ethanalamine, and silane coupling agent were chosen to modify the surface of CSBF. It was found by measuring water retention value (WRV) that these five kinds of modifiers were all effective and the silane coupling agent was best modifier among all. The optimal modifying conditions of silane coupling agent were obtained: modifier concentration was 5%, the mixing temperature was 20°C, the mixing time was 1 h, and vacuum drying time was 1 h. Under the optimal condition, the WRV of the modified CSBF was 89%. It is expected that these modified CSBF may be a filler with strengthening effect in wood plastic composites (WPC) fields.

1. Introduction

The plastics substitutes have been receiving more attention due to its applications in solving the problem of white pollution [1, 2]. Among the plastics substitutes, renewable biomass material from agricultural by-product such as cotton stalk is one of the considerable candidates [2]. It was reported that adding wood fiber into plastics to produce wood plastic composites (WPC) could improve the mechanical properties of plastics such as tensile strength, reduce the dosage of plastic materials, and decrease the cost [3].

Cotton is an important human subsistence and industrial raw material. Xinjiang is the largest province of commercial cotton planted in China. In 2013, the cotton output in Xinjiang reached 3.4 million tons, occupying more than 58 wt% of that in China. Akdeniz et al. [4] reported that the cotton stalk was equivalent to three times the weight of the cotton fiber. Nowadays, the cotton stalk after harvest is mostly taken back into farmland or directly burned as fuel in low utilization value. When the cotton stalk is smashed and scattered into soil of the same field for several years, it is prone to induce cotton diseases on this field, which is a big problem affecting cotton growth. Therefore, development of simple and low

cost methods for the high value-added biomaterials produced by cotton stalk is of great importance for broadening and improving its applications [5]. It was reported that 26 wt% of cotton stalk was bark [6], which was composed of 41 wt% of cellulose, 21 wt% of hemicellulose, 18 wt% of lignin, 5 wt% of pectin, 10 wt% of water-soluble matter, and 4 wt% of wax [7]. Dong et al. [8] reported that the fibers extracted from cotton stalk bark (CSB) displayed tensile properties close to cotton fibers. Young's modulus of cellulose of crystal state was reported as 250 Gpa, which was three times that of E-glass [9]. In all, the cellulose fiber extracted from cotton stalk displayed potential applications in structural materials.

Generally, the cotton stalk bark fiber (CSBF) is obtained through degumming under the condition of alkali solution at normal pressure [5–7]. In addition, steam explosion was also reported to extract the CSBF [8, 10, 11]. CSBF has strong water imbibition property due to its hydroxyl groups of cellulose, leading to a short service life of WPC in the natural environment. In recent years, rapid progress has been made in the modification of plant fibers including silane treatment [12], alkaline treatment [6], copper amine [13], acetylation [14], maleated coupling [15], and enzyme treatment [16]. For example, Park et al. [17] found that jute fiber treated by silane

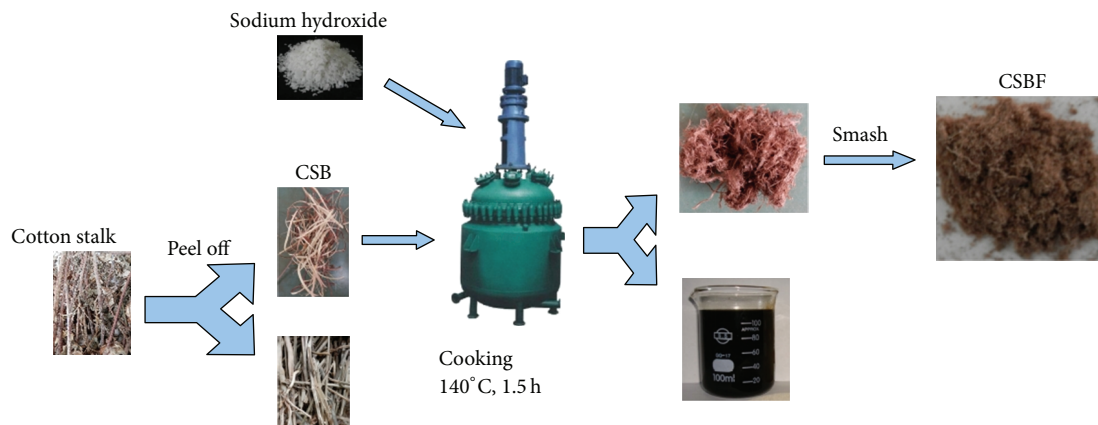


FIGURE 1: The extraction process of cotton stalk bark fiber.

made the surface coherence of fiber and polypropylene tight. Islam et al. [18] reported that the modulus of elasticity (MOE) and compressive modulus of wood were significantly boosted after treatment with MMA (methyl methacrylate)/PVA (polyvinyl alcohol), indicating improvement of mechanical properties of the wood samples. Hydroxyl in cellulose and guaiacol in lignin could react with epoxypropane to form ether [19], which reduced the hydrophilicity of cellulose or lignin. Jiang and Kamdem [13] reported an increase up to around 45% in unnotched impact strength using 0.2 wt% copper amine-treated WF at the 60 wt% PVC loading level, compared with untreated wood flour. In all, the five modifiers including MMA, MMA plus initiator, epoxypropane, copper ethanolamine, and silane coupling agent were effective and low cost. However, as far as we know, the modification of CSBF using the five modifiers MMA, MMA plus initiator, epoxypropane, copper ethanolamine, and silane coupling agent has not been reported yet. Comparative study about the validity of these five modifiers will help understand the modification mechanism on CSBF.

Herein, CSBF was extracted by using the alkali method under high temperature and high pressure. Then, five modifiers including MMA, MMA plus initiator, epoxypropane, copper ethanolamine, and silane coupling agent were chosen to process CSBF, respectively. Moreover, the influences of the modification conditions were also investigated in detail. It is believed that these modified CSBF may be a potential application in wood plastic composites fields.

2. Material and Methods

2.1. Materials. Cotton stalks were taken from 314 Tuan, Shihezi, in October 2014. Sodium hydroxide, anhydrous ethanol, ethanol amine, alkali type copper carbonate, potassium persulfate, methyl methacrylate, epoxypropane, and silane coupling agent are all analytically pure, used as purchased from Sinopharm Chemical Reagent Co., Ltd.

2.2. Extraction of CSBF. In a typical experiment, cotton stalk bark (CSB) was peeled off first. Then the CSB was put into a kettle at 140°C for 1.5 h with NaOH under vigorous stirring

(Figure 1). The weight of NaOH was 11% in comparison with that of CSB. The product was separated from the solution by centrifugation, dried in air at 50°C, and smashed for further modification process.

Determination of Residual Alkali Content in Black Liquid. 10 mL black liquid and 10 mL 6 wt% barium chloride were pipetted to 100 mL volumetric flask and then lignin was completely precipitated. The solution was diluted with distilled water to the scale line, shaken well, and let stand. Upper clear liquid in the volumetric flask was pipetted into conical flask. Using phenolphthalein as indicator and hydrochloric acid as standard solution, titration was done until the solution color changed from light yellow to red at the end point. Alkaline residue was calculated according to the dosage of hydrochloric acid solution.

2.3. Modification of CSBF. In a typical procedure, 0.5 g dry CSBF and 1 g modifier (MMA, MMA plus initiator, epoxypropane, copper ethanolamine, and silane coupling agent) were added into the mixture of 8.5 g ethanol and 0.5 g water. The mixture was stirred for 1.5 h at room temperature. After that, the product was filtered and transferred to a vacuum oven at 105°C for 2 h. In the process, the condensation dehydration, grafting, and polymerization reaction occurred. Finally, the modified CSBF was washed for 5 times with mixture of ethanol and water and dried in wind drying oven until constant weight.

2.4. Water Retention Value. Water retention value (WRV) was analyzed as previously reported by Raj et al. [20]. In a typical procedure, 2 g absorbent paper was placed at the bottom of the centrifuge tube (3 mL), and copper net of 100 meshes was placed on the absorbent paper. At the same time, a filter paper was cut and folded into a cone shape and filled with approximately 0.15 g CSBF, which had been immersed into deionized water for 2 h. Subsequently, the cone paper was placed on the copper net. In the end, the centrifugal tube was closed and the determination component of WRV was ready. After centrifugation, the weight of wet CSBF was

TABLE I: The WRV of various fibers modified by different reagents.

Code name	A	B	C	D	E	F	G
Fibers	CSB	CSBF	CSBF modified by MMA	CSBF modified by initiator + MMA	CSBF modified by epoxy propane	CSBF modified by copper ethanolamine	CSBF modified by silane coupling agent
WRV/%	127	322	175	148	126	125	122

determined as m_1 . Afterwards, the wet CSBF was dried in an air-circulating oven and its weight was determined as m_2 . The WRV is calculated by the formula below:

$$\text{WRV} = \frac{m_1 - m_2}{m_2} \times 100\%. \quad (1)$$

2.5. Fourier Transform Infrared (FT-IR) Spectroscopy. Fourier transform infrared (FT-IR) spectroscopy was carried out on an FT-IR spectrophotometer (EQUINOX55) using the KBr disk method. Before testing, the CSBF was dried at 105°C for 24 h and the testing samples were prepared with the mass ratio between CSBF and dried KBr of 1 : 300. Thirty-two scans were taken for each sample and data were recorded from the range 4000–400 cm^{-1} at a resolution of 4 cm^{-1} in the transmission mode.

3. Result and Discussion

3.1. Yield of CSBF Extraction. Consider

$$\text{Extraction yield} = \frac{m(\text{CSBF})}{m(\text{CSB})} \times 100\%. \quad (2)$$

The CSBF makes up 26 wt% of the mass of CSB [6]. In this work, the extraction yield of CSBF was 27.3%, implying the approximately complete removal of lignin, hemicellulose, pectin, and other impurities.

The CSB was cooked under high temperature and high pressure, and the alkali mass was set 11% in relation to that of CSB (the alkali aqueous solution was 3.1 g/L). After cooking, the alkali residue was 2.1% (aqueous solution concentration was 0.61 g/L). Alkali concentration dropped substantially. The reaction was more fully accomplished among alkali and lignin, hemicellulose, pectin, and so forth. Previous literature needed NaOH solution with concentration of about 30 g/L at normal temperature [21]. In this work, the similar result was obtained at high temperature with the concentration of NaOH solution of only 3.1 g/L. These results showed that the amount of NaOH dosage was greatly decreased, which reduced the amount of alkali waste emission and disposal.

3.2. Water Retention Value. One of the simple methods to study the hydrophilicity of the cellulose fiber surface is to measure the water retention value (WRV). Under the premise of same fiber fineness, WRV can reflect the fiber hydrophilic property; that is, the fiber with high value of WRV shows being more hydrophilic. The WRV of various fibers were shown in Table 1. The WRV of CSB was 127%. As for CSBF, its WRV dramatically increases to 322%.

In this work, the lignin and other weak hydrophilic substance in cotton stalk were almost removed by alkali cooking. The residue was cellulose, which displayed strong hydrophilicity.

When the CSBF was modified by five modifiers including MMA, the MMA plus initiator, epoxypropane, copper ethanolamine, and silane coupling agent, their WRV are 175%, 148%, 126%, 125%, and 122%, respectively. These values obviously decrease, compared with that of CSBF. The hydrophobicity of CSBF was greatly improved after being modified by those five kinds of reagents. The enhancement of hydrophobicity could be achieved by the addition of initiator to MMA (samples C and D), since the initiator could enhance the MMA grafting efficiency on the surface of CSBF. All the three latter modifiers in Table 1 including epoxypropane, copper ethanolamine, and silane coupling agent displayed good hydrophobicity effects. In the previous literature [12, 13, 19], the mechanisms by these three modifiers had been explained. We try to explain the interaction mechanisms between silanes and natural fibers [12]. First of all, the silane monomers are hydrolyzed in the presence of water. Then, during the hydrolysis process, the concomitant condensation of silanols (aging) also takes place. After that, the reactive silanol monomers or oligomers are physically adsorbed to hydroxyl groups of natural fibers. Finally, under heating conditions, the hydrogen bonds between the silanols and the hydroxyl groups of fibers could be converted into the covalent bonds and liberating water.

3.3. FT-IR Spectra. The FT-IR spectrum of CSB was shown in Figure 2(a). The band at 3424 cm^{-1} is O-H stretching vibration peak. The band at 2927 cm^{-1} is C-H peak. The band at 1739 cm^{-1} is the absorption of carbonyl stretching of ester or carboxyl groups in hemicelluloses. The band at 1633 cm^{-1} is the bending vibration peak of water. The band at 1515 cm^{-1} is the absorption of aromatic skeletal vibration in lignin. The band at 1250 cm^{-1} is the absorption of stretching vibrations of carbonyl groups in hemicelluloses. The band at 1047 cm^{-1} is a strong peak of C-O stretching vibration linked to hydroxyl. As for the FT-IR spectrum of CSBF (Figure 2(b)), most of the peaks are similar to those in Figure 2(a). However, the peaks at 1739 cm^{-1} , 1515 cm^{-1} , and 1250 cm^{-1} are weaker than those in Figure 2(a), indicating the removal of hemicellulose and lignin after the extraction process. The band intensity at 891 cm^{-1} is obviously increased, suggesting the increase of cellulose content. The band at 891 cm^{-1} was assigned to β -1,4 glycosidic bond characteristic absorption between the monosaccharides of cellulose [7, 8, 22].

TABLE 2: The factor-level design.

Levels	Factors			
	A stirring temperature (°C)	B stirring time (h)	C vacuum drying time (h)	D concentration of modifier
1	0	1.5	2	10%
2	20	1	1	5%
3	40	2	3	1%

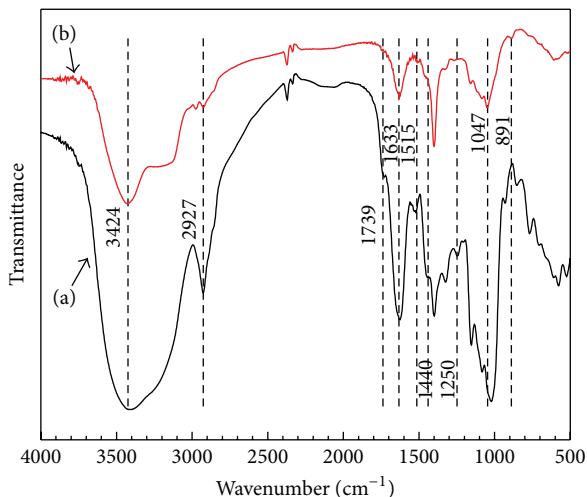


FIGURE 2: FT-IR spectra of (a) raw cotton stalk bark and (b) the extracted cotton stalk bark fiber.

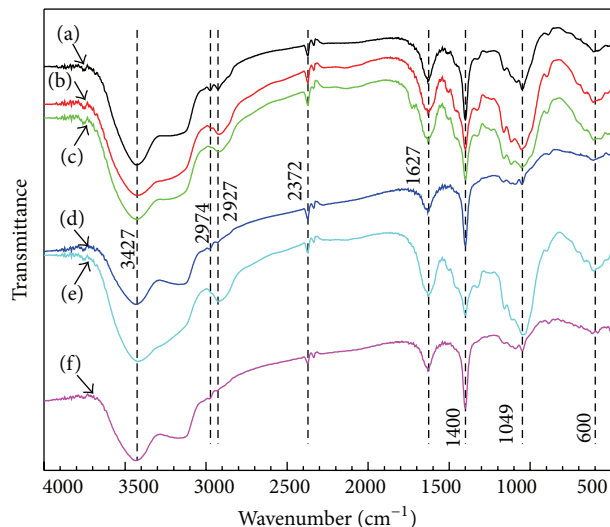


FIGURE 3: FT-IR spectra of CSBF and 5 kinds of modified fibers: (a) CSBF; (b) CSBF modified by MMA; (c) CSBF modified by initiator + MMA; (d) CSBF modified by epoxypropane; (e) CSBF modified by copper ethanolamine; (f) CSBF modified by silane coupling agent.

Figure 3 displayed the FT-IR spectra of raw and modified CSBF. The band at 3427 cm^{-1} is O-H stretching vibration peak. The bands at 2974 cm^{-1} and 2927 cm^{-1} are C-H peaks. The band at 2372 cm^{-1} is the triple bond or cumulative double bond stretching vibration peak. The band at 1627 cm^{-1} is

TABLE 3: The results of optimization experiment.

Test number	Factors				Result WRV
	A	B	C	D	
1	1	1	1	1	113%
2	1	2	2	2	90%
3	1	3	3	3	108%
4	2	1	2	3	108%
5	2	2	3	1	102%
6	2	3	1	2	101%
7	3	1	3	2	103%
8	3	2	1	3	99%
9	3	3	2	1	109%

the bending vibration peak of water. The band at 1400 cm^{-1} is a strong peak. The band at 1049 cm^{-1} is a strong peak of C-O stretching vibration linked to hydroxyl. The band at 600 cm^{-1} is the fingerprint absorption of hexatomic ring in carbohydrate. It is found that there is little difference among these FT-IR spectra, which is the consequence of the little changing of functional groups induced by surface modification [23].

3.4. Optimization of Experiment Condition. After a theoretical analysis, one can determine that all the stirring temperature, stirring time, vacuum drying time, and the concentration of modifier had an important effect on the modification of CSBF. Therefore, the influences of these four factors were marked as A, B, C, and D, and every factor was investigated in three levels marked as levels 1, 2, and 3, as shown in Table 2. For example, the stirring temperature was set as 0, 20, and 40°C for different tests, and these three levels were marked as levels 1, 2, and 3, respectively.

The experiment result and analysis are shown in Tables 3 and 4, respectively. The influence order of the four factors was followed as $B > C > D > A$. Because the influences of both A and C factors were extremely small, they could be negligible factors and the levels of these two factors were determined as follows: stirring temperature was room temperature and vacuum drying time was 1 h. The optimal levels of B and D factors were both level 2; that is, the mixing time was 1 h, and modifier concentration was 5%. At last, the optimum conditions were determined as A2, B2, C2, and D2. Under the optimal experiment conditions, the WRV of the modified CSBF was 89%. This result verified that the above combination is the optimal conditions: the stirring temperature was 20°C , stirring time was 1 h, vacuum drying time was 1 h, and modifier concentration was 5%.

TABLE 4: The analysis of optimization experiment.

K value	Factors			
	A	B	C	D
K1	311%	324%	312%	324%
K2	311%	291%	307%	295%
K3	311%	318%	313%	314%
k1	104%	108%	104%	108%
k2	104%	97%	103%	98%
k3	104%	106%	104%	105%
Spannweite	0	11.1%	1.9%	9.8%
Optimum	A2	B2	C2	D2

4. Conclusions

In summary, CSBF was extracted under the low concentration of alkali by an environmentally-friendly extraction method using high temperature and high pressure reaction kettle. Five modifiers including MMA, the MMA plus initiator, epoxypropane, copper ethanalamine, and silane coupling agent were used to modify CSBF. It was found that all the five modifiers could raise the hydrophobic property of CSBF. The as-modified CSBF by silane coupling agent displayed excellent hydrophobic property among five kinds of modifiers. The optimal condition of silane coupling agent on CSBF was studied in detail. It was found that the WRV of as-modified CSBF was 89% at 20°C with stirring time of 1 h and vacuum drying time of 1 h using modifier concentration of 5%. It is believed that these modified CSBF may be a potential application in WPC fields.

Competing Interests

The authors declare that they have no competing interests.

Acknowledgments

The authors are indebted to the Xinjiang Agriculture University for financial support by Projects of the Prophase-Sustentation Foundation (Grant no. XJAU201414).

References

- [1] Z. Fei, S. Huang, J. Yin, F. Xu, and Y. Zhang, "Preparation and characterization of bio-based degradable plastic films composed of cellulose acetate and starch acetate," *Journal of Polymers & the Environment*, vol. 23, no. 3, pp. 383–391, 2015.
- [2] F. Razza, F. D. Innocenti, A. Dobon, C. Aliaga, C. Sanchez, and M. Hortal, "Environmental profile of a bio-based and biodegradable foamed packaging prototype in comparison with the current benchmark," *Journal of Cleaner Production*, vol. 102, pp. 493–500, 2015.
- [3] O. Faruk, A. K. Bledzki, H.-P. Fink, and M. Sain, "Biocomposites reinforced with natural fibers: 2000–2010," *Progress in Polymer Science*, vol. 37, no. 11, pp. 1552–1596, 2012.
- [4] R. C. Akdeniz, M. Acaroglu, and A. Hepbasli, "Cotton stalk as a potential energy source," *Energy Sources*, vol. 26, no. 1, pp. 65–75, 2004.
- [5] N. Reddy and Y. Yang, "Properties and potential applications of natural cellulose fibers from the bark of cotton stalks," *Bioresource Technology*, vol. 100, no. 14, pp. 3563–3569, 2009.
- [6] L. Li, J. Sun, and G. Jia, "Properties of natural cotton stalk bark fiber under alkali treating," *Journal of Applied Polymer Science*, vol. 125, no. 2, pp. E534–E539, 2012.
- [7] L. Zhou, J.-Z. Shao, X.-X. Feng, and J.-Y. Chen, "Effect of high-temperature degumming on the constituents and structure of cotton stalk bark fibers," *Journal of Applied Polymer Science*, vol. 125, no. 2, pp. E573–E579, 2012.
- [8] Z. Dong, X. L. Hou, F. F. Sun, L. Zhang, and Y. Q. Yang, "Textile grade long natural cellulose fibers from bark of cotton stalks using steam explosion as a pretreatment," *Cellulose*, vol. 21, pp. 3851–3860, 2014.
- [9] A. K. Bledzki and J. Gassan, "Composites reinforced with cellulose based fibres," *Progress in Polymer Science*, vol. 24, no. 2, pp. 221–274, 1999.
- [10] F. M. V. Oliveira, I. O. Pinheiro, A. M. Souto-Maior, C. Martin, A. R. Gonçalves, and G. J. M. Rocha, "Industrial-scale steam explosion pretreatment of sugarcane straw for enzymatic hydrolysis of cellulose for production of second generation ethanol and value-added products," *Bioresource Technology*, vol. 130, pp. 168–173, 2013.
- [11] X. Hou, F. Sun, L. Zhang, J. Luo, D. Lu, and Y. Yang, "Chemical-free extraction of cotton stalk bark fibers by steam flash explosion," *BioResources*, vol. 9, no. 4, pp. 6950–6967, 2014.
- [12] Y. Xie, C. A. S. Hill, Z. Xiao, H. Militz, and C. Mai, "Silane coupling agents used for natural fiber/polymer composites: a review," *Composites Part A: Applied Science & Manufacturing*, vol. 41, no. 7, pp. 806–819, 2010.
- [13] H. Jiang and D. P. Kamdem, "Characterization of the surface and the interphase of PVC-copper amine-treated wood composites," *Applied Surface Science*, vol. 256, no. 14, pp. 4559–4563, 2010.
- [14] A. K. Bledzki, A. A. Mamun, M. Lucka-Gabor, and V. S. Gutowski, "The effects of acetylation on properties of flax fibre and its polypropylene composites," *Express Polymer Letters*, vol. 2, no. 6, pp. 413–422, 2008.
- [15] K. Suzuki, A. Sato, H. Okumura, T. Hashimoto, A. N. Nakagaito, and H. Yano, "Novel high-strength, micro fibrillated cellulose-reinforced polypropylene composites using a cationic polymer as compatibilizer," *Cellulose*, vol. 21, no. 1, pp. 507–518, 2014.
- [16] A. K. Bledzki, A. A. Mamun, A. Jaszkievicz, and K. Erdmann, "Polypropylene composites with enzyme modified abaca fibre," *Composites Science and Technology*, vol. 70, no. 5, pp. 854–860, 2010.
- [17] J.-M. Park, P.-G. Kim, J.-H. Jang, Z. Wang, B.-S. Hwang, and K. L. DeVries, "Interfacial evaluation and durability of modified Jute fibers/polypropylene (PP) composites using micromechanical test and acoustic emission," *Composites Part B: Engineering*, vol. 39, no. 6, pp. 1042–1061, 2008.
- [18] M. S. Islam, S. Hamdan, M. B. Ahmad et al., "Effect of PVA-co-MMA copolymer on the physical, mechanical, and thermal properties of tropical wood materials," *Advances in Materials Science and Engineering*, vol. 2014, Article ID 626850, 8 pages, 2014.
- [19] K. K. Pandey and T. Vuorinen, "Study of kinetics of reaction of lignin model compounds with propylene oxide," *Holzforchung*, vol. 62, no. 2, pp. 169–175, 2008.
- [20] R. G. Raj, B. V. Kokta, F. Demele, and B. Sanschagrain, "Compounding of cellulose fibers with polypropylene: effect of fiber treatment on dispersion in the polymer matrix," *Journal of Applied Polymer Science*, vol. 38, no. 11, pp. 1987–1996, 1989.

- [21] L. Li and L. H. Zhao, "Preparation of natural cellulose fibers from cotton stalk and their structure and morphology," *Journal of Textile Research*, vol. 34, no. 2, pp. 13–17, 2013.
- [22] A. Kaushik, M. Singh, and G. Verma, "Green nanocomposites based on thermoplastic starch and steam exploded cellulose nanofibrils from wheat straw," *Carbohydrate Polymers*, vol. 82, no. 2, pp. 337–345, 2010.
- [23] M. Abdelmouleh, S. Boufi, A. B. Salah, M. N. Belgacem, and A. Gandini, "Interaction of silane coupling agents with cellulose," *Langmuir*, vol. 18, no. 8, pp. 3203–3208, 2002.

Research Article

Synthesis and Characterization of Uniform Spherical Nanoporous TiO₂ Aerogel Templated by Cellulose Alcohol-Gel with Enhanced Photocatalytic Activity

Zhiming Liu,¹ Peng Wu,¹ Shaoli Yang,¹ Haiying Wang,¹ and Chunde Jin²

¹Northeast Forestry University, Harbin 150040, China

²Zhejiang Agriculture and Forestry University, Hangzhou 311300, China

Correspondence should be addressed to Zhiming Liu; zhimingliuwhy@126.com

Received 3 March 2016; Accepted 26 April 2016

Academic Editor: Zhouyang Xiang

Copyright © 2016 Zhiming Liu et al. This is an open access article distributed under the Creative Commons Attribution License, which permits unrestricted use, distribution, and reproduction in any medium, provided the original work is properly cited.

The spherical nanoporous TiO₂ aerogels were prepared by a simple ethanol-thermal method, using spherical cellulose alcohol-gel as the template. The morphology, crystalline structure, pore size, specific surface area, and the photocatalytic activity of obtained TiO₂ aerogel were separately characterized by scanning electron microscopy (SEM), transmission electron microscopy (TEM), X-ray diffraction (XRD), X-ray photoelectron spectroscopy (XPS), N₂ adsorption-desorption isotherms, and double beam UV-VIS spectrophotometer. The characteristics of TiO₂ aerogels presented uniform sphere shape, good internal structural morphology, high specific surface area (ranging from 111.88 to 149.95 m²/g), and good crystalline anatase phase. Moreover, methyl orange dye was used as the target pollutant to characterize the photocatalytic activities and the adsorption performance. The photocatalytic experiment shows that the obtained spherical TiO₂ aerogels had a higher degradation ratio of 92.9% on methyl orange dye compared with aspherical TiO₂ aerogels prepared from other concentrations of tetrabutyl orthotitanate (TBOT).

1. Introduction

In the early 1990s, the ordered mesoporous silica was found for the first time [1, 2]. Since then, mesoporous materials have become one of the most important materials for catalysis [3–5]. With the fascinating properties of high specific surface areas, tunable large pore sizes, large pore volumes, controllable framework compositions, and alternative pore shapes, mesoporous materials can also be used in drug delivery, separation, sorption, fuel cells, gas separators, and magnetism areas [6–8]. Recently, researchers have paid much more attention to the mesoporous materials, such as TiO₂, ZnO, and SnO₂, which have the photocatalytic oxidation abilities to degrade the organic pollutants in water and air [9–11].

Among various oxide semiconductor photocatalysts, TiO₂ has successfully attracted a great deal of interest and also has been the most promising photocatalyst due to its strong oxidizing potential, the low cost, high chemical stability against photocorrosion, and excellent degradation for organic pollutants [12, 13]. However, practical applications

of titanium dioxide are still quite limited, mainly because of its low quantum efficiency and the broad bandgap which responds only to UV light [14]. In addition to the VB position, the pore configuration and particle size distribution of photocatalyst also influence the activity of a photocatalyst. In order to obtain nanoporous structure and high dispersibility of TiO₂, there are three approaches: the template synthesis [15–19], the anodic oxidation [20–22], and the hydrothermal synthesis [23–25]. Among those, the template-based synthesis route takes the advantage of straightforward controlling over the morphology of the resulting TiO₂ nanoporous structured materials and maintaining TiO₂ good disperse stability on the surface of the template [19]. Recently, cellulose fiber has been used as a template to synthesize nanoporous structured materials, such as TiO₂, CdS, and Fe₂O₃. Furthermore, cellulose alcohol-gel or hydrogel not only takes over cellulose fiber's excellent characteristics, including high tensile strength, high water holding capacity, high crystallinity, and good biocompatibility but also generates the dimensional and porous structure and the uniform nanopore size [26].

The unique structure of cellulose aerogel bestows it on unusual properties. Herein we reported our research work in the preparation of spherical nanoporous TiO₂ aerogel using spherical cellulose aerogel as the host matrix, employing tetrabutyl orthotitanate (TBOT), urea, and dehydrated alcohol as the starting materials. The resulting TiO₂ spheres were characterized by transmission electron microscopy (TEM), X-ray diffraction (XRD), and the nitrogen gas adsorption (Micromeritics, ASAP 2020 analyzer) techniques. The influence of the concentration of TBOT on the morphologies and size of TiO₂ nanoparticles was investigated. Meanwhile, the excellent photocatalytic activity for the degradation of methyl orange dye (MO) in aqueous solution was also demonstrated under UV irradiation at room temperature. We hope to provide a novel method for easily creating nanoporous TiO₂ aerogel. Our findings may provide a new and “green” pathway for the design and fabrication of photocatalytic materials to solve the problem of organic pollution.

2. Materials and Methods

2.1. Materials. The commercial natural bamboo fiber, which was manufactured by slicing, steaming, cooking, and enzymatic process, was used as raw materials for preparation of spherical cellulose alcohol-gels. The fiber with 1.5 D (denier) and 38 mm length was purchased from Mingtong Bamboo Charcoal Products Co., Ltd., China. All other chemicals were of analytical grade and used without further purification.

2.2. Preparation of Spherical Cellulose Alcohol-Gels. The spherical cellulose alcohol-gels were synthesized using the hand-dropping procedure as follows. A solution with NaOH/urea/H₂O of 7:12:81 (mass ratio) was cooled to -12°C as solvent system. 2.0 g natural bamboo cellulose fiber was dispersed into 100 g solvent system under vigorous stirring to obtain the transparent cellulose solution. Then, the cellulose solutions were added drop by drop to the well-mixed regenerate solution with a certain proportion of trichloropropane, ethyl acetate, and acetic and solidified at room temperature for 10 min before rinsing under running deionized water for 12 h. Finally, the spherical cellulose alcohol-gels were obtained after adequate exchanging for several times with ethanol.

2.3. Preparation of Spherical TiO₂ Aerogels. The spherical TiO₂ aerogels were prepared by an ethanol-thermal method. Firstly, 0.1 g of urea was added to a 100 mL beaker with 40 mL of anhydrous ethanol under magnetic stirring. Meanwhile, 0.1 mL of TBOT was put into the mixed solution. When TBOT mixed the urea and anhydrous ethanol, 1.0 g of spherical cellulose alcohol-gels was added into the solution. After placing it for 2 h to form sol-gel at room temperature, the final reactant was transferred into a 50 mL Teflon-lined stainless steel autoclave through heat treatment at 120°C for 10 h. Then the products were separately washed with deionized water, ethanol, and t-butyl alcohol three times every day for two days and freeze-dried overnight at 30–40 Pa of vacuum. Finally, the TiO₂ with spherical cellulose

aerogel template was calcined in oxygen atmosphere at 500°C for 3 h (heating rate: 1°C/min). Similarly, various nanoporous TiO₂ aerogels prepared from 0.5 mL and 5 mL of TBOT were also synthesized for comparison while the other experimental conditions were not changed.

2.4. Characterization of Spherical TiO₂ Aerogels. The morphology of spherical TiO₂ aerogels was observed on the scanning electron microscopy (SEM; Quanta 200, FEI, Hillsboro, OR, USA) and the transmission electron microscopy (TEM; JEOL 2011, FEI Holland). X-ray diffraction (XRD) patterns of spherical TiO₂ aerogels were measured by a Rigaku D/Max-rB diffractometer (Tokyo, Japan) with Cu-K α radiation (45 kV, 40 mA, $\lambda = 1.54178 \text{ \AA}$) ranging from 4° to 90° (2θ angle). The pore size and the BET specific surface areas of the samples were calculated using N₂ adsorption-desorption isotherms measured at -196°C with an ASAP 2020 instrument (Micromeritics, American). The elemental compositions and states were tested by X-ray photoelectron spectroscopy (XPS, Chanhassen, MN, USA) with Al-K α radiation ($h\nu = 1486.6 \text{ eV}$).

2.5. Photocatalytic Experiment. The photocatalytic activities of the spherical nanoporous TiO₂ aerogel were investigated in terms of the photocatalytic degradation of 10 mg/L methyl orange dye (MO) solution under illumination of UV light at 254 nm. Before the illumination, 50 mg of the spherical TiO₂ aerogels was first added to photocatalytic device filled with 150 mL of 10 mg/L MO, and the mixture was stirred for 30 min to reach a saturated state. Simultaneously, the adsorption/desorption of MO and O₂ molecules on the spherical TiO₂ aerogels surface reached an equilibrium in the darkness. Then the stirring solution was illuminated by the vertically incident UV light. During the photocatalytic reaction, samples were carried from the supernatant solution at every 15 min and were immediately centrifuged at 2000 r/min for 5 min. The concentration of MO after catalyzing was measured by a TU-1901 UV-visible spectrometer at 460 nm.

3. Results and Discussion

3.1. Morphology Analysis. Figure 1 shows the photographs of TiO₂ aerogel prepared from different concentrations of TBOT. With the increasing concentration of TBOT, TiO₂ aerogel was shifted to spherical structure, and these TiO₂ aerogels had the uniform shapes showed in Figure 1(c). For the morphology of TiO₂ aerogel, the cellulose alcohol-gel played a role of template and morphology guiding in the preparation of nanoporous TiO₂ aerogel.

To observe the internal structure of the TiO₂ aerogel, these TiO₂ aerogels were broken into two parts, and the surface of the fracture surface could be imaged by scanning electron microscopy (SEM). Figures 2(a)–2(c), respectively, represented morphology of TiO₂ aerogel prepared from different concentrations of TBOT. The formation of the network structure of TiO₂ aerogel could be attributed to the accumulation of the TiO₂ nanoparticles. When the concentration of TBOT was increasing, the network structure

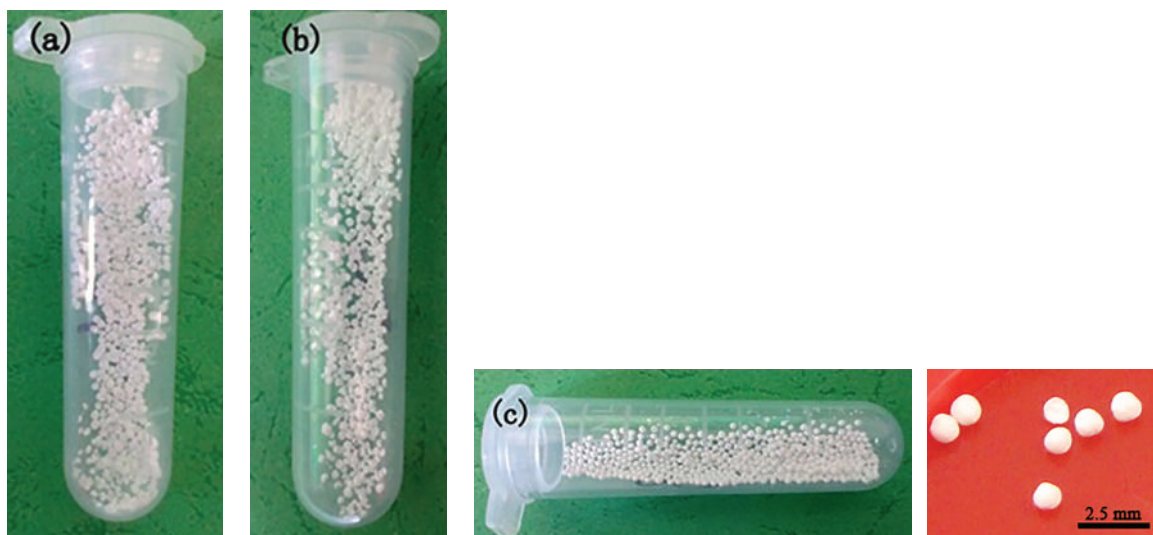


FIGURE 1: Photographs of TiO_2 aerogel: (a) aspherical TiO_2 aerogel-0.1 mL of TBOT, (b) aspherical TiO_2 aerogel-0.5 mL of TBOT, and (c) spherical TiO_2 aerogel-5.0 mL of TBOT.

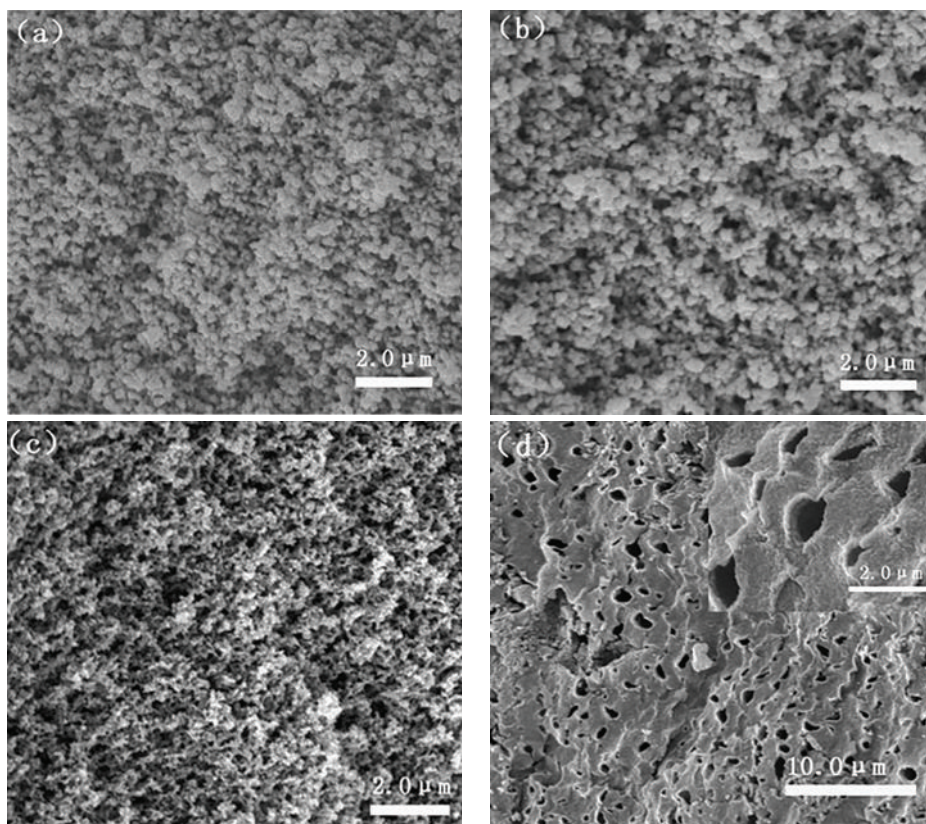


FIGURE 2: SEM images of TiO_2 aerogel: (a) internal structure of aspherical TiO_2 aerogel-0.1 mL of TBOT, (b) internal structure of aspherical TiO_2 aerogel-0.5 mL of TBOT, (c) internal structure of spherical TiO_2 aerogel-5.0 mL of TBOT, and (d) external surface structure of spherical TiO_2 aerogel.

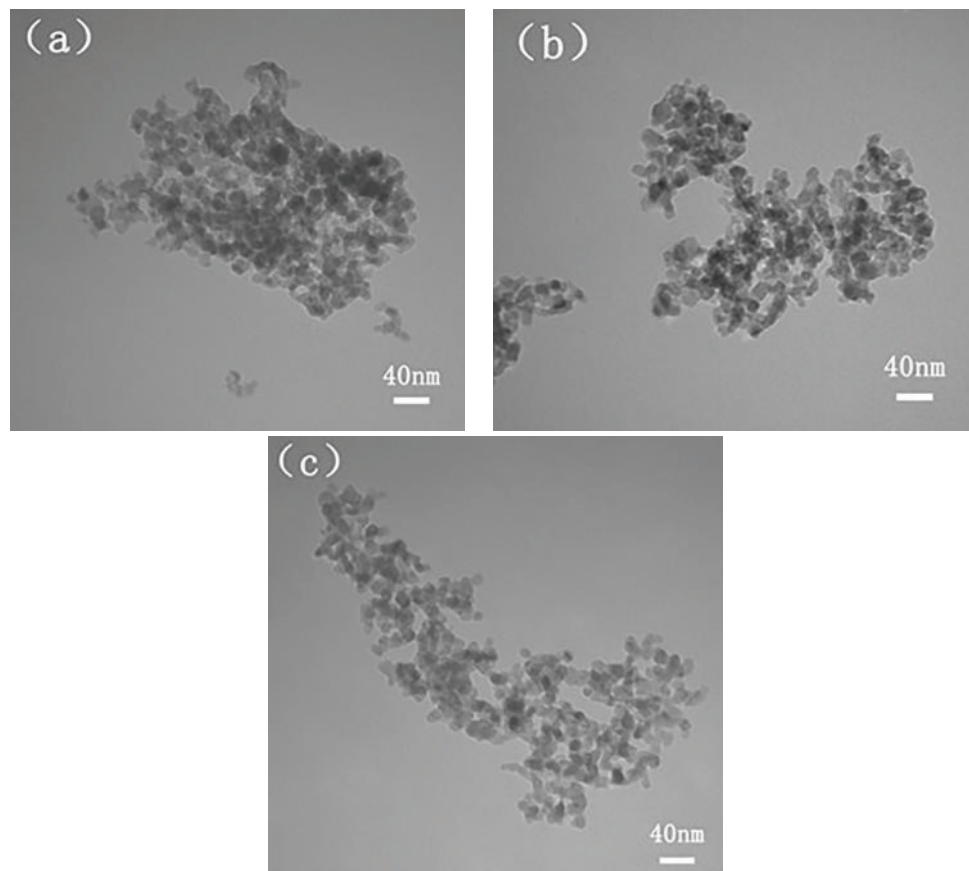
of TiO_2 aerogel was more obvious. Moreover, the external surface of spherical TiO_2 aerogel was filled with pores shown in Figure 2(d). These pores mainly inherited the porosity of spherical cellulose aerogels matrix while the spherical TiO_2 -cellulose complex aerogel was calcined. Detailed information

concerning the pore size and the specific surface area was analyzed in pore structure.

The TEM images of these TiO_2 aerogels were shown in Figure 3. The shape of TiO_2 particle prepared from 0.1 mL of TBOT was irregular and the agglomeration could be clearly

TABLE 1: Specific surface area and pore structure parameters of TiO₂ aerogel prepared from different concentrations of TBOT.

Samples	S_{BET} (m ² /g)	Mesoporous volume (cm ³ /g)	Average pore diameter (nm)
TiO ₂ -0.1 mL of TBOT	129.32	0.52	16.20
TiO ₂ -0.5 mL of TBOT	111.88	0.42	15.04
TiO ₂ -5.0 mL of TBOT	149.95	0.49	12.96

FIGURE 3: TEM images of TiO₂ aerogel: (a) aspherical TiO₂ aerogel-0.1 mL of TBOT, (b) aspherical TiO₂ aerogel-0.5 mL of TBOT, and (c) spherical TiO₂ aerogel-5.0 mL of TBOT.

observed in Figure 3(a). But when the concentration of TBOT was added to 0.5 mL of TBOT, the TiO₂ particle's shape was almost in conformity and had minor agglomeration shown in Figure 3(b). The shape of TiO₂ particle was uniform sphere and scarcely had agglomeration until the concentration of TBOT was up to 5.0 mL, which was shown in Figure 3(c). Furthermore, the diameter of TiO₂ particle was about 15–20 nm, implying that the single TiO₂ particle that consisted of TiO₂ aerogel was nanoparticle.

3.2. Pore Structure. Figure 4 shows nitrogen adsorption-desorption curves (inset) and corresponding pore-size distribution of TiO₂ aerogel prepared from different concentrations of TBOT. The isotherms were measured to be Type IV, according to the IUPAC classification. The hysteresis loops were obviously observed at $P/P_0 = 0.8-1.0$, and the shapes of these hysteresis loops conformed to H3 hysteresis loops, indicating that obtained TiO₂ aerogels were mesoporous

materials [27–30]. The pore-size distribution results show that every sample had a bimodal distribution (2-3 nm and 10–100 nm), and the peak pore was around 2.3 nm and 34 nm. The different diameters of the pores may result from the different stacking styles of the TiO₂ particles, which were confirmed by SEM.

Detailed information in terms of the specific surface areas and the porosities of the TiO₂ aerogels was summarized in Table 1. With the increasing concentration of TBOT, the shape of the TiO₂ aerogel was shifted to sphere, leading to an increase in the specific surface areas and a drop in the pore size. When the consumption of TBOT was 5.0 mL, the specific surface area of obtained TiO₂ aerogel can reach 149.95 m²/g, and the corresponding pore size was 12.96 nm. In addition, the increased specific area of spherical TiO₂ aerogel compared with the aspheric TiO₂ aerogels mainly came from these mesoporous areas, which agreed with the pore volume and pore-size distributions.

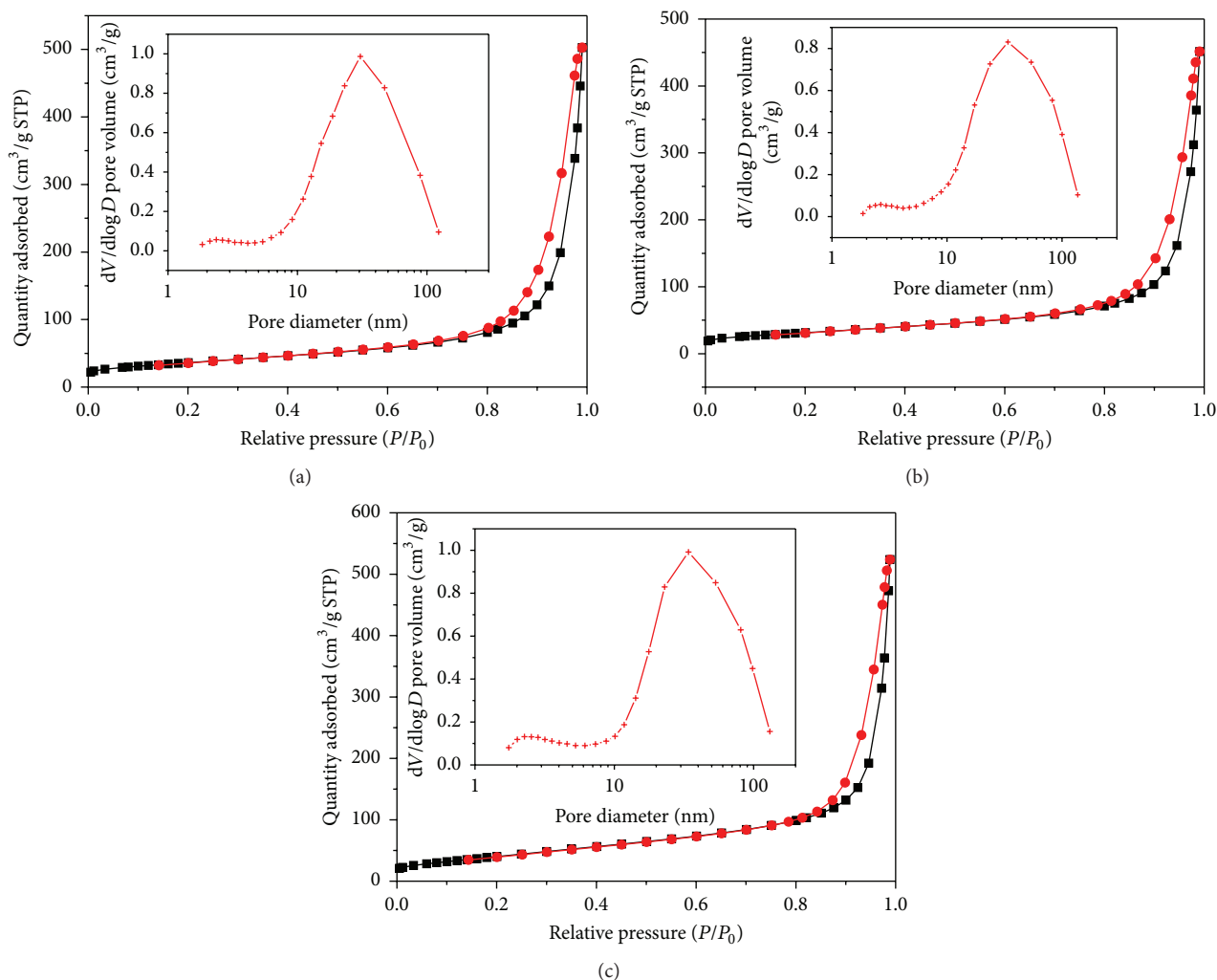


FIGURE 4: N₂ adsorption-desorption isotherm curves and corresponding pore-size distribution of (a) aspherical TiO₂ aerogel-0.1 mL of TBOT, (b) aspherical TiO₂ aerogel-0.5 mL of TBOT, and (c) spherical TiO₂ aerogel-5.0 mL of TBOT.

3.3. XRD and XPS Results. The X-ray diffraction (XRD) patterns of TiO₂ aerogel are shown in Figure 5. With the increasing concentration of TBOT, the (101) peak position of TiO₂ aerogel shifted to the higher-angle region shown in Figure 5(a). And the obvious characteristic diffraction peaks of TiO₂ aerogel could be seen in Figure 5(b), which was attributed to anatase TiO₂ crystals [31]. No peaks from other impurities were detected in this XRD pattern. Furthermore, the strong and sharp diffraction peaks shown in Figure 5 indicated that the obtained spherical TiO₂ aerogel had high crystallinity [32].

The chemical compositions and elemental environments of the catalysts were tested by X-ray photoelectron spectroscopy (XPS); the specific spectra are shown in Figure 6. Three elements, Ti, O, and C, were revealed in Figure 6(a). Among them, the existence of C elements may result from trace organic pollutants in the vacuum measurement of XPS instrument. High-resolution spectra of Ti 2p and O 1s region were separately shown in Figures 6(b) and 6(c). The obvious peaks, where binding energies were 458.59 eV

and 464.34 eV, were the characteristic peaks of Ti 2p_{1/2} and Ti 2p_{3/2}. Furthermore, the binding energy of Ti 2p_{1/2} was 5.75 eV lower than that of Ti 2p_{3/2}, which was the important criterion of existence of Ti⁴⁺ [33, 34]. Figure 6(c) shows the XPS spectra of O 1s with a broad and asymmetrical peak, suggesting that the oxygen species on the surface of spherical TiO₂ aerogel was not a single species. The O 1s region could be fitted with three peaks, whose binding energies were 529.78, 531.11, and 531.98 eV. These peaks were in accordance with the binding energy data of lattice oxygen, hydroxyl, and physically adsorbed oxygen [35]. O 1s mainly existed as lattice oxygen in Ti-O-Ti bonds observed from the areas of the peaks. This reveals that the obtained spherical TiO₂ aerogel consisted of titania and some Ti-OH generated in the reaction process [35].

3.4. Photocatalytic Activity. The photocatalytic activities of the spherical nanoporous TiO₂ aerogel were investigated in terms of the photocatalytic degradation of 10 mg/L MO

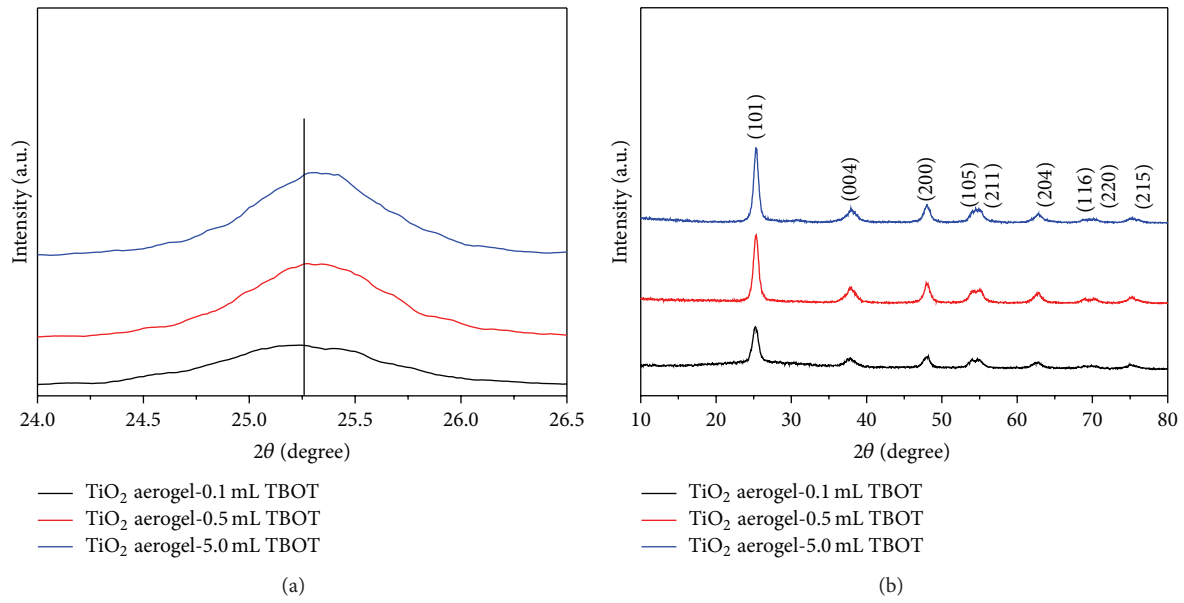


FIGURE 5: XRD patterns of Ti diffraction peak at $2\theta = 25.26^\circ$ (a) and TiO₂ aerogels calcinated at 500°C for 3 h.

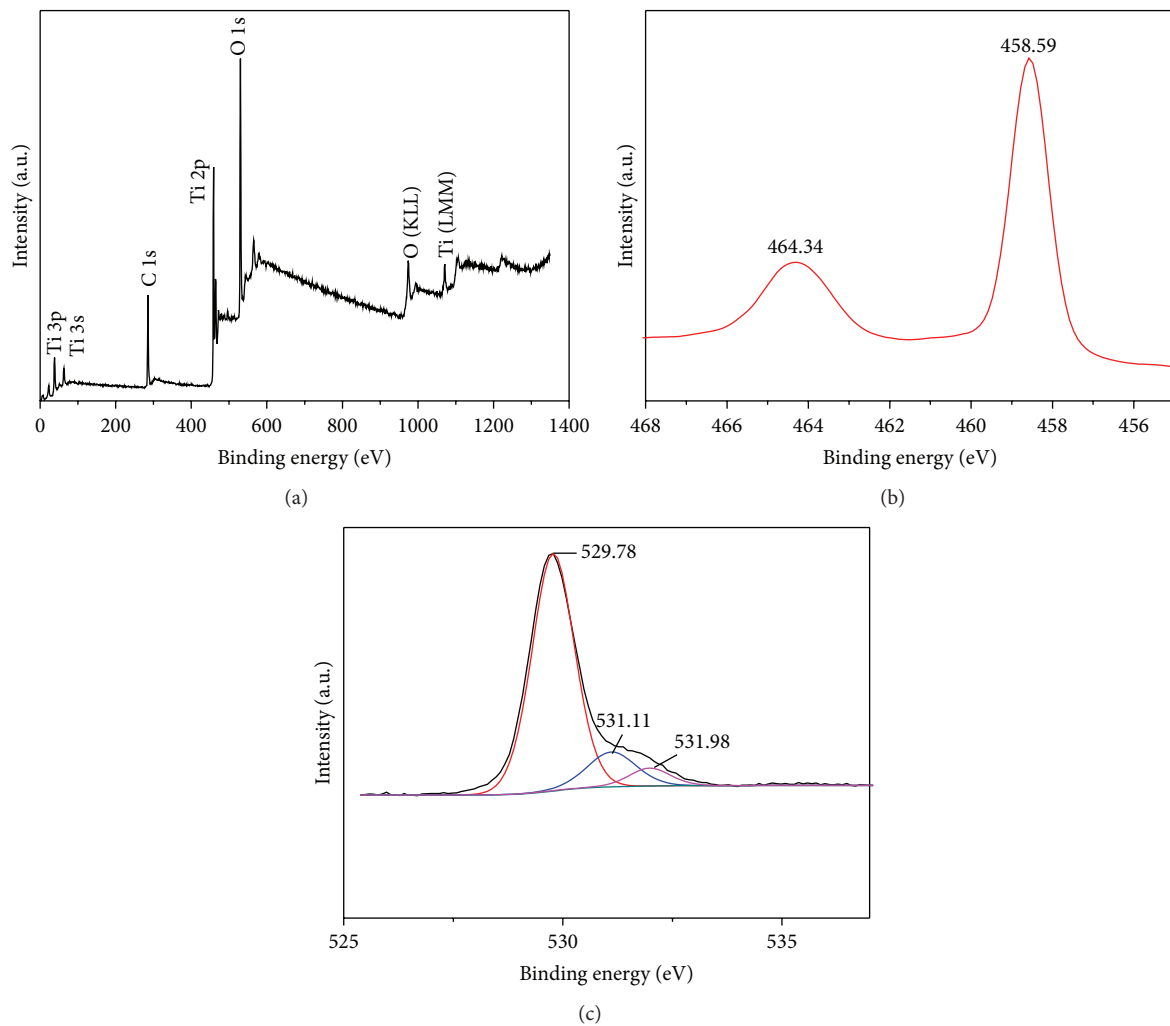


FIGURE 6: XPS spectra of TiO₂ aerogel (a) total spectrum; high-resolution spectrum of the (b) Ti 2p and (c) O 1s region.

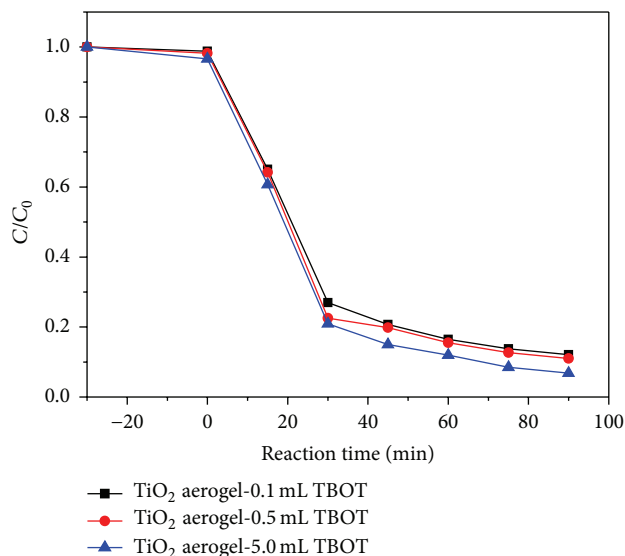


FIGURE 7: The degradation curves of MO in the presence of the TiO₂ aerogels prepared from 0.1 mL of TBOT, 0.5 mL of TBOT, and 0.5 mL of TBOT.

under illumination of UV light within 90 min (Figure 7). As a control, the activities of aspherical TiO₂ aerogels were also examined under the same conditions. Results of the photocatalytic investigation are shown in Figure 7. Obviously, the photocatalytic activity of spherical TiO₂ aerogel prepared from 5.0 mL of TBOT was higher than the aspherical TiO₂ aerogels prepared from 0.1 mL of TBOT and 0.5 mL of TBOT. In the process of adsorption equilibrium, the first reaction time of 30 min, the removal rate of MO with the spherical TiO₂ aerogels was higher than that of aspherical TiO₂ aerogels. This phenomenon may result from the fact that spherical TiO₂ aerogels had the higher specific surface area than aspherical TiO₂ aerogels. Moreover, with the increase in degradation time, the concentration of MO decreased rapidly, and, after 90 min of irradiation, the decomposition ratio of MO over the spherical TiO₂ aerogels prepared from 5.0 mL of TBOT was about 92.9%, while those of aspherical TiO₂ aerogels prepared from 0.1 mL and 0.5 mL of TBOT were 87.8% and 88.8%. Therefore, both the spherical TiO₂ aerogels and the aspherical TiO₂ aerogels had excellent photocatalytic activity of MO, which can be attributed to special anatase phase, specific surface areas, and unique structure [7].

4. Conclusions

Spherical TiO₂ aerogels were prepared by a simple ethanol-thermal method, using spherical cellulose aerogel as the template and TBOT as raw material. The obtained TiO₂ aerogels consisted of TiO₂ nanoparticles with the diameter 15–20 nm. The high specific surface area, ranging from 111.88 m²/g to 149.95 m²/g, and good porosity of the network structures provided a large number of active sites for photocatalysis. The highest UV light activity, giving methyl orange degradation of 92.9%, was achieved by spherical TiO₂ aerogel prepared from 5.0 mL of TBOT under the calcination condition of 500 °C for 3 h.

Competing Interests

The authors declare that there are no competing interests regarding the publication of this paper.

Acknowledgments

This research was financially supported by the Industry Research Special Funds for Public Welfare Project under Grant no. 201504602, the Key Laboratory of Wood Science and Technology, Zhejiang Province, under Grant no. 2014lygcz002, and the Fundamental Research Funds for the Central Universities under Grant no. 2572014EB01-02. Special thanks are due to Professor Shujun Li for her equipment and analysis.

References

- [1] A. A. Ismail and D. W. Bahnemann, "Mesoporous titania photocatalysts: preparation, characterization and reaction mechanisms," *Journal of Materials Chemistry*, vol. 21, no. 32, pp. 11686–11707, 2011.
- [2] R. Y. Zhang, A. A. Elzatahry, S. S. Al-Deyab, and D. Zhao, "Mesoporous titania: from synthesis to application," *Nano Today*, vol. 7, no. 4, pp. 344–346, 2012.
- [3] J. L. Vivero-Escoto, Y.-D. Chiang, K. C.-W. Wu, and Y. Yamauchi, "Recent progress in mesoporous titania materials: adjusting morphology for innovative applications," *Science and Technology of Advanced Materials*, vol. 13, no. 1, Article ID 013003, 2012.
- [4] L. P. Kumaresan, A. Prabhu, M. Palanichamy, E. Arumugam, and V. Murugesan, "Synthesis and characterization of Zr⁴⁺, La³⁺ and Ce³⁺ doped mesoporous TiO₂: evaluation of their photocatalytic activity," *Journal of Hazardous Materials*, vol. 186, no. 2-3, pp. 1183–1192, 2011.
- [5] L. Kumaresan, A. Prabhu, M. Palanichamy, and V. Murugesan, "Synthesis of mesoporous TiO₂ in aqueous alcoholic medium and evaluation of its photocatalytic activity," *Materials Chemistry and Physics*, vol. 126, no. 1-2, pp. 445–452, 2011.
- [6] P. Wang, J. Wang, X. F. Wang et al., "One-step synthesis of easy-recycling TiO₂-rGO nanocomposite photocatalysts with enhanced photocatalytic activity," *Applied Catalysis B: Environmental*, vol. 132-133, pp. 452–459, 2013.
- [7] J. F. Ye, W. Liu, J. G. Cai et al., "Nanoporous anatase TiO₂ mesocrystals: additive-free synthesis, remarkable crystalline-phase stability, and improved lithium insertion behavior," *Journal of the American Chemical Society*, vol. 133, no. 4, pp. 933–940, 2011.
- [8] J. G. Yu, W. Liu, and H. G. Yu, "A one-pot approach to hierarchically nanoporous titania hollow microspheres with high photocatalytic activity," *Crystal Growth and Design*, vol. 8, no. 3, pp. 930–934, 2008.
- [9] Y. Liu, H. B. Jin, S. M. Zhu et al., "A facile method for fabricating TiO₂ @ mesoporous carbon and three-layered nanocomposites," *Nanotechnology*, vol. 23, no. 32, Article ID 325602, 2012.
- [10] B. Cheng, Y. Le, and J. Yu, "Preparation and enhanced photocatalytic activity of Ag@TiO₂ core-shell nanocomposite nanowires," *Journal of Hazardous Materials*, vol. 177, no. 1-3, pp. 971–977, 2010.
- [11] E. J. W. Crossland, N. Noel, V. Sivaram, T. Leijtens, J. A. Alexander-Webber, and H. J. Snaith, "Mesoporous TiO₂ single

- crystals delivering enhanced mobility and optoelectronic device performance,” *Nature*, vol. 495, no. 7440, pp. 215–219, 2013.
- [12] A. L. Linsebigler, G. Q. Lu, and J. T. Yates Jr., “Photocatalysis on TiO₂ surfaces: principles, mechanisms, and selected results,” *Chemical Reviews*, vol. 95, no. 3, pp. 735–758, 1995.
- [13] R. Asahi, T. Morikawa, T. Ohwaki, K. Aoki, and Y. Taga, “Visible-light photocatalysis in nitrogen-doped titanium oxides,” *Science*, vol. 293, no. 5528, pp. 269–271, 2001.
- [14] Z. Yanqing, S. Erwei, C. Zhizhan, L. Wenjun, and H. Xingfang, “Influence of solution concentration on the hydrothermal preparation of titania crystallites,” *Journal of Materials Chemistry*, vol. 11, no. 5, pp. 1547–1551, 2001.
- [15] D. Eder and A. H. Windle, “Morphology control of CNT-TiO₂ hybrid materials and rutile nanotubes,” *Journal of Materials Chemistry*, vol. 18, no. 17, pp. 2036–2043, 2008.
- [16] D. Eder, M. S. Motta, I. A. Kinloch, and A. H. Windle, “Anatase nanotubes as support for platinum nanocrystals,” *Physica E*, vol. 37, no. 1–2, pp. 245–249, 2007.
- [17] D. Eder, I. A. Kinloch, and A. H. Windle, “Pure rutile nanotubes,” *Chemical Communications*, no. 13, pp. 1448–1450, 2006.
- [18] D. Eder and A. H. Windle, “Carbon-inorganic hybrid materials: the carbon-nanotube/TiO₂ interface,” *Advanced Materials*, vol. 20, no. 9, pp. 1787–1793, 2008.
- [19] N. Bouazza, M. Ouzzine, M. A. Lillo-Ródenas, D. Eder, and A. Linares-Solano, “TiO₂ nanotubes and CNT-TiO₂ hybrid materials for the photocatalytic oxidation of propene at low concentration,” *Applied Catalysis B: Environmental*, vol. 92, no. 3–4, pp. 377–383, 2009.
- [20] Y. S. Sohn, Y. R. Smith, M. Misra, and V. (Ravi) Subramanian, “Electrochemically assisted photocatalytic degradation of methyl orange using anodized titanium dioxide nanotubes,” *Applied Catalysis B: Environmental*, vol. 84, no. 3–4, pp. 372–378, 2008.
- [21] R. P. Antony, T. Mathews, A. Dasgupta, S. Dash, A. K. Tyagi, and B. Raj, “Rapid breakdown anodization technique for the synthesis of high aspect ratio and high surface area anatase TiO₂ nanotube powders,” *Journal of Solid State Chemistry*, vol. 184, no. 3, pp. 624–632, 2011.
- [22] A. Tighineanu, T. Ruff, S. Albu, R. Hahn, and P. Schmuki, “Conductivity of TiO₂ nanotubes: influence of annealing time and temperature,” *Chemical Physics Letters*, vol. 494, no. 4–6, pp. 260–263, 2010.
- [23] B. D. Yao, Y. F. Chan, X. Y. Zhang, W. F. Zhang, Z. Y. Yang, and N. Wang, “Formation mechanism of TiO₂ nanotubes,” *Applied Physics Letters*, vol. 82, no. 2, pp. 281–283, 2003.
- [24] R. Yoshida, Y. Suzuki, and S. Yoshikawa, “Syntheses of TiO₂(B) nanowires and TiO₂ anatase nanowires by hydrothermal and post-heat treatments,” *Journal of Solid State Chemistry*, vol. 178, no. 7, pp. 2179–2185, 2005.
- [25] G. Mogilevsky, Q. Chen, A. Kleinhammes, and Y. Wu, “The structure of multilayered titania nanotubes based on delaminated anatase,” *Chemical Physics Letters*, vol. 460, no. 4–6, pp. 517–520, 2008.
- [26] S. Y. Chen, B. H. Zhou, W. L. Hu, W. Zhang, N. Yin, and H. Wang, “Polyol mediated synthesis of ZnO nanoparticles templated by bacterial cellulose,” *Carbohydrate Polymers*, vol. 92, no. 2, pp. 1953–1959, 2013.
- [27] F. Liu, J. Lu, J. Shen, and Z. Zhang, “Preparation of mesoporous nickel oxide of sheet particles and its characterization,” *Materials Chemistry and Physics*, vol. 113, no. 1, pp. 18–20, 2009.
- [28] M. Q. Chu and G. J. Liu, “Synthesis of liposomes-templated CdSe hollow and solid nanospheres,” *Materials Letters*, vol. 60, no. 1, pp. 11–14, 2006.
- [29] J. G. Yu, X. J. Zhao, and Q. N. Zhao, “Photocatalytic activity of nanosized TiO₂ thin films prepared by the sol-gel method,” *Materials Chemistry and Physics*, vol. 69, no. 1–3, pp. 25–29, 2001.
- [30] Q. Zhang, W. Li, and S. X. Liu, “Controlled fabrication of nanosized TiO₂ hollow sphere particles via acid catalytic hydrolysis/hydrothermal treatment,” *Powder Technology*, vol. 212, no. 1, pp. 145–150, 2011.
- [31] D.-Y. Choi, J.-Y. Park, and J.-W. Lee, “Adsorption and photocatalysis of spherical TiO₂ particles prepared by hydrothermal reaction,” *Materials Letters*, vol. 89, pp. 212–215, 2012.
- [32] G. G. Tang, D. Zhang, L. Zhao et al., “Template-free synthesis of uniform TiO₂ mesoporous microspheres with enhanced photocatalytic activity,” *Materials Letters*, vol. 118, pp. 192–195, 2014.
- [33] F. Mei, C. Liu, L. Zhang et al., “Microstructural study of binary TiO₂:SiO₂ nanocrystalline thin films,” *Journal of Crystal Growth*, vol. 292, no. 1, pp. 87–91, 2006.
- [34] M. P. Casaletto, G. M. Ingo, S. Kaciulis, G. Mattogno, L. Pandolfi, and G. Scavia, “Surface studies of in vitro biocompatibility of titanium oxide coatings,” *Applied Surface Science*, vol. 172, no. 1–2, pp. 167–177, 2001.
- [35] G. Li, Z. Q. Liu, Z. Zhang, and X. Yan, “Preparation of titania nanotube arrays by the hydrothermal method,” *Chinese Journal of Catalysis*, vol. 30, no. 1, pp. 37–42, 2009.

Research Article

Self-Shrinkage Behaviors of Waste Paper Fiber Reinforced Cement Paste considering Its Self-Curing Effect at Early-Ages

Zhengwu Jiang,¹ Xiuyan Guo,^{1,2} Wenting Li,¹ and Qing Chen¹

¹Key Laboratory of Advanced Civil Engineering Materials, Ministry of Education, Tongji University, Shanghai 200092, China

²School of Mechanical & Electrical Engineering, Jingtangshan University, Jian, Jiangxi 343009, China

Correspondence should be addressed to Zhengwu Jiang; jzhw@tongji.edu.cn

Received 10 February 2016; Revised 8 April 2016; Accepted 27 April 2016

Academic Editor: Zhouyang Xiang

Copyright © 2016 Zhengwu Jiang et al. This is an open access article distributed under the Creative Commons Attribution License, which permits unrestricted use, distribution, and reproduction in any medium, provided the original work is properly cited.

The aim of this paper was to study how the early-age self-shrinkage behavior of cement paste is affected by the addition of the waste paper fibers under sealed conditions. Although the primary focus was to determine whether the waste paper fibers are suitable to mitigate self-shrinkage as an internal curing agent under different adding ways, evaluating their strength, pore structure, and hydration properties provided further insight into the self-cured behavior of cement paste. Under the wet mixing condition, the waste paper fibers could mitigate the self-shrinkage of cement paste and, at additions of 0.2% by mass of cement, the waste paper fibers were found to show significant self-shrinkage cracking control while providing some internal curing. In addition, the self-curing efficiency results were analyzed based on the strength and the self-shrinkage behaviors of cement paste. Results indicated that, under a low water cement ratio, an optimal dosage and adding ways of the waste paper fibers could enhance the self-curing efficiency of cement paste.

1. Introduction

Because of the need of long spans, towering, and overloading and harsh conditions in modern engineering, the high-performance concrete (HPC) has been widely used in the infrastructure, such as bridges, high-rise buildings, port, and underground projects, due to the high strength and high performance [1, 2]. However, self-desiccation leading to self-shrinkage causes the early cracks of concrete, which have been recognized to be a major shortcoming of HPC [3–5].

Because of a low water-binder ratio of HPC, a large amount of unhydrated cement within concrete can attract water from the capillary and begin to hydrate. Yet external moisture is difficult to penetrate into the inside of the concrete due to the compacting concrete structure and the capillary dehydrates and forms a vacuum even, leading to the self-shrinkage of concrete. With the early hardening of concrete, the shrinkage deformation is greater than the ultimate stretching deformation, which always causes the cracking and then decreases the permeability and the carbonation resistance of concrete. Thus the self-desiccation shrinkage of concrete is closely related to the drop of its internal relative

humidity; this is confirmed in the previous studies [6–8]. In order to effectively control and improve the self-shrinkage of concrete, an absorbent polymer as a self-curing agent is developed to improve the hydration degree of concrete and reduce the compressive stress and the sensitivity to cracking [9–11].

Cellulose fibers that owned the amorphous structure are evenly dispersed in concrete, which efficiently restrain crack formation and delay crack growth [12, 13]. In addition, cellulose fibers have a nature hydrophilic property [14], which plays a key role in the concrete. Internal curing is explored from water-saturated porous cellulose fibers to provide additional curing water in the early hydration process of concrete. This strategy is effective because the additional curing water can replenish the emptying pores more quickly than traditional external curing water [15]. This process accelerates hydration of cement and then enhances the interfacial cohesiveness between cellulose fibers and cementing material, which increases the compactness, improves the permeability resistance of concrete, and gives the concrete better durability and service life [16].

Waste paper fibers (WPFs) are affiliated with cellulose fibers and have their advantages, such as an amorphous

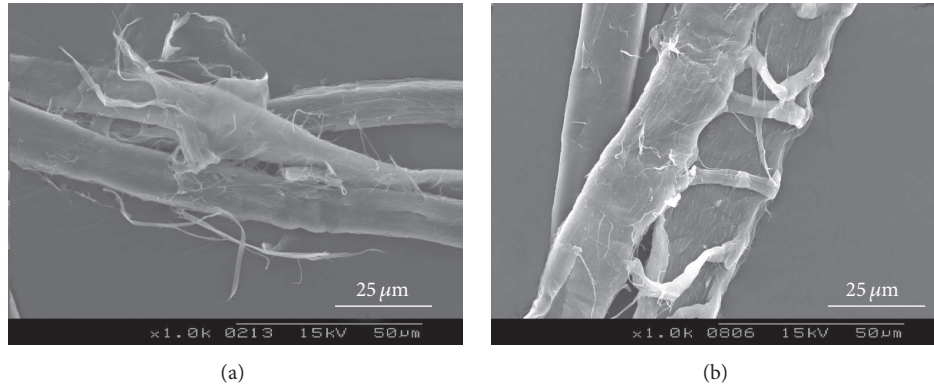


FIGURE 1: SEM surface morphologies of WPFs.

TABLE 1: Chemical component of the waste paper fibers (wt%).

Component	Cellulose	Hemicellulose	Fillers
Content (%)	~93	~5	~2

structure and a nature hydrophilic property [17]. Theoretically speaking, the WPFs can be used as a substitute for the cellulose fibers and applied in concrete. Moreover, the WPFs used in concrete do not require the use of the deinking and bleaching processes, thereby greatly reducing the emissions of hazardous substances in the wastewater [18]. Previous studies had shown that cheap WPFs could enhance the concrete [19] and reduce the dosage of cement [20]; the mechanical property and the durability of the WPFs concrete were also researched [21]. However, the use of the WPFs to enhance the shrinkage resistance and self-curing effect of concrete has not been yet reported. This research aims to contribute to filling this lack of knowledge.

It is generally known that the shrinkage of concrete is influenced by many factors except low water ratios; in order to truly reflect the self-shrinkage and self-curing behaviors of the WPFs reinforced cement-based materials, the cement paste instead of concrete is selected as the matrix which does not consider other factors. The self-shrinkage and self-curing behaviors of cement paste with the WPFs are researched in this paper. In addition, the reasonable addition ways and dosage of WPFs in cement paste at a low water cement ratio are discussed, which can provide theoretical basis for actual production.

2. Experimental

2.1. Materials. Waste paper fibers (WPFs) from newsprint were pretreated and modified surfaces in our own lab [22]. They have an average length of 1.6 mm, an average diameter of $24\ \mu\text{m}$, and a specific surface area of $2.3\ \text{m}^2/\text{g}$. The chemical content of the WPFs was listed in Table 1. From the chart, the content of cellulose was about 93%, showing that the WPFs owned good alkali resistance. The SEM surface morphologies of WPFs were shown in Figure 1. The fiber bundle was layered along the long end; many microfibrils were produced

and exist on the fiber surfaces (Figure 1(a)), and the WPF that owned porous hollow structure was shown quite clearly (Figure 1(b)), which allows it to absorb and retain water.

A Portland cement P.II 52.5 and tap water were used in all mixes, a polycarboxylic high-performance water-reducing agent (SD-600P-01) was used to adjust the workability of cement paste, and the fluidities of all the samples were controlled at $140 \pm 10\ \text{mm}$. The chemical compositions of clinker were listed in Table 2.

2.2. Mix Design. All the mixtures were designed to have a fluidity indice of $140 \pm 10\ \text{mm}$. Two main differences between the mixes were the dosage and the adding ways of the WPFs. The dosages of the WPFs were 0.1%, 0.2%, 0.3%, and 0.4% by mass of cement, respectively. Wet mixing and dry mixing were implemented at a water cement ratio of 0.3. Among them, wet mixing was that both the WPFs and the total quotas of water were weighed firstly, and then the fibers were soaked in the normed water at least 30 min until the WPFs were treated to be fully dispersible in water, at which point this mixture was mixed with cement. However, dry mixing was that the preweighed dry WPFs were mixed with cement firstly, and then suitable water was added to compound. The mix designs of cement pastes were shown in Table 3.

2.3. Testing Methods. To improve the testing accuracy, three same specimens of every curing age were prepared and tested for each sample, as described below.

2.3.1. Compressive Strength and Flexural Strength. According to the Chinese National Standard GB/T 17671-1999 [23], cement pastes were casted in $40\ \text{mm} \times 40\ \text{mm} \times 160\ \text{mm}$ molds and vibrated at the time of casting to remove air bubbles. The molded pastes were kept at temperature $20 \pm 2^\circ\text{C}$ and relative humidity exceeding 95% for 24 h and then removed from the molds. The demoulded samples were sealed with high density polypropylene film and epoxy resin sealant and then cured in a room with temperature 20°C and relative humidity 60% for the set ages. The compressive and flexural strengths of all specimens were determined using a ACE-201 strength test machine. Three same specimens of every curing age were measured and the arithmetic average

TABLE 2: Chemical components of clinker (wt%).

Components	SiO ₂	Al ₂ O ₃	Fe ₂ O ₃	CaO	MgO	SO ₃	K ₂ O	Na ₂ O	Total
Content (%)	21.74	5.06	3.56	66.6	0.88	0.81	0.55	0.05	99.25

TABLE 3: Mix proportion of cement paste.

Code	W/C	Water/(kg/m ³)	Cement/(kg/m ³)	Superplasticizer (by mass of cement)/%	WPFs dosage (by mass of cement)/%	WPFs adding way
A0	0.25	200	800	2.8	—	—
A1	0.25	200	800	3.5	0.1	Wet mixing
A2	0.25	200	800	4.2	0.2	Wet mixing
A3	0.25	200	800	5	0.3	Wet mixing
A4	0.25	200	800	5.8	0.4	Wet mixing
B0	0.3	240	800	1.8	—	—
B1	0.3	240	800	2.2	0.1	Wet mixing
B2	0.3	240	800	2.8	0.2	Wet mixing
B3	0.3	240	800	3.5	0.3	Wet mixing
B4	0.3	240	800	4.4	0.4	Wet mixing
B5	0.3	240	800	3	0.2	Dry mixing

was taken as the ultimate strength of cement paste. Based on these data, the compressive to flexural strength (σ_C/σ_F) was calculated. Finally, the central parts of specimens were dried and stored in alcoholic solution for micro measurements.

2.3.2. Self-Shrinkage Characteristics. According to the Chinese National Standard JGJ/T 70-2009 [24], all specimens were casted in the 40 mm × 40 mm × 160 mm shrinkage molds and shocked slightly at the time of casting to remove air bubbles. The molded specimens were kept at 20 ± 2°C and relative humidity exceeding 95% for 24 h and then removed from the molds and measured length (L_0). All specimens were sealed and cured under the same conditions as those mentioned above. The length of specimen cured for each age (L_t) was measured. The linear shrinkage strain of cement paste was determined according to

$$\varepsilon_{at} = \frac{L_0 - L_t}{L - L_d}, \quad (1)$$

where ε_{at} is the linear shrinkage ratio of specimen cured for t days ($t = 1, 3, 7, 28, 56, 90$); L_0 is the initial length of specimen with feeder head; L_t is the actual length of specimen cured for t days ($t = 1, 3, 7, 28, 56, 90$); L is the length of specimen (160 mm); and L_d is the sum length of two feeder heads buried in the specimen.

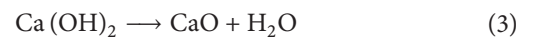
2.3.3. Hydration Characteristics

(1) TG-DSC. The contents of calcium hydroxide in the hardened cement paste were assessed by a thermogravimetry-differential scanning calorimetry (TG-DSC). To do so, the specimens were dried at 40°C for approximately 24 h; these dried specimens were crushed, pestled, and sieved, and small particles ranging from 200 μm to 500 μm were collected as samples. In a thermal analysis, about 30 mg of a sample

was put in an alumina top-opened crucible and heated from room temperature to 850°C at a rate of 10°C/min. The weight loss data and energy compensation data were determined and recorded for further analysis. Nitrogen gas was chosen as the dynamic atmosphere and corundum as the reference material.

The hydration degree of cement paste was quantitatively calculated by the thermal analysis. The following was the calculating method [25]:

$$G_t(\text{CH}) = \frac{\Delta m}{m_0} \times \frac{M_{\text{CH}}}{nM_{\text{loss}}} \times 100\% \quad (2)$$



where Δm is the loss of quality in the calculating temperature range; m_0 is the original quality; M_{loss} and M_{CH} are the molecular weights of the loss of gas (H_2O) and predicted component ($\text{Ca}(\text{OH})_2$), respectively; and n is the mole number of lost gas in one mole sample ($n = 1$).

(2) XRD. Mineral phases of cement pastes were identified by a D/max 2550VB3/PC* X-ray powder diffractometer (XRD). All samples were prepared as described above. The patterns produced using Cu-K- α radiation ($\lambda = 0.15418$ nm) at 40 kV and 100 mA were recorded in the range of 2θ at 5°~70°, in 0.02° steps, counting by 4 s per step.

2.3.4. Pore Structure. The pore structure of cement paste was determined by a mercury intrusion porosimeter (Poremaster GT-60). Pore size is related to the pressure by Washburn's equation, which assumes that the pores have circular cross sections:

$$P = \frac{-2\sigma' \cos \theta}{r}, \quad (4)$$

TABLE 4: The strengths of cement pastes at a different water cement ratio for sealed curing.

Code	W/C	WPF (%)	Flexural strength (MPa)					Compressive strength (MPa)					σ_C/σ_F				
			1 d	3 d	7 d	28 d	90 d	1 d	3 d	7 d	28 d	90 d	1 d	3 d	7 d	28 d	90 d
A0	0.25	—	10.9	11.6	10.8	8.1	17.5	72.6	88.2	90.3	104.4	113.8	6.64	7.59	8.3	12.8	6.5
A1	0.25	0.1	11.4	12.5	11.3	10.1	16.8	74.6	89.0	91.4	107.3	115.9	6.55	7.13	8.1	10.6	6.9
A2	0.25	0.2	11.8	13.2	12.9	12.6	16.5	76.9	89.4	95.0	108.0	120.5	6.5	6.8	7.3	8.6	7.3
A3	0.25	0.3	10.2	12.5	12.0	10.6	15.1	73.8	85.9	94.0	100.9	110.4	7.27	6.9	7.8	9.5	7.3
A4	0.25	0.4	8.7	9.8	9.7	9.1	14.8	71.1	82.2	86.9	94.2	103.6	7.7	8.4	8.9	10.3	7
B0	0.3	—	6.6	7.5	9.0	10.2	11.4	49.4	73.5	82.0	89.4	93.5	7.5	9.8	9.1	8.8	8.2
B1	0.3	0.1	6.0	7.7	9.5	10.4	9.9	42.0	69.4	77.8	87.1	91.5	7	9.1	8.2	8.4	9.2
B2	0.3	0.2	5.9	9.1	9.3	9.8	9.2	33.1	67.9	72.2	81.0	86.4	5.6	7.5	7.8	8.3	9.4
B3	0.3	0.3	5.6	8.6	8.9	9.2	8.5	31.2	67.6	71.8	80.0	82.1	5.6	7.9	8.1	8.7	9.7
B4	0.3	0.4	5.5	6.6	7.1	8.9	6.5	29.3	65.4	69.7	79.6	74.8	5.3	9.8	9.8	11.1	11.6

where P is the pressure exerted (N/m^2); r is the pore radius (μm); σ is the surface tension of mercury (N/m^2); and θ is the contact angle ($^\circ$).

In this study, a maximum pressure of $14 \times 10^8 \text{ N/m}^2$ was applied. The surface tension σ of 0.480 N/m and the contact angle (θ) of 140° were used for the calculation of pore size.

Small pieces of cement paste weighing 1.2 g obtained from the middle part of 60 mm cement paste specimens were used for Mercury Intrusion Porosimetry (MIP) testing. In order to stop the hydration, the specimens were dried at 105°C for approximately 24 h until a constant weight was achieved, and then they were kept in sealed containers until the day of the test. Two MIP tests were conducted for each sample, and the average values of the MIP results were used for data comparison.

3. Results and Discussion

3.1. Strength. Cement-based material is typical heterogeneous brittle materials; shrinkage cracking is one of the significant factors of its failures. To improve its brittleness, toughness is especially important. The σ_C/σ_F is one of the toughness indices of materials; the lower the σ_C/σ_F , the better the toughness and the stronger the shrinkage resistance of materials.

3.1.1. The Effect of the WPFs Dosage on Strength. WPFs were mixed with cement using wet mixing, dealing with strength, and compressive to flexural strength ratio σ_C/σ_F of samples is as shown in Table 4.

At water cement ratio of 0.25 , the flexural strengths of all samples increased in the first three days and then decreased gradually with curing age, and the decline degrees of flexural strengths were different. After curing for 28 d , the flexural strengths of all samples were greatly raised. The flexural strength of cement paste is influenced by hydration and water cement ratio. In principle, the lower the water cement ratio and the quicker the hydration process, the higher the flexural strength. The WPF has mainly an impact on the flexural strength of cement paste because of its absorbing and releasing moisture. Before sealed curing for 3 d , the

humidity dropped down and more gels were formed with hydration, which made the flexural strength of specimen increase. However, after curing for 3 d , once the negative pressure water supply occurred, the WPF would release water to compensate it. The actual water cement ratio increase caused by release moisture was likely to play a leading role. On the one hand, moisture from WPFs promoted the hydration process and improved the flexural strength further; on the other hand, it is just because released moisture increased the actual water cement ratio, causing the reduction of the flexural strength; these two contradictory factors caused the decrease of the flexural strength of specimen cured for $3\text{--}28 \text{ d}$. After curing for 28 d , the hydration forced the rapid water loss of WPFs and formed more hydration products, which caused the rapid growth of the flexural strength. When the dosages of the WPFs were $0.1\%\text{--}0.3\%$ by mass of cement, the flexural strengths of cement pastes cured for $3 \text{ d}\text{--}28 \text{ d}$ were higher than those of control samples. Among them, the dosage of the WPFs was 0.2% by mass of cement and the flexural strength of cement paste cured for 28 d was significantly the highest and increased by 55.6% . However, when the dosage of the WPFs was 0.4% , the flexural strengths of cement pastes were obviously lower than those of control samples except 28 d , and thus, under the quantity, the WPFs had a negative effect on the flexural strength. At the same water cement ratio, the compressive strengths of cement pastes increased with the dosage of the WPFs and reached highest at the dosage of 0.2% . However, the flexural strengths of cement pastes were slightly larger than those of control samples when water cement ratio was 0.3 and the dosage of the WPFs was less than 0.2% . Besides, the flexural strength and the compressive strength of cement paste decreased with the dosage of the WPFs.

Whatever water cement ratios, when the dosage of the WPFs was $0.1\%\text{--}0.3\%$ by mass of cement, the σ_C/σ_F of cement paste cured for $3 \text{ d}\text{--}28 \text{ d}$ was lower than that of standard sample. When a water cement ratio was 0.25 , the σ_C/σ_F of cement paste containing 0.2% WPFs was lowest and dropped by more than 30 percent when cement paste was cured for 28 d ; as for the WPFs dosage of 0.3% , the σ_C/σ_F of cement paste cured for 1 d was higher than that of standard sample, which could be because of experimental mistakes. However, when cement paste was cured for 90 d , the σ_C/σ_F of cement

TABLE 5: The strengths of cement pastes at a water cement ratio of 0.3 for sealed curing.

Code	WPFs (%)	Adding ways	Flexural strength (MPa)					Compressive strength (MPa)					σ_C/σ_F				
			1 d	3 d	7 d	28 d	90 d	1 d	3 d	7 d	28 d	90 d	1 d	3 d	7 d	28 d	90 d
B0	—	—	6.6	7.5	9.0	10.2	11.4	49.4	73.5	82.0	89.4	93.5	7.5	9.8	9.1	8.8	8.2
B2	0.2	Wet mixing	5.9	9.1	9.3	9.8	9.2	33.1	67.9	72.2	81.0	86.4	5.6	7.5	7.8	8.3	9.4
B5	0.2	Dry mixing	5.3	7.7	8.7	9.0	8.4	47.5	64.3	86.0	87.3	82.5	8.9	8.3	9.9	9.7	9.9

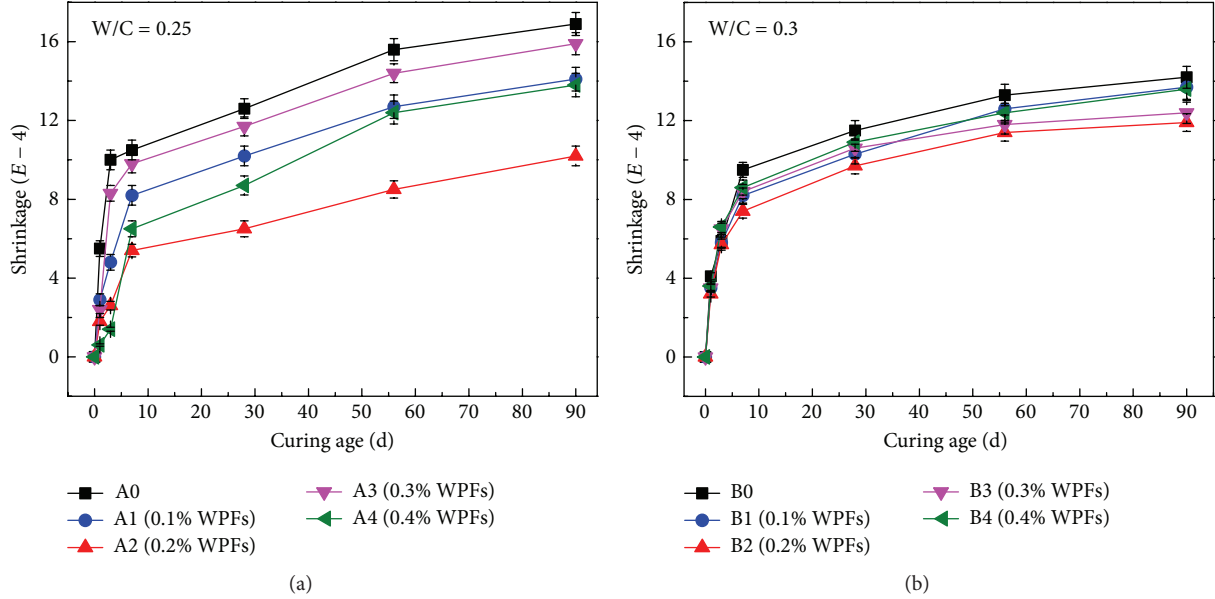


FIGURE 2: The shrinkages of cement pastes at a water cement ratio of 0.25 (a) and 0.3 (b).

paste containing WPFs was higher than that of standard sample, which means that, with the dosage of 0.1%~0.3% by mass of cement, the WPFs were able to improve the toughness of cement paste cured for early-age. The lower the water cement ratio, the better the WPFs improving the toughness of cement paste. In addition, when the dosage of the WPFs was 0.2% by mass of cement, the toughness of cement pastes cured for early-age was optimal.

3.1.2. The Effects of the WPFs Adding Ways on Strength. At water cement ratio of 0.3, the WPFs of 0.2% by mass of cement were mixed with cement using wet mixing and dry mixing, respectively. The strength and the σ_C/σ_F of cement pastes are as shown in Table 5.

Throughout these data in Table 5, the values of compressive strength had no obvious variety regulation, but when the WPFs were added with wet mixing, the flexural strengths of cement pastes (B2) were higher than those of dry mixing (B5). From σ_C/σ_F , we found that σ_C/σ_F of sample B2 cured within 28 days was lower than those of B0 and B5, which showed that the WPFs could improve the toughness of cement paste, but the degree of improvement was about the adding ways of WPFs. The adding ways of the WPFs directly affected the dispersion degree of fibers and then affected the performance of cement paste. It was difficult to disperse WPFs in the condition of dry mixing, causing WPFs to agglomerate in

matrix, which was unfavorable to improve the toughness of cement paste. Thus, compared with dry mixing, the adding way of WPFs with wet mixing was suitable.

3.2. Shrinkage Characteristics

3.2.1. The Effect of Fiber Dosage on the Self-Shrinkage. It is widely understood that adding cellulose fiber to cement-based materials can control the drying shrinkage cracking and the plastic shrinkage [26–28]. In addition, cellulose fibers can be dispersed in hydrating cement paste and have the capacity to absorb and release water to enhance the internal curing and inhibit the self-shrinkage of cement paste [15]. Figure 2 gives an overview on how the WPFs dosages affect the shrinkage of cement paste at different water cement ratios.

Figure 2(a) shows that the WPFs effectively decreased the shrinkage of cement paste at a water cement ratio of 0.25. As mentioned previously, the WPFs belong to the cellulose fibers, which could absorb some water and maintain saturated state before being mixed with cement. The humidity of matrix gradually dropped with the hydration of cement; at this point, the WPFs would release moisture to compensate it and promote the hydration further. More hydration gels were generated and growing along the surface of the WPFs-like bridge, which enhanced the strength and the shrinkage resistance. However, the reinforcing effects related to the

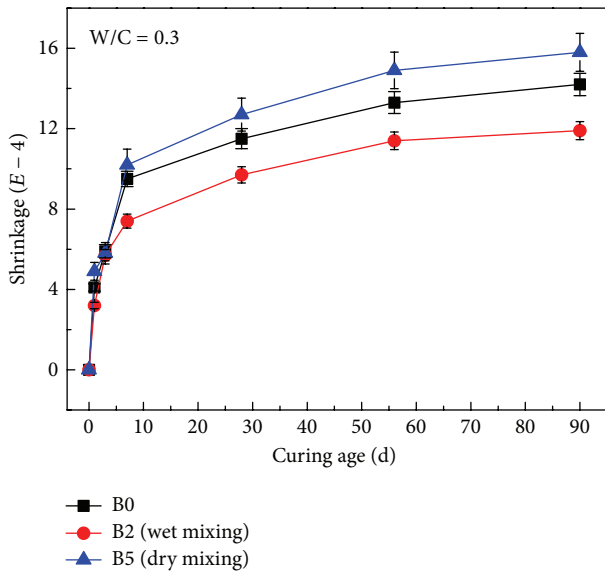


FIGURE 3: The shrinkage of cement paste containing WPFs using different adding ways.

dispersion of the WPFs. Smaller amounts of the WPFs have no effect on antishrinkage, while bigger amounts of the WPFs were not distributed in cement paste well, causing the weaker antishrinkage. When the dosage of the WPFs was 0.2% by mass of cement, the shrinkage of cement paste was lowest. The shrinkage of cement paste cured for 1 d decreased by 67% based on control sample, and when cement paste was cured for 3 d and 7 d, the shrinkages of cement paste were decreased by 74% and 50%, respectively. Although the shrinkage of cement paste containing 0.4% WPFs was also lower, the flexural strength of this sample decreased by about 30% when it was cured for 3 days (Table 3), causing the negative impact on paste, so excessive amounts of WPFs were improper.

Compared with Figure 2(a), although adding the WPFs to cement paste reduced the shrinkage of paste, the effect was obviously smaller at a water cement ratio of 0.3 (Figure 2(b)). When the WPFs dosage was 0.2% by mass of cement, similarly, the cement paste had a minimum linear shrinkage strain. When cement paste was cured for 1 d and 3 d, its shrinkage was decreased by 22.0% and 22.1% based on control sample, respectively.

Taken together with the σ_C/σ_F and the shrinkage of cement paste, the WPFs dosage of 0.2% by mass of cement is optimal in either water cement ratio, which improved the toughness and antishrinkage of cement paste. However, it is easy to see that the lower the water cement ratio, the better the antishrinkage capability of the WPFs in cement paste.

3.2.2. The Effects of Fiber Adding Ways on the Self-Shrinkage.

The WPFs dosage of 0.2% by mass of cement was mixed with cements using wet mixing and dry mixing, respectively. The linear shrinkage strain is shown in Figure 3. The WPFs were mixed with cement using dry mixing way, which increased the shrinkage of cement paste. However, using wet mixing, the WPFs decreased the shrinkage of cement paste. This

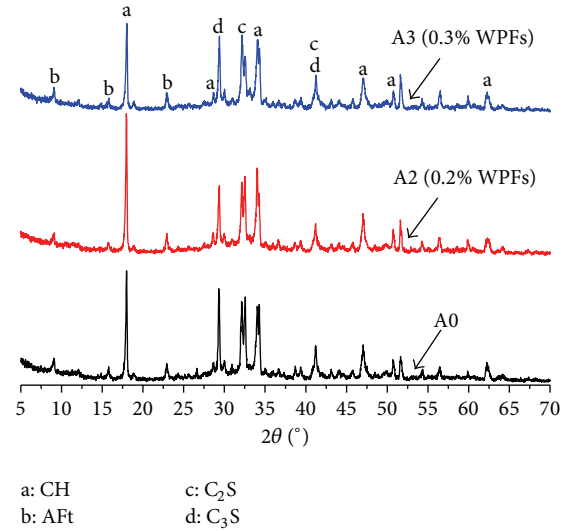


FIGURE 4: XRD patterns of cement pastes at a water cement ratio of 0.25.

illustrates that the WPFs adding way of wet mixing was better than that of dry mixing even with the same content of WPFs.

3.3. Hydration Characteristic. $\text{Ca}(\text{OH})_2$ is an important hydration product of cement-based materials. Some properties of cement-based materials, such as carbonation resistance and alkalinity, are about the content of $\text{Ca}(\text{OH})_2$. A fast rate for carbonation caused by low levels of $\text{Ca}(\text{OH})_2$ leads to the decrease of pH, inducing the corrosion of rebar in cement-based materials [29, 30]. So some levels of $\text{Ca}(\text{OH})_2$ in cement-based materials are necessary but not sufficient condition for durability.

The crystalline phase compositions of cement pastes cured for 7 d were identified by XRD, and their XRD patterns are given in Figure 4. In addition to the typical characteristic peaks of C_2S and C_3S , the cement hydration product $\text{Ca}(\text{OH})_2$ was found in all specimens. Although the diffraction peak intensity was not directly proportional to the content of crystalline phase, some important information can be obtained from comparisons of the relative intensity of $\text{Ca}(\text{OH})_2$. When cement paste was cured for 7 days, it was found that the diffraction intensity which was in $\text{Ca}(\text{OH})_2$ peak at about 18° of cement paste containing 0.2% WPFs was significantly higher than control sample and cement paste containing 0.3% WPFs; it showed that more hydration products were formed in cement paste containing 0.2% WPFs.

To further confirm the content of $\text{Ca}(\text{OH})_2$ in the hydration products, the losses of quality of cement pastes cured for 7 d are analyzed. TG-DSC patterns of the standard sample and the cement paste containing 0.2% WPFs cured for 7 d are shown in Figure 5.

From Figure 5, there was an endothermic peak near 440°C in the DSC curve of cement paste, which resulted from the dehydration of structural water from $\text{Ca}(\text{OH})_2$ [31]. According to the loss of quality in the TG curve of paste, the content of $\text{Ca}(\text{OH})_2$ in hydration products was calculated

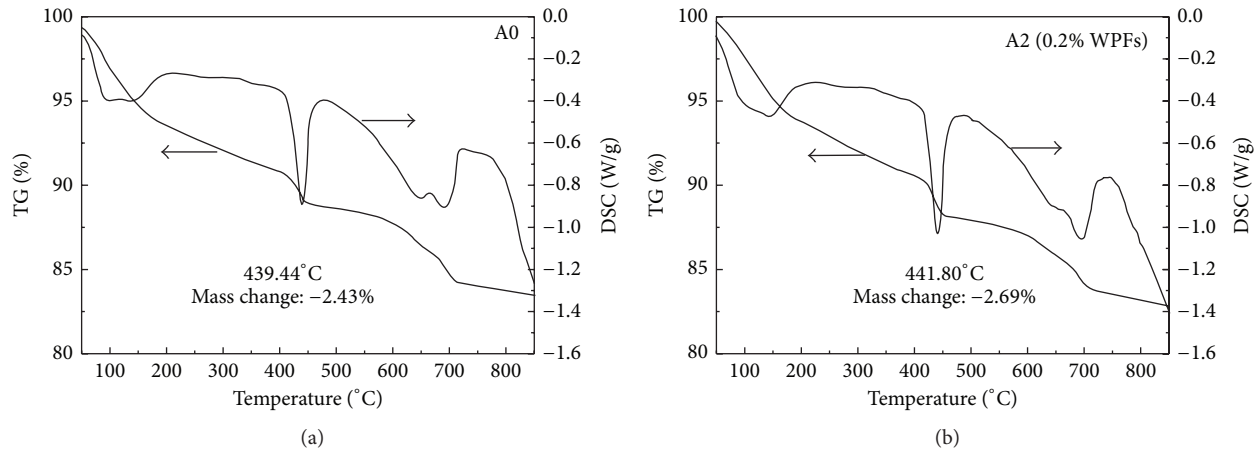


FIGURE 5: TG-DSC patterns of cement pastes cured for 7 d at a water cement ratio of 0.25.

TABLE 6: The content of $\text{Ca}(\text{OH})_2$ of cement pastes under different conditions.

Project	W/C	Adding dosage (%)	Curing age (d)	Mass change (%)	$\text{Ca}(\text{OH})_2$ (%)
A0	0.25	—	7	-2.43	9.99
A1	0.25	0.1	7	-2.48	10.20
A2	0.25	0.2	7	-2.69	11.06
A3	0.25	0.3	1	-2.24	9.21
A3	0.25	0.3	7	-2.51	10.32
A3	0.25	0.3	28	-2.67	10.98
A4	0.25	0.4	7	-2.50	10.28
B0	0.3	—	7	-2.83	11.63
B2	0.3	0.2	7	-2.87	11.80
B5	0.3	0.2	7	-2.85	11.72

B5: dry mixing; other samples: wet mixing.

and listed in Table 6. The content of $\text{Ca}(\text{OH})_2$ in hydration products continuously increased with the dosage of WPFs. When the WPFs dosage was 0.2% by mass of cement, the content of $\text{Ca}(\text{OH})_2$ of cement paste cured for 7 d increased to 11.06% from 9.99%. However, if the WPFs dosage continued to increase, the content of $\text{Ca}(\text{OH})_2$ in hydration products decreased instead. In addition, when a water cement ratio was 0.3, the content of $\text{Ca}(\text{OH})_2$ in hydration products increased with the curing age. When the cement pastes were identical in the water cement ratio, the WPFs dosage, and curing age, the content of $\text{Ca}(\text{OH})_2$ in hydration products was different because of the WPFs adding ways. The content of $\text{Ca}(\text{OH})_2$ was higher in cement paste which mixed with WPFs using wet mixing than that of using dry mixing.

3.4. Pore Structure. The compactness of cement-based materials is closely related to mechanical property and antishrinkage. The pore size distribution and pore volume are inevitable to change with the hydration process of cement paste. The

WPFs have different effect on pore structure of cement-based materials. The mercury cumulative intrusion curves and their derivatives are shown in Figure 6.

From Figure 6(a), when cured for 7 d, the cumulative intrusion of paste containing WPFs was lower than that of paste without fibers, among them, when adding 0.2% WPFs, the cumulative pore volume of cement paste was lowest. Adding the same dosage of the WPFs, the cumulative intrusion of cement paste decreased with the curing age (Figure 6(b)). The cumulative porosity of cement paste cured for different ages is shown in Table 7. With a water cement ratio of 0.25 and curing for 7 d, whatever WPFs dosage, the total porosity of sample decreased. In addition, the percentages of the pore which was smaller than 50 nm and the pore which was greater than 100 nm in the total porosity increased and decreased, respectively. Among them, the total porosity of the sample containing 0.2% WPFs decreased by 2.59% over the control sample. When the W/C and the WPFs dosage were same, the total porosity of sample decreased with the curing age; the total porosities of cement pastes cured for 7 d and 28 d decreased by 4.42% and 7.72% over cured for 1 d, respectively. With a water cement ratio of 0.3, the total porosity of paste which mixed with the WPFs using wet mixing decreased obviously in comparison with two other samples.

3.5. Self-Curing Efficiency

3.5.1. The Proposing of Self-Curing Efficiency. Through the above analysis, the WPFs could enhance toughness and self-shrinkage of cement paste. Supporting the cement paste without the WPFs as control sample, the flexural strength, compressive strength, and linear shrinkage strain were σ_{F0} , σ_{C0} , and ϵ_0 , respectively. Those of the cement paste with WPFs were σ_{Ff} , σ_{Cf} , and ϵ_f , respectively. Now drawn up η (%) as the self-curing efficiency of WPFs enhanced cement paste, in which η_1 was strength efficiency, including flexural strength efficiency η_{F1} and compressive strength efficiency η_{C1} and η_2 was shrinkage efficiency. η_1 was the ratio of the reduction of

TABLE 7: Cumulative porosity of cement paste under different conditions.

Code	W/C	Adding dosage (%)	Curing age (days)	Cumulative porosity (%)			Total porosity
				<50 nm	50 nm~100 nm	>100 nm	
A0	0.25	—	7	4.45	8.66	3.02	16.13
A1	0.25	0.1	7	4.34	8.36	2.25	14.95
A2	0.25	0.2	7	4.42	8.24	0.88	13.54
A3	0.25	0.3	1	6.10	8.99	3.85	18.94
A3	0.25	0.3	7	3.70	8.76	2.06	14.52
A3	0.25	0.3	28	2.23	7.56	1.43	11.22
A4	0.25	0.4	7	3.36	9.29	2.71	15.36
B0	0.3	—	7	6.15	7.84	5.22	19.21
B2	0.3	0.2	7	6.03	6.22	3.95	16.13
B5	0.3	0.2	7	6.34	7.43	4.89	18.66

B5: dry mixing; other samples: wet mixing.

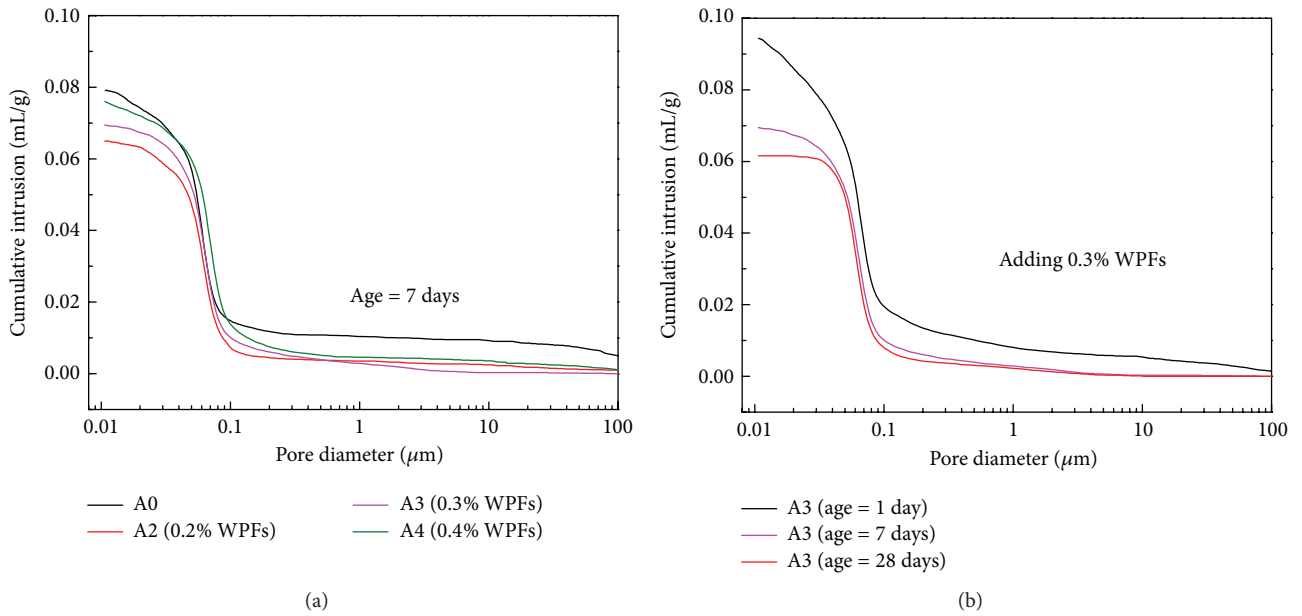


FIGURE 6: Cumulative intrusion of cement paste at a water cement ratio of 0.25.

relative strength to reference strength and η_2 was the ratio of the reduction of linear shrinkage strain to reference shrinkage strain, as shown in the following formula:

$$\begin{aligned}\eta_{F1} &= \frac{\sigma_{Ff} - \sigma_{F0}}{\sigma_{F0}} \times 100\%, \\ \eta_{C1} &= \frac{\sigma_{Cf} - \sigma_{C0}}{\sigma_{C0}} \times 100\%, \\ \eta_2 &= -\frac{\varepsilon_f - \varepsilon_0}{\varepsilon_0} \times 100\%.\end{aligned}\quad (5)$$

Suppose the WPFs are distributed evenly in the cement paste; pore systems of the prewetting WPFs and cement paste should be considered as a whole. Moisture also transfers from the large pores to tiny pores, the pore size of the WPFs is far greater than the porous size of cement paste, so the moisture from the WPFs migrates progressively to the cement

paste. The more the moisture the WPFs contain, the more the moisture transfer and the slower the relative humidity decreases, so the capillary stress and shrinkage of cement paste are smaller and the self-curing efficiency of cement paste is higher.

3.5.2. The Model of Self-Curing Efficiency. According to the formulas (5), the self-curing efficiencies of cement paste were obtained, as shown in Figure 7. Only $\eta > 0$; the WPFs were effective for the improvement of cement paste.

When water cement ratio was 0.25, WPFs could be able to enhance the self-curing efficiency of cement paste. From Figure 7(a), the flexural strength efficiency of the WPFs enhanced cement paste was best when the dosage of the WPFs was 0.2% by mass of cement. When cured for 7 d and 28 d, the flexural strength efficiencies of cement paste were increased by 19% and 56%, respectively. This means that the WPF gradually released moisture from itself and promoted

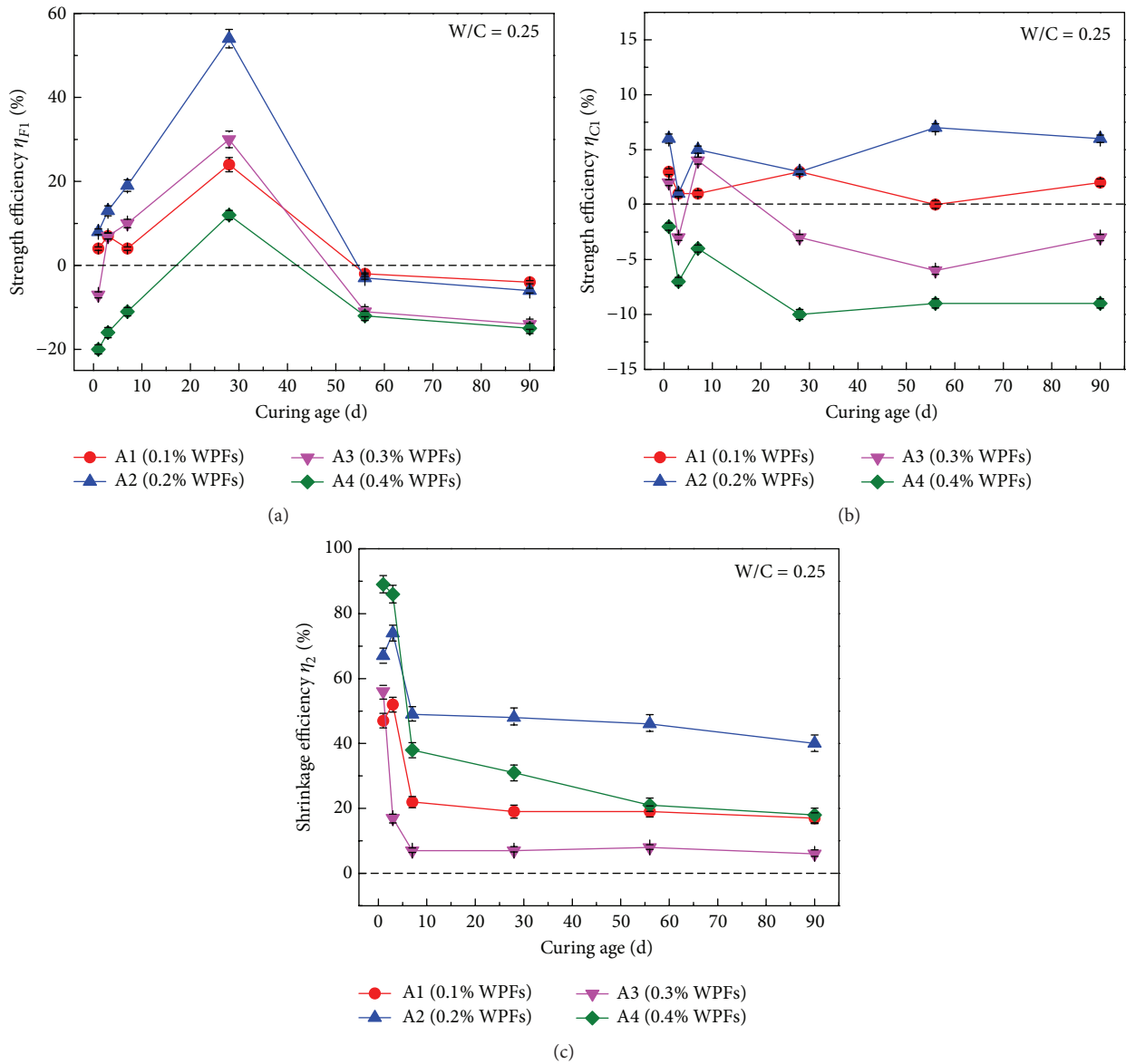


FIGURE 7: Self-curing efficiency of cement paste with WPFs at a water cement ratio of 0.25. (a) Flexural strength efficiency η_{F1} , (b) compressive strength efficiency η_{C1} , and (c) shrinkage efficiency η_2 .

the hydration of the cement paste. However, the compressive strength efficiency η_{C1} of WPFs enhanced cement paste was not obvious (Figure 7(b)). The shrinkage efficiencies of the cement paste with 0.2% WPFs cured for 1 d and 3 d were improved 67% and 74%, respectively. When cement was cured for 7 d, the shrinkage efficiency was improved 50% or so (Figure 7(c)).

Taking part of samples, nonlinear fitting η_{F1} , η_{C1} , and η_2 using least square method, the multiple regression equation about η and the dosage of WPFs x was obtained, as shown in Table 8.

According to the fiber spacing theory [32], the fiber is equal to the secondary reinforcement and can be evenly dispersed in concrete, which hinders the development of microcrack; thus the concrete structure is more compact. In

addition, it is generally known that some moisture will be consumed during the hydration process of cement. Without external water in a sealed environment, the water that the hydration reaction needs comes mainly from internal water of paste, so a water cement ratio is one of the most important factors in the hydration reaction and the shrinkage of cement paste [33, 34]. The WPF is a type of cellulose fiber, which plays a fiber bridge role in cement paste and improves the interface bonding state. Besides, the WPFs that owned porous structures (Figure 1) act as a storage reservoir, which can absorb and store moisture during mixing with cement, leading to the decrease of the effective water cement ratio. With the hydration reaction, water consumption causes self-desiccation of capillary in concrete [35]; just then the WPF releases moisture from itself to compensate the capillary and

TABLE 8: The regression equation of the self-curing efficiency of cement paste.

W/C	Age (d)	Self-curing efficiency η	Dosage of WPFs	R^2
0.25	1	$\eta_{F1} = -378.57x^2 + 100.43x - 0.3714$	$0 \leq x \leq 0.4$	0.9519
		$\eta_{C1} = -150x^2 + 55x - 0.2$	$0 \leq x \leq 0.4$	0.9239
		$\eta_2 = 5916.7x^3 - 3971.4x^2 + 864.4x - 1.1286$	$0 \leq x \leq 0.4$	0.9795
0.25	7	$\eta_{F1} = 1916.7x^3 + 621.43x^2 + 30.595x - 0.6714$	$0 \leq x \leq 0.4$	0.937
		$\eta_{C1} = -833.33x^3 + 335.71x^2 - 10.952x - 0.0857$	$0 \leq x \leq 0.4$	0.9899
		$\eta_2 = 245x - 0.8333$	$x < 0.2$	0.9965
0.25	28	$\eta_2 = 3650x^2 - 2245x + 352$	$0.2 \leq x \leq 0.4$	1
		$\eta_{F1} = -985.71x^2 + 424.29x - 1.7143$	$0.2 \leq x \leq 0.4$	0.8758
		$\eta_{C1} = -185.71x^2 + 42.286x + 0.0857$	$0.2 \leq x \leq 0.4$	0.9888
0.25	28	$\eta_2 = 240x - 1.6667$	$x < 0.2$	0.9857
		$\eta_2 = 3250x^2 - 2035x + 325$	$0.2 \leq x \leq 0.4$	1

maintain the pressure in capillary pore at higher levels during the early-age curing period of cement-based materials, accelerating the hydration reaction of cement. The self-curing efficiency of WPFs in cement paste is realized based on the above process. The lower the water cement ratio, the better the self-curing efficiency of cement pastes; this is in line with existing research results [36–38].

The dosage and adding ways of the WPFs directly affect the effective water cement ratio. Proper WPFs will release more moisture to promote the hydration and more C-S-H gels grow along the WPFs to fill the space caused by the WPFs dehydration. More capillary pores are replaced by gel pores, which decrease the total porosity of cement paste. However, with adding too little WPFs, the absorbable and releasable moisture of WPFs are limited, causing the self-curing effect to be ineffective. If there are too many WPFs or uneven dispersion by dry mixing, which absorb substantial quantities of water and reduce the water cement ratio in an indirect way, WPFs could not unevenly distribute in cement paste; the moisture from the WPFs is fail to long-distance transport in time, leading to a weakened self-curing efficiency of cement paste and a relatively low $\text{Ca}(\text{OH})_2$ production. In addition, the WPFs volume contraction after releasing water causes a plenty of spaces between the WPFs and the cementing material. These spaces form some weak spots in stress state of cement paste, which have negative impact on strength and antishrinkage of cement paste.

Based on the analysis above, under a low water cement ratio, an optimal dosage and adding ways of the WPFs could enhance the self-curing efficiency of cement paste. In this text, adding 0.2% WPFs to cement paste and wet mixing ways are optimal.

4. Conclusions

This study discussed the fact that WPFs reinforced the self-curing behavior of cement paste. The important conclusions are summarized below.

Under a low water cement ratio and wet mixing ways, the WPFs can decrease σ_C/σ_F and improve the toughness of cement paste. The lower the water cement ratio, the better the toughness of cement paste. When a water cement ratio is 0.25

and the dosage of the WPFs is 0.2% by mass of cement, the flexural strengths and the σ_C/σ_F of cement pastes cured for 28 d increase by 55.6% and decrease by 30%, respectively.

The WPFs in cement paste could promote the hydration process, decrease the cumulative pore volume, and increase the self-curing efficiency of cement paste. When water cement ratio is low and the WPFs dosage is 0.2% by mass of cement, the $\text{Ca}(\text{OH})_2$ diffraction intensity of cement paste cured for 7 d is significantly higher than other samples and increases to 11.06%.

The WPFs could enhance the self-curing efficiency of cement paste. When a water cement ratio was 0.25 and the dosage of the WPFs was 0.2% by mass of cement, the flexural strength efficiencies of cement paste cured for 7 d and 28 d were increased by 19% and 56%, respectively. The shrinkage efficiencies of the cement paste cured for 1 d and 3 d were improved 67% and 74%, respectively.

Competing Interests

The authors declare that they have no competing interests.

Acknowledgments

The authors gratefully acknowledge the financial supports provided by National Basic Research Program of China (973 Program: 2011CB013805), National Natural Science Foundation of China (51278360, 51078269), National Key Project of Scientific and Technical Supporting Programs of China (no. 2014BAL03B02, no. 2012BAJ20B02), the Specialized Research Fund for the Doctoral Program of Higher Education of China (no. 20130072110047), the science and technology program of Jiangxi province (GJJ150775), and the Fundamental Research Funds for the Central Universities.

References

- [1] T. A. Hammer, "Mix design of high strength concrete, economic design and construction with high strength concrete," Brite EuRum Projet 5480, SINTEF Structures and Concrete, 1994.
- [2] K. Mitsui, "Application of 100 MPa high strength, high fluidity concrete for prestressed concrete bridge with span-depth ratio

- of 40,” in *Proceedings of the PCI/FHWA International Symposium on High Performance Concrete*, vol. 10, pp. 669–680, New Orleans, La, USA, 1997.
- [3] B. Persson, “Self-desiccation and its importance in concrete technology,” *Materials and Structures*, vol. 30, no. 199, pp. 293–305, 1997.
- [4] Q. Yang, “Inner relative humidity and degree of saturation in high-performance concrete stored in water or salt solution for 2 years,” *Cement and Concrete Research*, vol. 29, no. 1, pp. 45–53, 1999.
- [5] A. Loukili, A. Khelidj, and P. Richard, “Hydration kinetics, change of relative humidity, and autogenous shrinkage of ultra-high-strength concrete,” *Cement and Concrete Research*, vol. 29, no. 4, pp. 577–584, 1999.
- [6] O. M. Jensen, “Thermodynamic limitation of self-desiccation,” *Cement and Concrete Research*, vol. 25, no. 1, pp. 157–164, 1995.
- [7] A. Loukili, D. Chopin, A. Khelidj, and J.-Y. Le Touzo, “New approach to determine autogenous shrinkage of mortar at an early age considering temperature history,” *Cement and Concrete Research*, vol. 30, no. 6, pp. 915–922, 2000.
- [8] O. M. Jensen and P. F. Hansen, “Influence of temperature on autogenous deformation and relative humidity change in hardening cement paste,” *Cement and Concrete Research*, vol. 29, no. 4, pp. 567–575, 1999.
- [9] M. Lopez, L. F. Kahn, and K. E. Kurtis, “Effect of internally stored water on creep of high-performance concrete,” *ACI Materials Journal*, vol. 105, no. 3, pp. 265–273, 2008.
- [10] O. M. Jensen and P. Lura, “Techniques and materials for internal water curing of concrete,” *Materials and Structures*, vol. 39, no. 293, pp. 817–825, 2006.
- [11] L. F. Pang, S. Y. Ruan, and Y. T. Cai, “Effects of internal curing by super absorbent polymer on shrinkage of concrete,” *Key Engineering Materials*, vol. 477, pp. 200–204, 2011.
- [12] G. Barluenga, “Fiber-matrix interaction at early ages of concrete with short fibers,” *Cement and Concrete Research*, vol. 40, no. 5, pp. 802–809, 2010.
- [13] R. D. Toledo Filho, K. Ghavami, M. A. Sanjuán, and G. L. England, “Free, restrained and drying shrinkage of cement mortar composites reinforced with vegetable fibres,” *Cement and Concrete Composites*, vol. 27, no. 5, pp. 537–546, 2005.
- [14] Y. Chen, J. Wan, X. Zhang, Y. Ma, and Y. Wang, “Effect of beating on recycled properties of unbleached eucalyptus cellulose fiber,” *Carbohydrate Polymers*, vol. 87, no. 1, pp. 730–736, 2012.
- [15] S. Kawashima and S. P. Shah, “Early-age autogenous and drying shrinkage behavior of cellulose fiber-reinforced cementitious materials,” *Cement and Concrete Composites*, vol. 33, no. 2, pp. 201–208, 2011.
- [16] G. H. D. Tonoli, M. N. Belgacem, G. Siqueira, J. Bras, H. Savastano Jr., and F. A. Rocco Lahr, “Processing and dimensional changes of cement based composites reinforced with surface-treated cellulose fibres,” *Cement and Concrete Composites*, vol. 37, no. 1, pp. 68–75, 2013.
- [17] G. Xiuyan, J. Zhengwu, and M. Guojin, “Property evaluation of various lignocellulosic fibers from waste paper,” *Journal of Harbin Engineering University*, vol. 36, no. 2, pp. 1–5, 2015.
- [18] M. A. Nassar, N. A. Abdelwahab, and N. R. Elhalawany, “Contributions of polystyrene to the mechanical properties of blended mixture of old newspaper and wood pulp,” *Carbohydrate Polymers*, vol. 76, no. 3, pp. 417–421, 2009.
- [19] R. S. P. Coutts, “Wastepaper fibres in cement products,” *International Journal of Cement Composites and Lightweight Concrete*, vol. 11, no. 3, pp. 143–147, 1989.
- [20] J. Pe’rea, J. Ambroise, J. Biermann, and N. Voogt, “Use of thermally converted paper residue as a building material,” in *Proceedings of the 3rd CANMET/ACI International Symposium on Sustainable Development of Cement and Concrete*, San Francisco, Calif, USA, September 2001.
- [21] B. J. Mohr, H. Nanko, and K. E. Kurtis, “Durability of kraft pulp fiber-cement composites to wet/dry cycling,” *Cement and Concrete Composites*, vol. 27, no. 4, pp. 435–448, 2005.
- [22] X. Guo, Z. Jiang, H. Li, and W. Li, “Production of recycled cellulose fibers from waste paper via ultrasonic wave processing,” *Journal of Applied Polymer Science*, vol. 132, no. 19, pp. 6211–6218, 2015.
- [23] Chinese National Standard, *GB/T 17671: Method of Testing Cements-Determination of Strength*, Chinese National Standard, Beijing, China, 1999.
- [24] Chinese National Standard, *JGJ/T 70: Standard for Test Method of Basic Properties of Construction Mortar*, Chinese National Standard, Beijing, China, 2009.
- [25] P. Wang, Y. Peng, and X. Liu, “Comparison of methods for determination of hydration degree of polymer modified cement paste,” *Journal of the Chinese Ceramic Society*, vol. 41, no. 8, pp. 1116–1123, 2013.
- [26] M. Sarigaphuti, S. P. Shah, and K. D. Vinson, “Shrinkage cracking and durability characteristics of cellulose fiber reinforced concrete,” *ACI Materials Journal*, vol. 90, no. 4, pp. 309–318, 1993.
- [27] P. Soroushian and S. Ravanbakhsh, “Control of plastic shrinkage cracking with specialty cellulose fibers,” *ACI Materials Journal*, vol. 95, no. 4, pp. 429–435, 1998.
- [28] J. R. Rapoport and S. P. Shah, “Cast-in-place cellulose fiber-reinforced cement paste, mortar, and concrete,” *ACI Materials Journal*, vol. 102, no. 5, pp. 299–306, 2005.
- [29] J. Bijen, “Benefits of slag and fly ash,” *Construction and Building Materials*, vol. 10, no. 5, pp. 309–314, 1996.
- [30] S. Ahmad, “Reinforcement corrosion in concrete structures, its monitoring and service life prediction—a review,” *Cement and Concrete Composites*, vol. 25, no. 4-5, pp. 459–471, 2003.
- [31] C. Wang, C. Yang, J. Qian, M. Zhong, and S. Zhao, “Behavior and mechanism of pozzolanic reaction heat of fly ash and ground granulated blastfurnace slag at early age,” *Journal of the Chinese Ceramic Society*, vol. 40, no. 7, pp. 1050–1058, 2012.
- [32] S. Wei and J. A. Mandel, “Effects of fiber spacing on interfacial layers,” *Journal of the Chinese Ceramic Society*, vol. 17, no. 3, pp. 266–271, 1989.
- [33] O. M. Jensen and P. F. Hansen, “Water-entrained cement-based materials—I. Principles and theoretical background,” *Cement and Concrete Research*, vol. 31, no. 4, pp. 647–654, 2001.
- [34] O. M. Jensen and P. F. Hansen, “Water-entrained cement-based materials: II. Experimental observations,” *Cement and Concrete Research*, vol. 32, no. 6, pp. 973–978, 2002.
- [35] A. Ming-zhe, Z. Jin-quan, and Q. Wei-zu, “Autogenous shrinkage of high performance concrete,” *Journal of Building Materials*, vol. 4, no. 2, pp. 159–166, 2001.
- [36] D. P. Bentz, M. R. Geiker, and K. K. Hansen, “Shrinkage-reducing admixtures and early-age desiccation in cement pastes and mortars,” *Cement and Concrete Research*, vol. 31, no. 7, pp. 1075–1085, 2001.

- [37] X. Kong and Q. Li, "Influence of super absorbent polymer on dimension shrinkage and mechanical properties of cement mortar," *Journal of the Chinese Ceramic Society*, vol. 37, no. 5, pp. 855–861, 2009.
- [38] H. Shu-Guang, Z. Yu-Fei, and W. Fa-Zhou, "Temperature controlling and monitoring for mass concrete construction of Huangpu bridge," *Journal of Huazhong University of Science and Technology*, vol. 25, no. 1, pp. 1–4, 2008 (Chinese).